

INAUGURAL-DISSERTATION

zur
Erlangung der Doktorwürde der
Naturwissenschaftlich-Mathematischen Gesamtfakultät
der
Ruprecht-Karls-Universität Heidelberg

vorgelegt von:

Frédéric F.R.M. Chesneau

aus Rouen, Frankreich

Tag der mündlichen Prüfung: 15 Juli 2011

Thema:

FABRICATION
OF METAL-INSULATOR-METAL
JUNCTIONS
FOR SPINTRONIC DEVICES
USING SELF-ASSEMBLED
MONOLAYERS

Gutachter: Pr. Dr. Michael Zharnikov
Pr. Dr. Hans-Robert Volpp

Kurzfassung

In dieser Arbeit wurden neue, effiziente und reproduzierbare Methode für die Herstellung von Metall-Isolator-Metall (MIM) Sperrschichten für Spintronik Anwendungen entwickelt. Die Sperrschichten wurden aus einem gold Substrat als unterem Kontakt, *p*-terphenyl-basierten selbstorganisierenden Monolagen (SAMs) als Isolator, und dünnen ferromagnetischen Metallschichten (nickel) als oberem Kontakt konstruiert. Unbestrahlte SAMs und Elektronenbestrahlte CL-SAMs aus [1,1':4',1''-terphenyl]-4,4''-dimethanthiol (TPDMT), (4'-(pyridin-4-yl)biphenyl-4-yl)alkanthiol (PPPn, n = 1,3) und perfluoroterphenyl-basierten alkanthiolen (FTPn, n = 2,3) auf Au(111) wurden als Testsysteme verwendet. Die Qualität von SAMs (z.B. die Dichte) war bei allen Molekülen hoch, was für nanoelektronische Anwendungen wichtig ist. Der Einfluss der Molekularen Architektur auf die Transporteigenschaften der SAMs wurde erforscht. Insbesondere wurde der Einfluss der kleinen Alkankette zwischen dem aromatischen Teil der Moleküle und dem Thiol geprüft. Durch die Alkankette wurde der aromatische Kern vom Substrat entkoppelt. Als nächstes wurde der Einfluss der Elektronenbestrahlung auf PPPn/Au und FTPn/Au SAMs erforscht. Beide SAMs wurden durch Elektronenbestrahlung stark modifiziert, besonders die Leitfähigkeit von FTPn/Au konnte durch die Kontrolle der Elektronenbestrahlung, fein eingestellt werden. Schliesslich wurde Nickel auf alle SAMs aufgedampft. Stabile, dünne Nickelschichten konnten auf SAMs aus TPDMT, CL-TPDMT, PPP1 und CL-PPP1 auf Au(111) nicht hergestellt werden. Eine Palladium Chlorid Monolage auf TPDMT/Au oder CL-PPPn/Au, konnte jedoch die Kernbildung und Wachstum einer dünnen Nickelschichte auf den jeweiligen SAMs fördern, da Nickel und Palladium eine Legierung bilden. Anschliessend wurde eine neue Klasse von dünnen Organometallischen Schichten durch die Reaktion von Nickel mit perfluorierten FTPn SAMs konstruiert. Nickel lagerte sich nur im oberen Bereich der SAMs an. Die Austrittsarbeit der FTPn SAMs, eine wichtige Eigenschaft eines Nanoelektronikgerätes, konnte durch Elektronenbestrahlung der FTPn SAMs präzise kontrolliert werden. Trotz des Verlustes von Fluor können ferromagnetische Schichten auf CL-FTPn/Au SAMs hergestellt werden. Die Eindringtiefe von Nickel in die CL-FTPn/Au SAMs nahm bei einer hohen Elektronendosis ($> 30 \text{ mC/cm}^2$) bis zu 30 % ab. FTPn SAMs sind dann besonders attraktive Systeme für die Herstellung von Nanoelektronikgeräten.

Abstract

New, efficient and reproducible methods for the fabrication of Metal-Insulator-Metal (MIM) junctions for applications in spintronic devices have been developed. The junctions consisted of a gold substrate as bottom contact, *p*-terphenyl-based self-assembled monolayers (SAMs) as insulator layer, and thin ferromagnetic metal films (nickel) as top contact. Both pristine and electron irradiated (denoted by the prefix CL-) SAMs of [1,1':4',1''-terphenyl]-4,4''-dimethanethiol (TPDMT), (4'-(pyridin-4-yl)biphenyl-4-yl)alkanethiol (PPPn, n = 1,3) and perfluoroterphenyl-substituted alkanethiols (FTPn, n = 2,3) on Au(111) were used as test systems. All molecules were found to form well-ordered, high quality SAMs, a prerequisite for the fabrication of SAM-based MIM devices. In addition, the influence of the SAMs' molecular architecture on its transport properties has been investigated. In particular, we have studied the effect of the small alkane linker (between the head group and the *p*-terphenyl backbone) found in all the molecules used in this work. The alkane linker was found act as an insulator, allowing us to decouple of the aromatic core's electronic system from the substrate. We then studied the effects of electron irradiation on PPPn/Au and FTPn/Au SAMs. Both SAMs were modified with electrons. In particular, the charge transport properties of the FTPn/Au surface could be fine-tuned simply by controlling the irradiation dose. Finally, nickel was deposited on all SAMs to test their usefulness as dielectric layers in MIM devices. Whereas nickel was found, by XPS and NEXAFS spectroscopy, to penetrate into and through the SAMs of TPDMT, CL-TPDMT, PPP1 and CL-PPP1 on Au(111), a single layer of palladium chloride, deposited from solution on either TPDMT/Au or CL-PPPn/Au, promoted the nucleation and growth of nickel thin films on top of the respective SAMs via alloying of nickel with palladium. Furthermore, reaction of nickel with the perfluorinated FTPn SAMs yielded a new class of organometallic thin films in which nickel was found to reside mainly at the top. Irradiation of the FTPn monolayers with electrons gave us precise control over the work function of the CL-FPTn/Au surfaces (a crucial parameter for the fabrication of nanoelectronic devices) while favouring the nucleation and growth of top ferromagnetic contacts. The penetration of nickel into and through CL-FPTn/Au SAMs was found to decrease by as much as 30 % at high irradiation doses ($> 30 \text{ mC/cm}^2$) making FTPn systems attractive as dielectric layers for nano junctions.

To my loving wife Muriel

"There's a fine line between wrong and visionary. Unfortunately, you have to be a visionary to see it."

— *Sheldon Cooper*, THE BIG BANG THEORY, 2010

Acknowledgements

The work presented in this thesis would not have been possible without the support and encouragement of the many friends, family and colleagues that I have had the privilege of knowing over the last eight years in England, Canada and Germany. I came to Heidelberg with a background in organic synthesis and little experience in the field of surface science. However, thanks to the constant scientific guidance of Pr. Dr. Zharnikov over the last three years, I was able to learn new techniques (XPS, NEXAFS, Kelvin probe and work at the synchrotron (BESSY II in Berlin and MaxLab in Lund, Sweden)), present my work at various conferences orally and overcome the hurdles I encountered in my project. I would especially like to thank him for letting me the freedom to try my sometimes crazy ideas.

Thanks also go to all my colleagues at the Angewandte Physikalische Chemie (APC) institute, past and present, for making my stay in Heidelberg pleasant and broadening my scientific horizons. Coming to work every day with them was always a pleasure. Equally important to me are the support staff, from the cleaners to the secretaries. Special thanks go to Mr. Meinus and Mr. Jehle for the countless hours spent helping me keep the LHS12 UHV system in top working condition, and Georg Albert for many fruitful discussions and providing the substrates used in all the experiments reported in this doctoral dissertation.

I would also like to thank Pr. Dr. Grunze for giving me the opportunity to work at the APC in Heidelberg and for his encouragement through our discussions either during the institute's weekly seminars or informally at various social gatherings.

Thanks also go to Pr. Dr. Volpp for agreeing to be my second examiner.

I also thank the Deutsche Forschungsgemeinschaft for their financial support over the past three years.

Finally, I would like to thank my wife, Muriel, for her constant support on this long journey we took together since we met almost 9 years ago now; and especially for her support over those past three years.

Contents

Kurzfassung	1
Abstract	2
Dedication	3
Quotation	4
Acknowledgements	5
Contents	6
1 Introduction	1
2 Theory	4
2.1 X-ray photoelectron spectroscopy	4
2.1.1 Elemental specificity	4
2.1.2 Surface sensitivity	5
2.1.3 Attenuation length and thickness calculation	6
2.1.3.1 Attenuation length	6
2.1.3.2 Thickness calculation	6
2.1.4 Enhancing the surface sensitivity of XPS	8
2.1.4.1 Angle-resolved XPS (ARXPS)	8
2.1.4.2 Energy-resolved XPS	8
2.2 Ultraviolet photoelectron spectroscopy	9
2.3 Inverse photoelectron emission spectroscopy	9
2.4 Near-edge X-ray Absorption Fine Structure (NEXAFS)	11
2.4.1 Introduction	11
2.4.2 Basic principle	12
2.4.3 Angle dependence of the NEXAFS signal	12
2.4.3.1 Basics	12
2.4.3.2 Linear dichroism and tilt angle	14
2.5 Ion Scattering Spectroscopy	15
2.5.1 Basic principle	15
2.5.2 Elemental selectivity	15

2.6	Contact angle goniometry	16
2.6.1	Basic principles	16
2.6.2	Advancing and receding contact angles	16
2.7	Kelvin Probe	17
2.7.1	Basic principle	17
2.7.2	Current Kelvin probe method	17
2.8	InfraRed Reflection Absorption Spectroscopy	18
3	Experimental methods	19
3.1	The LHS 12 UHV analysis and preparation station	19
3.1.1	The preparation chamber	19
3.1.2	The analysis chamber	19
3.2	Synchrotron – The experimental station	19
3.3	XPS experimental setup	20
3.3.1	XPS measurements	20
3.3.2	HRXPS measurements	20
3.3.3	Spectra fitting	21
3.4	UPS and IPES experimental setup	21
3.5	The NEXAFS experimental setup	21
3.5.1	Experimental setup	21
3.5.2	Spectra processing	22
3.6	The ion scattering spectroscopy (ISS) experimental setup	22
3.7	The contact angle goniometry experimental setup	22
3.8	Fourier transform infrared spectroscopy (FT-IR) experimental setup	22
3.9	The Kelvin probe experimental setup	23
3.10	The Scanning electron microscopy experimental setup	23
3.11	Metal evaporation	23
3.11.1	Experimental setup	23
3.11.2	Definition of a monolayer	25
3.12	Sample preparation	25
3.12.1	Substrates	25
3.12.2	Self-assembled monolayers preparation	25
3.13	Theoretical calculations	26
4	Novel SAM systems for molecular electronics	27
4.1	Introduction	27
4.1.1	Short introduction to self-assembled monolayers	27
4.1.2	Short introduction to molecular electronics	27
4.2	Terphenyl with terminal pyridine ring	29
4.2.1	Introduction	29
4.2.2	XPS characterisation of PPPn films	29
4.2.2.1	A clean SAM-ambient interface	29
4.2.3	Electronic structure and molecular orientation in PPPn films	31

4.2.3.1	Molecular orientation of PPPn films	31
4.2.4	Summary	31
4.3	Fluorinated terphenyl molecules	32
4.3.1	Introduction	32
4.3.2	Conformation of FTPn molecules in the self-assembled monolayers	33
4.3.3	Molecular orbitals and molecular orientation of FTP moieties in SAMs . .	34
4.3.3.1	General features of the NEXAFS spectrum of FTP3	34
4.3.3.2	Molecular orientation of the FTP moieties in the film	35
4.3.4	Chemical characterisation, packing density and thickness of the FTP3 films: XPS and HRXPS	39
4.3.4.1	Chemical characterisation of FTP3 films	39
4.3.4.2	Packing density and thickness of FTP3 films	39
4.3.5	Overlayer structure of FTP3 films probed by scanning tunnelling microscopy	40
4.3.6	Summary	43
4.4	The electronic structure of aromatic SAMs	44
4.4.1	HOMO-LUMO gaps measured by UPS and IPES	45
4.4.2	Relationship between the HOMO and the surface's work function	45
4.4.3	The role of the spacer in the Ant3, TP3 and FTP3 molecules	47
4.4.4	Confirmation of the trends by optical spectroscopy	49
4.4.5	Summary	51
5	Modification of SAMs by electrons	52
5.1	Irradiation induced processes in alkanethiols	54
5.1.1	Introduction	54
5.1.2	Experimental data	54
5.1.3	Discussion	57
5.1.3.1	Effect of the matrix on the branching of irradiation-induced re- actions	58
5.1.3.2	Quenching of the excited states	59
5.1.4	Summary	60
5.2	Irradiation induced processes in PPPn	62
5.2.1	Modification of the PPP1 carbon matrix upon electron irradiation	62
5.2.1.1	Changes in the hydrocarbon matrix probed by C1s HRXPS . . .	62
5.2.1.2	Rehybridisation of the matrix observed by NEXAFS spectroscopy	64
5.2.1.3	Changes in the molecular orientation of PPP1 films	65
5.2.2	Damage to the SAM-substrate interface	67
5.2.3	Changes to the SAM-ambient interface	67
5.2.3.1	Reaction pathways of PPP1 films upon electron irradiation . . .	69
5.2.3.2	Irradiation kinetics of PPP1 films	69
5.2.3.3	Extent of crosslinking of PPP1 films	70
5.2.3.4	Survival of the terminal groups of PPP1 upon irradiation	71
5.2.4	Changes in the electronic structure of PPP1 films upon electron-irradiation	71
5.2.5	Summary	72

5.3	Electron irradiation of FTPn films	73
5.3.1	Introduction	73
5.3.2	Irradiation-induced chemical changes in FTP3 films	73
5.3.2.1	The destiny of fluorine	73
5.3.3	Extensive crosslinking of FTP3 SAMs	76
5.3.3.1	Chemical evidence	76
5.3.3.2	A new electronic structure	77
5.3.4	Modification of the molecular conformation upon electron irradiation . . .	78
5.3.5	Chemistry of the SAM-ambient interface	79
5.3.6	FTPn as templates for molecular electronics	80
5.3.7	Modification of the transport properties of FTPn SAMs	81
5.3.8	Summary	82
6	Metal deposition on SAMs	84
6.1	Introduction to metal deposition on SAMs	84
6.1.1	The Metal-SAM-Metal system	84
6.1.2	Top contact formation and metal penetration	84
6.1.3	Preventing metal penetration at the SAM level	85
6.1.3.1	Reactive terminal groups	86
6.1.3.2	Closing the space - modification of the spacer	86
6.1.3.3	Reactive spacers - a novel approach	86
6.2	Metal evaporation on TPDMT SAMs	89
6.2.1	Change in the carbon matrix upon metal evaporation	89
6.2.2	Change in molecular order of CL-TPDMT SAMs upon metal evaporation	89
6.2.3	Changes to the SAM-ambient and SAM-substrate interfaces	89
6.2.3.1	Changes to the sulphur environment upon nickel evaporation . .	89
6.2.4	Estimate of the top nickel thickness	91
6.2.5	Summary	93
6.3	Metal evaporation on PPPn films	94
6.3.1	Change in the carbon matrix upon metal evaporation	94
6.3.2	Change in molecular order of CL-PPPN SAMs upon metal evaporation . .	94
6.3.3	Changes to the SAM-ambient and SAM-substrate interfaces	94
6.3.3.1	The SAM-ambient interface	95
6.3.3.2	The SAM-substrate interface	96
6.3.4	Estimate of the top nickel thickness	97
6.3.5	Summary	97
6.4	Solution-deposited metal overlayers on SAMs	99
6.4.1	Palladium on self-assembled monolayers	99
6.4.1.1	Changes to the SAM-ambient interface	99
6.4.1.2	Thickness of the palladium chloride layer	99
6.4.1.3	Changes in the molecular order of CL-PPP3 and TPDMT films upon adsorption of PdCl ₂	100
6.4.2	Evaporation of nickel on Pd/SAM films	101

6.4.2.1	Reaction of nickel with palladium	101
6.4.2.2	Changes to the SAM-ambient interface - the SAM-nickel interface	101
6.4.2.3	Changes in the molecular order of Pd/CL-PPP3 and Pd/TPDMT films upon evaporation of nickel	102
6.4.2.4	The mechanism of nickel deposition on Pd/SAM assemblies . . .	104
6.4.3	Summary	106
6.5	Metal evaporation on FTP3 SAMs	108
6.5.1	Reaction of nickel with the FTP matrix	108
6.5.1.1	Changes to the carbon matrix	108
6.5.1.2	Modification of the electronic structure	108
6.5.1.3	The nickel film	111
6.5.1.4	The fate of fluorine	111
6.5.2	Distribution of nickel through FTP3 SAMs	114
6.5.2.1	Change in average molecular order in FTP3 SAMs upon metal evaporation	114
6.5.2.2	Distribution of nickel throughout FTP3 SAMs probed by XPS .	115
6.5.3	The effect of crosslinking on metal penetration in FTP3 SAMs	117
6.5.3.1	Fluorine loss upon metal evaporation as a function of irradiation dose	117
6.5.3.2	Distribution of nickel in irradiated FTP3 SAMs probed by ARXPS	118
6.5.4	Rough estimate of the penetration depth of nickel in FTP3 SAMs	118
6.5.5	Summary of nickel deposition on FTP SAMs	119
7	Side subjects and perspectives	121
7.1	Work function and band gap of Metal-SAM-Metal systems	121
7.1.1	Modifying the work function of metal electrodes with SAMs	121
7.1.2	Change in work function upon metal deposition	122
7.1.2.1	Change in the work function of F-SAMs upon nickel deposition .	122
7.1.2.2	Summary	124
7.2	Nanoparticles on crosslinked SAMs	125
7.2.1	Introduction	125
7.2.2	Pyridine terminated monolayers for nanoparticle immobilisation	126
7.2.3	Thiol terminated monolayers for nanoparticle immobilisation	127
7.2.4	Nanoparticles as seeds for metal films on top of self-assembled monolayers	128
7.2.5	Summary	128
7.3	SAM-Metal-SAM-Metal assemblies	129
7.3.1	Introduction	129
7.3.2	SMSM systems based on FTP3 and nickel.	129
7.3.3	Summary	130
8	Conclusion	132
	Bibliography	138

A List of scientific contributions	152
A.1 Published scientific papers	152
A.2 Scientific papers in preparation	152
A.3 Conference contribution	153
List of Tables	154
List of Figures	155

Chapter 1

Introduction

The fabrication of nanoelectronic devices has been the subject of intense research in the past 20 years.¹⁻⁴ Metal-Insulator-Metal (MIM) assemblies are a promising class of such devices which, in addition to being of academic interest,^{5,6} have found applications as displays,⁷ antenna-coupled detectors⁷ and spintronic devices.⁸ Spintronic devices, which use not only the electron's charge but also its spin, bring the promise of non-volatile memory, increased processing speed (35 ns read time vs 0.1 ms for the best Solid State Drives) and lower power consumption for electronic applications.^{8,9} The current state of the art spintronic-based memory devices are capable of storing 16 Mb of data in a 2.5 cm^2 package (Everspin Technologies, Inc.). MIM devices (whether for spintronic applications or not) are usually based on dielectric layers (1-3 nm) prepared by plasma oxidation of crystalline metal films.¹⁰ The thickness of the insulating layers controls, to a large extent, the final electrical properties, magnetic properties and performance of the device.⁷ Recently, both Drew *et al.*^{11,12} and Pramanik and coworkers¹³ have successfully prepared MIM devices for spintronic applications using a 26-30 nm thick organic insulating layer *in lieu* of the metallic insulators (figure 1.1). Importantly, the spin relaxation time through the organic layers was found to be in excess of 1 second¹³ suggesting that organic materials could be used for spin transport in MIM assemblies.

MIM devices based on single molecule dielectric layers rather than bulk materials are of interest since the dielectric layer can easily and precisely be scaled in the technologically relevant low nanometre range (1-5 nm).¹⁴⁻²¹ Combined with various lithography techniques partly developed in our institute,²²⁻²⁴ the relatively high footprint-to-storage ratio of the current generation of devices could, in principle, be overcome.

Devices based on ultrathin organic films are usually fabricated using self-assembled monolayers (SAMs).^{4,25-34} Self-assembled monolayers are one molecule-thick molecular films which can be prepared from solution on a metal substrate such as gold, silver, copper, silicon or nickel.³⁴⁻⁴⁵ They can act as dielectrics as well as modulate the transport properties of a metal surface depending on their molecular architecture.^{25,46-48} While hydrocarbon monolayers decrease the work function of gold, fluorocarbon SAMs increase it.⁴⁹ For instance, fluorinated thiols can be used to decrease the hole injection barrier (HIB) between a metal electrode and a physisorbed polymer.⁵⁰ The HIB can be gradually tuned by more than 1 eV in this way⁵¹ thus giving us great control over the transport properties of the dielectric layer.

The fabrication of a suitable top metallic contact on self-assembled monolayers (e.g. by evaporation of a metal layer on top of the SAMs^{4,52,53}) remains a major stumbling block for their use in the fabrication of MIM devices for spintronics applications. Penetration of the deposited metal into and through the monolayer is undesirable since it can short circuit the top (evaporated

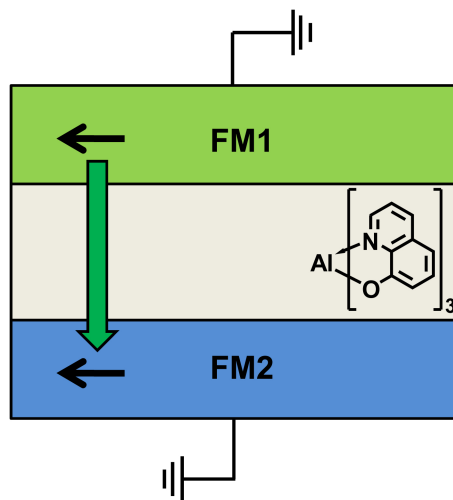


Figure 1.1: Schematic representation of an organic-based spintronic device. Black arrows indicate the spins. The transport of a spin through the insulating layer is indicated by the green arrow. The size of the insulator (in gray) was greatly exaggerated for clarity.

metal) and bottom (metallic substrate) contacts thus rendering the device inoperative. However, with the right combination of metal and monolayer, the formation of a stable top metal contact can be achieved.^{54–56} For instance, while gold, a non-magnetic metal, can be successfully immobilised on dithiol SAMs,⁵⁴ it penetrates through alkanethiol monolayers.⁵⁷ Most approaches to metal immobilisation on SAMs rely on either thiol^{26,27,54,57,58} or carboxylic acid^{55,56} terminal groups. Pyridine has also been used for the deposition of rhodium and palladium from solution using electrochemical methods.^{59–63} However, the latter approach is limited to submonolayer coverages.^{59,62} Physical vapour deposition (PVD) remains the best method for the evaporation of the continuous thin films of magnetic metals required for the fabrication of spintronic MIM devices.

The metal penetration problem was previously addressed in our group by utilising the treatment of terphenyldithiol (TPDMT, figure 1.2) monolayers with electrons.^{26,27,58,64–66} Upon irradiation with low energy electrons (≤ 50 eV), new carbon-carbon bonds between individual TPDMT molecules are formed, yielding a strong, crosslinked, quasi-polymeric organic layer (CL-TPDMT).^{24,27,37,38,67–74} This, combined with the presence of a thiol reactive group at the top of the SAMs for the nucleation and growth of metal thin films, rendered TPDMT films impermeable to nickel,^{26,27} one of the potential magnetic materials for the fabrication of spintronic devices and the metal used in our test experiments.^{11,12}

As mentioned above, for the fabrication of MIM devices, it is desirable to have control over both the thickness and the electronic properties of the insulating layer while retaining the metal impermeability. To this end, in the course of this doctoral work, the SAMs formed by two new classes of molecules, PPPn and FTPn (figure 1.2), have been characterised and tested, along with TPDMT films as reference, for the nucleation of nickel thin films on top of their respective SAMs. PPPn molecules are TPDMT analogues for which the terminal ring of the terphenyl unit has been replaced by a pyridine moiety. As well as providing nucleation sites for nickel through coordination to the nitrogen atom, pyridine, like fluorine in the FTPn systems, modulates the

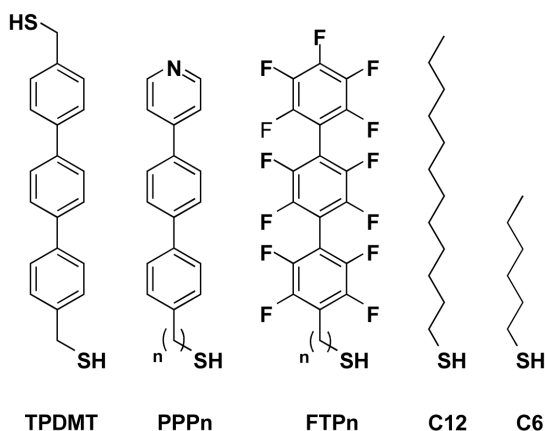


Figure 1.2: The molecules studied in this work. TPDMT: [1,1':4',1''-terphenyl]-4,4''-dimethanethiol; PPPn: ω -amino-4,4'-terphenyl substituted alkanethiols; FTPn: perfluoro-*p*-terphenyl-4-yl-alkanethiol; C12: dodecanethiol; C6: hexanethiol.

electronic properties of the SAM-modified metal surface. FTPn molecules consist of a perfluorinated *p*-terphenyl core and a short aliphatic thiol unit for attachment to metal substrates. We expect them to favour nucleation of nickel thin films via reaction of their fluorocarbon matrix with nickel atoms. The theory of the most important characterisation techniques used during the course of this doctoral work and the experimental conditions will be described in chapters 2 and 3 respectively. In chapter 4, the characterisation of the PPPn and FTPn derived SAMs will be presented along with the effect of the SAM constituents on the electronic properties of SAM covered metallic substrates. In chapter 5, the effect of low energy electron irradiation on alkanethiol, used as resists for nanodevice fabrication, PPPn and FTPn films will be discussed with special emphasis on the irradiation-induced processes for all systems. The deposition of nickel on various SAMs will be discussed in chapter 6. In particular, two new strategies based on metal alloying (on TPDMT monolayers) and reaction of nickel with the fluorocarbon matrix (FTPn) will be highlighted. Finally, future directions and prospects for this work will be proposed in chapter 7.

Chapter 2

Theory

2.1 X-ray photoelectron spectroscopy

X-ray photoelectron spectroscopy^a or XPS is one of the most widely used surface analytical techniques.⁷⁵ Using XPS, the elemental composition of a sample up to a depth of 10-20 nm can be quickly obtained. During an XPS experiment the atoms in the sample of interest (solid, liquid or gas) are excited with X-rays of a given energy $h\nu$ leading to ionisation of the atoms and emission of photoelectrons of defined kinetic energies (figure 2.1). The kinetic energy of the ejected photoelectron is characteristic of the element under study and is given by equation **2.1**.

$$KE = h\nu - BE \quad (2.1)$$

Where KE is the kinetic energy of the photoelectrons, $h\nu$ the excitation energy and BE is the binding energy of the corresponding core level. The energy scale of an XPS spectrum is typically in binding energy units (figure 2.2). The intensity of the XPS signal for a given element is described by the following equation:

$$I = N \times \sigma \times \lambda \times \cos(\theta) \times K \quad (2.2)$$

where N is the average atomic concentration of the atom under consideration, σ the ionisation cross-section as defined by Scofield,⁷⁷ θ the take-off angle and K an instrument constant that depends on several experimental factors such as the transmission function of the analyser, the yield of the detector and the photon flux.

2.1.1 Elemental specificity

As explained above, XPS is element specific. In addition, it is also sensitive to the environment of the atom under study (figure 2.2). It follows that one can not only distinguish between the different elements in a sample but also between the different species of a single element. For example, as shown in figure 2.2, it is easy to distinguish between carbon atoms bound to hydrogen and carbon atoms bound to fluorine. But it is equally easy to distinguish the various CF_n species with CF₂ and CF₃ being well resolved. The same is true for all elements.

^aFor a view of the latest trends in X-ray photoelectron spectroscopy, the reader is directed to the May 2010 issue of the *Journal of Electron Spectroscopy and Related Phenomena*.

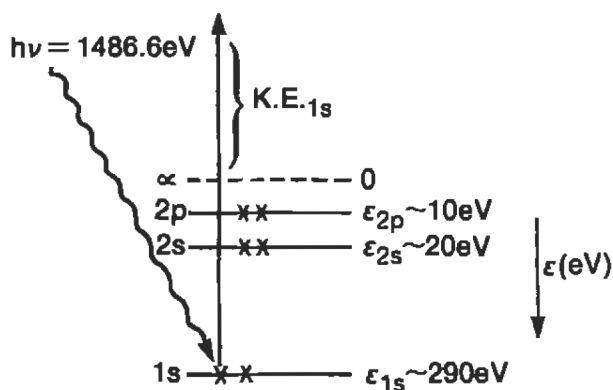


Figure 2.1: The XPS process. The photoelectrons are ejected with a kinetic energy equal to the difference between the excitation energy ($h\nu$) and the binding energy of the core electrons. The carbon energy levels are shown. The figure was taken from Brundle *et al.*⁷⁶

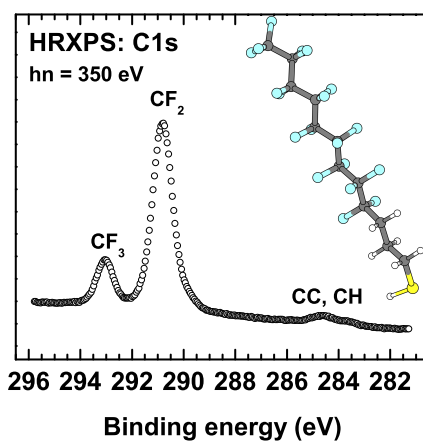


Figure 2.2: $C1s$ High Resolution XPS (HRXPS) spectrum of F10H2/Au acquired at a photon energy of 350 eV.

2.1.2 Surface sensitivity

Owing to their high probability of interaction with matter, photoelectrons originating more than a few nanometers under a sample's surface do not significantly contribute to the XPS signal.^{75,76} Indeed, in XPS, only the electrons that have not lost energy contribute to the signal. Inelastically scattered electrons contribute to the background. This process is quantitatively described by the attenuation length.

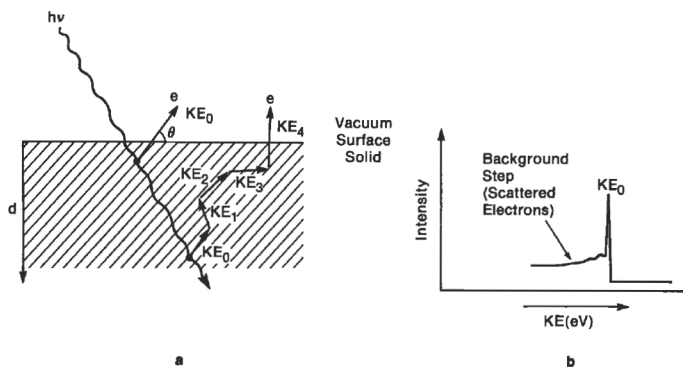


Figure 2.3: The effect of inelastic collisions of electrons in the substrate on the XPS signal. a. A scheme showing elastically and inelastically scattered electrons; b. the effect of inelastically scattered electrons on the XPS spectrum. $KE_0 > KE_1 > KE_2 > KE_3 > KE_4$. The figure was taken from Brundle *et al.*⁷⁶

2.1.3 Attenuation length and thickness calculation

2.1.3.1 Attenuation length

The attenuation length λ ^{78–81} is defined as the average distance travelled by an electron between two inelastic collisions.⁷⁵ It is derived using a model in which elastic collisions are neglected and thus differs from the inelastic mean free path (IMFP).⁸² λ varies with the kinetic energy of the electrons (for a given material) according to the so-called universal curve⁸³ (figure 2.4). However, the nature of the material through which the electrons travel also influences λ . For instance, electrons passing through a nickel matrix will be more attenuated than if they were travelling through a carbon matrix (table 2.1). The attenuation length of photoelectrons through alkanethiol self-assembled monolayers is given by:^{84,85}

$$\lambda = 0.3 \times KE^{0.64} \quad (2.3)$$

This equation holds true for a wide variety of carbon-containing thiolates on a variety of substrates and was used throughout this work. In addition to alkanethiols, attenuation lengths have been calculated for a large selection of elements and materials.^{86–91} When necessary, the literature values were used in this work. A selection of attenuation lengths is given in table 2.1.

2.1.3.2 Thickness calculation

The intensity of an XPS signal is directly related to the attenuation length of the photoelectrons (see above). This allows for the thickness of overlayers to be calculated, e.g. the thickness of a self-assembled monolayer on gold or of an evaporated metal layer on silicon. The thickness of an overlayer is typically calculated using either the attenuation of the substrate signal (equation 2.4) or the ratio between the overlayer and the substrate's signals (equation 2.5).

$$\frac{I}{I_0} = \exp - \frac{d}{\lambda_{sub} \sin \theta_{em}} \quad (2.4)$$

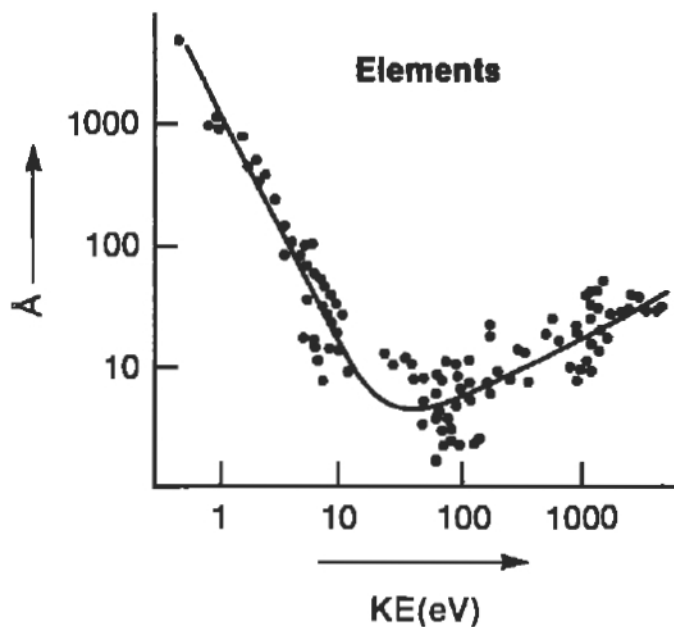


Figure 2.4: The universal curve for elements. The figure was taken from Brundle *et al.*⁷⁶

$h\nu$	350 eV		580 eV		750 eV		1254 eV	
Matrix	C	Ni	C	Ni	C	Ni	C	Ni
Ni 3p _{3/2}	9.1	5.95	14.6	9.20	18.5	11.35	29.2	17.02
Au 4f _{7/2}	8.5	5.67	14.2	8.96	18.1	11.13	28.8	16.83
S 2p _{3/2}	6.7	4.40	12.4	7.91	16.3	10.16	27.2	16.00
C 1s	3.61	2.02	9.4	6.12	13.5	8.55	24.6	14.66
N 1s			6.5	4.26	10.8	6.94	22.2	13.36
O 1s			3.5	1.61	7.5	4.90	19.3	11.81
F 1s					3.6	2.01	15.9	9.92
Ni 2p _{3/2}							13.90	7.67

Table 2.1: Selection of attenuation lengths for a carbon and a nickel matrix. All values are in Å. The data was calculated with the equation from Tanuma *et al.*⁸¹ For a complete set of data please see the NIST EAL database.⁸⁶

$$\frac{I_{ov}}{I_{sub}} = \frac{1 - \exp - \frac{d_{ov}}{\lambda_{ov} \sin \theta_{em}}}{\exp - \frac{d_{ov}}{\lambda_{sub} \sin \theta_{em}}} \quad (2.5)$$

Where d_{ov} is the overlayer thickness, θ_{em} the angle of photoelectron emission and λ_{sub} the attenuation length of the substrate's photoelectrons through the overlayer and λ_{ov} the attenuation length of the overlayer's photoelectrons through the overlayer. In the case of equation 2.4, a reference (e.g. a dodecanethiol monolayer on Au and Ag) is used to determine the thickness (equation 2.6).

$$d = d_{ref} + \lambda \ln \frac{I_{ref}}{I} \quad (2.6)$$

In the case of equation 2.5, a reference (e.g. a dodecanethiol monolayer for Au and Ag) is used to determine the spectrometer-specific coefficients and the equation is evaluated using a software developed in our research group by Martin Schmid.

2.1.4 Enhancing the surface sensitivity of XPS

In some cases, the analysis depth of XPS might still be too large. This is typically the case for inhomogeneous or layered samples for which the various elements are located within the sampling depth (3λ) of XPS. In this case, the depth distribution of the elements in the sample can not be obtained from a routine XPS measurement. However, one can overcome this limitation by making use of the properties of λ in two ways presented below.^b

2.1.4.1 Angle-resolved XPS (ARXPS)

In a typical laboratory setup, the analyser is mounted normal to the sample's plane. The path of the photoelectrons emanating from the various layers of the sample is the shortest in this geometry ($\theta_{em} = 90^\circ$, equation 2.4). By tilting the sample as shown in figure 2.5, the escape path of the photoelectrons (d in equation 2.4) is effectively lengthened. This effect is more pronounced as the layer is closer to the substrate. Figure 2.5 shows the schematic of a typical ARXPS experiment. For a more in depth explanation of angle-resolved XPS the reader is referred to several extensive reviews⁹²⁻⁹⁶ and references therein.

2.1.4.2 Energy-resolved XPS

Whereas ARXPS takes advantage of the dependence of the XPS intensity on the attenuation length, energy-resolved XPS (ERXPS) exploits the fact that λ varies with the kinetic energy of the photoelectrons. This results in a change in the sampling depth of our XPS experiment. By changing the excitation energy $h\nu$, the KE of the photoelectron varies thus reducing or increasing λ (figure 2.6). This allows us to probe the sample composition up to a given information depth since 95 % of the XPS signal intensity comes from within 3λ .

The drawback of this technique is that one needs to know how the photoionisation cross-section^{77,97-99} varies with the excitation energy to obtain meaningful quantitative information for multi-element samples.¹⁰⁰ However, this limitation should not be a problem if one is only concerned with a single element and intensity ratios are used.

^bNote that such techniques are only useful for inhomogeneous samples. There is no benefit to using these techniques on homogeneous samples.

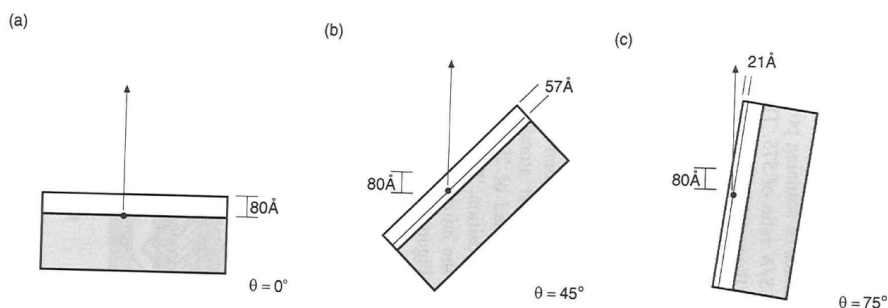


Figure 2.5: Schematic representation of an ARXPS experiment. The effective sampling depth is shown. (a) normal geometry; (b) sample rotated at a take-off angle of 45° ; (c) sample rotated at a take-off angle of 75° . The figure was taken from Ratner *et al.*⁷⁵

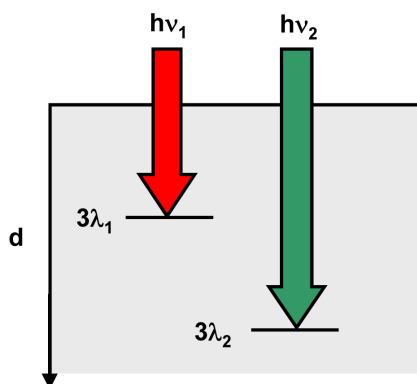


Figure 2.6: Schematic representation of an ERXPS experiment. $h\nu_1 < h\nu_2$.

2.2 Ultraviolet photoelectron spectroscopy

The principles of Ultraviolet photoelectron spectroscopy (UPS) are similar to XPS and will not be repeated here. The difference lies in the energy of the excitation radiation. In UPS, a helium lamp ($h\nu = 21.2\text{ eV}$) is typically used.⁷⁶ This means that only the electron energy levels below that of the radiation source can be measured. At such low energies, only the valence levels, and not the core levels can be probed (figure 2.7). These are distributed over the whole molecule. Consequently, UPS only probes molecular states.⁷⁶ Note that for solid surfaces, the energy distribution of photoemitted electrons varies somewhat with the direction of emission. The technique is surface sensitive and does not provide information about the bulk. For a more in depth look at UPS the reader is directed to the book by Brundle⁷⁶ and references therein.

2.3 Inverse photoelectron emission spectroscopy

In an Inverse PhotoElectron Spectroscopy (IPES) experiment, a beam of electrons of energy E is directed at a surface. Upon entering the empty states of the system, the electrons decay either

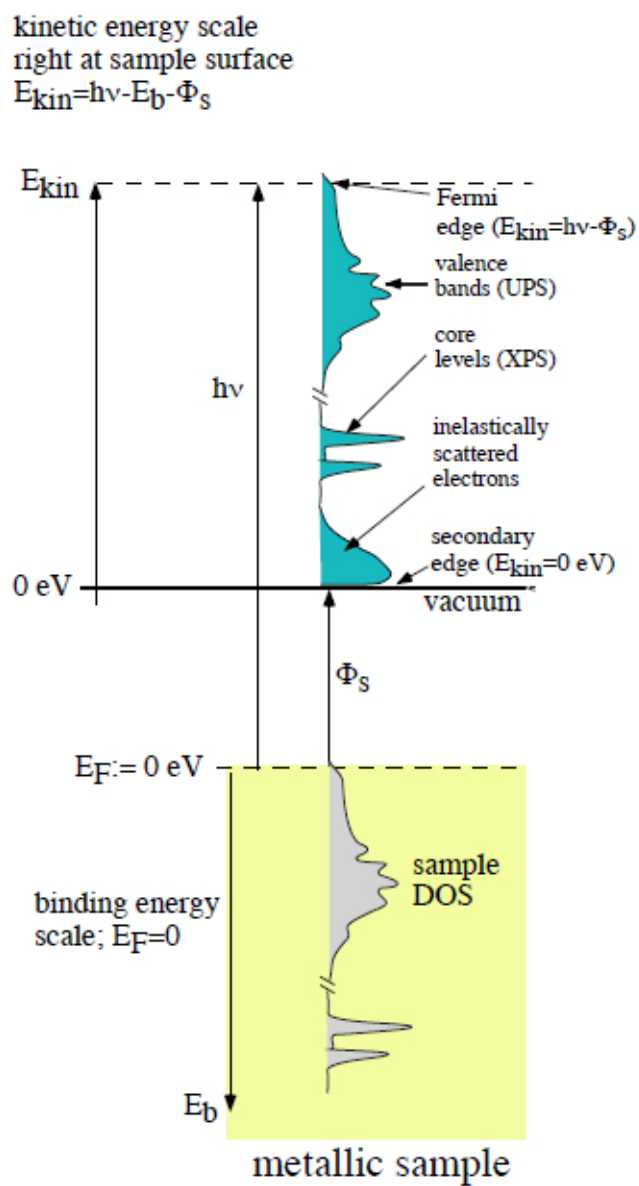


Figure 2.7: Schematic representation of an UPS experiment. The figure was taken from <http://rsl.eng.usf.edu/Pages/Tutorials.htm>.

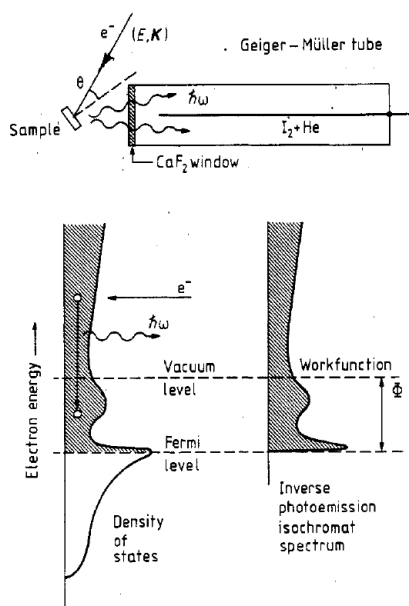


Figure 2.8: Schematic representation of an IPES experiment. The figure was taken from Smith.¹⁰¹

radiatively or non-radiatively to states of lower energy (figure 2.8).¹⁰¹ If the decay is radiative, a photon of energy corresponding to the energy difference between the incoming electron and the energy of the final state ($\hbar\omega$) can be detected.¹⁰¹ This forms the basis of IPES. IPES is complementary to UPS which probes the occupied states of a surface. By using both techniques concomitantly, the HOMO-LUMO gap of molecules immobilised on surfaces can be measured. In a typical IPES experiment, the energy of the detected photons is kept constant ($\hbar\omega = 9.7$ eV is typical) and the energy of the incoming electrons is varied. The signal intensity in an IPES experiment is typically low, being often several orders of magnitude lower than in UPS experiments.¹⁰¹ Both the electron source and the detector have to be optimised.¹⁰¹ A full treatment of this subject is beyond the scope of this thesis and the reader is referred to the review by Smith.¹⁰¹ A mathematical treatment of the technique can also be found in Smith's review.

2.4 Near-edge X-ray Absorption Fine Structure (NEXAFS)

2.4.1 Introduction

Near-edge X-ray Absorption Fine Structure (NEXAFS) spectroscopy samples the electronic structure of unoccupied molecular orbitals (figure 2.9). By doing so, it provides information about the chemical identity, i.e. bond type, of the adsorbed film. Furthermore, using the angular dependence of the transition matrix elements for resonant excitations,¹⁰² the average orientation of the constituents can be probed. Note: This section only presents a brief overview of the basic principles of NEXAFS spectroscopy; for a complete review of the NEXAFS technique, including the mathematics behind it, the reader is referred to the book by Joachim Stöhr.¹⁰²

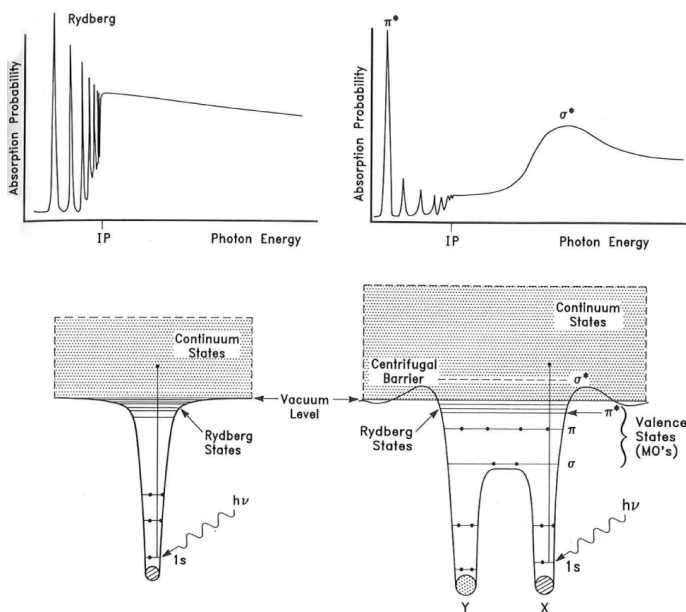


Figure 2.9: Schematic representation of the transitions probed by NEXAFS spectroscopy. The ionisation potential is marked (IP). The figure was taken from Stöhr.¹⁰²

2.4.2 Basic principle

The sample is irradiated with monochromatic X-rays (synchrotron light) of varying energies below and up to 50 eV above the ionisation potential (IP \sim 291 eV for the carbon K-edge).¹⁰³ This results in the production of electrons and photons (figure 2.10). The proportion of each depends on the relative cross-sections of the processes, the latter being atomic number dependant.¹⁰⁴ Several methods are used to quantify the NEXAFS signal as shown in figure 2.11. Of these methods, partial electron yield (PEY, used throughout this work) and Auger electron yield (AEY) are the most surface sensitive detection methods. In a NEXAFS experiment, unlike XPS, both elastically and inelastically scattered electrons are collected. In the partial electron yield method, heavily scattered, low kinetic energy electrons are excluded by applying a threshold voltage thus making the technique more surface sensitive.

2.4.3 Angle dependence of the NEXAFS signal

2.4.3.1 Basics

The absorption resonance intensity, i.e. of a C 1s \rightarrow π^* transition, depends on the orientation of the electric field vector of the synchrotron light with respect to the molecular orbital of interest (figure 2.12). The absorption resonance intensity is proportional to the square of the dot product of the electric field vector of the X-rays (\vec{E}) and the orbital vector (\vec{O} , equation 2.7).

$$I \propto |\vec{E} \cdot \vec{O}|^2 \quad (2.7)$$

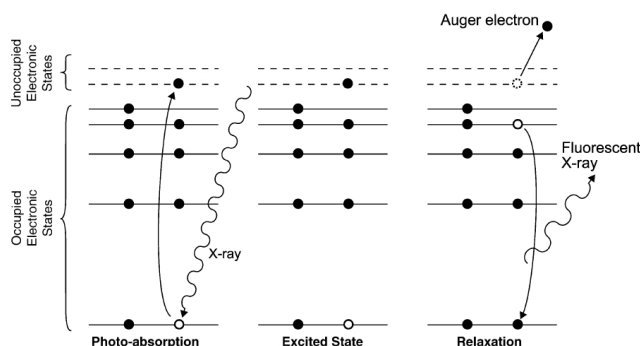


Figure 2.10: Schematic representation of the processes occurring during a NEXAFS experiment. The figure was taken from Watts *et al.*¹⁰⁴

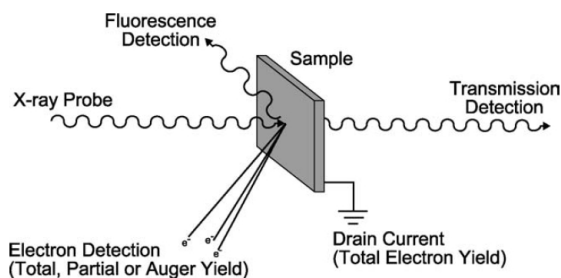


Figure 2.11: Schematic representation of the different NEXAFS measurement methods. The figure was taken from Watts *et al.*¹⁰⁴

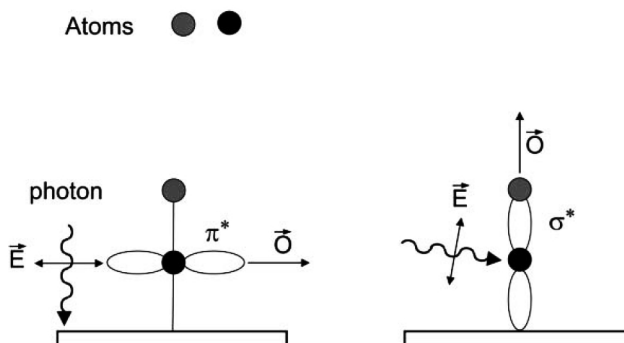


Figure 2.12: Schematic representation of the interaction of X-rays with π^* (left) and σ^* (right) orbitals of a diatomic molecule standing perpendicular to a surface. The intensity of the resonance associated with the π^* resonance is maximum if the electrical field vector of the X-rays is perpendicular to the surface ($\theta = 90^\circ$). By contrast, the intensity of the resonance associated with the σ^* resonance is maximum if the electrical field vector of the X-rays is in the grazing incidence geometry ($\theta < 30^\circ$). The figure was taken from Hähner.¹⁰³

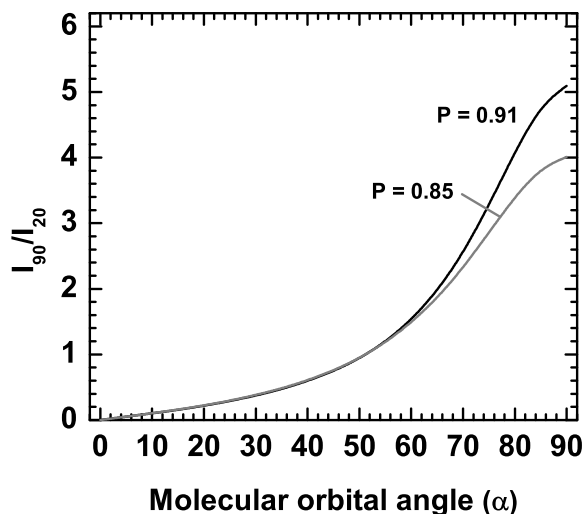


Figure 2.13: Plot of the ratio of NEXAFS intensities measured at 90° and 20° as a function of the molecular orbital angle. The data is shown for two X-ray polarisation factors.

It is evaluated according to the theoretical expression for a vector-type orbital (equation 2.8).¹⁰²

$$I(\alpha, \theta) = A \left\{ P \times \frac{1}{3} \left[1 + \frac{1}{2} (3 \cos^2(\theta) - 1) (3 \cos^2(\alpha) - 1) \right] + (1 - P) \frac{1}{2} \sin^2(\alpha) \right\} \quad (2.8)$$

where A is a constant, P is the polarisation factor of the synchrotron light, θ is the X-rays' incidence angle and α is the average tilt angle of the molecular orbital. For π^* orbitals, for which the transition dipole moment (TDM) is oriented perpendicular to the plane of the respective ring, the tilt angle of the orbital is directly related to the tilt angle of the molecular backbone β by the following formula:²³

$$\cos(\alpha) = \sin(\beta) \cos(\gamma) \quad (2.9)$$

where γ is the twist angle of the corresponding ring with respect to the plane spanned by the surface normal and the molecular axis; $\gamma = 0$ corresponds to the TDM of the π orbital laying in this plane.^{21,23}

2.4.3.2 Linear dichroism and tilt angle

A fingerprint of the orientation of molecular orbitals is the linear dichroism, i. e. the dependence of the absorption resonance intensity on the orientation of the electric field vector of the synchrotron light with respect to the molecular orbital of interest. The linear dichroism is conveniently monitored by plotting the difference of the NEXAFS spectra acquired at normal (90°) and grazing (20°) angles of X-ray incidence. In contrast, a spectrum acquired at the so-called magic angle of X-ray incidence (55° in our experiments) is not affected by any effects related to the molecular orientation and only gives information about the chemical identity of the investigated samples.¹⁰² In addition, as shown in figure 2.13, the angle of the molecular orbital of interest can be evaluated using the ratio $I(\theta)/I(20)$. An angle of 90° was used throughout this work. The molecular tilt angle can then be derived using equation 2.9.

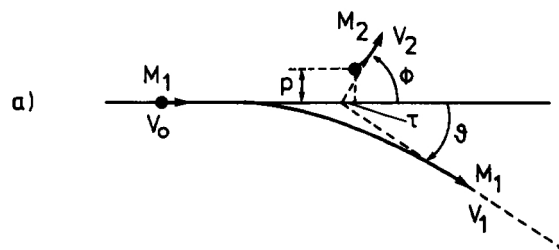


Figure 2.14: Schematic representation of an ISS experiment. p is an impact parameter; θ is the scattering angle of the ions; V_1 is the velocity of the scattered ions; ϕ is the recoil angle of the surface ions; V_2 is the velocity of the recoiled ions. The figure was taken from Niehus *et al.*¹⁰⁵

2.5 Ion Scattering Spectroscopy

Note: for a complete review of Ion Scattering Spectroscopy, the reader is directed to an extensive review by Niehus *et al.*¹⁰⁵

2.5.1 Basic principle

Ion Scattering Spectroscopy (ISS) also referred to as Low Energy Ion Scattering Spectroscopy (LEISS) is a technique which employs low energy noble gas ions (keV range). The technique is highly surface sensitive due to the high cross-sections for ion-atom interactions and the high neutralisation rate of the noble gas ions at the energies employed¹⁰⁵ and only information about the outermost atomic layer is obtained. Only ions scattered from the outermost surface give rise to sharp peaks in the ISS spectrum.

Slow sputtering of the sample and simultaneous acquisition of ISS spectra is possible provided the right gas is chosen. The nature of the gas controls both the resolution and the sputter rate.⁷⁶ For instance, carbon, nitrogen and oxygen are well resolved using $^3\text{He}^+$. The same atoms are not well resolved by $^4\text{He}^+$.⁷⁶ The sputter rate is higher if Ar^+ is used. However, no elements lower than calcium can be resolved with argon ions. Furthermore, increasing the energy of the primary ion beam also increases the sputter rate.

2.5.2 Elemental selectivity

The primary ion beam is scattered, in the case of single collisions, as shown in figure 2.14. The following equation for the energy of the scattered ions can be derived:¹⁰⁶

$$E_1 = k \times E_0 = \left(\frac{\cos \theta + \sqrt{\left(\frac{M_2}{M_1}\right)^2 - \sin^2 \theta}}{1 + \frac{M_2}{M_1}} \right)^2 \times E_0 \quad (2.10)$$

Where E_0 is the primary ion energy, E_1 is the energy of the scattered ions, θ is the scattering angle, M_1 the mass of the primary ions and M_2 the mass of the surface atoms. In our experiments, the scattering angle was fixed by the ion source-analyser geometry at $\sim 145^\circ$. This equation holds true for $\frac{M_2}{M_1} > 1$. In the case of nickel, the metal used throughout this work, $E_1 \sim 0.8 \times E_0$ using our experimental setup.

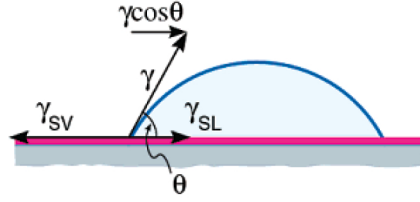


Figure 2.15: Schematic representation of a drop on a surface. The figure was taken from Tadmor.¹⁰⁹

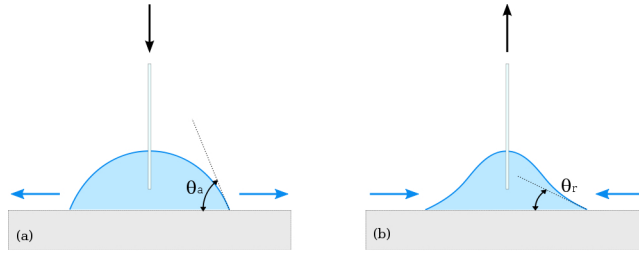


Figure 2.16: Schematic representation of the advancing and receding contact angles of a drop on a surface. The figure was taken from <http://en.wikipedia.org>.

For a more complete review of ISS, the reader is directed to the following reviews: Brongersma et al.¹⁰⁶ and Niehus et al.^{105,107} The book by Brundle⁷⁶ also contains a quick overview of the capabilities of ISS with a special emphasis on its use in industrial settings.

2.6 Contact angle goniometry

2.6.1 Basic principles

In contact angle goniometry, one measures the angle between a drop of liquid and a surface at equilibrium (θ).¹⁰⁸ The shape of the drop is defined by the properties of the liquid (L), the surface (S) and the vapour (V) as described in figure 2.15. This is described by the Young equation:

$$\gamma_{SL} + \gamma \cos \theta = \gamma_{SV} \quad (2.11)$$

where γ_{SL} is the interfacial tension between the liquid and the solid, γ is the interfacial tension between the liquid and the vapour, γ_{SV} is the interfacial tension between the solid and the vapour and θ is the equilibrium contact angle the drop makes with the surface.¹⁰⁹

2.6.2 Advancing and receding contact angles

As shown in figure 2.16, by either advancing or receding the drop on/from a surface, one can measure the advancing and receding contact angles, θ_{adv} and θ_{rec} respectively. The difference

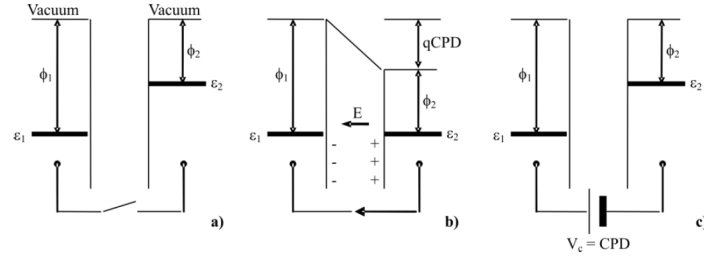


Figure 2.17: Schematic representation of a KP experiment. The figure was taken from Palermo.¹¹¹ See text for details.

between these two values gives a measure of the surface homogeneity. In practice, θ_{adv} and θ_{rec} rarely have the same value and a small hysteresis is observed.¹¹⁰ The difference between these two angles is influenced by a variety of factors, e.g. surface roughness, molecular (re)orientation and interaction between the liquid and the solid.^{108,109}

2.7 Kelvin Probe

2.7.1 Basic principle

The Kelvin Probe (KP) is used to measure the work function of surfaces. It measures the contact potential difference (CPD) between two metals brought in close proximity. The two metals do not touch thus forming a capacitor.¹¹¹ One of the two metals is the tip of the Kelvin Probe itself and the second is the sample of interest (figure 2.17(a)). If both surfaces are in electrical contact, the electrons will flow from the metal with the lowest work function to that with the highest work function (figure 2.17(b)), leading to the generation of opposite charges on the sample and the tip of the KP. The electric field thus generated is sensed and an external voltage (V_c) is applied to nullify it (figure 2.17(c)).¹¹¹ Provided that the work function of the KP's tip is known, the sample's work function can be determined by the following equation:

$$\phi_{sample} = \phi_{ref} - qV_c \quad (2.12)$$

The nature of KP measurements mean that only relative work function values can be measured. However, absolute values can be obtained through calibration with known standards such as a clean gold surface.

2.7.2 Current Kelvin probe method

Most if not all Kelvin probe apparatus sold nowadays use the vibrating capacitor setup developed by Zisman.¹¹¹ The mechanical oscillation of the KP tip induces changes in the capacitance. These produce in a small alternating current, $i(t)$, expressed according to the following equation:

$$i(t) = V_c \omega \Delta C \cos \omega \quad (2.13)$$

where V_c is the CPD, ω the frequency and ΔC the change in capacitance. An external voltage is applied until the electric field is nullified and $i(t)$ goes to zero.¹¹¹ This is the basis for the

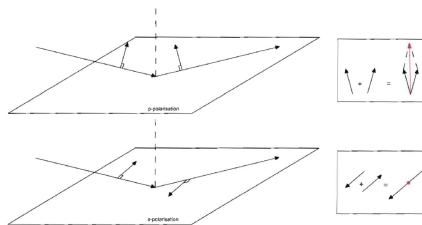


Figure 2.18: Selection rules for the reflection of the electrical component of an infrared light off of a metal surface. The sum of the electrical component vectors is shown on the right. A red point denotes a sum of zero. Top: p-polarised light, the electrical component vector is within the plane of incident light. The phase of the reflected vector is shifted by 90° with respect to the incident vector therefore, the sum of the incident and reflected electrical component vectors result in an electric field at the surface. Bottom: s-polarised light, the electrical component vector is rotated 90° with respect to the plane of incident light. The phase of the reflected vector is shifted by 180° with respect to the incident vector, therefore, the sum of the incident and reflected electrical component vectors does not result in an electric field at the surface. The figure was taken from Chesneau.¹¹³

instrument used in this doctoral work. Using this technique, work function measurements were found to be reproducible within 2 mV.

2.8 InfraRed Reflection Absorption Spectroscopy

InfraRed Reflection Absorption Spectroscopy is a kind of infrared spectroscopy performed on surface. As in a typical infrared (IR) experiment, the IR signal results from the interaction of the electromagnetic field of an infrared radiation with the oscillation dipole associated with a particular normal vibrational mode.¹¹² However, molecules on surfaces are subjected to the so-called surface selection rules (figure 2.18).

If the transition dipole moment (TDM) associated with the vibration of interest lies perpendicular to the surface or has a major component perpendicular to the surface, it will give rise to an absorption band in the IR spectrum. If the TDM lies parallel to the surface, then no absorption band will be visible for the associated vibration.

For a complete treatment of infrared spectroscopy at surfaces, the reader is directed to the book by Yates and Madey.¹¹²

Chapter 3

Experimental methods

3.1 The LHS 12 UHV analysis and preparation station

The LHS12 laboratory setup used for this work consists of one analytical chamber and two preparation chambers linked by an UFO transfer chamber (figure 3.1).

3.1.1 The preparation chamber

Only the Präp II chamber was used for preparation. This chamber was fitted with an Argon sputter gun, a 10 eV electron gun as well as a e-beam metal evaporator (Omicron) and a quartz crystal microbalance used to deposit metal and estimate the deposition rate respectively. The pressure in the chamber was typically $1\text{--}2 \times 10^{-8}$ mbar during metal evaporation and below 3×10^{-8} mbar during electron irradiation.

3.1.2 The analysis chamber

The analysis chamber was fitted with a dual anode (Mg $K\alpha$, Al $K\alpha$) X-ray source for XPS analysis, an ion gun for Ion Scattering Spectroscopy and an LHS11 hemispherical analyser. The pressure in the analysis chamber was typically below 6×10^{-10} mbar during XPS analysis. The pressure in the analysis chamber during Ion Scattering Spectroscopy measurements varied but never exceeded 5×10^{-8} mbar.

3.2 Synchrotron – The experimental station

The end station at the HE-SGM beamline at BESSY II consisted of:

- a preparation chamber fitted with an argon sputter-gun for sample cleaning, a LEED setup and a Quartz Crystal Microbalance for metal evaporation calibration
- a transfer system similar to that found in the LHS12 laboratory machine
- an analysis chamber fitted with a 10-500 eV electron gun, a Scienta R3000 analyser (XPS, Auger) and a NEXAFS detector

Synchrotron radiation produced from the BESSY II storage ring was used for excitation. The radiation was channelled to the experimental station by a set of mirror, monochromator and gratings.

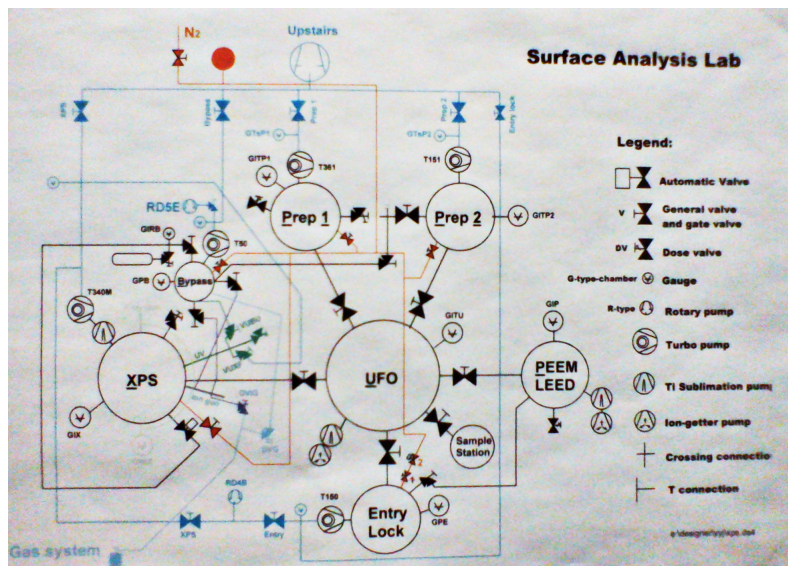


Figure 3.1: Schematic representation of the LHS12 UHV system.

3.3 XPS experimental setup

3.3.1 XPS measurements

XPS measurements were performed using a Mg $K\alpha$ X-ray source and a LHS 11 analyser. The spectra acquisition was typically carried out in normal emission geometry with an energy resolution of ~ 0.9 eV. The X-ray source was operated at a power of 240 W (HV = 12.04 kV, $I_{em} = 20$ mA) and positioned ~ 1.5 cm away from the samples. The thickness of all SAMs was determined on the basis of the I_{Au4f} intensity, assuming a standard exponential attenuation of the photoelectron signal and using the attenuation lengths reported by Lamont and Wilkes⁸⁴ in the case of alkanethiols or by Tanuma *et al.*^{89,90,114,115} for metal overlayers. The procedure was verified for several reference samples.

3.3.2 HRXPS measurements

The HRXPS experiments were performed either at the D1011 beamline (bending magnet) at the MAX II storage ring of the MAX-lab synchrotron radiation facility in Lund, Sweden or at the HE-SGM beamline (bending magnet) of the synchrotron storage ring BESSY II in Berlin, Germany, using a Scienta R3000 spectrometer. The synchrotron light served as the X-ray primary source. The spectra were acquired in normal emission geometry at photon energies of 350 and 580 eV for the C 1s, Cl2p and Ni3p regions, 350 eV for the S 2p regions, 580 eV for the N 1s and Pd 3d regions and 750 eV for the F 1s region, respectively. The energy resolution was better than 100 meV allowing a clear separation of individual spectral components (~ 0.3 eV in BESSY II). The energy width of the individual emissions was close to the intrinsic energy spread of the respective core-level photoemission process. The binding energy (BE) scale of every spectrum was individually calibrated using the Au 4f_{7/2} emission line of either the underlying Au substrate at 83.95 eV.¹¹⁶ The latter value is given by the latest ISO standard. It is very close to a value of

83.93 eV, which has been obtained by us for Au $4f_{7/2}$ using a separate calibration to the Fermi edge of a clean Pt-foil.^{116,117}

3.3.3 Spectra fitting

The fitting of the XPS and HRXPS spectra was performed using the XPSPEAK 4.1 software. All spectra were fitted by symmetric Voigt functions and a Shirley-type background. To fit the S $2p_{3/2,1/2}$ doublet we used two peaks with the same full width at half-maximum (fwhm), the standard¹¹⁸ spin-orbit splitting of ~ 1.18 eV (verified by fit), and a branching ratio of 2 ($S2p_{3/2}/S2p_{1/2}$). The fits were performed self-consistently: the same fit parameters were used for identical spectral regions.

3.4 UPS and IPES experimental setup

The ultraviolet photoemission (UPS) and inverse photoemission (IPES) spectra were taken in a single ultrahigh vacuum (UHV) chamber at room temperature. The IPES spectra were obtained by using variable kinetic energy incident electrons while detecting the emitted photons at a fixed energy (9.7 eV) using a Geiger-Müller detector. The inverse photoemission spectroscopy was limited by an instrumental linewidth of approximately 400 meV. The angle integrated photoemission (UPS) studies were carried out using a helium lamp at $h\nu = 21.2$ eV (He I) and a Phi hemispherical electron analyser with an angular acceptance of $\pm 10^\circ$ or more. The photoemission experiments were made with the photoelectrons collected along the surface normal, while the inverse photoemission spectra were taken with the incident electrons normal to the surface. This restriction of the electron emission (photoemission) or electron incidence (inverse photoemission) to the surface normal was done to preserve the highest point group symmetry and eliminate any wave vector component parallel with the surface. In both photoemission and inverse photoemission measurements, the binding energies were referenced with respect to the Fermi edge of gold in intimate contact with the sample surface and the UPS data are expressed, in terms of $E-E_F$ (thus making occupied state energies negative).

3.5 The NEXAFS experimental setup

3.5.1 Experimental setup

The NEXAFS measurements were performed at the HE-SGM beamline (bending magnet) of the synchrotron storage ring BESSY II in Berlin, Germany and at the beamline D1011 at the MAX II storage ring of the MAX-lab synchrotron radiation facility in Lund, Sweden. The results obtained at both facilities are consistent even though the shape of the spectra can be somewhat different, which is related to the individual parameters of the respective experimental setups. The spectral acquisition was carried out both at the carbon and fluorine K-edge in the partial electron yield mode with retarding voltages of -150 and -450 V, respectively. In the case of the nitrogen K-edge, a retarding voltage of -300 V was used. Linear polarised synchrotron light with polarisation factors of $\sim 91\%$ (BESSY II) or $\sim 95\%$ (MAX-lab) was used. The energy resolution was either ~ 0.40 eV (BESSY II) or better than 100 meV (MAX-lab). The incidence angle of the light was varied from 90° (\vec{E} in the surface plane) to 20° (\vec{E} nearly normal to the surface) in steps of $10\text{--}20^\circ$ to monitor the orientational order of the molecules within the films.

3.5.2 Spectra processing

The raw NEXAFS spectra were normalised to the incident photon flux by division through a spectrum of a clean, freshly sputtered gold sample. In the case of thick metal overlayers (> 3 monolayers), a spectrum of clean silver was subtracted from the raw spectrum of a SAM sample before normalisation.⁶⁴ Furthermore, the spectra were reduced to the standard form by subtracting a linear pre-edge background and normalising to the unity edge jump (determined by a nearly horizontal plateau 40-50 eV above the respective absorption edges). The energy scale was referenced to the most intense π^* resonance of highly oriented pyrolytic graphite (HOPG) at 285.38 eV.¹¹⁹ For the absolute energy calibration of the F K-edge NEXAFS spectra, we utilised the apparent shift in the position of the Au 4f_{7/2} core level of a clean Au wafer on going from the beamline settings used for the C K-edge NEXAFS data collection to those for the F K-edges; a similar approach was previously used for the measurement of NEXAFS spectra of proteinogenic α -amino acids and nucleobases.¹²⁰ The resultant energy positions are expected to be accurate and reproducible to within ± 0.05 eV.

3.6 The ion scattering spectroscopy (ISS) experimental setup

ISS measurements were performed with a focused ion gun (Leybold-Heraeus) and a LHS 11 analyser (CRR = -4). Under the conditions of our experiments the primary ion beam (He^+ , MESSER 99.999%) was accelerated to 1 keV and operated at a current of -150 nA/cm². The beam was focused to a spot with a diameter of ca. 500 μm by two focal lenses and rastered over a 2×2 mm² area. The angle between the primary beam and the sample surface was 35° , i.e. the scattering angle of the He^+ ions was 145° . The depth profiles of Ni and Au were measured by sequential acquisition of the ISS spectra with an energy window from 700 to 1000 eV during the erosion of the samples by the ISS beam; both the Ni and Au signals were recorded in a single scan.

3.7 The contact angle goniometry experimental setup

Advancing and receding contact angles of millipore water were measured on freshly prepared samples using a Kruss goniometer, Model G1. The measurements were performed under ambient conditions with the needle tip in contact with the drop. At least three measurements at different locations on each sample were made. The averaged values are reported. Deviations from the average were less than $\pm 1^\circ$.

3.8 Fourier transform infrared spectroscopy (FT-IR) experimental setup

Infrared absorption spectra of the target SAMs were measured in reflection mode using a Vertex 70 Fourier transform spectrometer (Bruker) equipped with a liquid-nitrogen-cooled mercury-cadmium-telluride detector. The spectra were taken using p-polarised light incident at a fixed angle of 80° with respect to the surface normal. The spectra were acquired at 2 cm⁻¹ resolution with accumulation of 1024 scans over the 4000-700 cm⁻¹ spectral range. The spectra are reported in absorbance units $A = \log(R/R_0)$, where R is the reflectivity of the substrate with the monolayer and R_0 is the reflectivity of the reference. Substrates covered with a perdeuterated

octadecanethiolate SAM were used as reference. The reference spectra of the bulk compounds were measured in ATR mode using a diamond cell on a Nicolet 6700 spectrometer.

3.9 The Kelvin probe experimental setup

Work function (WF) measurements were carried out using the Kelvin probe (KP) fitted in the Praep I chamber of the LHS12 experimental setup in Heidelberg (KP Technology Ltd, Caithness, UK). The voltage between the tip and the sample was varied from -7000 mV to 7000 mV in one step. The work function (at $V = 0$ mV) was then extrapolated from those measurements. A gradient value of ~ 300 was used for all measurements. The error in the measurements was typically lower than 3 mV.

Absolute work function values for self-assembled monolayers (SAMs) and Metal-SAM-Metal (MSM) systems were determined as follows:

1. the work function of the SAM-covered surface or Metal-SAM-Metal (MSM) assemblies was measured
2. the SAM or MSM assembly was sputtered away using argon (6kV, 10 mA, 10^{-5} mbar). Typical sputter times are 5-10 minutes for a SAM and 20-25 min for a MSM assembly
3. the work function of the clean metallic substrate was measured until the value stopped rising. The rise in the work function with time is a consequence of the argon sputtering. The WF of the clean substrate was found to vary by ~ 100 mV. Alternatively, the sample was irradiated for 1-2 min with 10 eV electrons (Dose ~ 0.3 mC/cm²)
4. the absolute WF was then calculated as follows: $WF_{sample} = WF_{substrate, lit.} + (WF_{sample} - WF_{substrate})_{measured}$

The error in the absolute work function is, owing to the non-homogeneity of our surfaces, 50-100 mV and is typical for work function measurements.

3.10 The Scanning electron microscopy experimental setup

The imaging of the fabricated patterns and nanoparticle assemblies was conducted using a LEO 1530 scanning electron microscope (SEM). The e-beam energy was 5 keV; the residual gas pressure was $\sim 5 \times 10^{-6}$ mbar.

3.11 Metal evaporation

3.11.1 Experimental setup

Nickel (Goodfellow, 99.999% purity) was evaporated using an Omicron electron-beam evaporator fitted with a W/Ta filament. The evaporator was placed 15-17 cm away from the sample. The deposition rate (figure 3.2) and deposition spot were calibrated using a quartz crystal microbalance (QCM). The rate of change of the quartz' frequency was measured and converted to the deposition rate using the following formula:[?]

$$\Delta T_f = \frac{K \times \Delta f}{d_f} \quad (3.1)$$

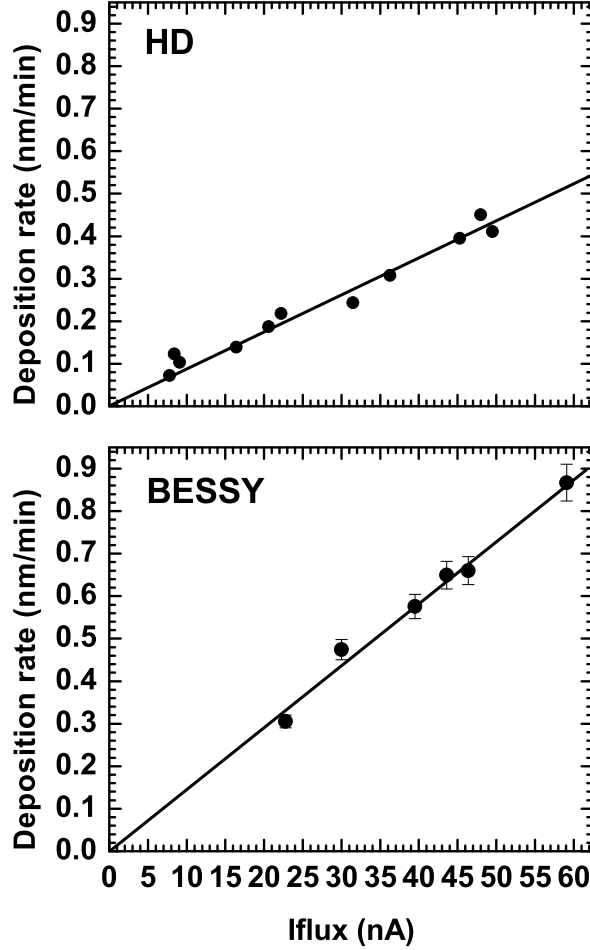


Figure 3.2: Metal evaporator calibration performed with a QCM. Nickel was used as metal. Top panel: the evaporator in Heidelberg; Bottom panel: the evaporator in BESSY.

$$K = \frac{N_{at} \times d_q}{f_q^2} \quad (3.2)$$

where T_f is the rate of deposition in $\text{\AA}/\text{min}$, Δf the rate of deposition in Hz/min , N_{at} the frequency constant of the AT cut quartz crystal (166,100 $\text{Hz}\cdot\text{cm}$), d_q the density of the quartz single crystal (2.695 g/cm^3), d_f the density of the film (8.9 g/cm^3 for nickel) and f_q the native frequency of the quartz (6.0 MHz). In BESSY, the geometry of the sample and QCM are similar ($\sim 45^\circ$ with respect to the evaporator) therefore the rates determined by QCM were used as is. However, in our laboratory set-up in Heidelberg (HD), while the geometry between the QCM and the metal evaporator is fixed ($\sim 90^\circ$), the angle between the sample and the evaporator is not. Therefore, if the metal was deposited in a geometry different from that of the QCM, a correction factor was applied. In a typical experiment in HD, the angle between the sample and the metal evaporator was $\sim 20^\circ$. We found that at this geometry, the metal deposition rate (verified by ISS and XPS) was about half of that calibrated with the QCM. In all cases, in BESSY and HD, the metal doses were checked using the substrate's strongest XPS line (e.g. Au $4f_{7/2}$ in the case of

	Solvent	Time (h)	Temp.	EtOH shake	Rinse
Alkanethiols	EtOH	24	RT	no	EtOH
F10H2	EtOH	24	RT	no	EtOH
TPn	THF	24	RT	yes	EtOH
TPDMT	THF	24	RT, 55°C	yes	EtOH
PPPn	EtOH	24	RT	no	EtOH
FTPn	THF	2-24	RT	yes	EtOH

Table 3.1: Preparation conditions for the samples used in the present work. THF: tetrahydrofuran; EtOH: ethanol; TPDMT: [1,1':4',1''-terphenyl]-4,4''-dimethanethiol; TPn: e.g. TP2: p-terphenyl-4-ethanethiol; PPPn: e.g. PPP1: (4-(4-(4-pyridyl)phenyl)phenyl)methanethiol; FTPn: e.g. FTP3: perfluoro-p-terphenyl-4-butanethiol; F10H2: 3,3,4,4,5,5,6,6,7,7,8,8,9,9,10,10,11,11,12,12,12-henicosafuorododecane-1-thiol.

gold) as described in section 2.1.3.2. The metal doses determined by XPS were within 0.1-0.2 nm of the QCM calibrated values, well within the error of our experiments and calculations.

3.11.2 Definition of a monolayer

A monolayer of nickel, the metal used in our studies, was taken as the spacing between two Ni(111) planes. Thus, one monolayer of nickel is equal to 0.2 nm or $1.2 \times 10^{16} \text{ cm}^{-2}$.

3.12 Sample preparation

3.12.1 Substrates

The gold substrates were prepared by thermal evaporation of 30-100 nm of gold (99.99% purity) onto polished single-crystal silicon (100) wafers (Silicon Sense) primed with a 5 nm titanium adhesion layer (rate 2 nm/s, temp. 340°C). The resulting metal substrates were polycrystalline, with predominant (111) orientation and a grain or terrace size of 20-50 nm.

3.12.2 Self-assembled monolayers preparation

The SAMs were prepared by immersion of the freshly prepared substrates into a 1 mM solution of the desired compound at room temperature, typically for 24 h. After immersion, the samples were carefully rinsed with pure solvent and blown dry with argon. If not used immediately, the samples were stored in Petri dishes flushed with argon, sealed with parafilm and protected from light. SAMs stored in this way proved stable over several months. Table 3.1 summarises the preparation conditions for the SAMs used in this work. We found the shake in ethanol to be crucial in order to obtain consistently good quality samples for SAMs prepared from THF. For these SAMs, the samples needed to be transferred quickly ($< 10 \text{ s}$) into an ethanol solution and shaken vigorously in order to dilute the residual THF film. After $\sim 1 \text{ min}$, the sample could be removed from ethanol, rinsed further with ethanol, blown dry with argon and stored. Note that if the samples prepared from THF solution were not shaken in ethanol, the solvent evaporated quickly, leaving deposits of the molecule of interest on the substrate. Typically, sonication was

not sufficient to completely clean such samples. The sample yield prepared without ethanol shake was $\sim 50\text{-}60\%$ whereas with the additional shaking step the yield increased to close to 100% .

3.13 Theoretical calculations

The molecular geometry of each molecule was optimised at the PM3 level and refined at the B3LYP/6-31G* level of theory. The orbital energies of single molecules were calculated using either the semiempirical ZINDO/S or the B3LYP/6-31G* methods. All calculations were performed with the Orca 2.8 software package.¹²¹ The orbital energies of the TPT and TP3 molecules were calculated with their terphenyl units in the coplanar geometry to reflect their molecular structure in the SAM.^{14,15,122–125} Model densities of states were obtained by applying equal Gaussian envelopes of 0.5 eV width to each molecular orbital at the ground state binding energies to account for the solid state broadening in photoemission and then summing, together with a rigid energy shift of a typical value of 5.4 eV and 3.5 eV applied to the calculated electronic structure by PM3 and DFT respectively^{65,66} unless stated otherwise.

Chapter 4

Novel SAM systems for molecular electronics

4.1 Introduction

4.1.1 Short introduction to self-assembled monolayers

Self-assembled monolayers are one molecule-thick molecular films that can be deposited from solution on a metal substrate such as gold, silver, copper, silicon or nickel.^{34–45}

A SAM constituent is comprised of three main parts, each playing a role in making a stable monomolecular film:

- the head group for attachment to the metallic substrate
- the spacer
- the terminal group for functionalisation of the SAM ambient interface

The make-up of the spacer is especially important since, for a given substrate-head group combination, the interactions between the individual spacer components and their orientation at the surface (are they lying parallel or perpendicular to the substrate?) dictate the structural quality and stability of the SAM.³⁵ Importantly for nanoelectronic applications, SAMs can act as dielectric layers as well as modulate the electrical properties of a metal surface depending on their molecular make up (see section 4.4).^{25,46–48} However, defects in the dipole layer formed by SAMs will significantly influence the effective modification of the charge injection barrier, therefore, the analysis and possible optimisation of the SAMs structure is crucial for the success of such applications. This problem has been directly identified in the very recent theoretical study analysing the application of SAMs for charge transfer optimisation in metal-organic material junctions.¹²⁶

4.1.2 Short introduction to molecular electronics

As mentioned in section 1, self-assembled monolayers of organic molecules are an efficient mean of modifying the properties of metallic surfaces.^{15,35} In particular, alkane and aromatic thiols have been used on gold (used in the present work),³⁵ silver,²⁰ palladium,^{127,128} copper^{43,44} and, of importance in the context of this doctoral work, nickel surfaces,^{39–41} to modify the transport properties at the respective metal surfaces. By forming a dipole layer at the electrode/semiconductor

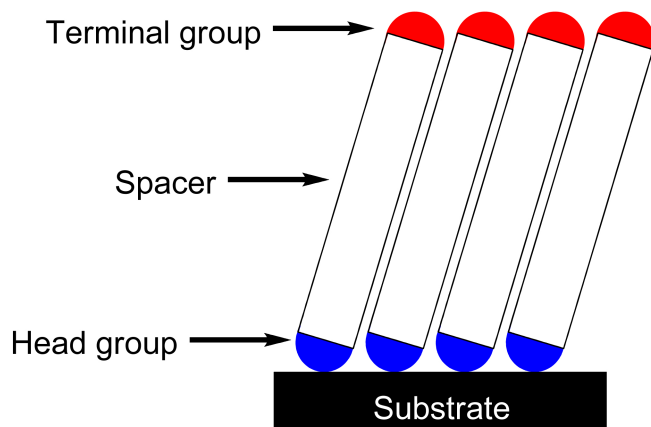


Figure 4.1: Schematic view of a SAM constituent.

interface, SAMs can lower the barrier for electron or hole injection.^{50,51,54,129,130} Alternatively, SAMs can serve as ultrathin organic insulators and possibly even good dielectric barrier layers. For instance the quasi two-dimensional cross-linked SAM of [1,1;4,1-terphenyl]-4,4-dimethanethiol (TPDMT) not only provided an effective barrier against the penetration of a metal adsorbate^{26,27} but also insulated the fabricated metal film at the SAM-ambient interface from the substrate,^{65,131} two critical factors for the successful fabrication of the spintronic devices targeted in the present work.^{132–135} The deciding parameter for the above applications of SAMs is their electronic structure. In particular, the positions of the highest occupied and lowest unoccupied molecular orbitals (HOMO and LUMO, respectively) of a SAM affects the height of the injection barrier for electrons and holes through the SAM-modified electrode/semiconductor interface or SAM-containing molecular junction.¹³⁶ Furthermore, the width of the HOMO-LUMO gap defines the insulator properties of a SAM, affecting its performance as a dielectric layer. In this context, the results of the spectroscopic characterisation of SAMs formed by PPPn and FTPn molecules (figure 4.2) as potential dielectric films (sections 4.2 and 4.3 respectively) are presented in this chapter. In addition, experimental and theoretical analysis of the electronic structure of a series of SAMs with aromatic backbones (figure 4.2) will be presented in section 4.4. We wanted to address the relationship between the identity of the aromatic spacer and the electronic structure of the related SAMs in particular. To avoid ambiguity regarding the quality of the aromatic SAMs, we decided to work with long-chain molecules, having either terphenyl (PPPN) or fluorinated terphenyl (FTP3²⁰) backbones and a short aliphatic linker as shown in figure 4.2.

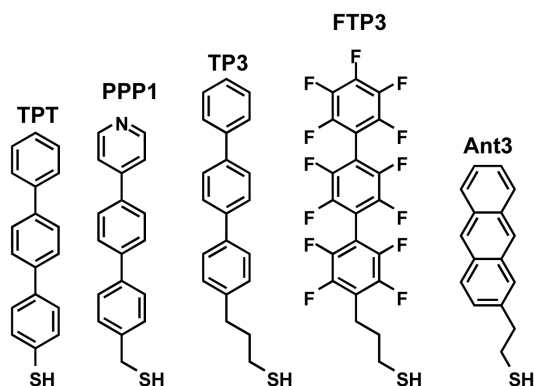


Figure 4.2: Chemical structure of the precursor molecules of the SAMs studied in this chapter. The abbreviations used in the text are shown.

4.2 Terphenyl with terminal pyridine ring

4.2.1 Introduction

Pyridine-terminated *p*-terphenyl thiols or PPPn (figure 4.2) were investigated as potential dielectric layers for metal-SAM-metal systems. The terminal pyridine group allows the binding of metals and charged molecules as well as hydrogen bonding. Notably, pyridine is known to bind to nickel, the metal used in our metallisation studies. As the characterisation of PPPn SAMs has been reported before, the characterisation of our pristine PPPn/Au SAMs will only be briefly presented below. For a complete characterisation of pristine PPP monolayers, see the work of Liu *et al.*¹³⁷

4.2.2 XPS characterisation of PPPn films

The C1s, N1s and S2p XPS spectra of PPP3/Au acquired at an excitation energy of 350 eV are shown in figure 4.3. The C1s spectrum (top panel) shows two main peaks at ~ 284.7 and ~ 285.5 eV corresponding to the C=C and C=N carbons respectively. The S2p spectrum shows only one major peak at 162 eV with a fwhm of 0.7 eV, consistent with high quality films. Furthermore, the N1s spectrum is typical for free pyridine with a single peak at ~ 398.8 eV.

4.2.2.1 A clean SAM-ambient interface

Unlike alkylamines, the nitrogen atom in pyridine is not strongly basic ($\text{pK}_a \sim 5$). Consequently, the high oxygen content observed for alkylamine SAMs (data not shown) is not observed for PPPn systems. Instead, a spectrum similar to that typical of hydrophobic C12 films is observed (figure 4.4). This is important since it means that, unlike in the case of alkylamines, all nitrogen atoms are free for binding to, e.g. metal atoms.

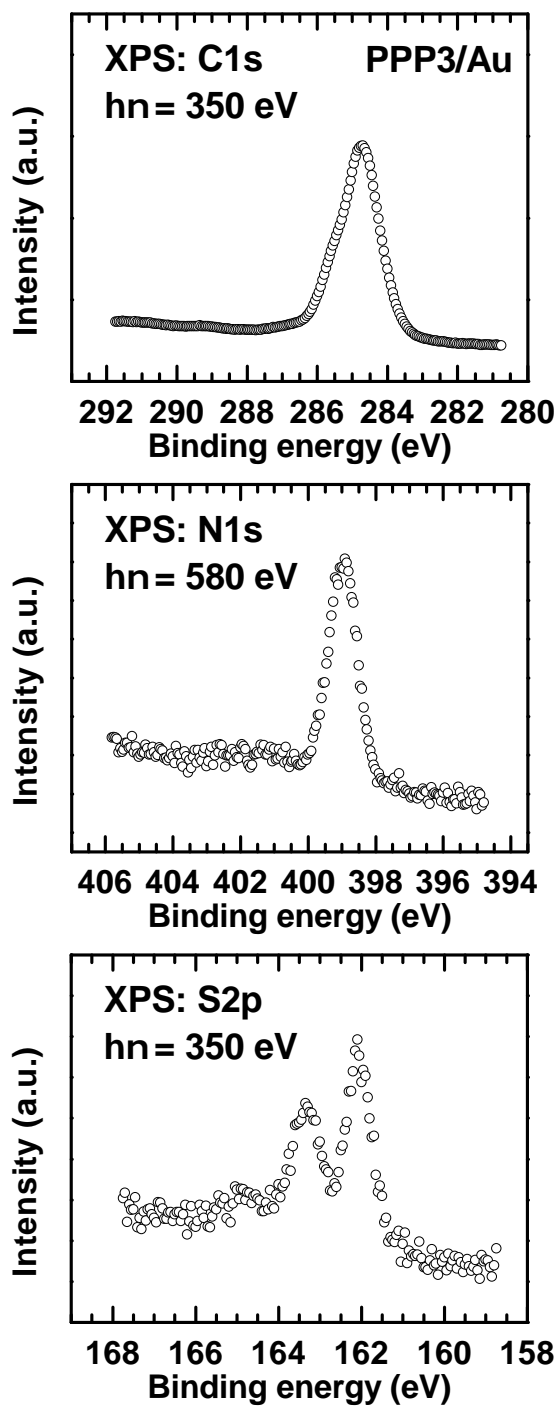


Figure 4.3: C1s (top panel), N1s (middle panel) and S2p (bottom panel) spectra of PPP3/Au.

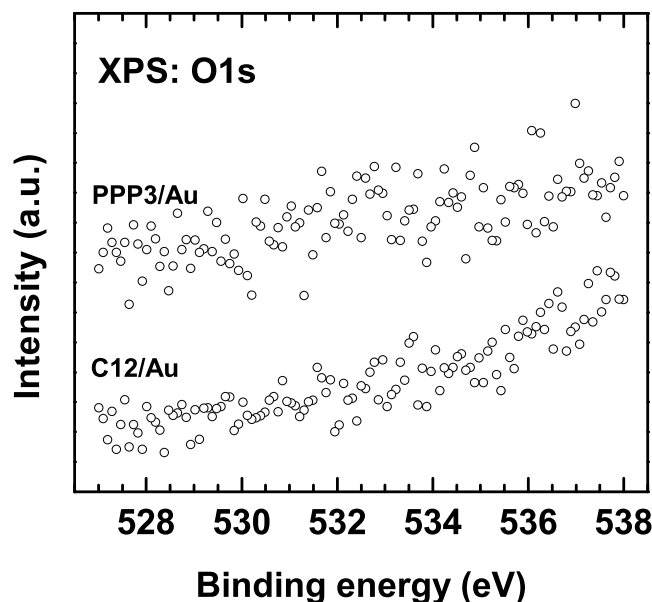


Figure 4.4: O1s spectra of PPP3/Au and C12/Au. The C12/Au spectrum is given as an example of a typical, oxygen-free SAM on gold.

4.2.3 Electronic structure and molecular orientation in PPPn films

4.2.3.1 Molecular orientation of PPPn films

As shown in figure 4.5, the dichroism of the NEXAFS signal is high, implying a highly ordered monolayer. The tilt angle of the molecular backbone was found to be $\sim 18^\circ$.

4.2.4 Summary

PPPn molecules form well ordered monolayers making them potential candidates as dielectric layers for molecular electronics. In addition, unlike alkylamine SAMs, PPPn films have a clean SAM-ambient interface making them useful for metal immobilisations. The effect of electron irradiation on PPPn systems will be presented in section 5.2. The evaporation of nickel on irradiated PPPn/Au SAMs will be presented in section 6.3.

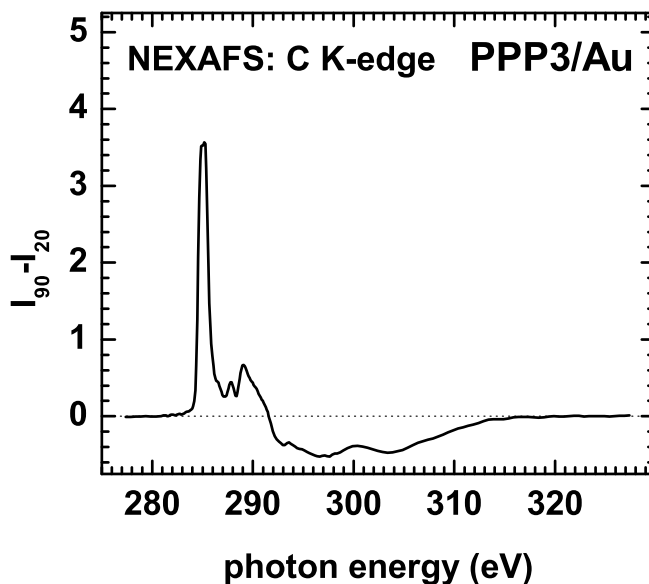


Figure 4.5: NEXAFS C K-edge difference spectrum of PPP3/Au.

4.3 Fluorinated terphenyl molecules

This section constitutes part of the following publication: F. Chesneau *et al.* *Phys. Chem. Chem. Phys.* **2010**, *12*, 12123-12137

4.3.1 Introduction

Most experiments on fluorinated compounds have been performed using fluorinated aliphatic SAMs,⁵¹ which enhance hole injection in metal-SAM junctions. Considering the much higher conductance of aromatic SAMs, one could expect that fluorinated aromatic films would improve charge transport compared to alkanethiol monolayers. The possibility to use such systems was indeed demonstrated using pentafluorothiophenol^{138,139} and partly fluorinated oligo(phenylene ethynylene),¹⁴⁰ with, however, little or no information regarding the structural quality of the monolayers, a crucial parameter for nanoelectronic applications (section 4.1). We therefore decided to modify the terphenyl-substituted alkanethiols, which forms SAMs of very high quality,^{15,141} by perfluorination of their aromatic core, i.e. prepare and characterise SAMs of perfluoroterphenyl-substituted alkanethiols (C6F5-C6F4-C6F4-(CH₂)_n-SH, *n* = 2, 3; see figure 4.2, page 29). These systems are novel; so far only SAMs of partly (one or two rings) fluorinated terphenyl thiols on Au(111) have been studied.^{142,143} Similar to terphenyl-substituted alkanethiols,^{15,141} we expect that the introduction of a short aliphatic linker between the perfluoroterphenyl (FTP) backbone and thiol group, will impart, at a suitable length of this linker, high structural quality to the respective SAMs. Furthermore, since the van-der-Waals radius of the fluorine atom is significantly larger than that of the hydrogen atom, a different conformation and packing of the fluorinated molecules in the monolayers is expected as compared to their non-fluorinated analogs. In this section, only results for the FTP3 molecule on gold substrates

Outer ring	PM3	STO3G
top	-54.8	-59.1
bottom	+55	+59.2

Table 4.1: Torsion angles of the outer rings of the perfluoroterphenyl moiety of FTP3. All values are in degrees and with respect to the middle ring. PM3 calculations performed with MOPAC2009. STO3G calculations performed using the GAMESS.08 software package.

will be discussed. For a more complete discussion of FTPn systems including odd-even and substrate effects, refer to *Phys. Chem. Chem. Phys.* **2010**, *12*, 12123-12137.

4.3.2 Conformation of FTPn molecules in the self-assembled monolayers

An important parameter for the formation of terphenyl self-assembled monolayers (SAMs) is the dihedral angle between the phenyl rings or torsion angle, δ . In the crystals of many oligophenyl derivatives, the steric repulsion of the ortho hydrogen atoms which is responsible for the torsion in the gas phase, can be overcompensated by the lattice energy, in particular by the T-shaped interaction,^{144,145} leading to the frequently observed herring-bone pattern with planar or almost planar conformations of the individual molecules.^{146,147} Similar conformations can also be assumed for oligophenyl-based SAMs.^{18,148,149} In contrast, such a planar conformation is hardly possible for the perfluoro-derivatives, where a substantially higher rotational barrier has to be assumed, certainly leading to different interactions and therefore different molecular arrangements.

In the molecular state (gas phase), the dihedral rotation is predominantly governed by two interactions, i.e. the interaction between the π orbitals of the adjacent phenyl rings and the repulsion between either hydrogen or fluorine atoms in the ortho-positions of these rings. The π orbital interaction tends to make the whole backbone planar thus achieving maximal conjugation between the rings. In contrast, the repulsion between the ortho-atoms forces a non-planar conformation. The balance of these interactions gives the final molecular structure (figure 4.6). The length of the aromatic C=C bond and, of particular importance in the present case, the C-C interring distance are not significantly affected by the substitution of hydrogen by fluorine. Only a slight shortening of the respective bond lengths is expected.¹⁵⁰ Therefore, and owing to the larger atomic radius of fluorine compared to hydrogen and the fact that the C-F bond is noticeably longer than the C-H bond (~ 1.34 Å vs ~ 1.09 Å), the planar conformation observed in terphenyls is not possible for the FTP moiety even in the molecular state the fluorine atoms in the ortho-positions of the adjacent rings can not come across one another.

As shown in table 4.1, both outer rings are rotated by about 57° in opposite directions such that all three rings form a helix (figure 4.6). Since rotation around the interring C-C bond is largely hindered in the FTP moiety, its structure should persist in the condensed state (figure 4.6). Indeed, published X-ray crystallographic structural data for closely related compounds (table 4.2) indicate the retention of the helical structure in the densely packed solid phase. This is in stark contrast to what is observed for most non-fluorinated terphenyl derivatives.¹⁵¹ Another interesting feature of the crystallographic structure of bulk (perfluoroterphenyl-4 yl)methanol is the relatively small spacing of ~ 4.5 Å between the parallel FTP moieties.¹⁵² Such a small spacing is presumably only achieved through a vertical shift (by ~ 1.4 Å) of the adjacent chains with respect to one another and due to the correlated orientation of the FTP helices of the

Outer ring	2H9FBP ¹⁵⁰	FBP ¹⁵⁰	FBPMeOH [?]
top	-59.5	-59.5	-57.0
bottom	+59.5	+59.5	+58.0

Table 4.2: Torsion angles of the outer rings of reference fluorinated compounds. All values are in degrees and with respect to the middle ring. 2H9FBP: 2H-nonafluorobiphenyl; FBP: perfluorobiphenyl; FBPMeOH: (perfluoroterphenyl-4-yl)methanol

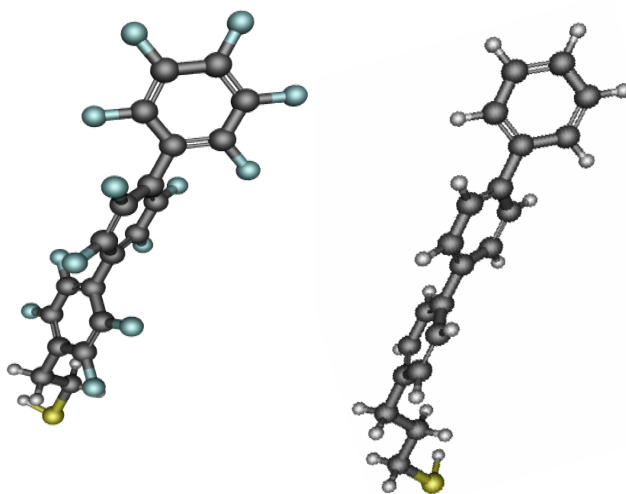


Figure 4.6: Calculated molecular structures of the perfluoroterphenyl (left) and tephenyl (right) moieties. Structures calculated and optimised using the GAMESS.08 software package

neighbouring molecules. Whereas such a vertical shift is possible to a limited extent only in the densely packed SAMs (by tilting), correlation of the FTP helix orientation can occur, allowing a dense molecular packing.

4.3.3 Molecular orbitals and molecular orientation of FTP moieties in SAMs

As explained in section 2.4, the electronic structure of the unoccupied molecular orbitals as well as the molecular orientation of molecules and individual orbitals can be determined using Near-Edge X-ray Absorption Fine Structure (NEXAFS) spectroscopy.

4.3.3.1 General features of the NEXAFS spectrum of FTP3

The carbon K-edge NEXAFS spectrum of FTP3/Au acquired at an X-ray incident angle of 55° is shown in figure 4.7. The most prominent absorption resonances in the spectra are marked by numbers and the respective photon energy positions are compiled in table 4.3.

The spectrum is dominated by two sharp resonances at 285.74 eV (**1**) and 287.63 eV (**2**) corresponding to the $\text{C1s} \rightarrow \pi^*$ transitions from the FTP carbon atoms which are not bonded

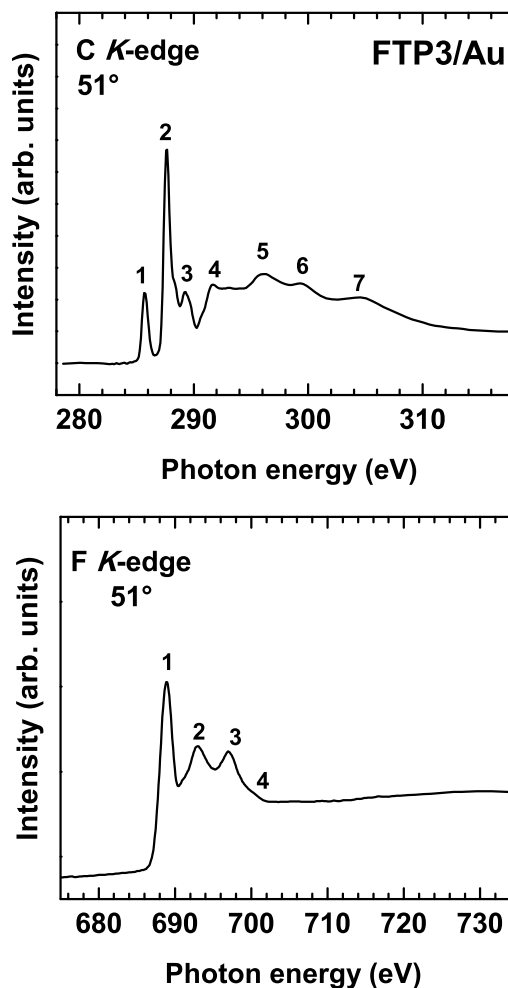


Figure 4.7: C-K edge (top) and F-K edge (bottom) NEXAFS spectra of FTP3 on gold acquired at an X-ray incident angle of 51° .

and directly bonded to fluorine atoms respectively. Further, several less intense π^* - and σ^* -like resonances are visible (table 4.3). The characteristic R^* resonance of the aliphatic linker at ~ 287.7 eV¹⁵⁵ is presumably weak and overlaps with the C1s C-F $\rightarrow \pi^*$ feature, so that no information on this linker can be obtained from the NEXAFS data.

In addition to the C K-edge data, the fluorine K-edge NEXAFS spectrum at an X-ray incident angle of 55° of FTP3 films on Au was measured (figure 4.7, bottom panel). The spectrum exhibits several characteristic resonances and the absorption edge corresponding to the F1s \rightarrow continuum transitions (table 4.4).

4.3.3.2 Molecular orientation of the FTP moieties in the film

The linear dichroism effects in the target films were monitored. As mentioned in section 2.4, a convenient way to follow the linear dichroism effects is to plot the difference between the NEXAFS spectra acquired at the normal and grazing incidence of the primary X-ray beam.

Peak	Energy (eV)	Assignment
1	285.74	$\text{C1s}^{C-C} \rightarrow 1\pi^*$
2	287.63	$\text{C1s}^{C-F} \rightarrow 1\pi^*$
2'	288.4	
3	289.25	$\text{C1s}^{C-F} \rightarrow \sigma^* \text{ (C-F)}$
3'	289.7	
3''	290.6	
4	291.6	$\text{C1s}^{C-F} \rightarrow 2\pi^*$
5	296.5	$\text{C1s}^{C-F} \rightarrow \sigma^*$
6	299.7	$\text{C1s}^{C-F} \rightarrow \sigma^*$
7	305.1	$\text{C1s}^{C-F} \rightarrow \sigma^*$

Table 4.3: Positions (eV) and assignments^{153,154}) of the most prominent absorption resonances in the C K-edge NEXAFS spectrum of FTP3 SAMs on Au (see figure 4.7).

Peak	Energy (eV)	Assignment
1	689.0	$\text{F1s} \rightarrow 1\pi^*$
2	693.1	$\text{F1s} \rightarrow 2\pi^*$
3	697.2	$\text{F1s} \rightarrow \sigma^*(\text{C-C})$
4	699.8	σ^*

Table 4.4: Positions (eV) and assignments (according to references¹⁵³) of the most prominent absorption resonances in the F K-edge NEXAFS spectrum of FTP3 SAMs on Au (see figure 4.7).

Such difference curves (90° - 20°) are presented in figure 4.8 for the C and F K-edges. According to these curves, the NEXAFS spectra of the FTP3 films exhibit a pronounced linear dichroism. This is a clear signature of orientational order. The signs of the observed difference peaks, i.e. the positive sign for the π^* -like resonances and the negative sign for the σ^* -like ones, suggest an upright molecular orientation. Significantly, the difference peak **2** in figure 4.8 has the same positive sign as that of peak **1**. This clearly implies π^* character for resonance **2**. In the present case, due to the presumable helical conformation of the FTP backbone, the twist angles of all three rings are different, with the outer rings turned by the torsion angles $+/-\delta$ with respect to the middle ring, as shown in figure 4.9. The absorption resonances related to the individual rings within the FTP backbone are undistinguishable, such that not the orientation of each individual ring but only their average orientation can be determined on the basis of the NEXAFS data. This refers not only to the twist angles of the rings but to the tilt angles of the π^* orbitals as well. Indeed, since the angle β is common to all rings, different values of γ mean different values of α for the individual rings. So, we are only left with the option to estimate the average α values for the FTP backbone in the target film and correct them later for the twist of the individual rings. As explained in section 2.4, the intensity ratios $I(\theta)/I(20^\circ)$ were evaluated; where $I(\theta)$ and $I(20^\circ)$ are the intensities of the resonance of interest at synchrotron light incidence angles of θ and 20° .¹⁰² The resulting angle dependencies of the relative intensities are displayed in figure

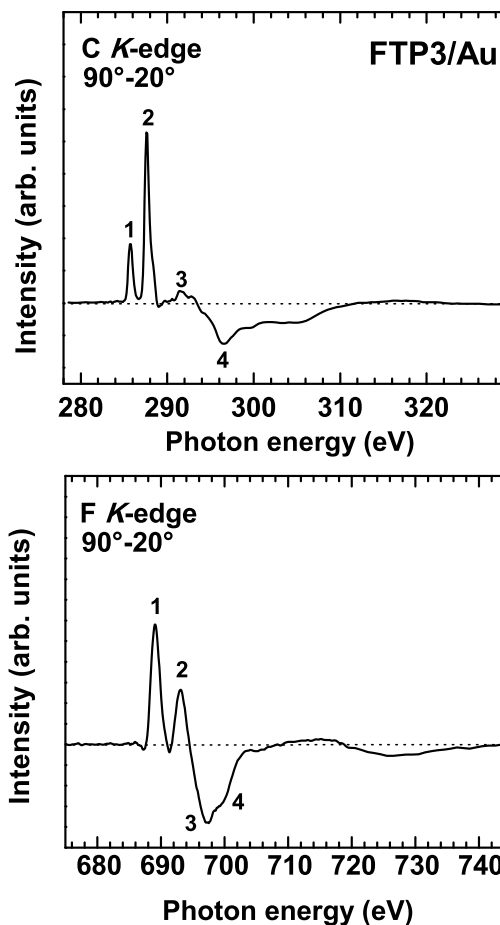


Figure 4.8: C-K edge (top) and F-K edge (bottom) NEXAFS difference spectra (90° - 20°) of FTP3 on gold.

4.10. The obtained values of the average tilt angles of the $1\pi^*$ orbitals are 75° and 73.5° for the $1\pi^*(\text{C}1s^{C-C})$ and $1\pi^*(\text{C}1s^{C-F})$ resonances respectively. To determine the average tilt angle of the FTP backbone in the target films, the values of the orbital tilt angles should be corrected for the twist of the individual rings. These values are not known but, from section 4.3.2, we can assume a helical conformation of the FTP backbone with torsion of the outer rings relative to the middle one by $\pm 57^\circ$. Since these values are close to 60° , the orientation of the π^* orbitals of the individual rings with respect to the molecular axis is characterised by close-to- C_3 symmetry. Under these circumstances, the average value of $\cos(\gamma)$ is only weakly dependent on the actual γ values of the individual rings. In particular, at $\gamma = 0$ for the middle ring, the weighted sum of $|\cos(\gamma_i)|$ is equal to 0.67, whereas at $\gamma_{\text{middle}} = 90^\circ$ this value is equal to 0.58. The average between these limiting cases (0.625) is mostly representative for the entire variety of possible torsion angles. Taking this value and the average tilt angles of the π^* orbitals (see above), the average tilt angle of the FTP backbone is 26° for FTP3/Au. These values are accurate to $\pm 5^\circ$, in view of the standard accuracy of the NEXAFS experiment and the difference between the two limiting values for the weighted sum of $|\cos(\gamma_i)|$.

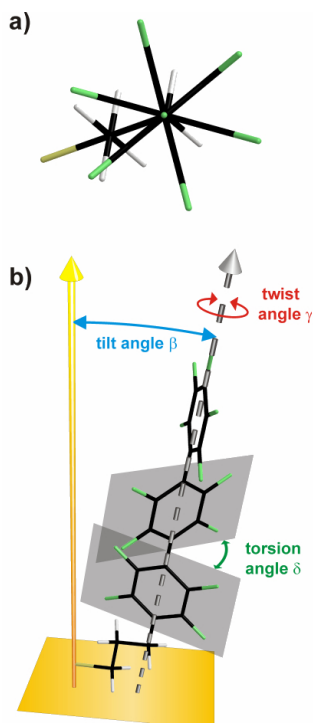


Figure 4.9: A schematic drawing of the FTP3 molecule: (a) view along the FTP backbone; (b) side view. The orientation of the FTP backbone is given by the tilt angle β , twist angle γ , and torsion angle δ . At $\gamma = 0$, normal to the ring plane (which is collinear with the π^* orbitals) lies in the plane spanned by the z - and the $4,4'$ -axes. The torsion results in different values of γ for the inner and outer rings.

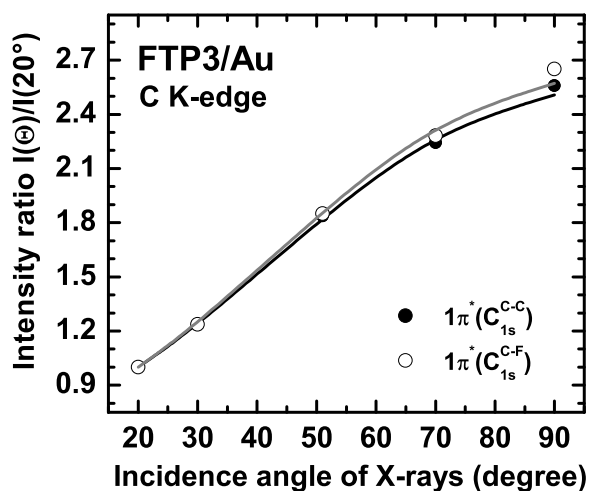


Figure 4.10: The angular dependence of the $1\pi^*(C1s^{C-C})$ (full circles) and $1\pi^*(C1s^{C-F})$ (hollow squares) intensity ratio $I(\theta)/I(20^\circ)$ for FTP3/Au. The best fits according to equation 2.8 are shown.

4.3.4 Chemical characterisation, packing density and thickness of the FTP3 films: XPS and HRXPS

Whereas NEXAFS probes the electronic structure of the unoccupied molecular orbitals, XPS gives us information on the chemical integrity as well as the thickness of thin films (section 2.1).

4.3.4.1 Chemical characterisation of FTP3 films

The S 2p spectrum in the top panel of figure 4.11 is dominated by a characteristic doublet at a BE of 161.8-161.9 eV (S 2p_{3/2}), which can be clearly assigned to the thiolate species bonded to the surface of gold.^{19,156,157} The fwhm of the S 2p_{3/2} and S 2p_{1/2} components of the thiolate-related doublet (0.5 eV) was close to the value expected in the case of equivalent adsorption sites for all SAM constituents,¹¹⁷ suggesting a single or at least dominant adsorption site for all FTP3 molecules. In addition to the thiolate-related doublet, a further, less intense doublet at a BE of 161.0 eV (S 2p_{3/2}) was observed; the intensity of this feature amounted to about 12 % of the total S 2p intensity and can be ascribed to either atomic sulphur¹⁵⁸ or a thiolate-type bound sulphur with a different binding chemistry and/or geometry compared to the standard thiolate-type bond observed in thiol-derived SAMs on coinage metals.^{157,159} Both assignments are discussed in detail in refs¹⁸ and,¹⁶⁰ but in most situations, including the present case, the different thiolate assignment can be favoured. No other features related to decomposed, physisorbed or oxidised FTPn molecules were observed in the S 2p spectra. The C 1s HRXPS spectrum of FTPn/Au in the bottom panel of figure 4.11 exhibits three emissions at 284.4, 285.8, and 287.5 eV assigned to the carbon atoms in the aliphatic linker (284.4 eV) and FTP moiety (285.8 and 287.5 eV) respectively. The 285.8 eV emission can be associated with the carbon atoms in the para positions (except for the terminal carbon), whereas the 287.5 eV emission can be related to the carbon atoms in the ortho and meta positions and the terminal carbon atom. This assignment is supported by comparison of the spectra of FTP3/Au acquired at photon energies of 350 and 580 eV in figure 4.12, which show, apart from a lower energy resolution at 580 eV, comparable intensities of the 285.8 and 287.5 eV peaks and considerably lower intensity of the 284.4 eV emission at $h\nu = 350$ eV. Indeed, the relative intensities of the two former peaks are expected to be almost independent on the photon energy since the respective carbon atoms are located in a similar manner along the FTP backbone. In contrast, the relative intensity of the peak associated with the alkyl linker is expected to increase with increasing photon energy due to a smaller attenuation by the FTP overlayer. The spectra in figure 4.12 coarsely reproduce the 3:5:13 intensity relation expected for the 284.4, 285.8 and 287.5 eV peaks respectively based on the molecular composition but are, as expected, modulated by attenuation and self-attenuation of the respective photoemission signals in the films.⁷⁵ The F 1s HRXPS spectrum of FTP3/Au in figure 4.13 exhibits a single emission at a BE of 687.4 eV which can be clearly assigned to the fluorine atoms of the FTP moiety.

4.3.4.2 Packing density and thickness of FTP3 films

Apart from the above analysis of the spectra, we used the HRXPS data to determine the packing density of the FTP3n molecules in the films as well as the film thickness. We estimated the effective thickness of the FTPn films on the basis of the XPS data as described in section 2.1.3. As reference films we used dodecanethiolate (DDT) on Au(111). This film has a thickness of 15 Å and a molecular density of $4.63 \times 10^{14} \text{ cm}^{-2}$ corresponding to an area per molecule of 21.6 Å².¹⁶¹ The effective thicknesses of the FTP3 films was estimated at 20.4 Å. Considering that

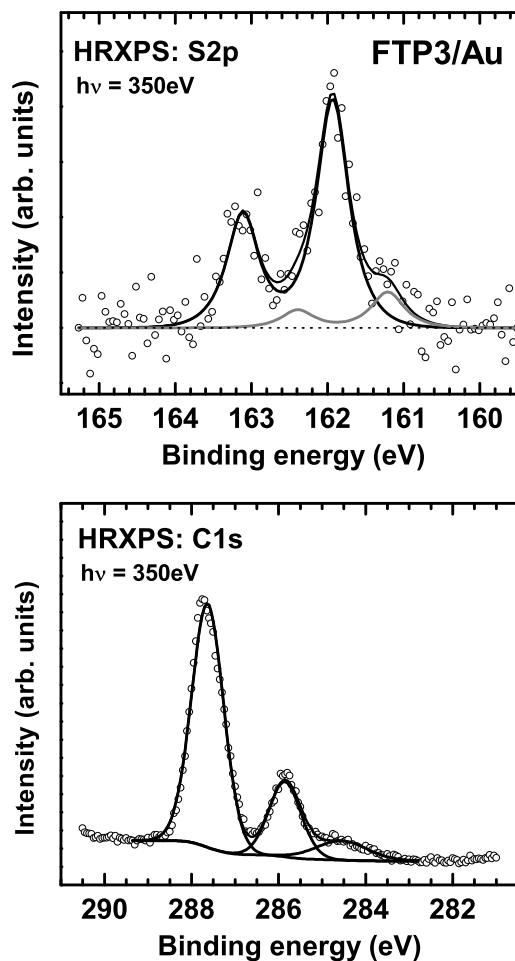


Figure 4.11: S2p (top) and C1s (bottom) HRXPS spectra of FTP3/Au.

the thickness of the FTP3 films in the case of the upright orientation of the SAM constituents is expected to be $\sim 20.2 \text{ \AA}$, the XPS results suggest a practically vertical molecular orientation in FTP3/Au. The comparison of the S2p/Au4f intensity ratios of the FTP3 films with those for the reference DDT system affords an estimate of the packing density of the films. The S2p/Au4f intensity ratios for C12/Au and FTP3/Au are 0.0103 and 0.00864 respectively. Considering that the area per molecule in C12/Au is 21.6 \AA^2 (see above), the area per molecule in FTP3/Au is 25.8 \AA^2 giving a packing density of $3.89 \times 10^{14} \text{ cm}^{-2}$.

4.3.5 Overlayer structure of FTP3 films probed by scanning tunnelling microscopy

An STM image obtained at high resolution is presented in figure 4.14(d); it shows that the adsorption of FTP3 molecules on the Au(111) surface at room temperature results in the formation of a dense network of depressions and islands visible as dark patches and bright spots, respectively. As documented by the cross-section A marked in this image, both the depth of the depressions and the height of the islands correspond (within experimental error) to the height

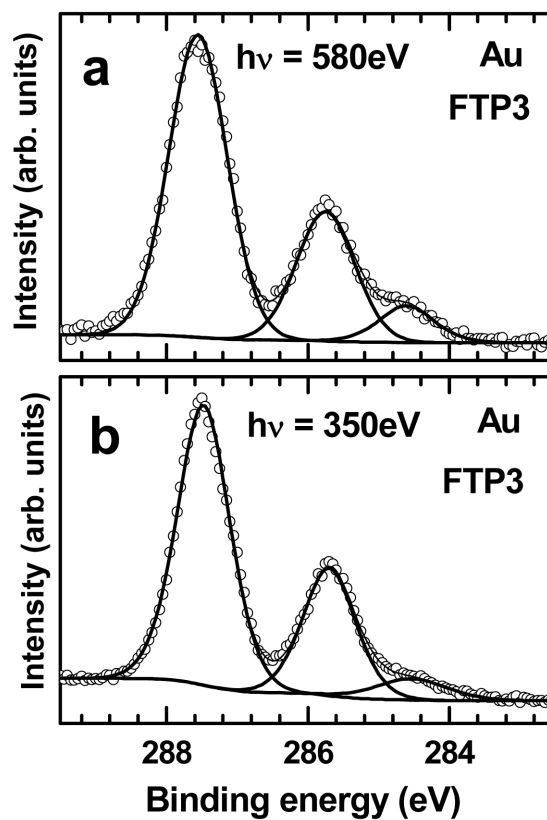


Figure 4.12: C1s HRXPS spectrum of FTP3/Au at different excitation energies.

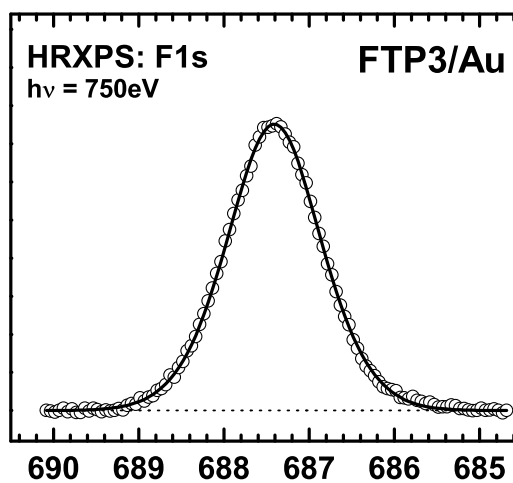


Figure 4.13: F1s HRXPS spectrum of FTP3/Au.

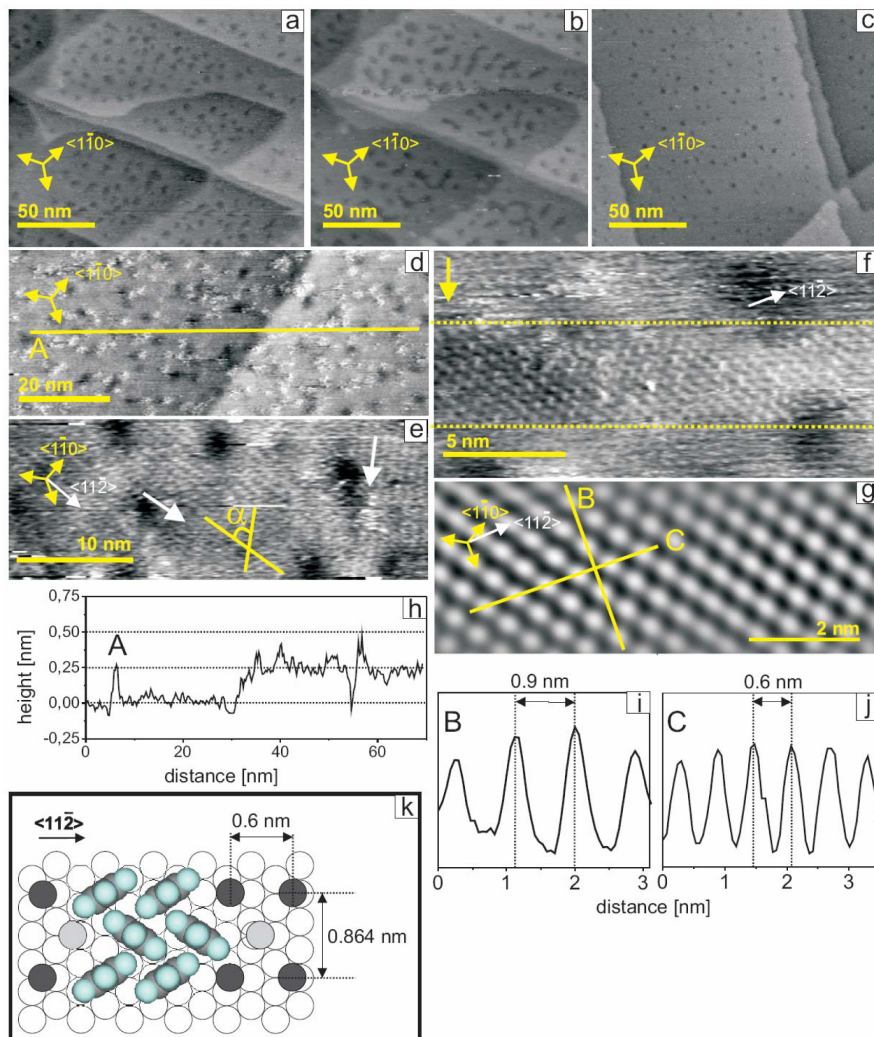


Figure 4.14: Summary of the STM data for FTP3 SAMs on Au(111). (a)-(g) STM images collected in constant current mode with $I = 200$ pA, $U = 700$ mV for (a)-(b) and $I = 20$ pA, $U = 700$ mV for (c)-(g). The panels (a) and (b) show two consecutive STM images of the same sample area to illustrate a modification of the sample by the STM tip at the high tunnelling current; such a modification does not occur at the low current. The yellow lines in (d) and (g) mark cross-sections A, B and C displayed in panels (h), (i) and (j), respectively. The angle $\alpha = 60^\circ$ in (e) marks the relative orientation (given by the white arrows) of the stripe pattern lines (see text for details). The dashed lines in (f) mark the scan lines where modification of the STM contrast took place (see text for details). A schematic illustration of the adsorption structure of FTP3 on Au(111) is depicted in (k). Open circles correspond to gold atoms on the Au(111) surface, light and dark grey filled circles correspond to S atoms with adsorption sites taken arbitrary. The presumable herringbone arrangement of the analogous phenyl rings in the neighbour molecules is marked only schematically by showing a single ring in the FTP3 molecule; no tilt is included.

of the monoatomic substrate step on a Au(111) surface, i.e. 2.4 \AA , and thus indicates modification of the topmost Au(111) substrate atomic layer upon adsorption of the molecules. Such a modification of the Au(111) substrate upon thiol adsorption has been previously reported for various SAMs,^{162–164} including the non-fluorinated analogue of the FTPn system - TPn/Au.¹⁴¹ However, the density of the substrate defects for FTP3/Au is significantly higher compared to its direct analogue, TP3/Au (for comparison, see the supplementary information in reference¹⁴¹). The faceting of the Au(111) substrate edges (the result of the flame annealing process) enables identification of the closest neighbour directions on the Au(111) substrate – these are the $\langle \bar{1}00 \rangle$ directions. A higher resolution image, presented in figure 4.14(e), shows domains with molecular rows separated by 8–9 \AA and running along two directions marked by white arrows which intersect each other at the angle $\alpha = 60^\circ$. In general, only three different directions of such stripe motive were observed, intersecting the $\langle \bar{1}10 \rangle$ substrate directions at 30° or 90° and, thus, oriented along the $\langle 11\bar{2} \rangle$ directions of the Au(111) substrate. High resolution images in figure 4.14(g) show FTP3 molecules assembled in a close-to-hexagonal structure. The cross-section B along the $\langle \bar{1}10 \rangle$ direction, displayed in figure 4.14(i), gives a next neighbour distance of about 9 \AA which corresponds to the period of the stripe motive visible in figure 4.14(e). These findings were associated with the same $(2\sqrt{3} \times \sqrt{3})R30^\circ$ packing motive as reported previously for TP3/Au.¹⁴¹ However, the cross-section C, presented in figure 4.14(j), shows that the intermolecular spacing along the $\langle 11\bar{2} \rangle$ direction (6 \AA) is noticeably larger than the value characteristic of the $(2\sqrt{3} \times \sqrt{3})R30^\circ$ structure (5 \AA). Thus, the structure of FTP3 on Au(111) corresponds to the $(2\sqrt{3} \times \sqrt{3})R30^\circ$ lattice uniaxially expanded along one of the $\langle 11\bar{2} \rangle$ directions as schematically shown in figure 4.14(k) (A standard^{141,164–167} herringbone arrangement of the individual rings was assumed). The respective area per molecule is about 26 \AA^2 , which corresponds to a packing density of $3.9 \times 10^{14} \text{ cm}^{-2}$, very similar to that found by XPS (section 4.3.4.2).

4.3.6 Summary

The high quality of the FTPn SAMs makes them promising candidates for use as semiconductor SAMs or for controlling energy barriers between organic semiconductors and metal electrodes. The Schottky energy barrier for defect electrons (holes) can be decreased significantly if fluorine-substituted or semifluorinated SAMs are used to modify the metal-organic interface. In addition, aromatic SAMs, such as FTPn films, generally provide a more efficient charge transport through the molecular backbone compared to the aliphatic SAMs which are frequently used for this purpose. The effect of low energy electron irradiation on FTPn films will be presented in section 5.3. In addition, the evaporation of nickel metal on FTPn/Au SAMs will be presented in section 6.5.

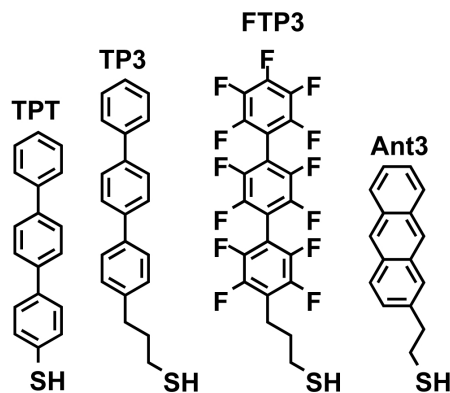


Figure 4.15: A schematic drawing of the SAM precursor molecules used in section 4.4 along with their acronyms.

4.4 The electronic structure of aromatic SAMs

Note: This section is largely based on an upcoming scientific publication: *The electronic structure of aromatic monomolecular films: the effect of molecular spacer and interfacial dipole*, Kong, L.; Chesneau, F.; Zhang, Z.; Staier, F.; Terfort, A.; Dowben, P. A. and Zharnikov, M.

Their well defined structure^{65,131–134} and the possibility to adjust their parameters, such as the electron or hole barrier width, by physical^{24,70} or chemical means⁷¹ make SAM attractive for nanoelectronic applications. Importantly, in the context of this work, organic self-assembled monolayers may be used as ultrathin insulating layers in spintronic devices.^{132–135}

The deciding parameter for the above applications of SAMs is their electronic structure. In particular, the positions of the highest occupied and lowest unoccupied molecular orbitals (HOMO and LUMO, respectively) of a SAM affect the height of the injection barrier for electrons and holes through SAM-modified electrode/semiconductor interfaces or SAM-containing molecular junctions.¹³⁶ Furthermore, the width of the HOMO-LUMO gap defines the insulator properties of a SAM, affecting its performance as a dielectric layer.

In this context, we present here the results of the spectroscopic characterisation and theoretical analysis of the electronic structure for a series of SAMs with various aromatic backbones (figure 4.15). In particular, we wanted to address the relationship between the identity of the aromatic spacer and the electronic structure of the related SAMs as well as the effect of the short aliphatic linkers between the thiol head group and the aromatic moiety.^{14–16,58} To avoid ambiguity regarding the quality of the aromatic SAMs, long-chain molecules, having either terphenyl (TPT and TP3), fluorinated terphenyl (FTP3), or anthracene (Ant3) backbone and a short aliphatic linker (TP3, FTP3, Ant3) were used (figure 4.15). All these molecules produce well-defined SAMs on Au(111), with especially high-quality in the case of TP3, FTP3, and Ant3.^{15,18,21,141,168} This quality is related to the presence of the aliphatic linker which enables an optimal packing of the aromatic moieties hardly possible in the case of the direct attachment of the aromatic backbone to the thiolate headgroup.^{73,169,170} Throughout this section, the term *band gap* will be used interchangeably with the term *HOMO-LUMO gap*.

4.4.1 HOMO-LUMO gaps measured by UPS and IPES

As shown in figure 4.16, the experimental UPS-IPES spectra of the target SAMs are in good agreement with the theoretical densities of state (DOS) of the respective molecules. In addition, the experimental values of the HOMO-LUMO gaps for the SAMs (figure 4.17), correlate well with the respective theoretical values for the molecules in the gas phase (figure 4.18), except probably in the case of TP3 for which the theoretical value is noticeably smaller than the experimental one.^a The agreement between the experimental and theoretical band gap values for the SAMs and the isolated molecules suggests that the substrate left the aromatic electronic system (AES) of the adsorbed molecules largely undisturbed. The highest disturbance is expected for TPT/Au since its AES is partly coupled to that of the substrate.¹³⁰ However, this coupling mostly affects the phenyl ring adjacent to the headgroup, therefore we expect the whole molecule (three phenyl rings) to be less affected than the corresponding benzenethiol and biphenylthiol.^{49,130} In contrast to TPT/Au, the AES of the TP3, FTP3, and Ant3 molecules in the respective films is presumably decoupled from the substrate due to the presence of the alkyl spacer which is a better insulator than their aromatic cores. This effect has been clearly demonstrated, using DFT calculations, for a series of biphenyl-substituted alkanethiol SAMs on Au(111), in which the insertion of just a single methylene group between the biphenyl unit and the headgroup resulted in decoupling of the AES from the substrate.¹³⁰ In addition, as shown for a series of oligophenyl and oligo(phenyleneethynylene) SAMs on Au(111), the characteristic charge transfer time through the molecular framework increases significantly upon the introduction of a single methylene group between the aromatic unit and the headgroup.¹⁷¹ Therefore, the electronic structure of the target SAMs, given by the respective UPS/IPES spectra, is mainly representative of the aromatic cores, at least with respect to the width of the HOMO-LUMO gap.

As expected, the narrowest band gap (3.5 eV) was observed for Ant3/Au which is based on the highly conjugated anthracene unit. Note that this value is somewhat smaller than our theoretical estimate for Ant3 (3.66 eV; see figure 4.18). The widest HOMO-LUMO gap, among the films in this study, was observed for FTP3/Au (4.86 eV). This is presumably due to the minimal orbital overlap between the benzene rings imposed by the helical conformation of the FTP3 molecule.²¹ The theoretical estimate (4.76 eV; see figure 4.18) is quite close to this value. Finally, the HOMO-LUMO gap in TPT/Au and TP3/Au was found to be 4.1 and 4.75 eV respectively. Interestingly, the value for TP3/Au is noticeably larger than that for TPT/Au. This tendency was reproduced by our theoretical calculations (figure 4.18) but the difference between the values for the TP3 and TPT molecules was much smaller (~ 0.2 eV). The large difference observed in the SAMs is probably related to matrix effects since the TP3 film has much higher crystalline perfection and packing density than the TPT SAM.¹⁵

4.4.2 Relationship between the HOMO and the surface's work function

Along with the differences in the width of the HOMO-LUMO gap, significant differences in its placement with respect to the substrate's Fermi level were observed (figure 4.17). These changes in molecular band offset are likely characteristic of the differences in the extended interface dipole.⁴⁶ In the case of thiol-derived SAMs, this dipole consists of two parts: the potential energy step at the substrate-thiol interface reflecting charge rearrangements upon bond formation, and a dipole associated with the molecular spacer.^{50,51,130,152} Note that the effect of the latter

^aThe theoretical calculations were performed for the in-plane geometry of the terphenyl unit (section 7.1.1, page 121). In this geometry, the band gap is noticeably smaller than that of the out of plane geometry.

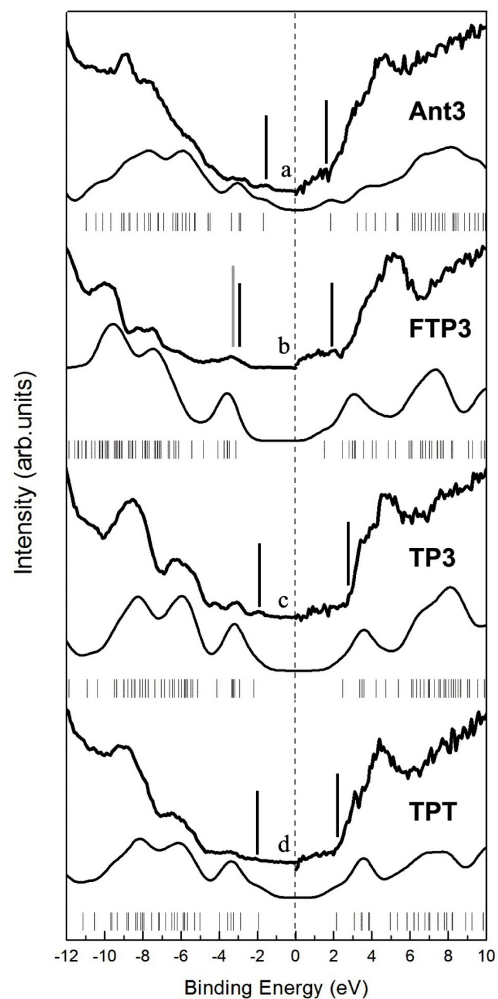


Figure 4.16: Combined UPS and IPES spectra of the TPT, TP3, FTP3, and Ant3 SAMs (from the bottom to the top), along with the calculated (DFT) ground state molecular orbital energies (vertical tick marks below the spectra) and the theoretical density-of-states (the curves below the experimental spectra) for the respective single molecules. Binding energies are denoted in terms of $E-E_F$. The presumable positions of the HOMO and LUMO are shown by vertical black lines. For FTP3/Au, the position of the HOMO-1 is also shown by a vertical gray line.

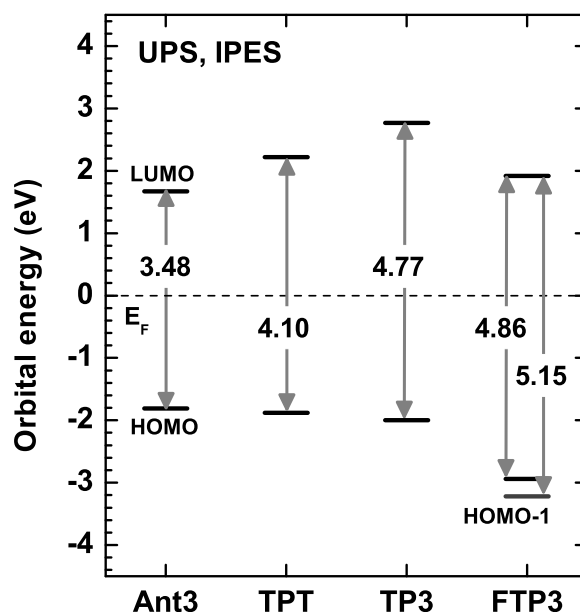


Figure 4.17: Positions of the HOMO and LUMO orbitals and the HOMO-LUMO gap for the TPT, TP3, FTP3, and Ant3 films determined on the basis of the experimental UPS and IPES spectra (figure 4.16). Binding energies are denoted in terms of $E-E_F$. For FTP3/Au, the position of the HOMO-1 orbital and the (HOMO-1)-LUMO gap are also presented.

could be especially strong for the molecules in this study since the molecular dipoles for non-fluorinated and fluorinated oligophenyls are of opposite sign.⁴⁹

The overall effect of the interfacial dipole could be monitored by WF measurements. The WF change compared to clean Au(111) was found to be -1.0, -0.8, and +0.6 eV for Ant3/Au and TPT/Au, TP3/Au, and FTP3/Au, respectively. The difference between these values correlates surprisingly well with the relative position of the HOMO orbital in these films (figure 4.17)), with the highest position for Ant3/Au and TPT/Au, slightly lower (by 0.1 eV) for TP3/Au, and the lowest (by 1 eV) position for FTP3/Au.^b Note that fluorination rather than aromaticity is responsible for the specific WF offset between FTP3/Au and TP3/Au. Indeed, a similar difference in work function was observed between SAMs of decanethiol and its fluorinated analogue on gold (-1.3 eV vs -1.4 eV for FTP3/Au and TP3/Au).¹⁷²

4.4.3 The role of the spacer in the Ant3, TP3 and FTP3 molecules

Since the alkane spacer in the TP3, FTP3, and Ant3 systems is a better insulator than the aromatic core, the partial density of state (DOS) related to the former unit should be located deeper with respect to the Fermi level as compared to the partial DOS associated with the latter moiety.¹³⁰ In accordance, as shown in figure 4.18, the electron density associated with the HOMO and LUMO orbitals of the TPT, TP3, and Ant3 molecules is located at the aromatic

^bThe similar values obtained for the Ant3/Au and TPT/Au films reflect the accuracy of our work function measurements (± 0.1 eV).

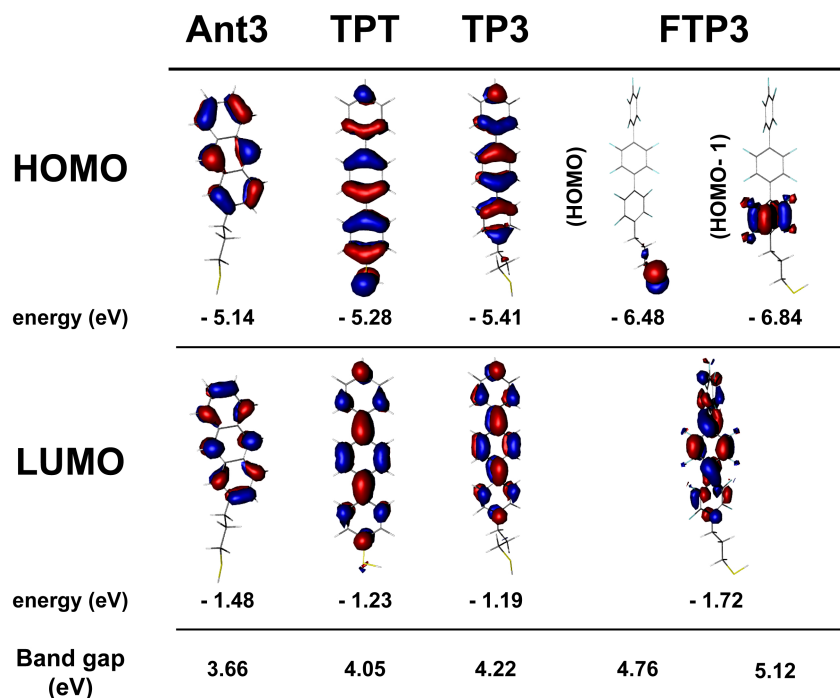


Figure 4.18: Calculated (DFT) HOMO and LUMO orbitals of the TPT, TP3, FTP3, and Ant3 molecules, along with their energy positions and the HOMO-LUMO gap. For FTP3, the data for the HOMO-1 orbital are also presented.

core. In contrast, due to the fluorine induced downward shift of the molecular orbitals of the terphenyl unit in FTP3,¹⁷³ the electronic states associated with the aromatic backbone are lower in energy than the HOMO, comprising HOMO-1 and deeper orbitals. The HOMO is then located at the alkyl linker and thiol head group. The different location of the electronic density associated with the HOMO are indirectly reflected in the UPS spectra in figure 4.16. Indeed, the feature dominated by the highest occupied molecular orbitals are very well defined in the photoemission spectra of all molecules, with narrow line shapes, indicative of a long lived photoemission associated excited state, except in the case of FTP3/Au. In the latter case, the HOMO is not highly delocalised over the aromatic moiety but the molecular orbital weight is close to the thiol termination and well screened by the gold substrate, so that a decay channel involving the gold substrate is likely.

The different offset of the electronic states associated with the HOMO in TP3 and FTP3 can be visualised as partial densities of state (DOS) related to their building blocks, i.e. a short alkanethiol and the aromatic unit (figure 4.19). It is clearly seen for TP3 that the states associated with the alkyl linker (C3-SH) and the headgroup (TP-H) are located lower with respect to the fermi level than the states related to the terphenyl unit. By contrast, the opposite situation occurs for FTP3, so that the HOMO is now comprised of the states associated with the alkyl linker and the headgroup. This put some doubt in our value for the width of the HOMO-LUMO gap in FTP3/Au. Indeed, the electronic densities associated with the HOMO and LUMO orbitals are located at different parts of the molecule, making the HOMO-LUMO transition hardly possible since the wave functions of the initial and final states in the respective

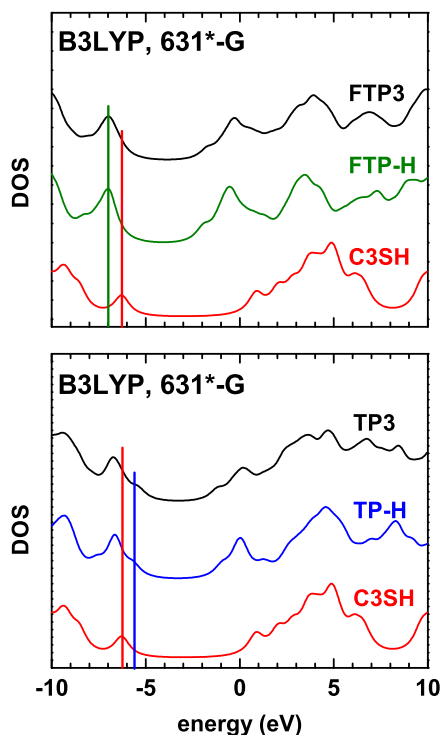


Figure 4.19: Calculated (DFT) DOS for TP3 (bottom panel) and FTP3 (top panel) and their building blocks, i.e. propanethiol (C3-SH) and terphenyl (TP-H) for TP3 and propanethiol (C3-SH) and perfluorelated terphenyl with the H-substituted terminal fluorine atom (FTP-H) for FTP3. The vertical lines are guides for the eye to monitor the respective contributions of the building blocks to the total DOS. Binding energies are denoted in terms of $E-E_F$.

transition integral will have no overlap. Therefore, not the HOMO but the HOMO-1 located, similar to the LUMO, at the aromatic unit of FTP3, is representative of the effective band gap for the electronic transitions in this particular system. In this context, the value of 4.85 eV we obtained for the HOMO-LUMO gap in FTP3/Au (4.76 eV calc.) can be substituted by a value of 5.15 eV for the (HOMO-1)-LUMO gap (figure 4.17). Note that the latter value correlates well with the theoretical estimate of 5.12 eV for FTP3 (figure 4.18).

4.4.4 Confirmation of the trends by optical spectroscopy

The relationship between the HOMO-LUMO gaps in the SAMs in this study were verified by optical measurements. The UV-vis spectra of the TPT, TP3, FTP3, and Ant3 molecules in solution are presented in figure 4.20. The onset of the optical absorption in these spectra corresponds to the optical gap which is generally assumed to be smaller than the HOMO-LUMO gap since it is an exciton gap with a valence hole interaction with an excited electron. The presumable position of the absorption offsets are marked by the vertical solid lines in figure 4.20. The relative values of the optical gap for the systems in this study correlate well with the UPS-IPES derived results. As expected, the smallest gap is observed for Ant3 (3.2 eV) and the widest for FTP3 (4.7 eV), with intermediate values for TPT (3.8 eV) and TP3 (4.0 eV).

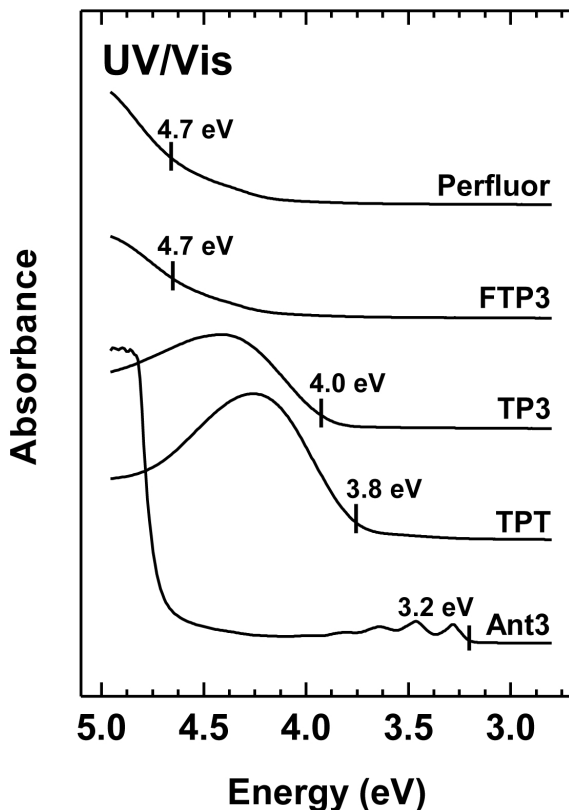


Figure 4.20: UV-vis spectra of the TPT, TP3, FTP3, Ant3, and perfluoroterphenyl molecules in solution. The presumable position of the optical gap is marked by the vertical solid lines. The respective values are given.

An optical spectrum of Ant3/Au is shown in figure 4.21 along with that of the molecule in solution. The spectrum of Ant3/Au exhibits the same transitions than the free molecule in solution although shifted to lower energy. The shift is consistent for all peaks indicating a reduction in the HOMO-LUMO gap of Ant3 upon binding to the gold surface. This behaviour is consistent with that typically observed for molecules chemisorbed onto a metal substrate.⁴⁶ However, we have shown above that the propylthiol linker of the Ant3 molecule insulates the anthracene moiety from the surface. Therefore, the decrease in the band gap must be caused by a different process. Ant3 SAMs being highly ordered,¹⁶⁸ we suggest that this change could be due to an increase in the intermolecular interaction between the Ant3 molecules in the SAM compared to the solution phase, rather than to a significant interaction of the anthracene moiety with the substrate. Indeed, a similar bathochromic shift has been observed for the liquid to solid transition of highly conjugated dye molecules and was attributed to an increase in intermolecular interactions leading to an improved ordering of the molecules.^{174,175}

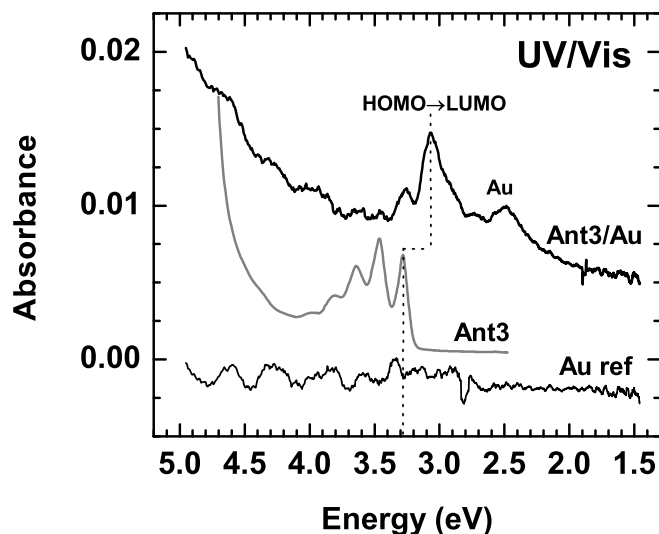


Figure 4.21: UV-vis spectra of the Ant3 molecule in solution (gray line) and on the surface (black line). The solution spectrum was multiplied by 0.024. The spectrum of the bare gold surface (thin black line) is shown for comparison.

4.4.5 Summary

The electronic structure of a series of well-defined SAMs with *p*-terphenyl and anthracene backbones was studied by a combination of UPS-IPES, WF, UV-Vis measurements, and DFT calculations of the SAM precursors' electronic structure. In all but one SAM, the aromatic backbone was separated from the thiol group by a short alkyl linker which improved the structural quality and packing density of the aromatic matrix. The width of the HOMO-LUMO gap was found to depend on the identity of the aromatic backbone, being smallest for the strongly conjugated anthracene moiety and widest for the perfluorinated terphenyl unit. The offset of this gap, and especially the position of the HOMO orbital correlated well with the interfacial dipole which could be monitored by WF measurements. In the case of the perfluorinated terphenyl (FTP3), which is characterised by a comparatively large upward molecular dipole, this results in a significant downward shift of the occupied electronic states with respect to the Fermi level (chemical potential), so that the film becomes more n-type than the corresponding non-fluorinated systems. Unlike the analogous TP3 molecule, the energy of the orbitals of the aromatic core was lower than for the alkyl linker. The electronic states associated with the latter moiety and the headgroup comprise the HOMO in FTP3, suggesting that the electronic and optical properties of the FTP3 system are better represented by the (HOMO-1)-LUMO gap rather than by the difference between the HOMO and LUMO.

Chapter 5

Modification of SAMs by electrons

The modification of SAMs by electrons is of interest for nanoelectronic applications since it allows for the modification of the transport properties of the aromatic SAMs.^{65,66} Electron can also be used to write patterns onto aliphatic SAMs²² The exposure of SAMs to electrons or X-rays was found to result in a variety of complex, closely interrelated processes, including partial decomposition of the SAM constituents, desorption of hydrogen and molecular fragments, orientational and conformational disordering, damage to the headgroup-substrate interface, and cross-linking within the residual film.^{70,169} The exact course, kinetics, and branching of these processes were found to depend on the molecular architecture of the SAM substituents,^{70,169} packing density of the SAM,⁶⁴ and the nature of the substrate.^{169,176} All these processes typically evolve at a high rate during the initial stage of the irradiation treatment and exhibit a levelling off behaviour at high doses.¹⁷⁷ In aliphatic SAMs, film decomposition prevails (section 5.1) whereas the cross-linking processes are dominant in aromatic spacers (section 5.2 and 5.3) thus transforming the primary molecular film into a 2D polymer-like layer^{70,71,178} that is capable of preventing metal penetration,^{26,27} a critical issue for the fabrication of the metal-SAM-metal junctions targeted in this work. The dominance of the cross-linking processes in the given case is primarily due to the stability of the aromatic skeleton. Whereas the C-H bonds in the phenyl rings can be easily cleaved by electrons or X-rays, the skeletons themselves remain intact and cross-link with the neighbouring moieties.^{70,161,177}

Both systems allow for patterning via e-beam irradiation but with a few major differences. Whereas the aliphatic systems are positive resists, meaning the pattern written with electrons is directly transferred onto the surface, the aromatic SAMs are negative resists. That is to say,

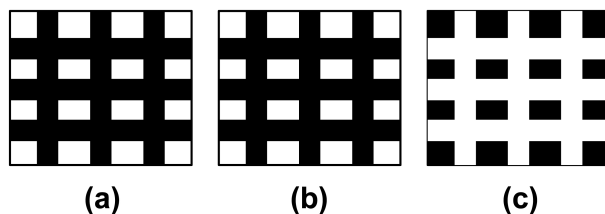


Figure 5.1: Schematic drawings of positive and negative resists. (a) original e-beam pattern (e.g. TEM grid mask; the white areas are irradiated with electrons), (b) pattern developed on alkane thiol SAMs, (c) pattern developed on aromaticthiol SAMs.

the end-pattern (for instance after etching) is the reverse of that originally written, i.e. it is a negative (figure 5.1). If SAMs are to be used either as resists⁷⁰ for e-beam lithography or as components of nanoelectronic devices after the irradiation treatment,^{26,27,131} it is crucial to develop an understanding of the effect of electrons on these films.

First, in order to introduce the various processes occurring in SAMs upon electron irradiation, a study of the effect of electron irradiation on self-assembled monolayers of two model aliphatic thiols (positive resists), namely hexanethiol(C6) and dodecanethiol (C12) will be presented. Second, the results of the electron irradiation of our model films, PPPn and FTPn (both negative resists), will be discussed with special attention to the structural modification of these layers. Finally, the modification of their charge transport properties of the aromatic SAMs induced by the irradiation treatment will be discussed for each system.

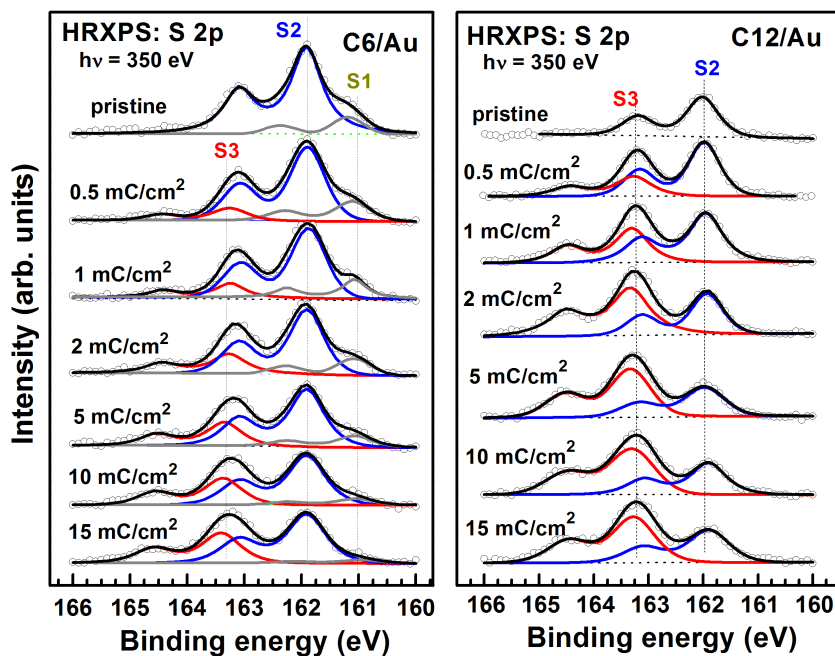


Figure 5.2: S 2p HRXPS spectra of pristine and irradiated C6 (left panel) and C12 (right panel) SAMs (open circles) acquired at a photon energy of 350 eV, along with the corresponding fits by the doublets related to the pristine thiolate (S2, solid blue line), pristine different thiolate (S1, solid dark yellow line) and irradiation-induced dialkylsulfide (S3, solid red line) moieties. The BE positions of the doublets (S 2p_{3/2}) are highlighted by the vertical dashed lines. The background of the individual spectra is shown by the horizontal dashed lines. The irradiation doses are indicated at the respective curves.

5.1 Irradiation induced processes in alkanethiols

Note: this section is largely based on a published research paper: Hamoudi, H. and Chesneau, F.; Patze, C. and Zharnikov, M. *J. Phys. Chem. C* **2011**, *115* (2), 534

5.1.1 Introduction

Monolayers of both short-chain and long-chain alkanethiols, C6 and C12 respectively, were used to study in detail the effect of electrons on SAMs and the distribution of the damage through the films. This will provide a basis for understanding the electron irradiation-induced modifications of the related aromatic SAMs, especially the vertical distribution of the electron-induced damage.

5.1.2 Experimental data

S 2p HRXPS spectra of pristine and irradiated C6 and C12 SAMs are presented in figure 5.2. The spectra of C6/Au and C12/Au exhibit typical changes over the course of electron irradiation. The intensity of the doublets related to the pristine thiolate species (162.0 eV and 161.0 eV for S 2p_{3/2}) decreases whereas a new doublet associated with the irradiation-induced dialkylsulfide species

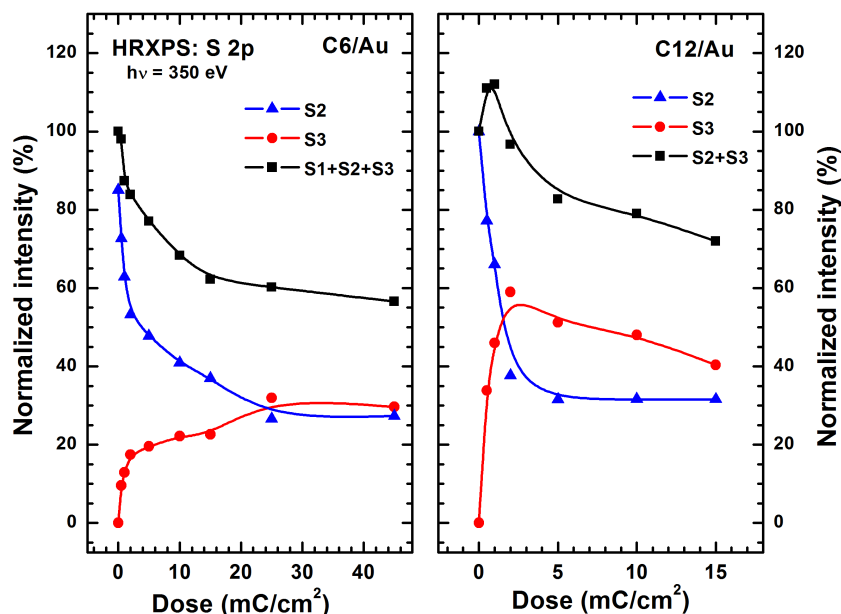


Figure 5.3: Dose dependencies of the intensities related to the headgroup-derived species in C6 (left panel) and C12 (right panel) on gold. The values are normalized to the total S 2p intensity for the pristine film: pristine thiolate moieties (S2, blue up triangles and solid line), irradiation-induced dialkylsulfide species (S3, red circles and solid line), and the total S2p intensity (S1+S2+S3 or S2+S3, black squares and line)

(163.4 eV) appears and increases in intensity. However, the rates and extents of the changes observed for C6/Au and C12/Au are noticeably different. In particular, whereas the intensity of the dialkylsulfide doublet (S3) for C6/Au does not exceed that of the thiolate doublet even at a maximum dose of 15 mC/cm², this happens at a dose of 2 mC/cm² in the case of C12/Au (figure 5.3). In the case of C12/Au (figure 5.3, right panel), the observed behaviour is in agreement with previous experiments.¹⁶⁹ In particular, the crossing of the curves describing the thiolate and dialkylsulfide species occurs at ~ 1.5 mC/cm² as previously observed.¹⁶⁹ Another characteristic feature is the initial increase and subsequent decrease of the total S 2p intensity. First, this behavior is related to the different location of the emerging dialkylsulfide species (S3) compared to the original thiols. The photoemission signal from the species trapped in the alkyl matrix is less attenuated than the signal from those located at the SAM-substrate interface.¹⁹ Thus, following the emerging dialkylsulfide moieties, the total S 2p signal increases. Second, the S 2p signals related to both thiolate and dialkylsulfide species increase due to the reduction of the film thickness (leading to less attenuation of the 2p signal) associated with the irradiation-induced desorption of chain fragments (see below). Along with the hydrocarbon pieces, sulfur-containing fragments desorb to some extent resulting, at higher doses, in the observed decrease in the total S 2p intensity. The behaviour of C6/Au is radically different (figure 5.3, left panel). First of all, the formation of the dialkylsulfide species occurs to a noticeably lower extent compared to C12/Au. Second, the total S 2p intensity does not exhibit a bump at low irradiation doses but decreases continuously and to a higher extent over the course of the irradiation treatment compared to C12/Au. Finally, the reduction of the thiolate species occurs at a lower rate relative

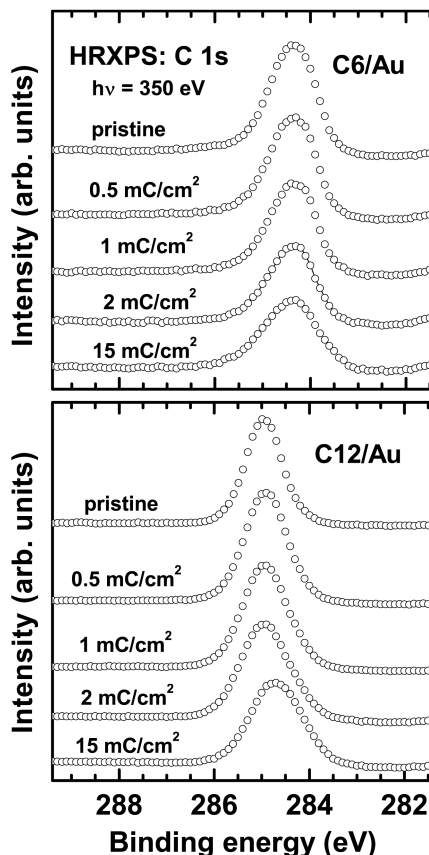


Figure 5.4: C 1s XPS spectra of pristine and irradiated C6 (upper panel) and C12 (bottom panel) SAMs. The irradiation doses are indicated at the respective curves.

to C12/Au (considering both types of thioliates (161 and 162 eV) together). At the same time, the reduction rate of the conventional thiolate in C6/Au is quite similar to that of C12/Au, at least during the initial stage of irradiation.

Complementary information about the irradiation-induced modification of C6 and C12 films is provided by the C 1s HRXPS spectra presented in figure 5.4. The spectra of pristine C6 and C12 films exhibit a single emission at 284.35 and 284.9 eV respectively, in accordance with literature data.²⁰ This emission is associated with the alkyl backbone of C6 and C12 SAMs. During irradiation, the C 1s emission of C12/Au shifted to lower BE, broadened, and decreased in intensity, which is a typical behaviour of AT SAMs.^{169,177} The downward shift is assigned to the progressive dehydrogenation of the film, the broadening to the chemical and structural inhomogeneity, and the intensity decrease to the desorption of the SAM constituents and their fragments.^{169,177} The dose dependency of the effective thickness of the C6 and C12 films, derived on the basis of the C1s and Au4f spectra (see section 2.1), are presented in figure 5.5. In contrast to the differences observed in the S 2p spectra (figure 5.2), the behaviour of the relative thickness in these films is almost identical, even though the absolute values are noticeably higher for the thicker C12 SAM.

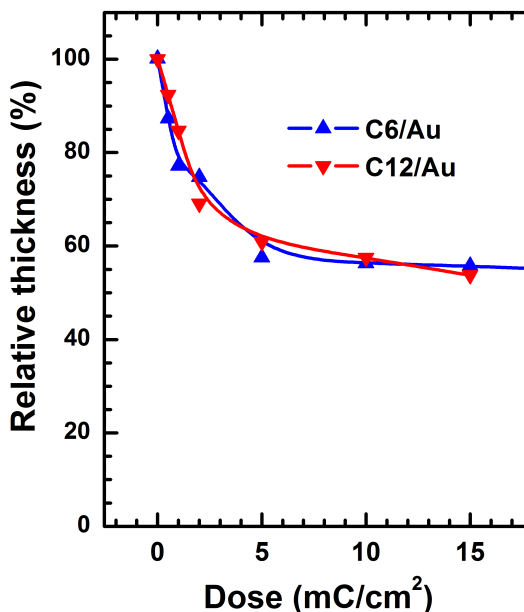


Figure 5.5: Relative thicknesses of C6 (blue up triangles and solid line) and C12 (red down triangles and solid line) SAMs as functions of the irradiation dose. The values are normalised to the thickness of the respective pristine film.

5.1.3 Discussion

The different behaviour of C6/Au and C12/Au with respect to ionising radiation is unexpected and not easy to explain. Indeed, the chemical compositions of the C6 and C12 molecules are almost identical, with the only difference being the length of the alkyl chain. Also, the crystallographic structures of these films are quite similar, even though the short chain C6 film is presumably characterised by a larger amount of gauche defects and larger orientational disorder compared to C12/Au.¹⁶¹ According to STM data, the dominant structural motif in both C6/Au and C12/Au is the $(2\sqrt{3} \times 3)\text{rect}$ lattice (the latter structure is also frequently denoted as $c(4 \times 2)$ superlattice).^{20,161} In C12/Au, this structure coexists with the $(\sqrt{3} \times \sqrt{3})\text{R}30^\circ$ arrangement, with the relative weights of both structures being elusive and presumably dependent upon the identity of the substrate and the exact parameters of the preparation procedure. Note that such a coexistence is typical for long-chain AT SAMs on Au(111), even though the $(2\sqrt{3} \times 3)\text{rect}$ lattice is dominating. However, the observed differences in the behaviour of C6/Au and C12/Au can not solely be related to the presence of a certain fraction of the $(\sqrt{3} \times \sqrt{3})\text{R}30^\circ$ motif in the latter SAM. Similarly, it appears unreasonable to associate this behaviour with the occurrence of differently bound thiolate species in C6/Au. First, the portion of these species is low (ca. 20 %). Second, not only these species but also conventional thiolate moieties in C6/Au behave differently under ionising radiation than C12/Au (data not shown, see full paper). A tentative explanation of this behaviour can be provided by the exact analysis of the experimental data in view of the specific course of the individual irradiation-induced processes in C6/Au and C12/Au. At first sight, the S 2p and C 1s HRXPS data seem to contradict one another. According to the former data (figure 5.2), the C6 SAM is considerably more stable toward ionising radiation as compared to C12. However, as shown in figure 5.5, the relative extents of irradiation-induced

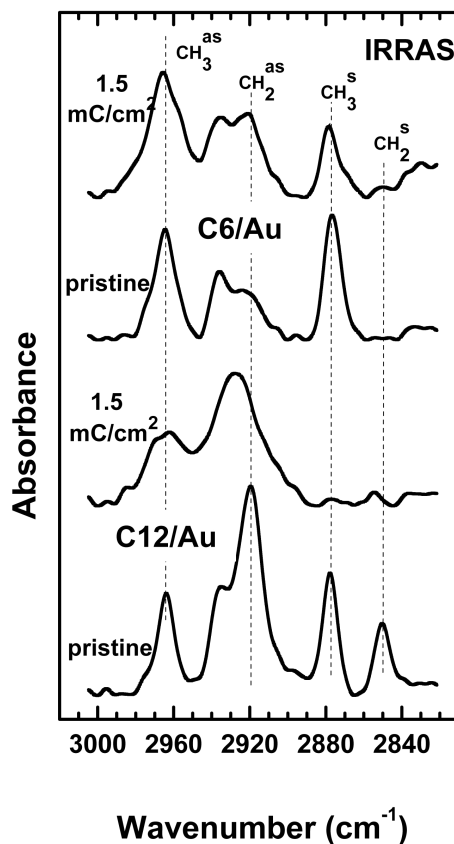


Figure 5.6: IRRAS spectra of pristine and irradiated (1.5 mC/cm^2) C6 and C12 SAMs acquired in the region of the characteristic stretching modes of methylene and methyl groups. The positions of these modes for pristine C12/Au are highlighted by the vertical dashed lines; the modes are marked.

desorption in C6/Au and C12/Au are similar, implying comparable sensitivities of these films to the irradiation treatment. This seeming contradiction can be partly resolved in view of the IRRAS data (figure 5.6). In the case of C12/Au, the loss of the methyl and methylene symmetric stretching vibrations suggests significant disordering and fragmentation of the film, accompanied by almost complete damage to the SAM-ambient interface. In contrast, the spectra of irradiated C6/Au are very similar to that of the intact molecular species, with the terminal methyl groups being only slightly affected by the irradiation treatment. In view of these observations, it is reasonable to assume that the major difference between the behaviour of C6/Au and C12/Au with respect to ionising radiation is a different branching of the irradiation-induced reactions, above all fragmentation and desorption.

5.1.3.1 Effect of the matrix on the branching of irradiation-induced reactions

In C12/Au, fragmentation of the alkyl backbone and almost complete damage to the SAM-ambient interface (methyl moieties), followed by desorption of a significant portion of the released hydrogen and hydrocarbon fragments occur. These processes are accompanied by damage to the

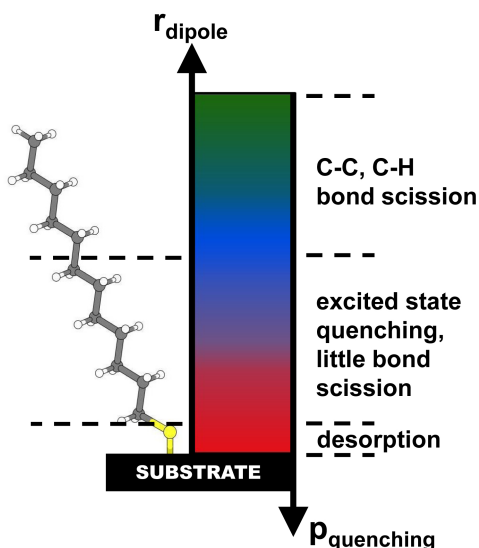


Figure 5.7: Schematic drawing of the excited state quenching in alkanethiol SAMs.

SAM-substrate interface associated with the cleavage of the pristine thiolate-gold bonds with most of the released alkylsulfide fragments being captured in the chemically active hydrocarbon matrix in the form of dialkylsulfides. The capture is mostly mediated by the broken bonds and radicals appearing after the cleavage of C-H bonds throughout the alkyl matrix. It should be noted that the analogous active sites appearing after the scission of C-C bonds likely contribute to some extent as well. Such an active matrix and the comparatively large length of the C12 moieties lead us to believe that the desorption of the complete molecule is unlikely for C12/Au. Note that the above behavior is typical for long-chain AT SAMs on Au(111), including films of hexadecanethiolates¹⁷⁹ and octadecanethiolates.^{169,180} In contrast to C12/Au, not fragmentation but release and desorption of the complete and almost complete C6 moieties occurring after the cleavage of the thiolate-Au bonds seem to be the dominating irradiation-induced processes for C6/Au. The thinner and less active (see below) alkyl matrix has a reduced ability to capture the released C6 moieties which are smaller and more volatile than the C12 ones. Since most of the released sulfur-containing moieties desorb, the dialkylsulfide species are not observed in the S 2p HRXPS spectra of C6/Au (figure 5.2, left panel) thus giving the impression that the C6 SAMs are stable toward ionizing radiation. There is, however, a noticeable thickness reduction associated with this desorption, as demonstrated in figure 5.5.

5.1.3.2 Quenching of the excited states

Apart from the comparatively thin hydrocarbon matrix and enhanced (compared to C12) volatility of the C6 species, another phenomenon is, in our opinion, mostly responsible for the observed branching of the irradiation-induced processes in C6/Au.

This phenomenon is the quenching of the excited dissociative states in the alkyl matrix due to the coupling of the respective dipole with the image dipole induced in the substrate (figure 5.7).¹⁸¹ If such a quenching event occurs fast enough, bond dissociation will not take place, leaving intact molecular fragments or entire molecules. In addition, the rate (or probability)

of quenching strongly depends upon the distance between the excited site in the SAM and the substrate as the strength of the dipole-image dipole coupling is proportional to the third power of the separation between the dipoles involved.¹⁸¹ An important consequence of this is the enhanced probability of C-C and C-H bond scission in the regions adjacent to the SAM-ambient interface as compared to those close to the SAM-substrate one. This results in a depth distribution of the irradiation-induced bond scission events in the SAM⁶⁸ and predominant damage at the SAM-ambient interface compared to the interior of the SAM.^{177,180,181}

Apart from the above effects, the enhanced quenching of the excited states in the vicinity of the substrate should also result in a comparatively small rate and extent of irradiation-induced scission of C-C and C-H bonds in short-chain AT SAMs on metal substrates, as was reported in the literature on the basis of electron-stimulated desorption data (hydrogen yield was monitored).¹⁸¹ This is what we observe here. Due to extensive quenching of the excited states in C6/Au, damage to the methyl groups at the SAM-ambient interface occurs at a considerably lower rate compared to C12/Au. Consequently, the cleavage of the C-C and C-H bonds in the C6 SAM is reduced, resulting in a less reactive matrix compared to C12/Au, thus diminishing the probability of capturing the alkylsulfide fragments released after cleavage of the thiolate-Au bond.

However, despite a low rate, C-C and especially C-H bond scission events occur in C6/Au to some extent leading, after extensive irradiation, to cross-linking between the residual C6 species in the SAM. This cross-linking seals the film, preventing further changes (except, probably, for progressive C-H bond scissions) and resulting in a leveling off behaviour for the majority of the irradiation-induced processes. Above all, further degradation of the thiolate-gold interface does not occur over the course of the prolonged irradiation treatment since cross-linking bonds between the SAM constituents prevent the release of individual molecular species. A similar situation takes place in aromatic thiol-derived SAMs where extensive cross-linking transforms these films in quasi-polymer sheets preventing the scission of the thiolate-gold bonds.^{70,72} Even if the latter bond is cleaved, it can reform as long as the released fragments stay in place, kept there by cross-linking bonds to their neighbours. Note that in contrast to the alkyl matrix, the cleavage of the pristine thiolate-gold bonds should occur at similar rates and to a similar extent in C6/Au and C12/Au since the locations of the headgroup-substrate interface are identical for both films. Indeed, this seems to be the case, as follows from figure 5.3. Therefore, it is not the release of the molecular fragments themselves but their subsequent destiny which is important for the behaviour of these systems. The further relevant difference is the extent of fragmentation of the alkyl chains as mentioned above.

5.1.4 Summary

During low-energy electron irradiation on AT SAMs on Au(111) both the alkyl matrix and the headgroup-substrate interface are affected by a variety of closely interrelated irradiation-induced processes. The branching of these processes is however distinctly different in the two systems studied here. In C12/Au, which exhibited the typical behaviour of long-chain AT SAMs, the dominant irradiation-induced processes are decomposition of the alkyl chains with subsequent desorption of the released fragments and damage to the SAM-ambient interface. The alkylsulfide species appearing after cleavage of the thiolate-gold bond are mostly captured in the alkyl matrix which becomes chemically active upon progressive cleavage of C-H and C-C bonds. In contrast, in C6/Au, the dominant irradiation-induced process is the desorption of the entire C6 moieties released after cleavage of the thiolate-substrate bonds. This occurs due to the comparatively high volatility of these species as well as the small depth and low chemical activity of the alkyl

matrix in the case of C6/Au. The behaviour of short-chain AT SAMs on Au during electron irradiation can affect both the course and kinetics of irradiation-induced exchange reactions,²² affording new opportunities for the fabrication of mixed SAMs and chemical lithography,²² a useful technique for device fabrication.

5.2 Irradiation induced processes in PPPn

Using *p*-terphenyl-4,4''-dimethylthiol (TPDMT) as building block, it was demonstrated in our laboratory that aromatic monolayers irradiated with electrons were capable of preventing metal penetration.^{26,27,58} However, about half of the terminal groups of TPDMT SAMs is lost during the irradiation treatment, thus dramatically reducing the density of metal nucleation sites. The (4'-(pyridin-4-yl)biphenyl-4-yl)methanethiol (PPP1) molecules (section 4.2) differ from the TPDMT molecules previously used in our laboratory for metal deposition^{26,27,58} in that their terminal group is part of the spacer unit. As such we expect the PPP1 molecules to, unlike TPDMT, largely retain their terminal group after electron irradiation thus increasing the density of terminal groups available for metal film nucleation. This should in turn diminish the probability of metal penetration into and through the SAM. This could also lead to an improvement in the uniformity of the evaporated metal films.

In this section we report on the irradiation-induced modification of PPPn thin films. Unlike TPDMT, PPP1 is asymmetrical thus potentially allowing us to resolve the irradiation-induced processes along the spacer unit. Data will be presented for the PPP1/Au system but all conclusions put forth in this section are valid for the whole series of molecules at our disposal (PPP1, PPP2 and PPP3) unless stated otherwise.

5.2.1 Modification of the PPP1 carbon matrix upon electron irradiation

IRRAS data (figure 5.8, top panel) shows that the PPP1 matrix is heavily modified upon electron irradiation. Consistent with IR data for biphenylthiol SAMs,⁶⁴ the symmetrical and asymmetrical ring and C=C stretches associated with the 4-(biphenyl-4-yl)pyridine unit (1487 and 1544 cm^{-1} respectively) disappear upon irradiation. Furthermore, the intensity of the pyridine ring stretches at 1595 and 1603 cm^{-1} is reduced. Simultaneously, new vibrations appear at 1518, 1610 and 1660 cm^{-1} . These were assigned, in accordance with theoretical calculations (figure 5.8, bottom panel), to the ring and C=C stretches of the crosslinked PPP1 film. In particular, the disappearance of the vibrations at 1487 and 1544 cm^{-1} and the appearance of a vibration at 1610 cm^{-1} are clear indicators of crosslinking between the PPP1 units. Furthermore, comparison of the experimental spectrum of the crosslinked PPP1 (CL-PPP1) film with the various theoretical spectra (figure 5.8, bottom panel, spectra (b)-(d)) suggests that not only the benzene rings, but also the terminal pyridine rings are crosslinked, as expected from literature^{68,181} and our own work on alkane thiols (section 5.1). The modification of the pyridine's environment should result in a modification of the properties of the SAM-ambient interface. Indeed, the water contact angle of PPP1/Au films increases from 40° to 55° at an irradiation dose of 30 mC/cm^2 . In an effort to better understand the modification of the PPP1 films by electrons, these were further studied by HRXPS and NEXAFS spectroscopy.

5.2.1.1 Changes in the hydrocarbon matrix probed by C1s HRXPS

At first sight, the hydrocarbon matrix of PPP1 films, probed by C1s HRXPS, seems largely unaffected by electrons (figure 5.9, top panel). This result is consistent with the data obtained for the corresponding *p*-terphenyl-4-methanethiol (TP1) films.¹⁸² However, it is in seeming contradiction with the IRRAS data presented above. Close inspection of the C1s HRXPS spectra reveals a continuous shift to higher binding energies (BE) (figure 5.9, bottom panel) of the main C1s peak. At 35 mC/cm^2 , the C1s peak at ~ 284.7 eV is shifted to higher binding energies by ~ 0.2 eV. This suggests a partial change in the hybridisation of the carbons in the PPP1 matrix

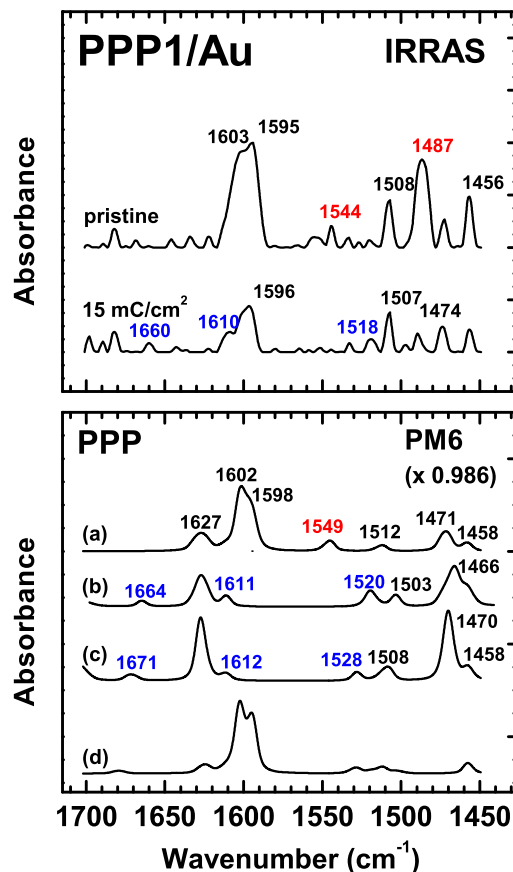


Figure 5.8: Top panel: Experimental IRRAS spectra of PPP1/Au before (top spectrum) and after (bottom spectrum) electron irradiation. The main vibrations are shown. The vibrations unaffected by electron irradiation are marked in black. Red: disappearing vibration; Blue: new vibration. Bottom panel: Calculated spectra for the PPP moiety. (a) pristine film; (b) top two rings crosslinked; (c) same as (b) except one of the pyridine rings was replaced by 1,4-dihydropyridine; (d) middle ring crosslinked. The theoretical spectra were calculated at the PM6 level using the MOPAC2009 software package. The wavenumber scale was calibrated with respect to the vibration at 1603 cm⁻¹. The scaling factor was 0.986. The highest absorbance in all calculated spectra was set as 1.

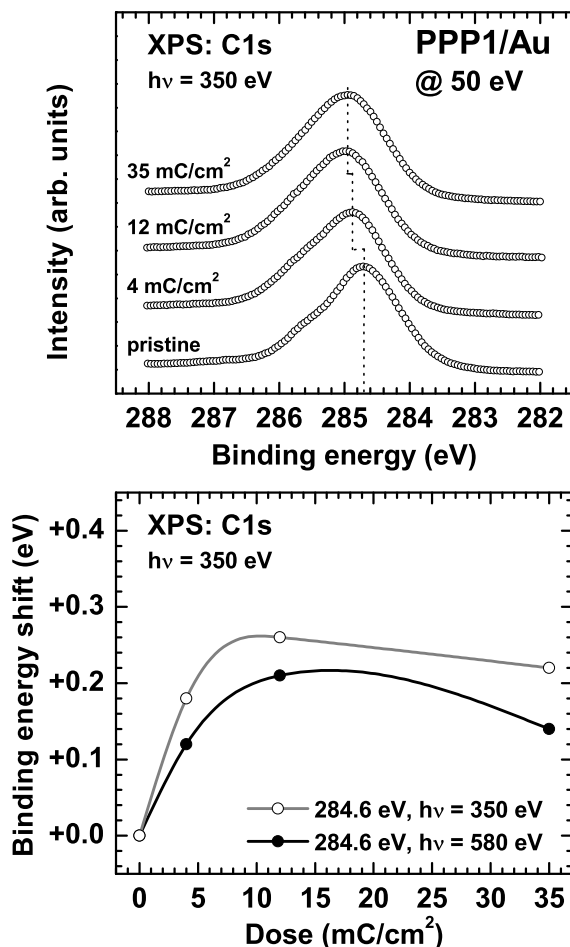


Figure 5.9: HRXPS C1s spectra of PPP1/Au monolayers at various electron irradiation doses (top panel). The binding energy shift of the C1s peak at 284.6 eV is shown in the bottom panel.

from sp^2 to sp^3 . Such a shift, albeit larger than the one in this study, was observed between graphite (sp^2 , 284.4 eV) and diamond (sp^3 , 285.2 eV) samples.^{183,184} Note that the BE shift is lower at higher excitation energy (~ 0.14 eV at $h\nu = 580$ eV) indicating that the rehybridisation occurs mainly toward the top part of the film. This behaviour is consistent with literature⁶⁸ and our observations for alkanethiols (section 5.1).

5.2.1.2 Rehybridisation of the matrix observed by NEXAFS spectroscopy

The electronic structure, and hence the change in the hybridisation of the carbons, of the PPP1 films upon electron irradiation was probed by NEXAFS spectroscopy at the so-called magic angle (55° , figure 5.10). Similarly to C1s HRXPS, the changes to the electronic structure are

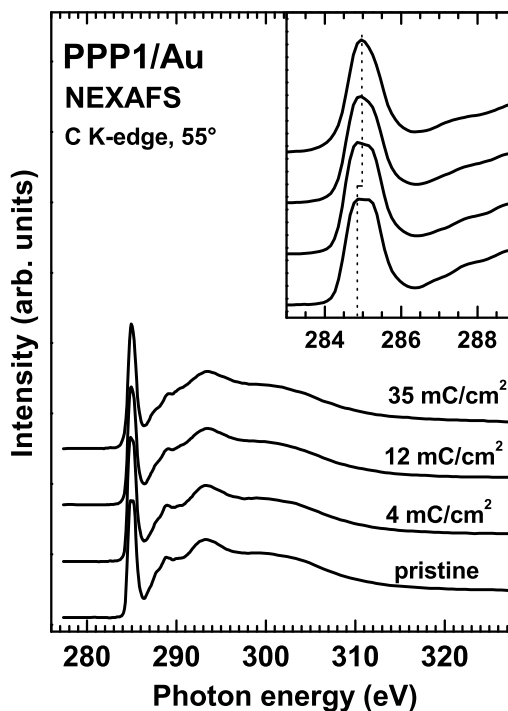


Figure 5.10: NEXAFS C K-edge spectra (55°) of PPP1/Au monolayers at various electron irradiation doses. Inset: pre-edge region (< 291 eV).

only revealed upon careful examination of the NEXAFS data. As shown in the inset of figure 5.10, the main C $1s \rightarrow \pi_1^*$ transition is shifted to higher photon energies by ~ 0.15 eV, consistent with the shift observed by C1s HRXPS (~ 0.2 eV). Simultaneously, the σ^* and Rydberg (R^*) transitions increase in intensity with increasing electron dose, suggesting, as C1s HRXPS, partial rehybridisation of the carbon matrix upon electron irradiation. A similar behaviour was observed for the pulsed laser evaporation of graphite on silicon targets.^{183,184} In addition, a small feature at 284.2 eV corresponding to the polymerisation of the PPP1 units^{185,186} was observed. A similar feature was found for the electron irradiation of TPDMT (284.3 eV, data not shown) and the perfluorinated terphenyl analogue FTP3 (284.6 eV, section 5.3).

5.2.1.3 Changes in the molecular orientation of PPP1 films

In addition to allowing us to probe the electronic structure of thin films, NEXAFS spectroscopy can be used to follow changes in molecular orientation (figure 5.11). The decrease in the π^* and σ^* difference peaks upon irradiation suggests an irradiation-induced loss of the average molecular order in the film.⁶⁴ Such a behaviour is typical for irradiated terphenyl-^{68,110,182} and biphenyl-based⁶⁴ monolayers. The loss of order translates into an increase in the tilt angle of the molecules from 18.6° for the pristine film to 25.6° at 35 mC/cm^2 (figure 5.12). As for the biphenylthiol⁶⁴ and terphenylthiol¹⁸² systems, we expect the changes in molecular order to be reflected at the SAM-substrate interface.

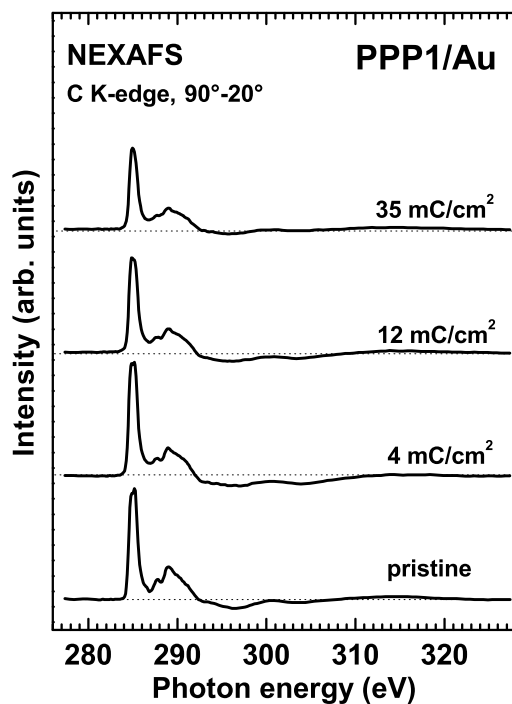


Figure 5.11: NEXAFS C K-edge difference spectra ($I_{90}-I_{20}$) of PPP1/Au monolayers at various irradiation doses. Electron energy: 50 eV.

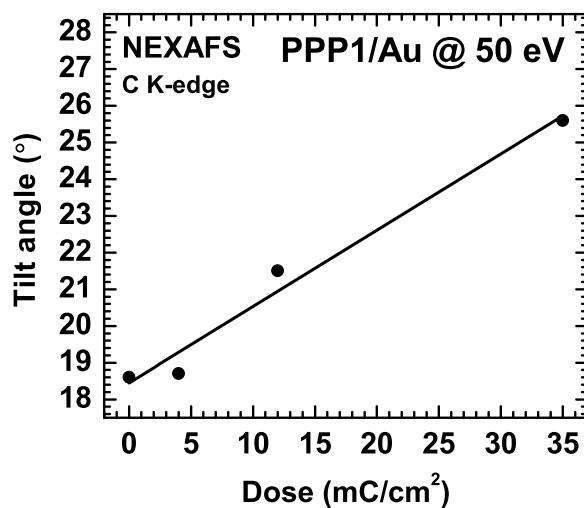


Figure 5.12: Variation of the average molecular tilt angle with irradiation dose. The variation reflects the disordering of the film. A higher value of the tilt angle means a more disordered film. Electron energy: 50 eV.

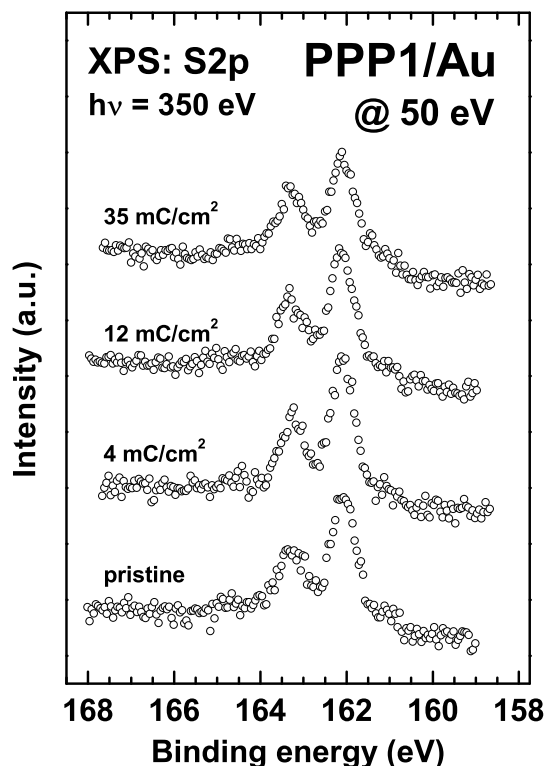


Figure 5.13: S2p HRXPS of PPP1/Au at various irradiation doses. Electron energy: 50 eV.

5.2.2 Damage to the SAM-substrate interface

As can be seen from S2p HRXPS data (figure 5.13), the damage to the SAM-substrate interface is minimal. Furthermore, the total sulphur intensity remained constant throughout the irradiation treatment, suggesting that no PPP1 molecule desorbed from the surface. This behaviour is consistent with data obtained for films of biphenyl-4-ylmethanethiol⁶⁴ (BP1) and the corresponding *p*-terphenylthiol TP1.¹⁸² The lack of significant damage to the SAM-substrate interface is advantageous for subsequent metal deposition since it indicates that the monolayer retains a high structural quality after irradiation. However, for successful nucleation of metal films on top of crosslinked SAMs, not only the SAM-substrate but also the SAM-ambient interface is of importance.

5.2.3 Changes to the SAM-ambient interface

The 4-(biphenyl-4-yl)pyridine unit is asymmetrical affording us, through the terminal pyridine, a unique chance to directly observe the changes at the top of the film. We have probed the changes to the SAM-ambient interface of PPP1 films using N1s HRXPS (figure 5.14). As shown in figure 5.14, the spectrum of pristine pyridine consists of a main peak assigned to pyridine¹⁷ (**1** at 398.9 eV) and two small peaks (**5** and **6**) at higher binding energies (> 401 eV) assigned to protonated pyridines (section 4.2). The presence of protonated pyridines is not surprising

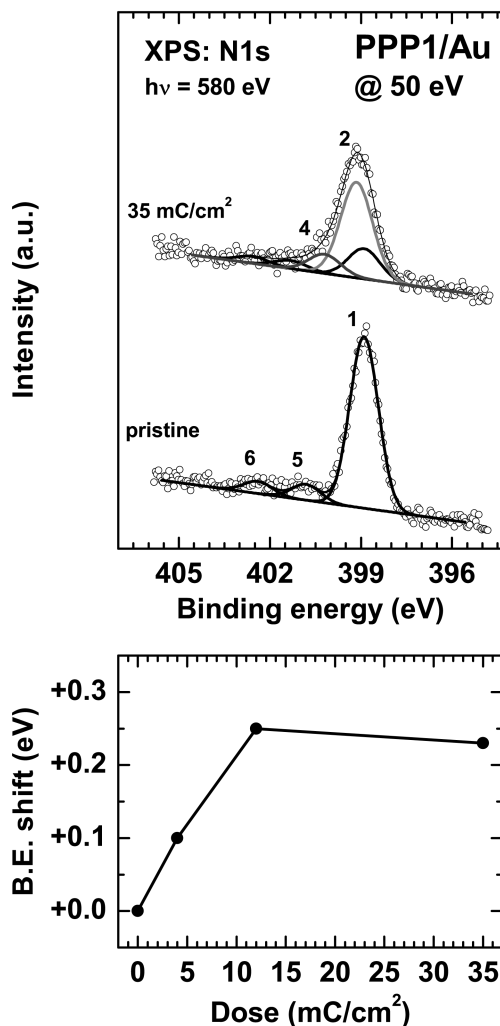


Figure 5.14: N1s HRXPS of PPP1/Au before and after irradiation (top panel) and binding energy shift of the N1s peak as a function of the irradiation dose (bottom panel). Electron energy: 50 eV.

since the samples were exposed to air before measurement^a. Upon electron irradiation, the main peak in the N1s HRXPS spectrum shifts to higher binding energies by ~ 0.25 eV (bottom panel), similar to the shift observed in the C1s HRXPS spectra.^b This suggests that the pyridines are strongly affected by electron irradiation, and could explain why the binding energy shift is larger at the top of the film in the case of carbon (figure 5.9). The N1s peak of the irradiated film is strongly asymmetrical thus suggesting that not one but several nitrogen species are present after irradiation. Spectral deconvolution of the N1s HRXPS spectra before and after irradiation is presented in the top panel of figure 5.14. Upon irradiation, the intensities of the pyridine peak

^aIn a typical synchrotron experiment, the samples were prepared between 3 and 7 days in advance and were kept under Argon prior to measurements.

^bThis shift was also observed by NEXAFS spectroscopy (data not shown)

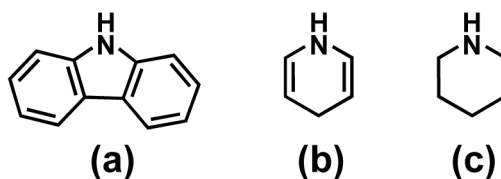


Figure 5.15: Various possible nitrogen-containing motifs. (a) carbazole; (b) 1,4-dihydropyridine; (c) piperidine.

(1) was dramatically reduced. Furthermore, two new high intensity features, **2** and **4**, are clearly visible at 399.2 eV and 400.2 eV respectively. Peak **2** was assigned to crosslinked pyridine.^{187,188} Peak **4** was more difficult to interpret. Since the protonated pyridine species appear above 401 eV,^{189–192} we can reasonably assume that **4** is not related to protonation of the pyridine units (see below). The appearance of this feature suggests that the PPP1 films react in two or more different ways to electron irradiation.

5.2.3.1 Reaction pathways of PPP1 films upon electron irradiation

The binding energy of peak **4** (400.2 eV) corresponds to that of carbazole (figure 5.15).¹⁸⁸ Although we do not expect carbazole to be formed during electron irradiation of PPP1, formation of dihydropyridine is possible. Indeed, pyridine is readily reduced to dihydropyridine (figure 5.15), a structural analogue of carbazole, either chemically^{193–197} or electrochemically.¹⁹⁸ Furthermore, the electron affinity of pyridine is significantly higher than that of benzene (the other component of PPP1 films), enabling a more efficient electron capture by the pyridine moiety (compared to benzene) thus facilitating the reduction of the pyridine moiety.^{199–201} Reduction of pyridine is not a facile process¹⁹³ as reflected by the relatively low intensity of peak **4**. However, it is unclear whether the dihydropyridine moieties are crosslinked to neighbouring pyridines in the film or not. Given that crosslinked films exhibit higher conjugation,^{65,66} thus lowering the energy of the unoccupied states, the formation of crosslinked dihydropyridine can not be discarded.

In summary, the N1s HRXPS data presented above, shows that not only crosslinking but also reduction of the pyridine unit likely occurs during upon irradiation of PPP1/Au films with electrons. Note that the electron irradiation of NO₂ terminated SAMs yields the equivalent amine.⁷¹

5.2.3.2 Irradiation kinetics of PPP1 films

The kinetics of irradiation were followed using N1s HRXPS spectroscopy (figure 5.16). The fraction of pristine pyridine units (filled circles) quickly drops from 82 to ~25 % of the total nitrogen intensity (N_{total}) at 12 mC/cm² and levels off to 20 % of N_{total} after ~25 mC/cm². Simultaneously, the proportion of crosslinked pyridine moieties rises to ~60 % and the dihydropyridine species represent ~12 % of the total N 1s intensity. Furthermore, the levelling off behaviour occurs much earlier than for biphenyl self-assembled monolayers (~50 mC/cm²)²⁰² suggesting that pyridine favours the electron-induced modification of SAMs, presumably by increasing the

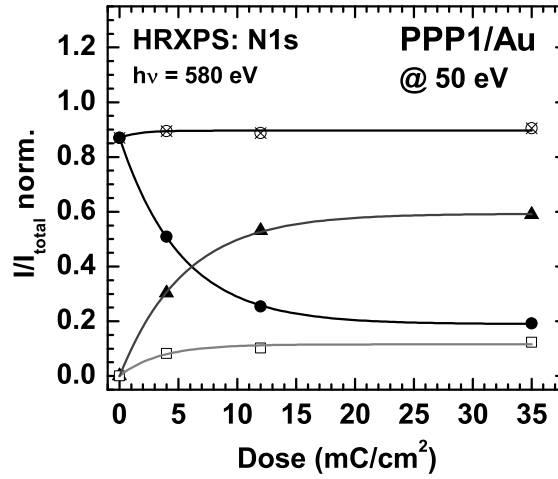


Figure 5.16: Variation of the N1s HRXPS intensity of the various species of PPP1 films with irradiation dose. The intensity is reported as a fraction of the total nitrogen intensity. Filled circles: pristine pyridine (398.9 eV); Filled triangles: crosslinked pyridine (399.2 eV); Open squares: dihydropyridine (400.2 eV); Crossed circles: total pyridine intensity without protonated pyridine species. The protonated pyridine species (BE > 401 eV) represent 12-15 % of the total N 1s intensity. Electron energy: 50 eV.

Peak	I_{norm}^0	A	τ
pristine	0.19	0.68	0.19
crosslinked	0.59	-0.59	0.18
reduced	0.12	-0.12	0.29

Table 5.1: Fitting parameters for the variation of the intensity of the N1s HRXPS features in PPP1 films upon electron irradiation. The cross-sections values are in cm^2/mC .

probability of electron uptake. Each set of data in figure 5.16 was fitted with equation 5.1.

$$I_{norm} = I_{norm}^0 + A \times \exp(-D * \tau) \quad (5.1)$$

Where I_{norm} is I/I_{total} , A is a preexponential factor, D the dose in mC/cm^2 and τ the cross-section. Table 5.1 lists the fit parameters for the data in figure 5.16.

Table 5.1 shows that while the crosslinking process and the disappearance of the free pyridine units occur at a similar rate, the reduction of pyridine occurs faster (the cross-section τ is larger). However, crosslinking is the prevailing process at all electron doses.

5.2.3.3 Extent of crosslinking of PPP1 films

As seen above, the N1s HRXPS spectra can be deconvoluted in crosslinked, reduced and pristine contributions, allowing us to not only study the kinetics of the irradiation process (see previous section) but also to estimate the extent of crosslinking. To date, such an estimate could

only be obtained by Temperature Programmed Desorption (TPD) measurements of irradiated biphenylthiol thin films.²⁰² Since the reduced species (figure 5.14) can not unambiguously be assigned as crosslinked or free in the matrix (section 5.2.3.1), only a rough estimate of the extent of crosslinking can be given. As seen in figure 5.16, the fraction of free pyridine units in the fully crosslinked film is $\sim 20\%$. This is in agreement with the TPD data obtained for biphenylthiol films.²⁰² However, if the reduced pyridine species (dihydropyridine at 400.2 eV in the N1s HRXPS spectrum of the crosslinked film) are assumed to also be free in the matrix, then the fraction of free pyridines in the crosslinked film rises to $\sim 30\%$, still in agreement with the TPD data for biphenylthiol films.²⁰² We expect such a high fraction of free molecules in the crosslinked films to have a negative impact over the metal permeability of the crosslinked PPPn films by creating metal penetration channels in the films. We surmise the quality of the crosslinked film (defined by the extent of crosslinking) could be improved if the quality starting film were improved by either preparing the pristine film at higher temperatures, thus increasing the average domain size²⁰ or annealing the film *in vacuo*.

5.2.3.4 Survival of the terminal groups of PPP1 upon irradiation

For improved nucleation of thin metal films on top of crosslinked SAMs, and to prevent metal penetration, the density of terminal groups should remain high after irradiation. Upon extensive irradiation (~ 45 mC/cm²), the density of terminal groups for TPDMT, our reference system, diminishes by $\sim 50\%$.^{26,27} As can be seen from N1s HRXPS data (figure 5.16), the total nitrogen intensity only varies slightly over the course of irradiation thus indicating that the terminal pyridine is largely retained in the irradiated film. This is, as explained above, of crucial importance for the immobilisation of metal on such films and is a definite advantage over our reference crosslinked TPDMT films.

5.2.4 Changes in the electronic structure of PPP1 films upon electron-irradiation

As seen in this chapter, electron irradiation of PPPn/Au SAMs leads to the modification of their electronic structure, consistent with the behaviour of *p*-terphenylthiol SAMs. In particular, electron-irradiated monolayers of our reference system TPDMT have been studied using a combination of UPS and IPES.^{65,66} After electron irradiation, the electronic structure of the TPDMT film was found to be modified and the band gap of this system was reduced by ~ 0.9 eV. Unfortunately, we have been unable to perform such experiments for PPPn/Au. However, we were able to measure the work function (WF) of both the pristine and irradiated (35 mC/cm²) films. As shown in section 4.4, the position of the Highest Occupied Molecular Orbital (HOMO) correlates to some degree with the work function of thiol-modified gold surfaces, and as such can give us some indication about the modification of the electronic structure of irradiated PPPn/Au monolayers. The WF of PPPn/Au decreases by ~ 0.1 eV after irradiation by electrons. This value is lower than that obtained for TPDMT (-0.2 eV) which is in agreement with the change in the position of the HOMO determined by UPS⁶⁶ (~ -0.18 eV).

However, the change in the WF can not alone give a full picture of the transport properties of such monolayers. Indeed, impedance spectroscopy measurements on pristine and irradiated TPDMT showed a two-fold increase in the interfacial resistance.¹³¹ TPDMT and PPPn SAMs being similar, we expect a similar behaviour. Impedance spectroscopy measurements should be carried out to confirm this hypothesis.

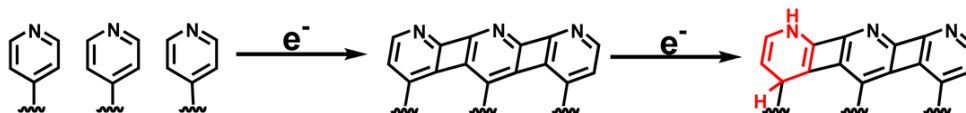


Figure 5.17: Electron irradiation-induced processes in PPP1 films.

5.2.5 Summary

We have studied the effects of low energy electron irradiation (50 eV) onto PPP1 films using IRRAS, HRXPS, NEXAFS spectroscopy and Kelvin probe measurements. The films exhibit a range of behaviours typical of terphenyl thiols such as moderate loss of molecular orientation and damage to the SAM-substrate interface as well as a lack of molecular desorption upon irradiation. In addition, PPP1 was found to undergo irradiation-induced processes that, to the best of our knowledge, have not been reported so far. In particular, close examination of the N1s HRXPS spectra revealed, in addition to crosslinking, the formation of reduced pyridine species such as 1,4-dihydropyridine upon electron irradiation (figure 5.17). The rate of change was rapid with the saturation behaviour being reached at about 25 mC/cm^2 , much sooner than the biphenyl or TPDMT system.^{26,65,202} The terminal nitrogen was found to survive the irradiation treatment and as such CL-PPP1 films, in contrast to CL-TPDMT films,^{26,27} provide a high density of sites for metal film nucleation. The extent of crosslinking was also estimated from N1s HRXPS data to be 70-80 % (20-30 % of non-crosslinked pyridine). However, the relatively high fraction of non-crosslinked molecules (20-30%) could have a deleterious effect on the metal permeability of the CL-PPPn films ($n = 1-3$). The e-beam deposition of nickel on CL-PPPn ($n = 1,3$) will be presented in section 6.3.

In addition, we have measured the change in work function upon electron-irradiation. The WF was found to only slightly decrease at a dose of 35 mC/cm^2 , in accordance with data for the reference TPDMT system.⁶⁶ This is an important first step toward using PPPn SAMs as dielectrics for the fabrication of nanoelectronic devices and further investigation of the transport properties of these films should be carried out.

5.3 Electron irradiation of FTPn films

Note: this section largely based on a published scientific journal article: Chesneau, F.; Hamoudi, H.; Schuepbach, B.; Terfort, A. and Zharnikov, M. *J. Phys. Chem. C* **2011**, *115*, 4773. The differences between the two systems in the above study (FTP2/Au and FTP3/Au) being minimal with respect to electron-induced damage, only data about the FTP3/Au system will be presented below with reference to the FTP2 system when appropriate. The full data set for the FTP2/Au system can be found in the article.

5.3.1 Introduction

An important advantage of the FTPn SAMs relative to the analogous hydrocarbon films with regard to electron irradiation, is the possibility to monitor the behaviour of the fluorine atoms which are analogues of the hydrogen atoms in the latter systems. For the hydrocarbon films, only desorption of hydrogen and the branching of the desorbed hydrocarbon fragments could be monitored by electron- and photon-stimulated desorption spectroscopy.¹⁸¹ As for the residual film, no information about the hydrogen content or hydrogen destiny could be obtained, even though possible structural motifs have been proposed on the basis of spectroscopic data and theoretical simulations.?? In contrast, in the case of FTPn SAMs, the fluorine content of the film can be directly probed by XPS and NEXAFS spectroscopy. Furthermore, we expect that treating FTPn/Au monolayers with electrons would allow us to easily and precisely modify their transport properties, a crucial parameter for the fabrication of Metal-SAM-Metal nanojunctions.

5.3.2 Irradiation-induced chemical changes in FTP3 films

5.3.2.1 The destiny of fluorine

Following fluorine by XPS C 1s and F 1s XPS spectra of FTP3/Au acquired in the course of exposure of this film to electrons (*ex-situ*) are shown in the left and right panels of figure 5.18. The individual components of the C 1s spectrum behave differently over the course of the irradiation treatment. The emission related to the carbon atoms directly bonded to fluorine (C-F) decreases in intensity while the intensities of the emissions assigned to the residual carbon atoms in the FTP moiety (C-C) and aliphatic linker (C-H) increase. This suggests a partial cleavage of the C-F bonds in the FTP moiety with subsequent desorption of the released fluorine, presumably in atomic or ionic form.²⁰³ The additional peaks observed at 288.2 eV and 290.1 eV at high doses ($> 10 \text{ mC/cm}^2$) are associated with the attachment of the released fluorine atoms to the rings, leading to the formation of CF₂ groups in the FTP matrix. The 290.1 eV peak can be assigned to CF₂ species themselves while the 288.2 eV can be ascribed to the C-F carbon adjacent to it. The above assignments are supported by the fact that these peaks were also observed in *in-situ* XPS spectra of the extensively irradiated FTPn films (data not shown). The positions of these features agree well with those of the analogous species produced during the electron irradiation and plasma deposition of hexafluorobenzene films.^{204–206} Note that the CF₂ related peaks are weak ($< 10 \%$), suggesting that fluorine reattachment plays a minor role. Note also that whereas no oxygen was observed for *in-situ* measurements of FTPn films, the O 1s *ex-situ* spectra of these systems (data not shown) showed a slight trace of oxygen related to its uptake upon exposure of the samples to ambient. Therefore, a contribution from C-O species for the peak at 290.1 eV can not be ruled out. Finally, the F 1s spectra of FTP3/Au (figure 5.18) exhibit a progressive decrease in intensity over the course of irradiation, mimicking the behaviour

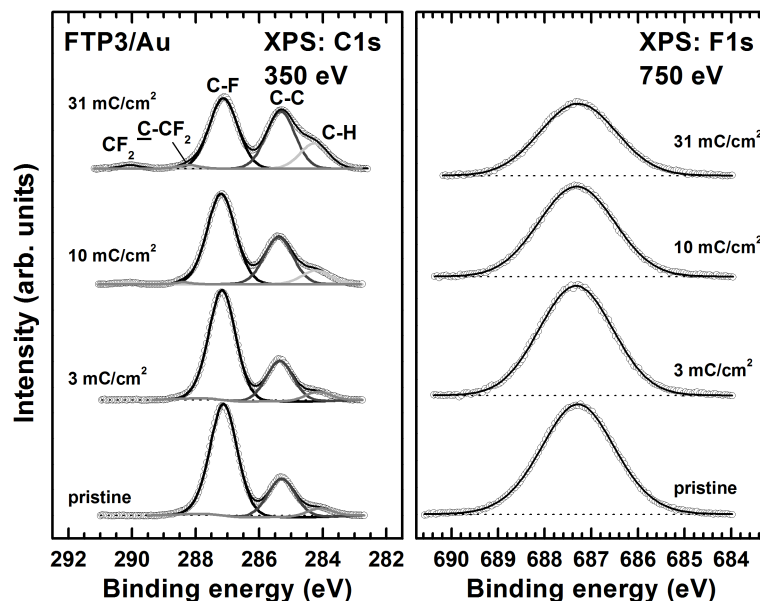


Figure 5.18: C 1s (left panel) and F 1s (right panel) XPS spectra of FTP3/Au acquired over the course of exposure of this film to electrons (open circles) along with the corresponding fits by several components (solid lines; see text for details). The individual components are assigned. The irradiation doses are indicated at the respective curves.

of the C 1s (C-F) emission, thus supporting our conclusion that the C-F bond is cleaved with subsequent desorption of the released fluorine atom. The relative intensities of the C 1s (C-F) and F 1s emissions for the FTP3 films are depicted in figure 5.19 as functions of irradiation dose, along with the data for a reference system, F10H2/Au. Both C 1s (C-F) and F 1s curves mimic each other qualitatively as well as quantitatively, exhibiting an intensity decrease of $\sim 31\%$ at a dose of 31 mC/cm^2 .

Fluorine loss followed by NEXAFS spectroscopy In addition to information about the electronic structure (section ??), information about the chemical composition of the probed monomolecular films can be gained from NEXAFS spectroscopy. As seen in figure 5.20, the intensity of the C-F π_2^* resonance (section ??) decreased significantly over the course of irradiation (about 40% decrease at a dose of 31 mC/cm^2), whereas that of the π_1^* (1) resonance remained almost constant as shown in the left panel of figure 5.23. Since the intensity of the π_2^* resonance can be considered as a measure of intact C-F bonds, its decrease over the course of irradiation suggests, in agreement with the XPS data (section 5.3.2), cleavage of these bonds. At the same time, the amount of cleaved and disturbed C-F bonds (e.g. ca. 40% at 31 mC/cm^2) is somewhat higher than the respective decrease in the C 1s (C-F) and F 1s XPS intensities (e.g. ca. 31% at a dose of 31 mC/cm^2). This can partly be related to the formation of CF_2 species. Another relevant effect is the self-attenuation of the photoemission signals, so that the real loss of fluorine is somewhat higher than the observed intensity decrease. Note that this effect should be less pronounced in the case of NEXAFS spectroscopy due to the comparatively high values of the effective attenuation length for the partial electron yield signal.²⁰⁷

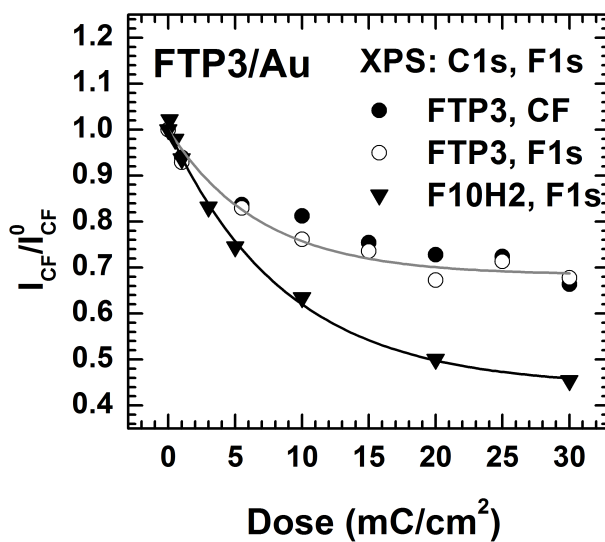


Figure 5.19: Normalised intensities of the C1s(C-F) and F1s emission for FTP3/Au (open and solid circles) and F10H2/Au (solid triangles) as functions of the irradiation dose. The intensities are normalized to the respective values for the pristine films.

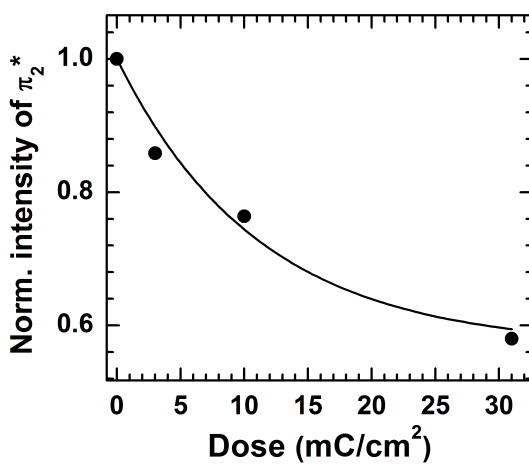


Figure 5.20: Normalised intensities of the π_2^* resonance in the carbon K-edge NEXAFS spectra of FTP3/Au (solid circles) as functions of irradiation dose. The intensities are normalized to the respective values for the pristine films.

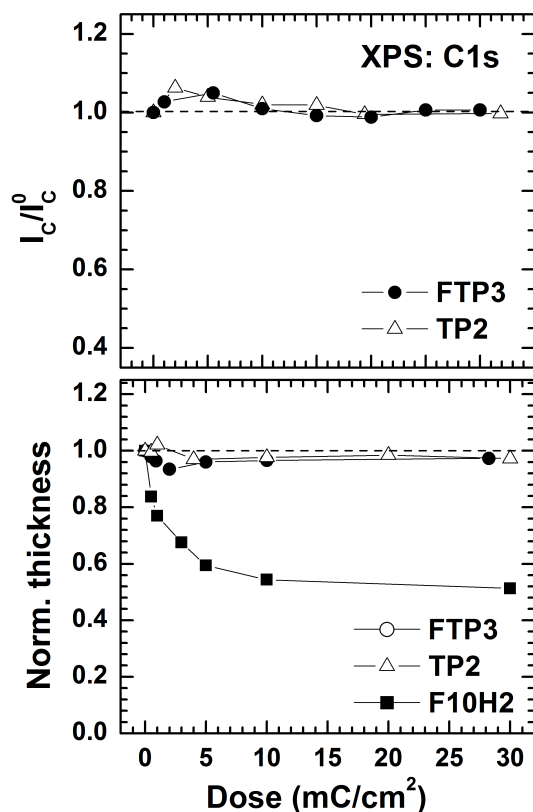


Figure 5.21: Upper panel: normalised total C1s intensities for FTP3/Au (solid circles) and TP2/Au (open up triangles) as functions of irradiation dose. Bottom panel: normalised thickness of FTP3/Au (solid circles), TP2/Au (open up triangles), and F10H2/Au (solid squares) as functions of the irradiation dose. The intensities and thicknesses are normalised to the respective values for the pristine films.

5.3.3 Extensive crosslinking of FTP3 SAMs

5.3.3.1 Chemical evidence

The total C 1s intensity for FTP2/Au and FTP3/Au, shown in the top panel of figure 5.21 remains constant over the course of the irradiation treatment, indicating that fluorine atoms/ions are the only species released from the film. Similarly, the effective thickness of the FTP3 SAMs (figure 5.21, bottom panel) exhibits only a slight reduction ($< 5\%$) even at high doses. This reduction can be attributed to the desorption of fluorine atoms/ions released after the cleavage of C-F bonds. No or almost no desorption of carbon-containing fragments occurred which can be explained by the stability of the aromatic skeleton. This conclusion is supported by the similar behaviour of the analogous aromatic hydrocarbon system - TP3/Au (figure 5.21). The behaviour of FTPn systems contrasts strongly with that of semifluorinated aliphatic films such as F10H2/Au which, similarly to C12/Au (figure 5.5, page 57), exhibits a significant decrease in thickness over the course of irradiation (figure 5.21, bottom panel). This decrease, especially at the early stages, can be mainly attributed to the desorption of fluorocarbon fragments²⁰⁸ as well as, to a minor extent, of entire molecules.^{203,209} The desorption of fluorocarbon fragments

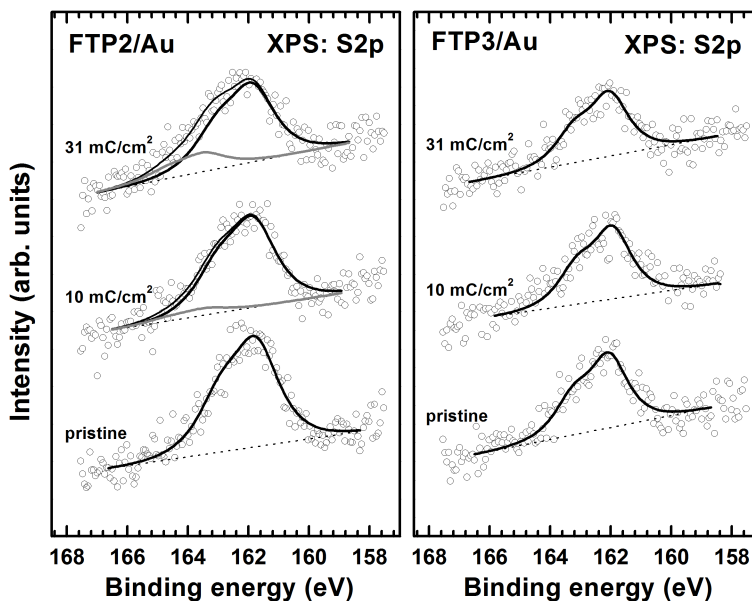


Figure 5.22: S 2p XPS spectra of pristine and irradiated FTP2/Au (left panel) and FTP3/Au (right panel) (open circles), along with the corresponding fits by the doublets related to the pristine thiolate (solid black line) and irradiation-induced sulfur-containing species (solid gray line) moieties. The background of the individual spectra is shown by the horizontal dashed lines. The irradiation doses are indicated at the respective curves.

represents an additional channel of fluorine atom release in F10H2/Au relative to FTP3/Au and occurs in parallel to the desorption of fluorine atoms/ions due to the cleavage of C-F bonds, the latter becoming more prominent at higher doses. This results in a higher rate and extent of fluorine release in F10H2/Au as compared to FTP3 SAMs (figure 5.18). Note that the release of CF_x fragments from F10H2/Au occurs mainly during the initial stages of irradiation ($< 10 \text{ mC/cm}^2$). When the film is sufficiently cross-linked, the fluorine release occurs mainly via C-F bond cleavage^{203,209} similarly to the FTPn/Au films. The cleavage of C-F bonds in FTPn SAMs causes the appearance of chemically active sites and free radicals which can combine to form cross-links with the neighbouring FTP moieties (figure 5.28, page 82). As a result, the SAM constituents cannot be released or move individually leading to a heightened stability of the thiolate-substrate interface, typical of aromatic hydrocarbon SAMs.^{64,70,208} Even if the S-Au bond is cleaved, it can reform quickly since the released molecules do not desorb or move to a noticeable extent from the bond cleavage site as seen in the S2p spectra of FTPn/Au (figure 6.31).

This is in stark contrast with aliphatic hydrocarbons where damage to the S-Au interface, as evidenced by the appearance of a dialkylsulfide feature at $\sim 163.5 \text{ eV}$, is a major effect of electron-irradiation (section 5.1).

5.3.3.2 A new electronic structure

An indirect fingerprint of the cross-linking process is an additional resonance (CL^* , 284.6 eV) appearing and progressively increasing in intensity at the low photon energy side of the π_1^* feature

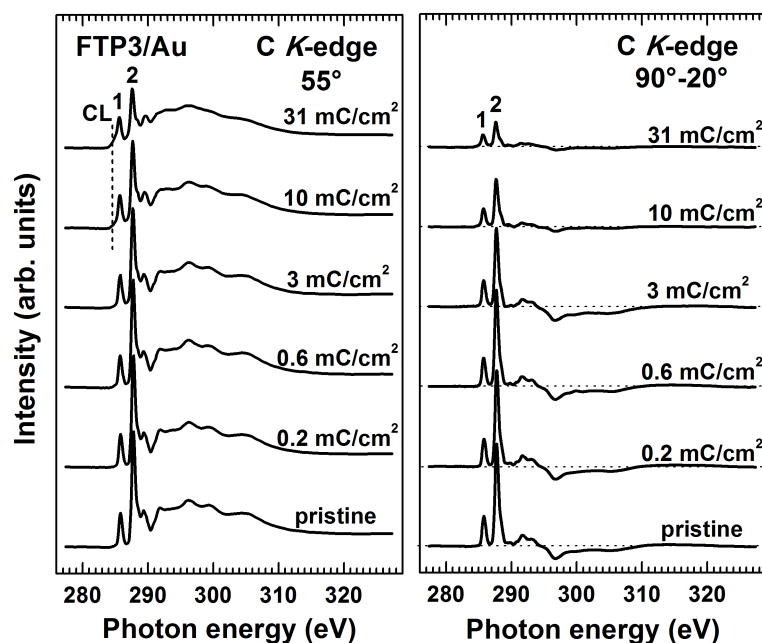


Figure 5.23: Carbon K-edge NEXAFS spectra of pristine and irradiated FTP3/Au acquired at an X-ray incident angle of 55° (left panel), along with the difference between the spectra acquired at X-ray incident angles of 90° and 20° (right panel). The irradiation doses are given at the respective curves. The characteristic absorption resonances π_1^* and π_2^* are indicated by 1 and 2 respectively; CL denotes the resonance from the cross-linked species. The dashed lines in the right panel correspond to zero.

in the NEXAFS spectra of irradiated FTPn SAMs (figure 5.23, left panel^c). The position of this resonance is analogous to the position of one of the most pronounced characteristic resonances of anthracene¹⁶⁶ which is a fused aromatic moiety representing one of the possible cross-linking motifs.²⁰² Note that time-of-flight secondary ion mass spectroscopy measurements on plasma-deposited benzene and hexafluorobenzene films suggest the formation of similar moieties including anthracene and perfluoroanthracene.²⁰⁵ Note also that films of benzene and perfluorobenzene prepared by plasma treatment or via electron/UV irradiation show similar spectral envelopes in XPS spectra suggesting analogous structural elements.²⁰⁶

5.3.4 Modification of the molecular conformation upon electron irradiation

The modification of the chemical composition of the FTPn films upon irradiation leads to a modification of their structure. NEXAFS difference spectra (section 2.4) of pristine and irradiated FTP3 SAMs are presented in the right panel of figure 5.23. The spectra of the pristine films exhibit pronounced difference peaks at the positions of the characteristic absorption resonances. These peaks are most prominent for the π_1^* and π_2^* features. The observed positive sign of the difference peaks for the π^* resonances suggests the expected²¹ upright orientation of the FTP moieties in the FTP3 SAMs. The amplitudes of the π_1^* and π_2^* peaks in the difference spectra

^cFor an analysis of the pristine spectrum see section 4.3.3

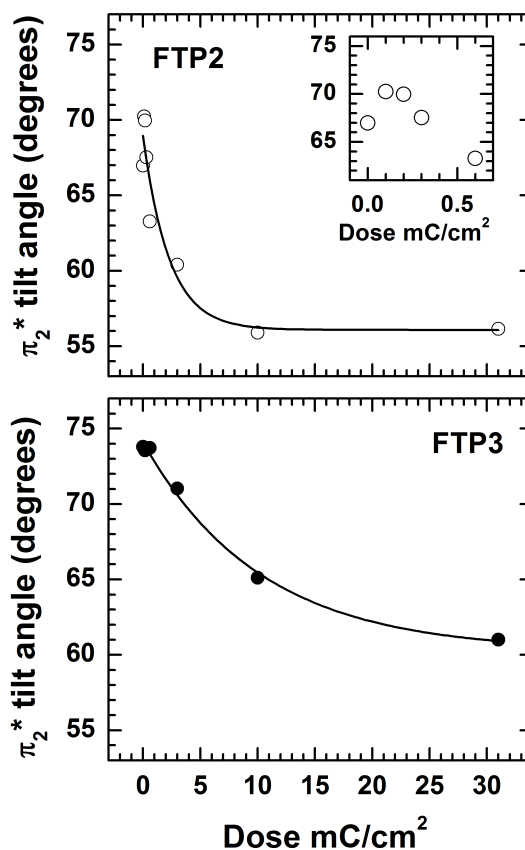


Figure 5.24: Average tilt angle of the π^* orbitals in FTP2/Au (top panel) and FTP3/Au (bottom panel). The insert in the top panel shows the region of small doses.

of FTP3/Au decreased monotonously over the course of irradiation suggesting a progressive disordering of the film. As a fingerprint parameter the average tilt angle (section 2.4) of the π_2^* orbital was used (figure 5.24). As seen in figure 5.24, the average tilt angle of the π_2^* orbital decreased monotonously over the course of irradiation approaching an angle of $\sim 60^\circ$ at a dose of 31 mC/cm^2 for both FTP2/Au and FTP3/Au with only the kinetics differing between those two systems. The tilt angle for the strongly irradiated systems is close to the value characteristic of a fully disordered system (55°)¹⁰² which suggests that the FTPn SAMs become almost completely disordered at 31 mC/cm^2 . It should be noted that FTP2/Au films show a slight increase in the tilt angle of the π_2^* typical for the relaxation of the kinetically trapped monolayer structure.^{21,22}

5.3.5 Chemistry of the SAM-ambient interface

The observed changes in chemical composition (loss of fluorine) as well as conformation of the single molecules (loss of orientation) should lead to a change in the SAM/air interface. Such changes are best probed using water contact angles (WCAs, figure 5.25). Except for a small increase at a dose of $\sim 0.2 \text{ mC}/\text{cm}^2$, both θ_{adv} and θ_{rec} decrease continuously over the course of the irradiation treatment to a value of $\sim 78^\circ$ at a dose of 30 mC/cm^2 . This indicates the

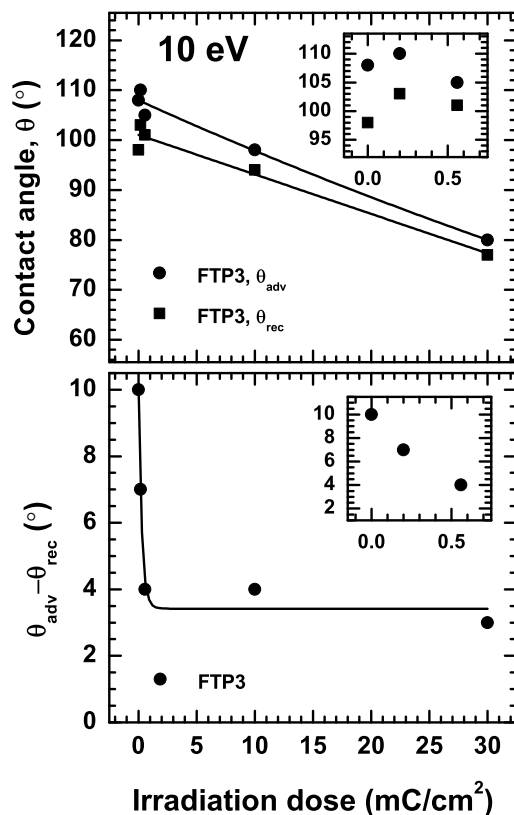


Figure 5.25: Top panel: advancing (circles) and receding (squares) water contact angles for pristine and irradiated FTP3/Au. Bottom panel: difference between the advancing and receding contact angles ($\theta_{adv} - \theta_{rec}$) for pristine and irradiated FTP3/Au. Insets in both panels: the contact angle data at low irradiation doses (< 1 mC/cm²).

continuous desorption of fluorine from the SAM-ambient interface following the cleavage of C-F bonds. The lack of saturation behaviour at high irradiation doses suggests that a certain amount of fluorine is still present at the interface. A small increase of θ_{adv} and θ_{rec} at a dose of ~ 0.2 mC/cm² corresponds to the irradiation-induced structural reorganization of the SAMs (section 5.3.4). Interestingly, it is accompanied by an abrupt change in the WCA hysteresis. A change in the domain structure of the film could explain the observed reduced WCA hysteresis. Significantly, WCA hysteresis exhibited a saturation behaviour at higher doses suggesting that the subsequent changes in the morphology of the SAM-ambient interface have only a minor influence and that the changes in θ_{adv} and θ_{rec} are mostly related to the progressive removal of fluorine from the interface.

5.3.6 FTPn as templates for molecular electronics

To be useful for molecular electronic applications or device fabrication in general, FTPn SAMs should act as resists. As for non-fluorinated bi- and terphenyl SAMs,^{70,208} the irradiation-induced cross-linking of the FTP moieties should increase the resistance of the irradiated areas towards etching agents as compared to the unexposed regions. To test this hypothesis, an FTP3/Au

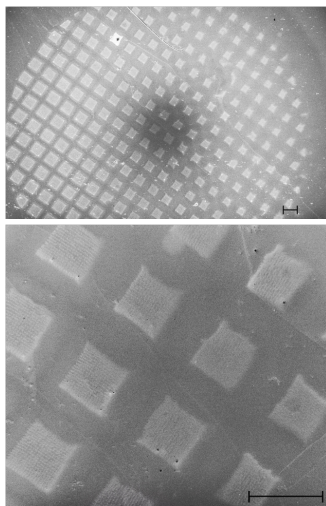


Figure 5.26: SEM images of an etched FTP3/Au template (10 min in cyanate solution) preliminary patterned by electrons in proximity printing geometry using a metal mesh as a mask. The scaling bars in the images correspond to 100 μm

template was patterned by electrons (10 eV; 30 mC/cm^2) in proximity printing geometry using a metal mesh as a mask. Subsequently, the patterned template was etched and imaged by SEM (figure 5.26). As seen in these images, the underlying gold substrate within the irradiated areas (bright squares) was mostly non-affected by the etching process whereas the non-irradiated regions (dark areas) were strongly etched. Thus, FTPn SAMs act as negative electron resists for lithographic applications, mimicking the typical behaviour of aromatic hydrocarbon SAMs.^{70,208} This behaviour contrasts with that of the aliphatic monolayers where electron-induced damage dominates over cross-linking.

5.3.7 Modification of the transport properties of FTPn SAMs

The results of Kelvin probe measurements of the work function of irradiated FTP3 SAM are presented in figure 5.27 along with the loss of fluorine from the film. At low doses ($< 0.5 \text{ mC}/\text{cm}^2$), the work function increases slightly. This behaviour indicates a reorientation of the molecular dipoles toward the surface normal and is consistent with the NEXAFS and contact angle data.

After the initial increase, the work function decreases monotonously to reach a relative value of -0.4 eV with respect to the pristine value ($\Phi_{\text{pristine}} = 5.8 \text{ eV}$) at 30 mC/cm^2 . Although the kinetics are different, the decrease in the work function correlates with the loss of fluorine from the film. Interestingly, no saturation behaviour was observed. Consequently, the work function of FTPn films could be tuned further if the films were subjected to higher doses. Indeed, up to $\sim 80\%$ of the fluorine was lost from FTPn/Au SAMs at a dose of 180 mC/cm^2 (data not shown). By extrapolating the exponential fit, a value of about -0.6 eV for the change in work function at 180 mC/cm^2 is obtained.

Although multiple component approaches to the modification of the work function have been successful at controlling the work function of aliphatic fluorinated SAMs, the results reported in this section are, to the best of our knowledge, the first example of fine-tuning of the work

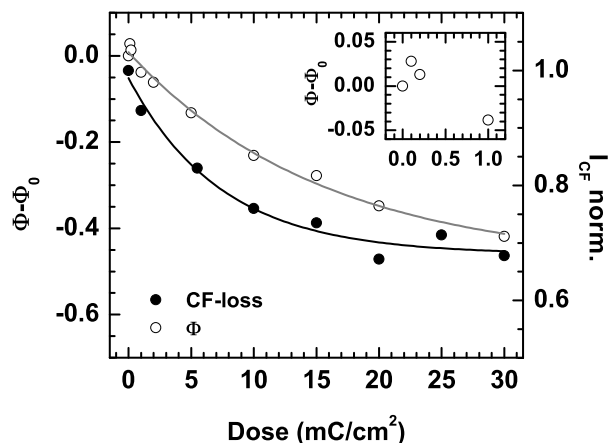


Figure 5.27: Variation of the work function of FTP films (hollow circles) and fluorine content (filled circles) of an FTP3/Au film as a function of irradiation dose.

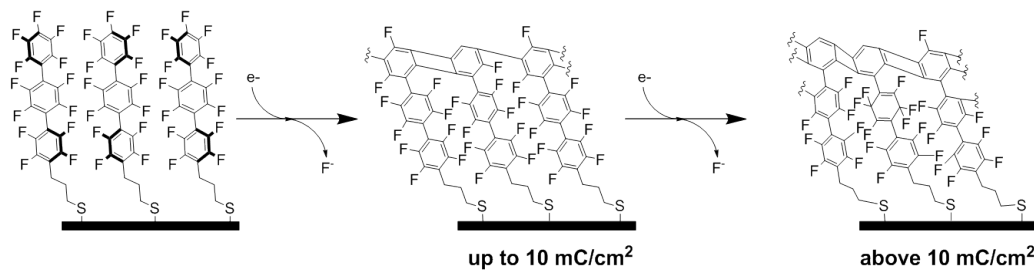


Figure 5.28: Schematic representation of electron-induced modification of FTPn/Au.

function of single-component fluorinated SAMs. The ability to precisely tune the work function of a SAM-covered metal surface simply by electron irradiation confers a definite advantage to FTPn monolayers for nanoelectronic applications.

5.3.8 Summary

The FTPn films mimic the typical behaviour of aromatic hydrocarbon SAMs under ionising radiation, i.e. these systems exhibit a clear dominance of cross-linking between the individual molecular species over their decomposition which makes these monolayers negative resists for lithographic applications. The cross-linking follows the cleavage of the primary C-F bonds in the FTP moieties, which, along with the comparably rapid loss of orientational and conformational order, is the dominant irradiation-induced process in the FTPn SAMs (figure 5.28). C-F bond cleavage, followed by the desorption of fluorine in atomic or ionic form, represents an exclusive pathway of fluorine release in the FTPn films in striking contrast to fluorocarbon aliphatic monolayers where the major channel for such a release is the desorption of fluorocarbon fragments. In addition to desorption, a small fraction of the fluorine atoms released from the cleavage of C-F bonds remain trapped in the matrix as CF_2 species. Both FTPn films studied ($n = 2,3$) react

similarly towards ionising radiation, the only differences being a lower stability of the headgroup-substrate interface in the less densely packed FTP2 SAMs and the faster loss of orientational and conformational order in FTP2/Au as compared to FTP3/Au.¹¹⁰

Furthermore, the work function of the FTPn modified gold surface could be tuned by more than 0.4 eV by electron irradiation. This is, to the best of our knowledge, the first example of fine-tuning of the work function of single-component fluorinated SAMs. The ability to precisely tune the work function of a SAM-covered metal surface simply by electron irradiation confers a definite advantage to FTPn monolayers for nanoelectronic applications.

Chapter 6

Metal deposition on SAMs

6.1 Introduction to metal deposition on SAMs

6.1.1 The Metal-SAM-Metal system

In order to be able to use SAMs for nanoelectronic devices, it is essential that electrical contact between the SAMs themselves and the macroscopic world is established. Among other means, this can be accomplished by depositing a thin metal layer at the SAM-ambient interface, yielding a metal-SAM-metal system (MSM, figure 6.1).^{32,52} Tunnel junctions, junctions between two materials (e.g. metals) through which electrons travel via quantum tunnelling, are an example of such MSM junctions. They are found, for example, as magnetic tunnel junctions used for spintronic applications. Such devices can be fabricated using a variety of techniques such as under potential deposition,^{210–217} electroless deposition^{218–220} or chemical or physical vapour deposition.^{26,27,53,221} The fabrication of the monolayer-substrate interface is well established.^{20,21,35,44,222–224} Similarly, the fabrication of stable metal films of gold and silver on top of SAMs has been achieved.^{54–56} However, fabricating stable top ferromagnetic contacts (e.g. Ni, Co, Fe) at the SAM-ambient interface remains a major challenge.^{52,58} Solving this problem would bring us one step closer to a working SAM-based spintronic device.

6.1.2 Top contact formation and metal penetration

The main problem when depositing a metallic contact on top of a self-assembled monolayer is metal penetration into and through the SAM.^{56,225} The penetration of the metal is driven by the high affinity of metals for each other.^a This is especially true if the top and bottom contact are made of the same metal. Penetration occurs because, even though SAM systems are well ordered, they are not free from defects.³⁵ There are two main types of defects: static and dynamic defects.

Static defects are present in the SAM before metal evaporation (e.g. by physical vapour deposition (PVD)) and provide channels for metal penetration.^{210,226} The proportion of this type of defects can be reduced by changing the preparation conditions, e.g. preparing SAMs on flat substrates or at higher temperatures. Dynamic defects on the other hand, occur upon metal evaporation and their formation depends on the SAM system,⁵⁶ the metal deposition process itself^{26,227} and the nature of the metal.⁵² At sub-monolayer coverages, individual molecules in

^aFor a more in depth look at the issue discussed in this section please see works by Herdt²²⁵ and Jung⁵⁶

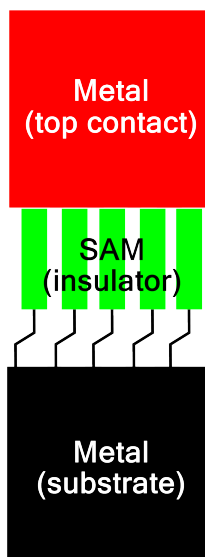


Figure 6.1: Schematic view of a Metal-SAM-Metal system. The substrate is shown in black, the top metal contact in red and the SAM in green.

the SAM reorganise upon adsorption of metal atoms, opening up channels for metal penetration (figure 6.2).^{58,228} Even if metal penetration into and through the SAM can be prevented, the formation of structural defects upon metal evaporation is a critical issue for the fabrication of SAM-based nanoelectronic devices since the charge-transfer behaviour in such thin films is dominated by these defects.^{30,226} Metal penetration can be avoided if the metal is deposited from solution.^{59,60,62,63,229} This method forms the basis of the results presented in section 6.4. However, such metal films are often limited to sub-monolayer coverages, thus making an incomplete top contact.^{60,62}

It should be noted that, in the case of PVD, the extent of metal penetration into and through the monolayer strongly depends upon the metal being deposited. FT-IR studies have shown that whereas gold, a largely inert metal, does not penetrate through a TPDMT monolayer, titanium does.⁵² Similarly, gold does not penetrate through a *p*-terphenyl-methylthiol monolayer whereas aluminum, a reactive metal, does.⁵² This becomes significant since we chose to use nickel, a metal which is reactive toward carbon matrices,^{230–232} as deposition metal. It was chosen for its ferromagnetic properties and could therefore be useful in spintronic applications such as computer memory and data storage.

6.1.3 Preventing metal penetration at the SAM level

As explained in section 6.1.2, the fate of the metal deposited on a SAM is partly governed by the stability of the latter throughout the metal evaporation process. In addition to allowing the modification of the transport properties of a metal surface (section 4.4), the terminal group (SAM-ambient interface) and spacer unit of the SAM constituents play crucial roles in preventing metal penetration.

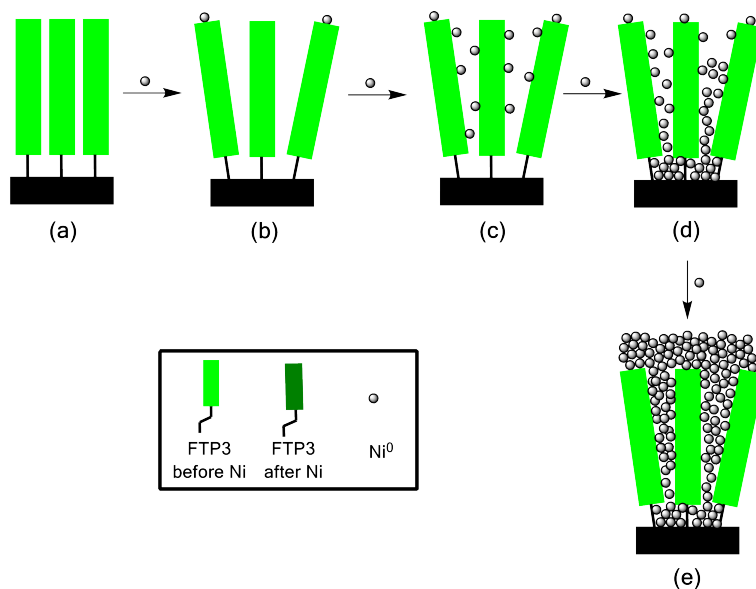


Figure 6.2: Channel creation upon metal evaporation on SAMs. (a) pristine SAM. (b) deposition of the first metal atoms disrupts the film. (c) and (d) upon further evaporation, the metal penetrates through the SAM and down to the substrate. (e) At large metal thickness the SAM can be fully covered with metal.

6.1.3.1 Reactive terminal groups

Previous approaches have focused mainly on the SAM-ambient interface.^{26,32,225} In this approach, the reactivity of the terminal group toward the evaporated metal is utilised to stop metal penetration through the SAM.^{56,225} Despite being useful to minimise metal penetration, this approach is rarely sufficient and further modification of the SAM is necessary to fully prevent metal penetration.^{26,27} This approach will be presented throughout this chapter with special emphasis on a novel solution deposition technique where a solution-deposited metal is used to seed the top metal layer (section 6.4).

6.1.3.2 Closing the space - modification of the spacer

By linking the individual SAM components together, thus forming a quasi-polymeric layer,^{69,72,202} one can expect to minimise metal penetration^{26,27} (figure 6.3). In this approach, the formation of dynamic defects upon metal deposition (section 6.1.2) is minimised. This approach will be explored in sections 6.2, 6.3 and 6.5.3.

6.1.3.3 Reactive spacers - a novel approach

Although the two previous approaches have been well studied,^{26,27,52,54,131} little attention has been paid to the reactivity of the spacer unit itself. It is well known that the deposition of a reactive metal such as titanium or nickel on an unreactive SAM leads to metal penetration.⁵² Conversely, by carefully crafting the spacer of the SAM monomers, one can expect to stop metal penetration through these films (figure 6.4). However, only the terminal group is usually made

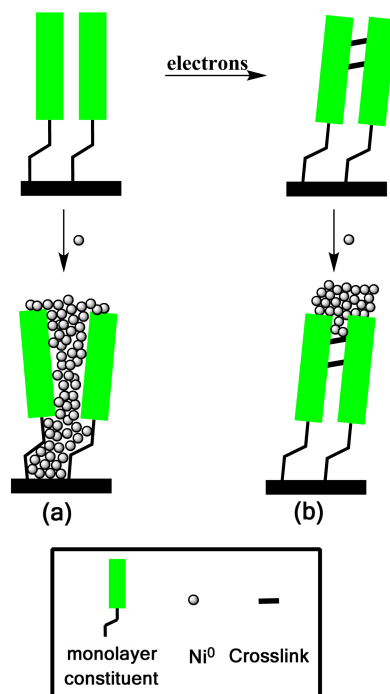


Figure 6.3: Difference in metal penetration upon crosslinking. (a) pristine SAM, (b) crosslinked SAM.

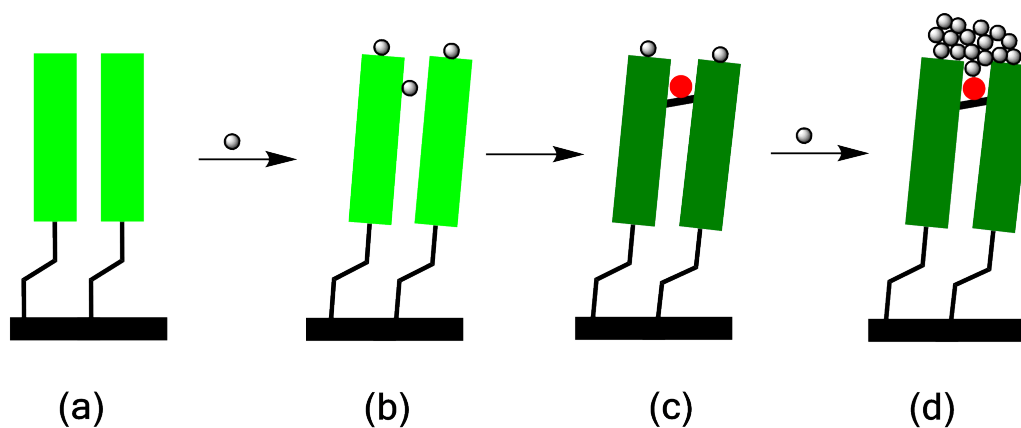


Figure 6.4: Using the spacer unit to stop metal penetration. (a) pristine SAM. (b) SAM with small amount of metal on top. (c) the metal reacts with the matrix to form bonds between the individual matrix components. (d) metal penetration is prevented and a stable metal film is formed on top of the SAM.

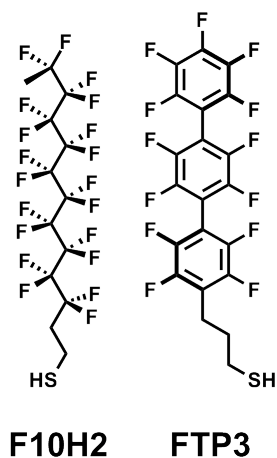


Figure 6.5: Structures of the F10H2 (left) and FTP3 (right) molecules

reactive,^{26,52} leaving the possibilities offered by the spacer unit largely unexplored. The field of organic chemistry provides us with many examples of metal insertion in either C-H^{233–241} or C-F bonds,^{230–233,242–248} the two main types of bonds, along with the C-C bond, found in most spacer units. Metal insertion in the C-H or C-F bonds, yielding C-M-H and C-M-F species respectively, is the basis for many C-C bond formation reactions.^{232,242} One can expect that, owing to the close proximity of the SAM constituents, that C-M-C and C-C bond formation upon metal evaporation will occur if the proper spacer is chosen. As a test case, the FTP3 molecule (figure 6.5 and sections 4.3 and 5.3) was chosen as test system. An F10H2 reference (figure 6.5) was also chosen to separate the matrix effects. The results of this study will be presented in section 6.5.

6.2 Metal evaporation on TPDMT SAMs

For the purpose of this discussion, the amount of deposited nickel will be referred to as *nickel dose* or *metal dose*. The formation of a stable metal layer on top of electron irradiated TPDMT monolayers (CL-TPDMT) has been previously demonstrated in our group^{26,27} and will be used as a benchmark for our studies. Our efforts at depositing nickel on CL-TPDMT SAMs are presented below.

6.2.1 Change in the carbon matrix upon metal evaporation

Upon evaporation of 1.2 nm nickel (~ 6 monolayers), a feature at ~ 283.5 eV appears in the C1s HRXPS spectrum of CL-TPDMT (figure 6.6, top panel). This peak was attributed to the interaction of nickel with the benzene rings of TPDMT..²⁴⁹ A similar feature, albeit at a slightly different energy, is observed in the 55° C K-edge NEXAFS spectrum (figure 6.6, bottom panel). The presence of the feature at 283.5 eV in the C1s spectrum is a clear indication of metal penetration into the SAM. However, the extent of penetration can not be determined from the data presented above. An estimate will be given in section 6.2.4.

6.2.2 Change in molecular order of CL-TPDMT SAMs upon metal evaporation

The molecular order of the CL-TPDMT SAMs was probed by NEXAFS spectroscopy. The difference spectra ($I_{90}-I_{20}$) of CL-TPDMT before and after nickel evaporation are presented in the top panel of figure 6.7. The strong reduction of the intensity of the difference peak at 285 eV indicates that the molecular order of the CL-TPDMT films was severely disrupted upon nickel deposition. The average tilt angle of the molecules, a marker of molecular order, was found to decrease by $5-10^\circ$ to 35° , close to that of a fully disordered system (38° in our experiments). Nickel penetration through the SAM was confirmed by the increase of the ratio of the XPS intensities of carbon and gold^b (figure 6.7, bottom panel). This is in stark contrast with the results previously obtained in our laboratory where no nickel penetration was observed.^{26,27} Nickel penetration was also observed by angle-resolved XPS at nickel doses as low as 0.1 nm for similarly crosslinked TPDMT monolayers (figure 6.8) and is therefore not related to the relatively high dose deposited in this study (6 monolayers) or a dose discrepancy between the present and previous studies. In an effort to explain the discrepancy between our results and the results previously obtained in our laboratory, the preparation conditions of our TPDMT films (temperature, solvent (THF, ethanol and Toluene+AcOH), rinsing conditions, electron dose) as well as the substrate (30-100 nm Au/Si, 300 nm Au/Mica, Ultra flat gold) were varied. No significant differences were observed and, despite our best efforts, metal penetration through crosslinked TPDMT films could not be prevented.

6.2.3 Changes to the SAM-ambient and SAM-substrate interfaces

6.2.3.1 Changes to the sulphur environment upon nickel evaporation

As can be seen in figure 6.9, the S2p XPS spectrum of CL-TPDMT is dramatically modified upon nickel deposition. First, the intensity of the **SH** feature, corresponding to the free terminal

^bNote that this is valid for a system whose constituents are not desorbed upon metal evaporation. This is largely the case for the present system. However, for systems such as C6/Au, significant desorption occurs and the C/Au ratio is actually reduced with increasing metal dose.

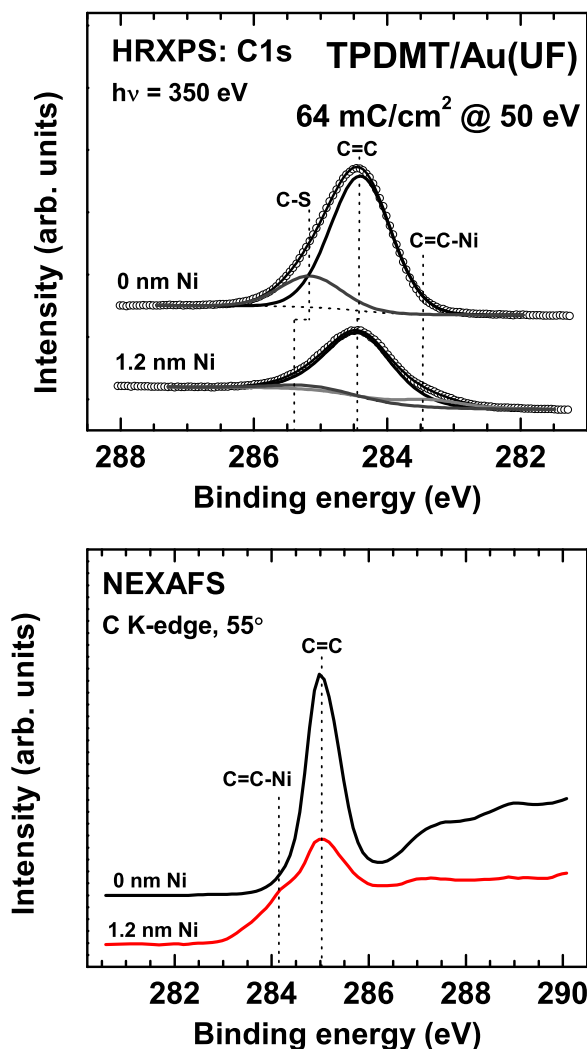


Figure 6.6: C1s HRXPS (top panel) and C K-edge NEXAFS (bottom panel) spectra of CL-TPDMT SAMs before and after deposition of 1.2 nm nickel. The irradiation dose used was 64 mC/cm² at an electron energy of 50 eV.

thiol, was strongly reduced (from 75 to 8 % of the total S2p intensity) indicating a change in the chemistry of the terminal sulphur. Second, a feature consistent with the interaction of nickel and sulphur (S-Ni) appears at 162.6 eV (~ 10 % of the total S2p intensity).^{250,251} Third, the **S2** feature, characteristic of thiolates (SAM/substrate interface), is shifted to lower binding energies (-0.2 eV), consistent with the formation of a nickel-sulphur bond.³⁹⁻⁴¹ However, due to the symmetry of the TPDMT molecule, it was not possible to distinguish between the SAM-ambient and the SAM-substrate interfaces solely on the basis of the **S2** peak. Finally, the **S1** peak, characteristic of species formed at the S-Au interface, vanishes upon nickel desorption indicating either the formation of a nickel layer atop the SAM/substrate interface or nickel penetration through the SAM.

The full width at half maximum of the S2p peak increases from 0.8 to 1.0 eV, indicating an

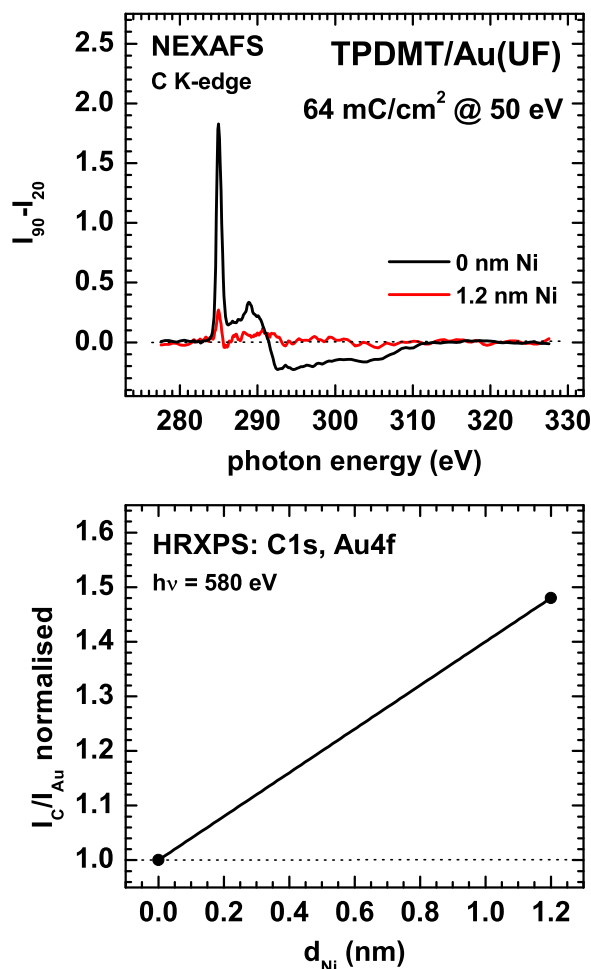


Figure 6.7: C K-edge NEXAFS difference spectra (top panel) and HRXPS carbon to gold ratio (bottom panel) of CL-TPDMT SAMs before and after deposition of 1.2 nm of nickel. The irradiation dose used was 64 mC/cm^2 at an electron energy of 50 eV.

increased inhomogeneity of the sulphur after metal deposition. Furthermore, the reduction of the total sulphur intensity indicates partial immobilisation of nickel on top of CL-TPDMT SAMs. An estimate of the nickel thickness on top of the CL-TPDMT SAMs was obtained.

6.2.4 Estimate of the top nickel thickness

The evaporated nickel thickness was estimated using the Au4f data acquired at $h\nu = 350$ and 580 eV. Using standard equations,^{81,115} the deposited nickel thickness was found to be 1.3 ± 0.1 nm, in good agreement with the expected value from our quartz crystal microbalance calibration (1.2 nm). Using the intensity data of the S2p HRXPS spectra collected at $h\nu = 350$ eV, one can in a similar way estimate the top nickel thickness. As seen previously, it is not possible to distinguish between the contributions of the head and terminal groups for CL-TPDMT. However, the contribution of the head group (SAM-substrate interface) is expected to be small compared to

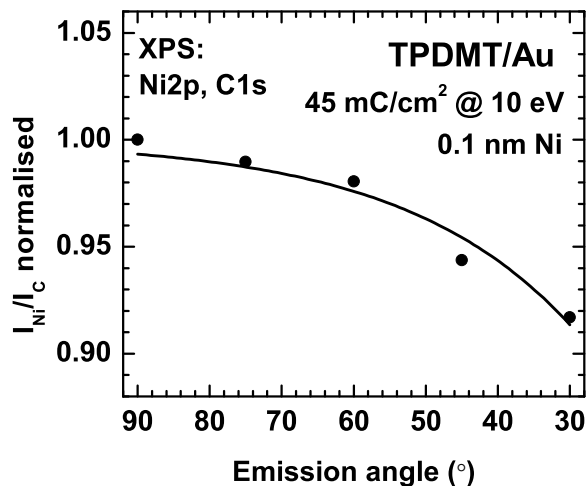


Figure 6.8: ARXPS (C1s, Ni2p) of a CL-TPDMMT film after deposition of 0.1 nm nickel. The emission angle is the angle between the substrate's surface and the analyser. The irradiation dose used was 45 mC/cm² at an electron energy of 10 eV.

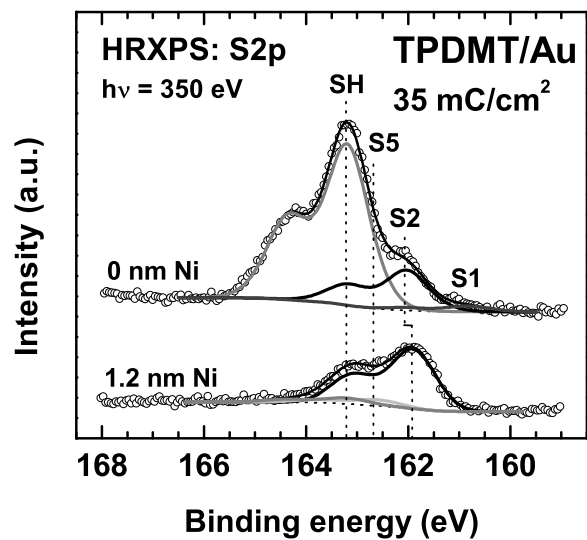


Figure 6.9: HRXPS S2p spectra of CL-TPDMMT SAMs before (top spectrum) and after (bottom spectrum) deposition of 1.2 nm of nickel. The irradiation dose used was 64 mC/cm² at an electron energy of 50 eV.

that of the terminal group. With these assumptions, the thickness of nickel on top of CL-TPDMT is expected to be 0.4 ± 0.1 nm or 31 % of the total nickel thickness. The low nickel thickness on top of CL-TPDMT definitely confirms that extensive penetration occurs when depositing nickel on CL-TPDMT SAMs.

6.2.5 Summary

We have evaporated nickel on crosslinked TPDMT monolayers on various gold substrates. Despite our best efforts, nickel penetration was found to dominate in all cases, even at low nickel doses (~ 0.1 nm), with only ~ 31 % of the total deposited nickel immobilised on top of CL-TPDMT films. Along with metal penetration, the electronic structure of the carbon matrix was modified due to the insertion of nickel. Furthermore, the HRXPS S2p spectra revealed that new sulphur species were formed when nickel was evaporated on CL-TPDMT, notably a peak at 162.6 eV corresponding to S-Ni species appears. In addition, the thiolate peak (**S2**) is shifted to lower binding energies (-0.2 eV) compared to thiols on gold. These two facts can be used as markers for nickel penetration for the other mercaptan molecules in this study. The observed nickel penetration through CL-TPDMT/Au is in stark contrast with data collected previously in our laboratory.^{26,27} It is not clear to us at this time why such a discrepancy should occur and careful re-evaluation of both datasets is under way. We surmise that we were unable to control subtle parameters in the preparation procedure that were unknown to us.

6.3 Metal evaporation on PPPn films

Unlike TPDMT, the end groups of PPPn monolayers are largely preserved after electron irradiation (section 5.2), giving PPPn SAMs a significant advantage for metal immobilisation on top of the films. Furthermore, PPPn films are based on the terphenyl unit and are thus potentially useful as dielectrics for metal-SAM-metal systems. In this section we present data on the evaporation of nickel on electron irradiated PPP1 and PPP3 SAMs (CL-PPP1 and CL-PPP3 respectively) as appropriate. In all cases, the data presented for one system is valid for the other.

6.3.1 Change in the carbon matrix upon metal evaporation

Similarly to CL-TPDMT (section 6.2), a feature appears at ~ 283.5 eV in the C1s HRXPS spectrum of CL-PPP1 (figure 6.10, top panel) upon evaporation of 1.2 nm nickel. This peak is attributed to the interaction of nickel with the benzene rings of PPP1.²⁴⁹ A similar feature, albeit at a slightly higher energy, is observed in the 55° C K-edge NEXAFS spectrum (figure 6.10, bottom panel). Furthermore, unlike CL-TPDMT, the C=C and C=N peaks shift to higher binding energy upon nickel deposition (+0.2 eV). A similar shift (+0.18 eV) was observed for the deposition of nickel on C6/Au (data not shown). This shift likely results from a change in the hole screening within the organometallic matrix. Like CL-TPDMT, the C1s HRXPS and NEXAFS data suggest, at the given metal dose, partial penetration of nickel into the CL-PPP1 film. However, the extent of penetration could not be determined solely from the data presented above. An estimate will be given in section 6.3.4.

6.3.2 Change in molecular order of CL-PPPn SAMs upon metal evaporation

The molecular order of the CL-PPP1 SAMs was probed by NEXAFS spectroscopy. The difference spectra ($I_{90}-I_{20}$) of CL-PPP1 before and after nickel evaporation are presented in the top panel of figure 6.11. The resonance at 285 eV vanishes upon metal evaporation, indicating that the molecular order of the CL-PPP1 films was severely disrupted upon nickel deposition. The tilt angle was found to decrease by 5-7° to 37°, close to that of a fully disordered system (38° in our experiments). Nickel penetration was confirmed by the increase of the ratio of the XPS intensities of carbon and gold for CL-PPP3 (figure 6.11, bottom panel). These results go against our hypothesis that preserving the terminal groups after irradiation increases the probability of stopping metal penetration. However, it is possible that the interaction between the incoming nickel atoms and the pyridine moieties is too weak to efficiently nucleate metal films on top of SAMs. Indeed, after immersion of PPP3 monolayers in nickel chloride solution for 7 minutes, only a small amount of nickel could be detected by XPS (figure 6.12) suggesting that the interaction between nickel and the surface-immobilised pyridine is very weak. A control experiment carried out with TPDMT showed significant immobilisation of nickel on the TPDMT film (figure 6.12, top spectrum).

6.3.3 Changes to the SAM-ambient and SAM-substrate interfaces

Unlike CL-TPDMT, CL-PPP1 films have different terminal (pyridine) and head groups (sulphur), allowing us to a better understanding of the fate of both the SAM-ambient and the SAM-substrate interface.

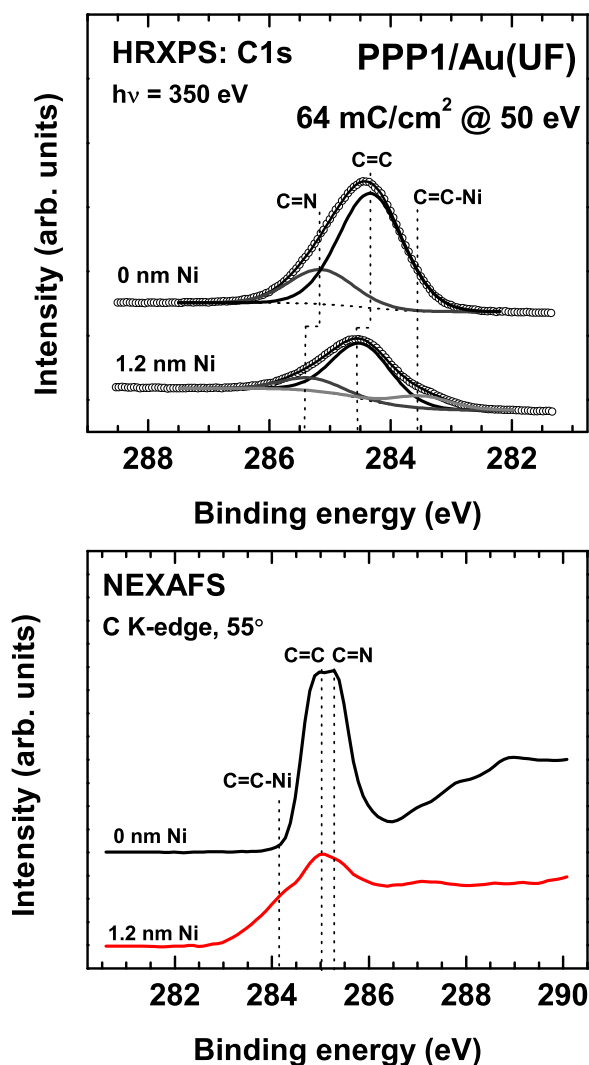


Figure 6.10: C1s HRXPS (top panel) and C K-edge NEXAFS (bottom panel) spectra of CL-PPP1 SAMs before and after deposition of 1.2 nm nickel. The irradiation dose used was 64 mC/cm² at an electron energy of 50 eV.

6.3.3.1 The SAM-ambient interface

Upon adsorption of nickel on CL-PPP1, a large proportion of the free pyridines (~40 %) binds to nickel (figure 6.13, top panel) upon metal evaporation (N-Ni, 387.8 eV) as determined by HRXPS. This suggests island growth of the nickel film. Indeed, since nickel atoms are only coordinated to pyridine, they are free to move across the surface. This is consistent with the growth of nickel films on graphite.²⁵² Furthermore, the nitrogen signal is more attenuated than the corresponding sulphur signal in Ni/CL-TPDMT thus suggesting that more nickel is retained

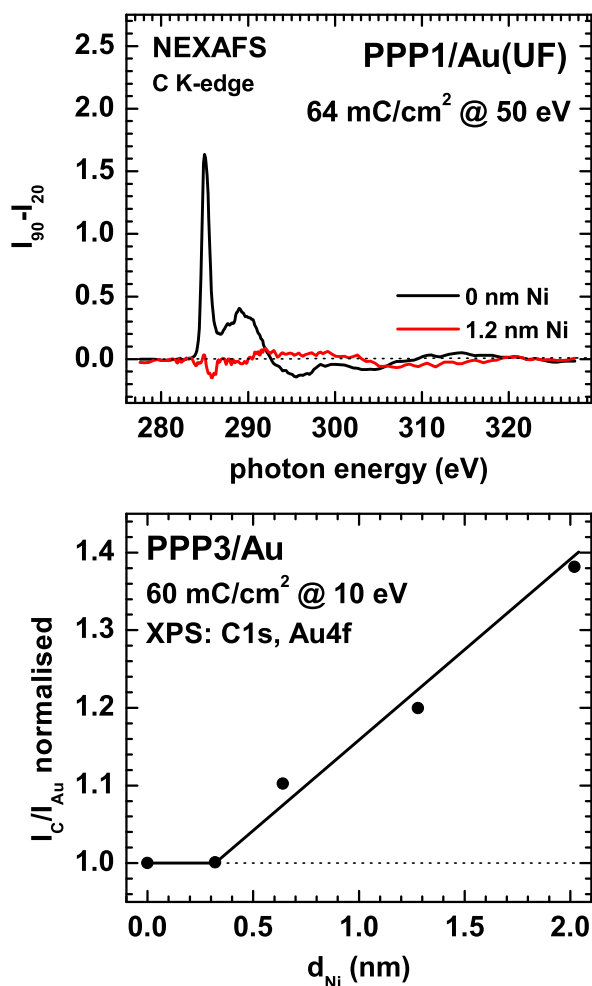


Figure 6.11: C K-edge NEXAFS difference spectra and XPS carbon to gold ratio of CL-PPP1 and CL-PPP3 SAMs before and after deposition of nickel. The irradiation dose used was ~ 62 mC/cm² at an electron energy of either 10 or 50 eV (PPP3 and PPP1 respectively).

on top of the film^c. An estimate will be given in section 6.3.4.

6.3.3.2 The SAM-substrate interface

Unlike TPDMT, in CL-PPP1, sulphur is only found at the SAM-substrate interface. Thus, S2p HRXPS spectra can be used to probe the CL-PPP1-Au interface (figure 6.13, bottom panel). Similarly to CL-TPDMT, the thiolate peak (**S2**) is shifted to lower binding energy and the **S1** peak disappears upon nickel evaporation. Furthermore, the S-Ni peak at 162.4 eV is present after metal evaporation. This suggests nickel penetration to the S-Au interface and is consistent with NEXAFS, N1s, Au4f and C1s XPS data. A similar shift of the **S2** peak to lower binding

^cExperiments on CL-PPP1 and CL-TPDMT samples were carried out simultaneously, i.e. both samples were placed on the same sample holder.

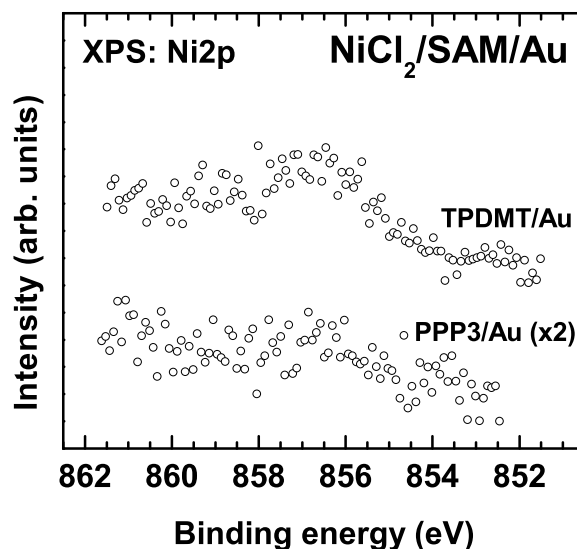


Figure 6.12: Ni2p XPS spectra of TPDMT and PPP3 SAMs after adsorption of nickel chloride. The incubation time was 7 min in both cases. Samples were rinsed with water and ethanol after incubation in a millimolar aqueous solution of nickel chloride.

energy was observed for C6/Au, a system for which strong metal penetration occurs (data not shown).

6.3.4 Estimate of the top nickel thickness

The evaporated nickel thickness was estimated by evaluating the Au4f data at $h\nu = 580$ eV. Using standard equations,^{81,115} the total nickel thickness was determined to be 1.4 ± 0.1 nm. This is in good agreement with the expected value from quartz crystal microbalance calibration (1.2 nm). By evaluating the N1s HRXPS data collected at $h\nu = 580$ eV, one can in a similar way estimate the top nickel thickness. The thickness of nickel on top of CL-PPP1 is estimated to be 0.6 ± 0.1 nm or 43 % of the total nickel thickness, slightly higher than for Ni/CL-TPDMT (~ 31 %). This result supports our hypothesis that increasing the density of surviving terminal groups after irradiation decreases the probability of metal penetration. The seeming contradiction with the nickel chloride adsorption experiments can be resolved by noting that whereas the e-beam evaporation of nickel on CL-PPP1 and subsequent measurements were carried out *in-situ*, the sample exposed to nickel chloride was rinsed before measurement, therefore, it is likely that most of the NiCl₂ was washed away. Thus, whereas nickel can be lost before measurement in the case of nickel chloride adsorption, this does not occur for the *in-situ* deposition of nickel metal.

6.3.5 Summary

We have evaporated nickel on crosslinked PPPn monolayers on various gold substrates. Despite our best efforts, nickel penetration was found to dominate in all cases although to a lesser extent than CL-TPDMT films (43 % of Ni on top for CL-PPPn vs 31 % for CL-TPDMT) thus validating our hypothesis that the survival of the terminal groups after irradiation could help

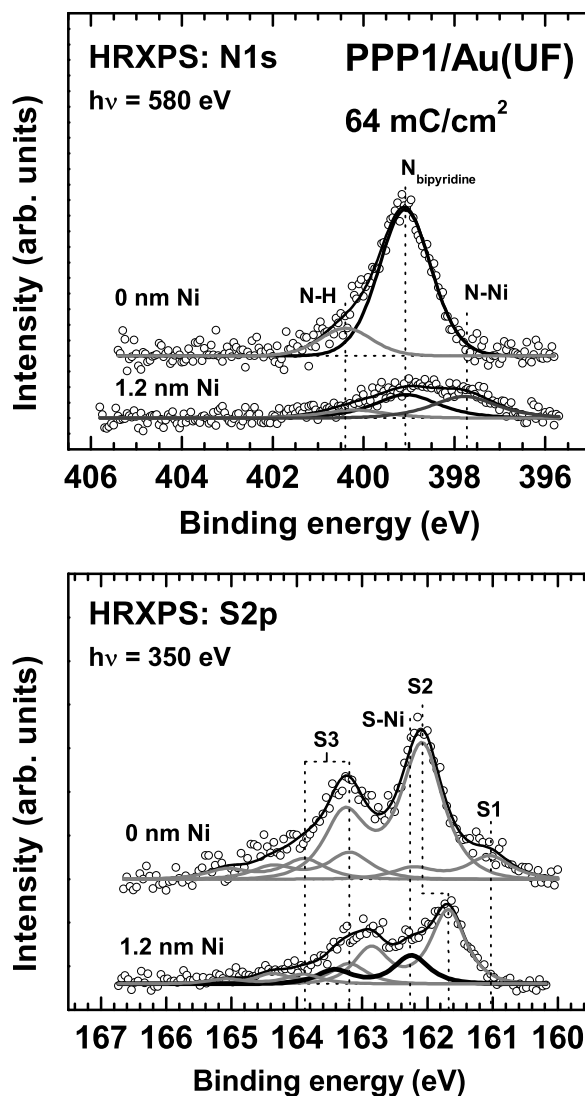


Figure 6.13: N1s (top panel) and S2p (bottom panel) HRXPS spectra of CL-PPP1 SAMs before and after deposition of 1.2 nm nickel.

reduce metal penetration through SAMs. Along with metal penetration, the electronic structure of the carbon matrix was modified due to the insertion of nickel, forming a new organometallic film. Furthermore, similarly to CL-TPDMT, the HRXPS S2p spectra revealed that new sulphur species were formed upon nickel evaporation on CL-PPPn, notably a peak around 162.4 eV attributed to S-Ni species appears and the thiolate peak (**S2**) is shifted to lower binding energies (-0.4 eV) compared to thiolates on gold.

6.4 Solution-deposited metal overlayers on SAMs

The evaporation of nickel on plain TPDMT and PPP3 SAMs (crosslinked and non-crosslinked) did not yield the expected metal-SAM-metal assemblies. Even though irradiated SAMs proved more resistant to metal penetration than their pristine counterparts, nickel could not be prevented from reaching the SAM-substrate interface. In an effort to solve this problem, we turned our attention to solution-deposited metals. In this section we propose to use metal ions as seeds for the nucleation and growth of nickel films on top of self-assembled monolayers. Palladium was chosen as seed metal since it forms ferromagnetic alloys with nickel,^{253,254} making PdNi films potentially useful for spintronics applications. The immobilisation of palladium at the SAM-ambient interface of pyridine terminated SAMs is well known.^{60,62,218,219} However, palladium is only coordinated to the pyridine. While this might be appropriate for electrochemical and electroless deposition of metals,^{219,255} we surmise that the lack of chemical bond between palladium and the SAM's terminal group could prove disadvantageous during e-beam evaporation, the technique used here. Palladium being known to form strong covalent bonds with sulphur,^{127,128,256} we chose to investigate palladium on pristine TPDMT as well. In all cases the samples were incubated in an ethanolic solution of commercial grade PdCl₂ for 4 minutes and then rinsed thoroughly with ethanol.

6.4.1 Palladium on self-assembled monolayers

6.4.1.1 Changes to the SAM-ambient interface

Upon adsorption of palladium, the SAM-ambient interface (-N for PPP3 and -SH for TPDMT) was profoundly modified (figure 6.14). In the case of CL-PPP3 (figure 6.14, top panel), the nitrogen peak for the free pyridine at ~ 399.2 eV was split into two major resonances at ~ 399.2 eV and ~ 400.2 eV corresponding to the free and palladium-bound pyridine respectively. Furthermore, a broad peak was observed at the lower binding energy side of the pyridine nitrogen peak. This peak was ascribed to the nitrogen-palladium interaction.²⁵⁷ Similarly, a shift of the terminal SH peak from 163.8 eV to 162.9 eV was observed for TPDMT, indicating the formation of palladium-sulphur bonds.¹²⁸ The coverage of palladium chloride was estimated using the ratio of the palladium-induced peak to the total peak intensity of either the N1s (CL-PPP3) or S2p (TPDMT) line. In the case of TPDMT, 92 % of all terminal thiols were bound to a palladium atom whereas only 65 % of all nitrogen atoms were coordinated to palladium at the CL-PPP3-Pd interface. It is not clear at present why such a discrepancy occurs since the packing density of both molecules is expected to be similar.

6.4.1.2 Thickness of the palladium chloride layer

The thickness of the palladium chloride layer was estimated using the gold 4f intensity before and after deposition of palladium chloride. Since no attenuation length value is known for palladium chloride, we evaluated its λ using the formula for compounds by Tanuma *et al.*^{115,258} This formula gives an inelastic mean free path of 2.36 nm at $h\nu = 1254$ eV and 0.825 nm at $h\nu = 350$ eV. With this data in hand, the thickness of the palladium chloride layer was calculated to be 0.6 ± 0.1 nm on TPDMT and 0.7 ± 0.2 nm on PPP3. Palladium chloride exists in two main forms, the metastable α -form,²⁵⁹ which is polymeric chain of PdCl₂ units with bridging chlorine atoms, and the β -form,^{259,260} a Pd₆Cl₁₂ cluster stable at room temperature. However, the form of commercial palladium chloride is not known.^{261,262} Assuming that palladium chloride is found in its β -form, the calculated thickness corresponds to $\sim 1.2 \pm 0.2$ ML of palladium chloride.

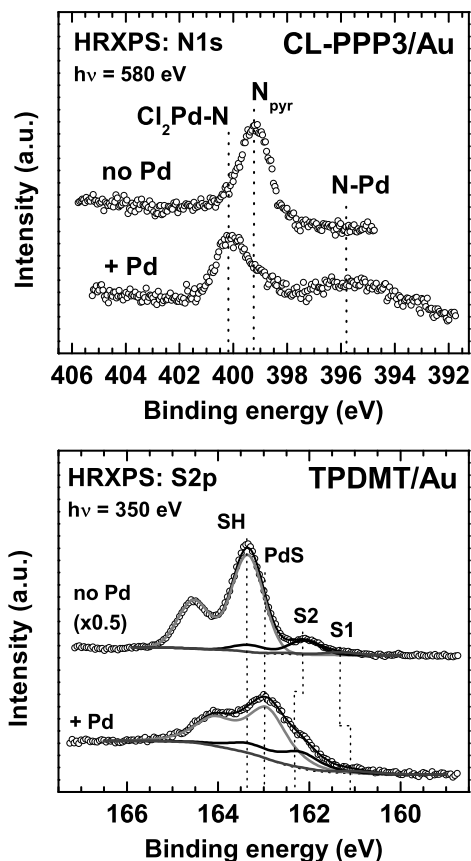


Figure 6.14: HRXPS N1s (top panel) and S2p (bottom panel) spectra of CL-PPP3 and TPDMT monolayers before (top spectrum) and after (bottom spectrum) palladium adsorption.

6.4.1.3 Changes in the molecular order of CL-PPP3 and TPDMT films upon adsorption of PdCl_2

The adsorption of palladium does not induce a significant disordering of the monolayers as shown by the NEXAFS difference spectra of CL-PPP3 and TPDMT (figure 6.15). The polar angle of the backbone resonance (285 eV) was estimated to be reduced by less than 2° upon adsorption of palladium, well within the error of our experiments. These results indicate that palladium did not penetrate to a significant extent through the SAMs used in this study, and forms a stable layer atop the films. This was confirmed by ARXPS (data not shown). With this data in hand, we turn our attention to the evaporation of nickel on the newly formed Pd/SAM systems.

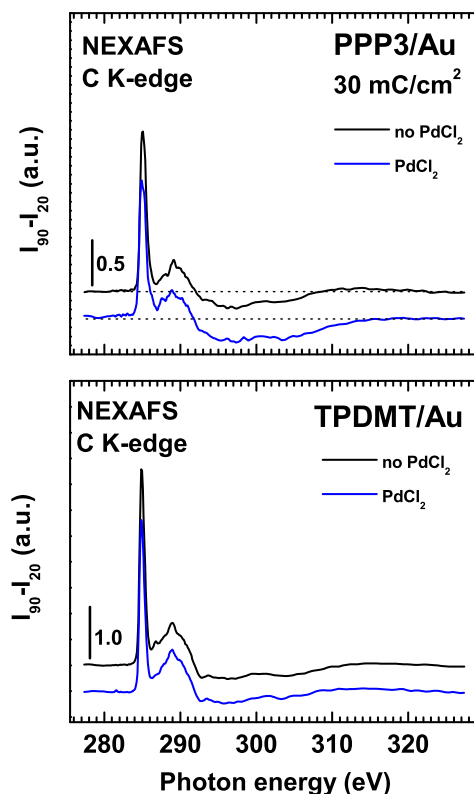


Figure 6.15: NEXAFS difference spectra of CL-PPP3 (top panel) and TPDMT (bottom panel) monolayers before (black) and after (blue) palladium adsorption.

6.4.2 Evaporation of nickel on Pd/SAM films

6.4.2.1 Reaction of nickel with palladium

In both cases, the Pd-Cl peak in the Pd_{3d} HRXPS spectrum (figure 6.16) of Pd/CL-PPP3 and Pd/TPDMT, 338.1 and 337.5 eV respectively, vanishes upon deposition of nickel. At the same time, a single new feature characteristic of the PdNi alloy^{263,264} appears at a lower binding energy (335.7 eV). Furthermore, the intensity of the palladium signal is strongly reduced, indicating that a significant portion of the evaporated nickel resides above the palladium layer. These results support our hypothesis that palladium ions can act as seeds for metal evaporation.

6.4.2.2 Changes to the SAM-ambient interface - the SAM-nickel interface

The SAM-ambient interface of both Pd/CL-PPP3 and Pd/TPDMT was strongly affected by the formation of the palladium-nickel alloy as evidenced in figure 6.17. In both cases, the SAM-palladium bond vanishes. This is especially clear for Pd/TPDMT films (figure 6.17, bottom panel). Upon evaporation of nickel on Pd/TPDMT, the Pd-S peak at 163 eV vanishes and a single peak, **S2**, is observed at 162.1 eV, a value typical for the adsorption of alkanethiols on nickel.³⁹⁻⁴¹ In addition, the **S1** feature does not vanish upon nickel evaporation and no feature at 162.4 eV is visible, a clear departure from what is observed for SAM systems where nickel

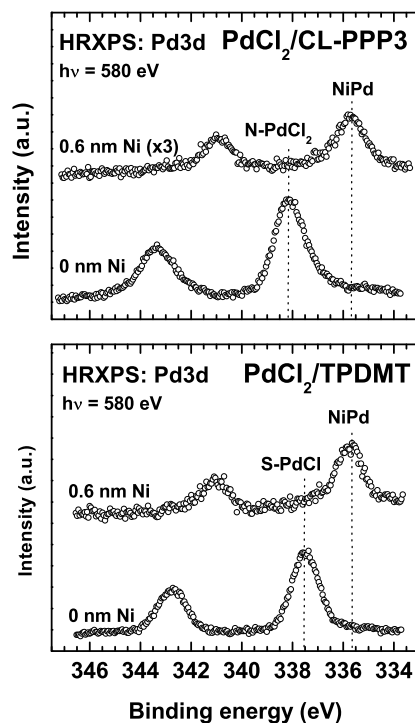


Figure 6.16: HRXPS Pd3d spectra of Pd/CL-PPP3 (top panel) and Pd/TPDMT (bottom panel) monolayers before (top spectrum) and after (bottom spectrum) nickel evaporation.

penetration does occur. Furthermore, assuming a nickel on top model (i.e. no penetration into the carbon matrix), the thickness of the nickel overlayer was calculated, from XPS data, to be 0.65 ± 0.05 nm in both cases, in very good agreement with the thickness value calibrated by quartz crystal microbalance (0.6 nm). This suggests that nickel does not penetrate significantly through the SAMs.

6.4.2.3 Changes in the molecular order of Pd/CL-PPP3 and Pd/TPDMT films upon evaporation of nickel

Compared to monolayers without palladium, the Pd/SAM assemblies exhibit more molecular order after nickel deposition (figure 6.18) thus supporting our conclusions from XPS data (see previous section). A direct measure of the order in monolayers is the polar angle for a given orbital. The angle does not change in systems for which no metal penetration occurs. As can be seen in table 6.1, in accordance with figure 6.18, the polar angle hardly varies at a nickel dose of 0.6 nm for the Pd/SAMs whereas it sharply drops for the films without palladium. Our data, backed up by ARXPS data (data not shown), shows that the shortcomings of the pristine monolayers²⁷ with respect to metal deposition can be overcome by a simple dipping

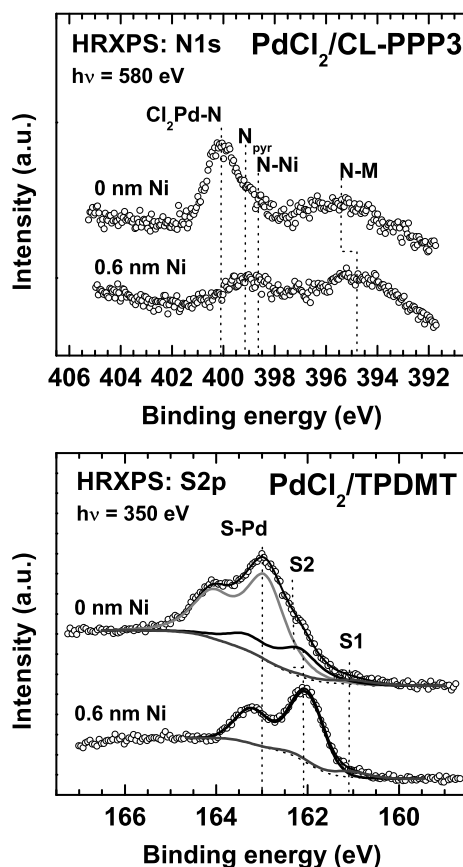


Figure 6.17: HRXPS N1s and S2p spectra of Pd/CL-PPP3 (top panel) and Pd/TPDMT (bottom panel) monolayers before (top spectrum) and after (bottom spectrum) nickel evaporation

	TPDMT	CL-PPP3
no Pd	66.1°	60.5°
no Pd + 0.6 nm Ni	55.6°	53.2°
Pd	65.3°	59°
Pd + 0.6 nm Ni	63.1°	58.9°

Table 6.1: Values of the polar angle for the resonance at 285 eV for TPDMT and CL-PPP3 films with and without palladium. Note: the values given for the TPDMT SAMs without palladium are for crosslinked monolayers. An angle of $\sim 51^\circ$ corresponds to a fully disordered system.

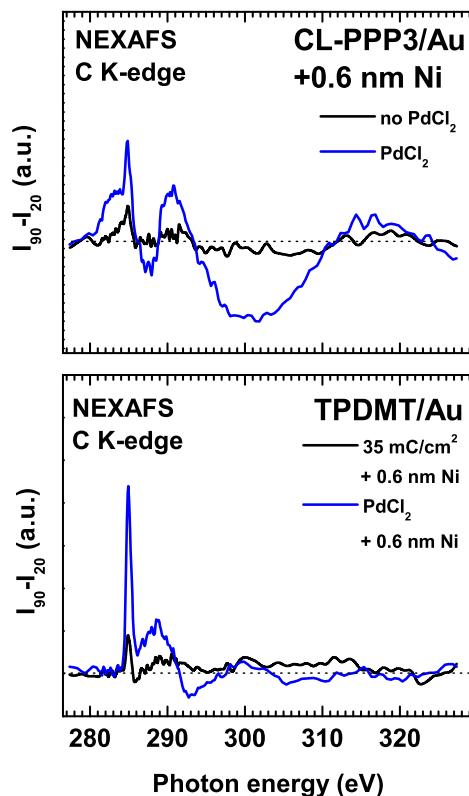


Figure 6.18: NEXAFS difference spectra of Pd/CL-PPP3 (top panel) and Pd/TPDMT (bottom panel) monolayers before and after nickel evaporation. The difference spectra of similar crosslinked films without palladium on top are given in black for comparison. The nickel dose is similar in all cases.

procedure. Upon adsorption of palladium chloride, the permeable (to metal) pristine SAMs become impermeable. This has clear technological implications since the lengthy crosslinking procedure can be replaced by a simple, short (≤ 4 min) bench-top procedure.

6.4.2.4 The mechanism of nickel deposition on Pd/SAM assemblies

We have tested SAMs that form two different types of bonds to palladium; coordination in the case of CL-PPP3 and covalent bond for TPDMT. We hypothesised that the difference in bonding to palladium might result in a difference in the SAMs' resistance to metal penetration. However, since no significant change in molecular orientation in both SAMs was observed and since the thickness of the top nickel layer for both CL-PPP3/Au and TPDMT/Au SAMs is similar, we conclude that the nature of the bond to palladium is not important for the persistence of a top metal layer. Thus, the adsorbed palladium chloride alone is responsible for the persistence of nickel on top of the monolayers. In an effort to further elucidate the mechanism of PdNi film formation, we turned our attention to the Cl2p and Ni2p XPS data of Ni/Pd/TPDMT (figure 6.19). The Pd-Cl peaks at 197.7 (S-Pd-Cl) and 198.6 eV (Pd-Cl) simplify to a single peak at 198.4 eV corresponding to nickel chloride.²⁶⁵ The presence of nickel chloride was also observed

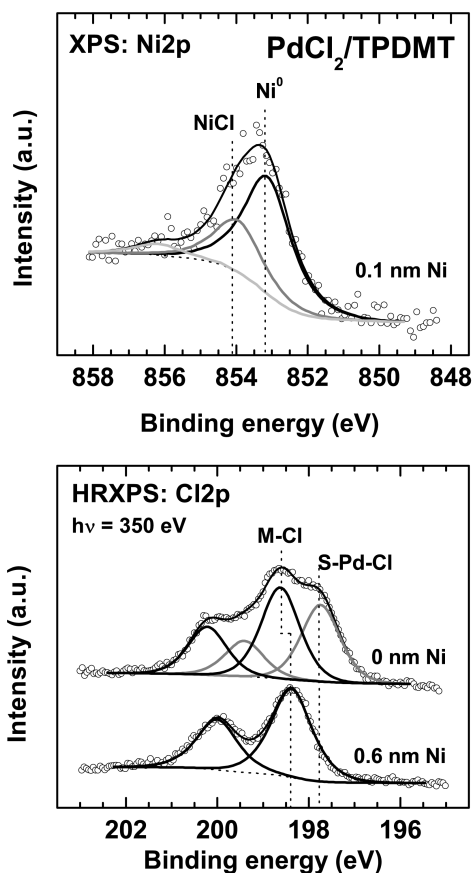


Figure 6.19: XPS Cl₂p (bottom panel) and Ni₂p (top panel) spectra of Pd/TPDMT monolayers. For clarity, the Ni₂p spectrum presented is for 0.1 nm nickel. In the bottom panel, the Cl₂p spectra before (top spectrum) and after (bottom spectrum) nickel evaporation are shown.

in the Ni₂p spectra (figure 6.19, top panel). Whereas the intensity of the Pd_{3d} line is strongly attenuated upon deposition of nickel, the intensity of chlorine, after an initial drop of 20-30 %, does not change significantly over the course of metal evaporation (figure 6.20). Furthermore, the intensity of the NiCl peak in the Ni₂p XPS spectra remains largely unchanged at all metal doses while the intensity of the Ni⁰ peak increases sharply (figure 6.21). With this data in hand we propose the following model, pictured in figure 6.22, for the growth of a nickel film on palladium chloride:

- palladium stays bound to sulphur and alloys with nickel
- chlorine atoms are transferred from palladium to nickel. This is supported by the respective bond strength ($D_{Pd-Cl} \sim 200$ kJ/mol,²⁵⁹ $D_{Ni-Cl} \sim 372$ kJ/mol[?])
- chlorine remains bound to the top layer of nickel throughout deposition ($D_{Pd-S} \sim 457$ kJ/mol,²⁶⁶ $D_{Ni-S} \sim 464$ kJ/mol²⁶⁷)

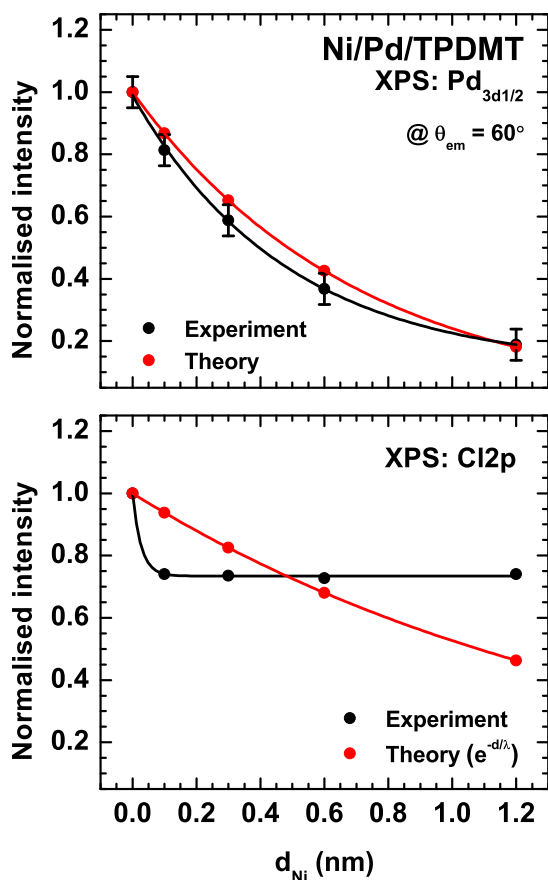


Figure 6.20: Variation of the Pd_{3d} (top panel) and Cl_{2p} (bottom panel) XPS intensity of Ni/Pd/TPDMT monolayers with nickel doses. The theoretical intensity decay for the nickel-on-top model is shown in red.

6.4.3 Summary

We have demonstrated the use of pyridine and thiol terminated terphenyl SAMs (CL-PPP3/Au and TPDMT/Au respectively) as substrates for the immobilisation of palladium on self-assembled monolayers. Palladium, deposited as palladium chloride from an ethanolic solution, was found to reside at the top of the monolayer without significantly penetrating through the SAMs. Furthermore, we have used these systems as substrate for e-beam metal evaporation. Upon evaporation, a stable metal layer is formed at the SAM-ambient interface with palladium atoms acting as seeds, regardless of the nature of the bond between palladium and the monolayer (covalent or coordinated). Thus, palladium chloride was able to fully stop metal penetration into ultrathin organic films (≤ 3 nm), a critical step toward the fabrication of SAM-based nanoelectronic devices. Most importantly, using TPDMT, we have shown that pristine monolayers could be used for e-beam evaporation thus eliminating the time-consuming crosslinking step usually required to stop metal penetration through thin films,^{26,27} and opening the door to the use of the many commercially available amine thiol and dithiol molecules, in particular the aliphatic ones which are readily and cheaply available. Furthermore, this method could be used in conjunction with

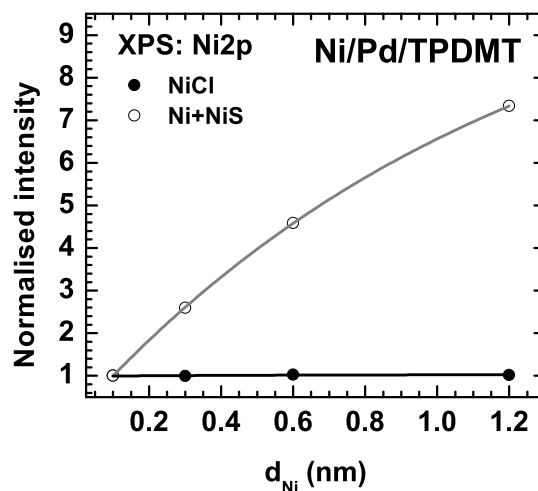


Figure 6.21: XPS Ni2p normalised intensities of the NiCl (filled circles, black line) and Ni⁰ peaks (open circles, gray line) of Ni/Pd/TPDMT at various nickel doses

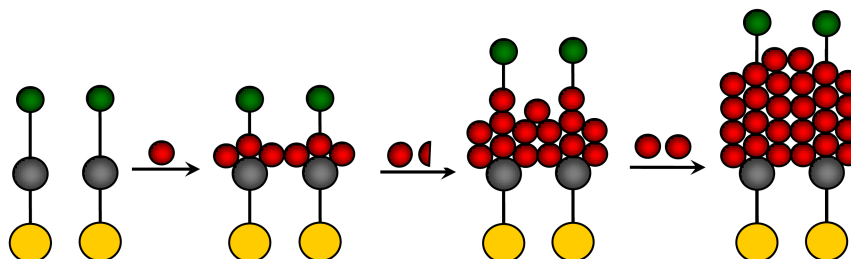


Figure 6.22: Model for the deposition of nickel on Pd/TPDMT SAMs. Colour code: sulphur: yellow circles, palladium: gray circles, nickel: red circles, chlorine: green circles.

the electron beam chemical lithography²² and UV-Vis chemical lithography²³ methods developed in our laboratory to rapidly and cheaply pattern nano-circuits onto gold wafers. So far we have only investigated the effect of the terminal group on metal penetration. In the next section we will look at a novel way to stop metal penetration: reactive linkers. FTP3 (see section 4.3) was used as test system and nickel as test metal.

Peak	Binding energy (eV)	Assignment
C-F	287.2	C-F ²¹
1	286.6	-H ₂ C-CF ₂ - in polymer ²⁷⁰
2	285.7	-H ₂ C-CHF- in polymer ²⁷⁰
C-C	285.2	interring C-C ²¹
3	284.6	conjugated carbon motif ²⁶⁹
C-H	284.0	C-H, ²¹ C-Ni ²⁶⁹
4	283.3	C-Ni ²⁷²⁻²⁷⁵

Table 6.2: Assignment of the C 1s HRXPS peaks of Ni/FTP3/Au

6.5 Metal evaporation on FTP3 SAMs

Nickel metal is known to react with fluoro- and hydrocarbons.^{231,232,247} In addition, its magnetic and electric properties²⁶⁸ make it the ideal model metal for the metallisation of fluorinated thin films for use in nanoelectronic devices. The results of the deposition of nickel on pristine and crosslinked FTP3 SAMs test systems is presented below

6.5.1 Reaction of nickel with the FTP matrix

6.5.1.1 Changes to the carbon matrix

Figure 6.24 shows the C 1s HRXPS spectra of FTP3/Au at various nickel doses. The spectral envelope of the C 1s spectra changes significantly over the course of irradiation, suggesting extensive modification of the fluorocarbon matrix. The peak associated with the C-F bonds (~ 287.5 eV) decreases in intensity with increasing nickel dose, implying cleavage of the C-F bonds upon metal deposition. Furthermore, the peaks due to the C-C and C-H bonds (~ 285.5 eV and ~ 284.4 eV respectively) show no visible decrease in intensity, save for that brought about by the attenuation of the C1s signal by nickel, indicating that the deposition does not induce significant decomposition or loss of molecules. This is emphasised by the stability of the I_{C1s}/I_{Au4f} ratio presented in the bottom panel of figure 6.29 (page 115). In striking contrast to the C-F signal, the peak at ~ 284.0 eV increases in intensity with increasing nickel dose. This is consistent with the formation of C-Ni bounds. A similar peak is observed for the deposition of nickel on graphite.²⁶⁹ In addition, new features, labelled **1** to **4**, appear and grow in intensity with increasing metal dose. These features point toward extensive polymerisation²⁷⁰ (**1** and **2**) and conjugation^{269,271} (**3**) of the FTP3 film during metal evaporation, consistent with nickel-catalysed carbon-carbon bond formation.²³² The feature at ~ 283.3 eV (**4**) is best ascribed to C-Ni bonds.²⁷² The various peaks observed in the C 1s HRXPS spectra of Ni/FTP3 SAMs and their assignment are summarised in table 6.2.

6.5.1.2 Modification of the electronic structure

The changes observed in the C1s HRXPS spectra (figure 6.24) indicate that the electronic structure of the monolayer changes dramatically upon metal evaporation. Figure 6.24 shows the 55° C K-edge NEXAFS spectra of FTP3 films at various metal doses. The spectral envelope exhibit a continuous change with increasing metal dose. The intensity of both the $C1s^{C-F} \rightarrow 1\pi^*$ and

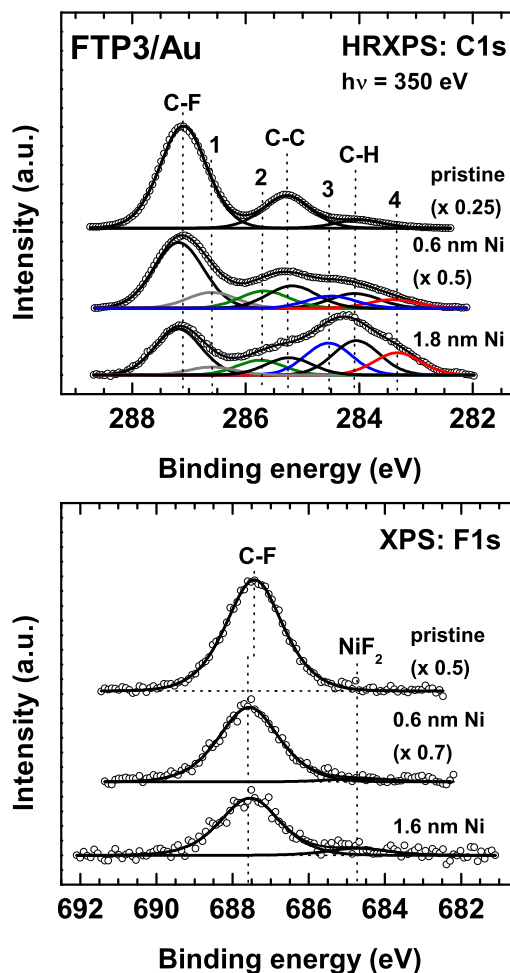


Figure 6.23: C 1s HRXPS spectra of FTP3 SAMs at various metal doses. The spectral deconvolutions are shown. The peaks associated with the pristine film are shown in black.

C1s^{C-F} \rightarrow 1 σ^* resonances diminishes sharply at 0.6 nm Ni, its intensity being reduced by ~ 50 %, and then more slowly after that, losing only ~ 10 % of its intensity. This supports our conclusions about C-F bond cleavage from XPS data. Furthermore, consistent with HRXPS results, several resonances appear at the lower energy side of the C1s^{C-C} \rightarrow 1 π^* resonance (< 285.6 eV) and grow in intensity over the course of deposition (figure 6.25). These are assigned to an increase in conjugation throughout the SAM (table 6.3). Indeed, NEXAFS data of polyacene molecules show a clear shift of the C1s^{C-C} \rightarrow π^* peak to lower photon energies with increasing conjugation; from 285 eV for benzene to 284.1 eV for pentacene.¹⁸⁵ In addition, many common polymers exhibit a C1s \rightarrow π^* transition in the 284.4 to 284.9 eV region.¹⁸⁶ Furthermore, on the basis of quantum mechanical calculations at the ZINDO/S level, Ti-C NEXAFS data,²⁷⁶ and our C 1s HRXPS data, the two low lying transitions were assigned to the C1s^{C-Ni} \rightarrow 1 π^* transitions.

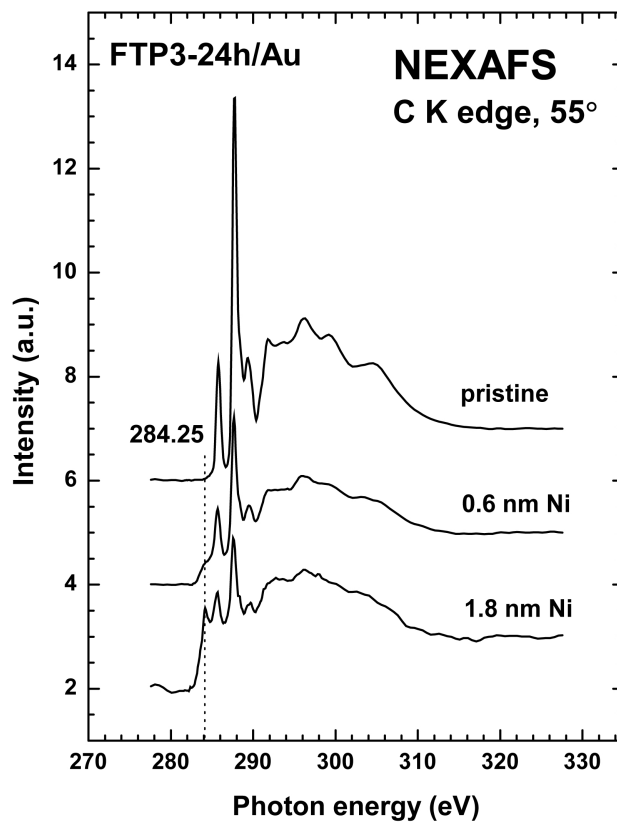


Figure 6.24: C K edge NEXAFS spectra of Ni/FTP3 at the magic angle (55°).

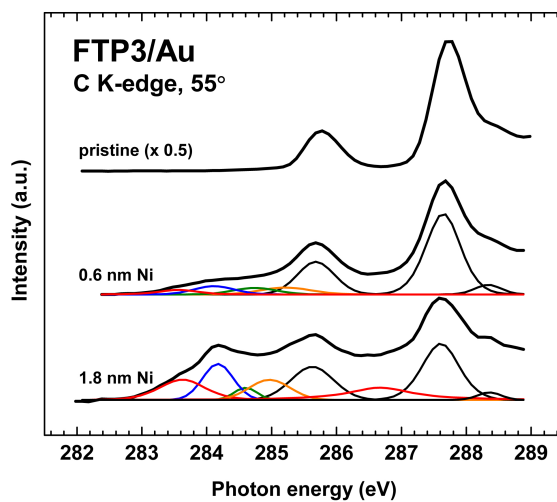


Figure 6.25: Deconvolution of the C K edge NEXAFS π^* region of Ni/FTP3 at the magic angle (55°). The peaks corresponding to the pristine film are shown in black.

Photon energy (eV)	Assignment
287.6	$\text{C1s}^{C-F} \rightarrow 1\pi^{*?}$
286.7	$\text{C1s} \rightarrow 1\pi^{*}$
285.6	$\text{C1s}^{C-C} \rightarrow 1\pi^{*?}$
285.0	$\text{C1s}^{C-C} \rightarrow 1\pi^{*185}$
284.6	$\text{C1s}^{C-C} \rightarrow 1\pi^{*185}$
284.2	$\text{C1s}^{C-Ni} \rightarrow 1\pi^{*269}$
283.6	$\text{C1s}^{C-Ni} \rightarrow 1\pi^{*276}$

Table 6.3: Assignment of the C K-edge NEXAFS π^{*} transitions of Ni/FTP3/Au.

Does the metal penetrate the FTP3 films? As can be seen from the data presented above, both the chemical composition and the electronic structure of the carbon matrix are heavily modified upon nickel deposition. Indicating that nickel penetrates into the FTPn/Au film to some extent. Furthermore, simultaneously to the cleavage of C-F bonds, new C-Ni bonds are formed leading to a new *organometallic* thin film. So far, we have not looked at the SAM-substrate interface.

6.5.1.3 The nickel film

The data from C 1s HRXPS suggest the formation of C-Ni bonds which are also observed at ~ 855.2 eV in the Ni2p spectra of FTP3 films at low nickel coverage (figure 6.26). For C-Ni bonds to form, nickel must insert into the carbon fluorine bond^{231,232,247} leading to the formation of either C-Ni-F or C-Ni-C and NiF_x compounds. The proportion of NiF_x calculated from Ni2p XPS data is small at all metal doses when compared to the analogous aliphatic F10H2 SAMs (data not shown) for which metal penetration is expected to dominate. The vast majority of the evaporated nickel remains in the metallic (Ni^0) state. This suggests either heterogeneous growth of the nickel film, or sealing of the FTP3 monolayer, thus preventing further reaction of nickel down the SAM. Furthermore, the shift of the Ni2p line toward lower binding energies (853.4 eV at 0.1 nm to 853 eV at 0.6 nm) and the reduction in the full width at half maximum from 2.1 eV at 0.1 nm to 1.6 eV at 0.6 nm, suggest the formation of a continuous nickel film. However, the growth mode and growth kinetics of nickel films on SAMs can not be established solely by XPS. They should be investigated using other techniques such as scanning tunnelling microscopy (STM), however, such work is beyond the scope of this thesis.

6.5.1.4 The fate of fluorine

Is nickel fluoride a minor byproduct? Along with the breaking of carbon-fluorine bonds, one can expect the formation of either F-F or Ni-F bonds. The formation of the former is thought unlikely since its bond energy is low and its reactivity high.¹¹⁰ Nickel fluoride (section 6.5.1.3) is therefore expected to be the main fluorine by-product. However, the F1s and Ni2p spectra of Ni/FTP3 monolayers reveal only traces of nickel fluoride (figure 6.27, top panel and figure 6.26 respectively). This is in striking contrast to the corresponding fluoroalkane system F10H2 for which the F1s nickel fluoride signal increases sharply in intensity with increasing metal dose (figure 6.27, bottom panel), consistent with the behaviour observed for the deposition of iron on similar fluoroalkane thin films.²⁷⁷ This suggests that either, unlike the F10H2 system, FTP3

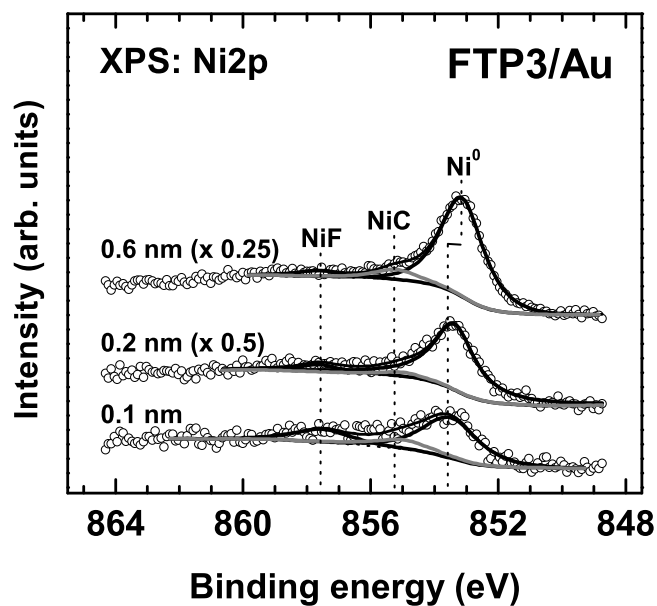


Figure 6.26: Ni2p XPS spectra of Ni/FTP3 at low nickel coverage (< 3ML). The NiF, NiC and Ni⁰ peaks are shown.

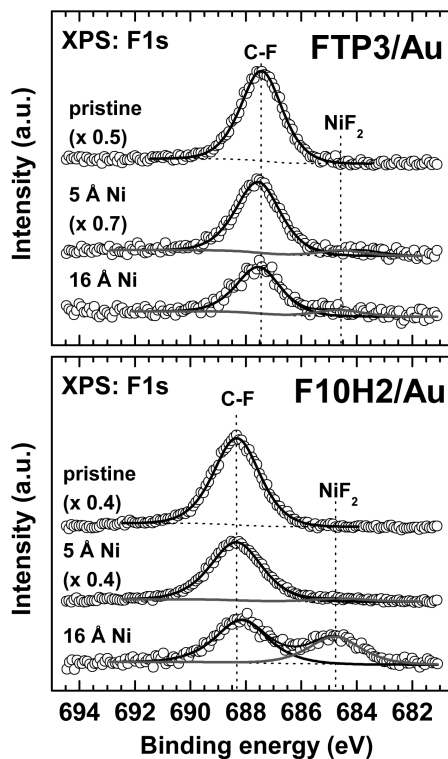


Figure 6.27: F1s XPS spectra of Ni/FTP3 and Ni/F10H2 at various nickel doses.

d_{Ni} (nm)		FTP3	F10H2
	experiment	0.15	0.15
0.5 (2.5 ML)	theory	0.81	0.50
1.6 (8 ML)	experiment	0.3	0.65
	theory	1	1

Table 6.4: Theoretical and experimental fluorine loss. A ratio of 1 means the loss of all fluorine atoms in the corresponding molecule. The number of monolayers is indicated in parentheses. For the theoretical calculations, a 100% efficiency of C-F bond cleavage by nickel was assumed for both systems. The experimental values given are the normalised I_{CF}/I_C ratio. For the purpose of these calculations one monolayer of nickel corresponds to 1.6×10^{15} atoms/cm² (value extracted from the work of Roesch *et al.*²⁸⁰). One monolayer of FTP3 corresponds to 4.94×10^{15} fluorine/cm² and a monolayer of F10H2 corresponds to 7.98×10^{15} fluorine/cm². For theoretical calculations, a 100% efficiency for Ni-F bond formation was assumed. The values for the number of fluorine atoms in FTP3 and F10H2 were extracted on the basis of previous STM measurements.²¹

SAMs prevent deep penetration of the evaporated metal, that nickel fluoride is located at the SAM-substrate interface, or that nickel fluoride is not a major product in the reaction of nickel with FTP moieties. These hypotheses will be addressed further in this section. However, nickel fluoride, represents only 11 % of the total fluorine F 1s signal in the case of FTP3 and 39 % in the case of F10H2 films, much lower than the total loss of fluorine determined from C 1s XPS ($\sim 30\%$ and $\sim 65\%$ respectively). This suggests that fluorine is released from the film, probably as F₂ (to some extent), F⁻ or, HF after reaction of a fluorine radical with H₂.^d

Are matrix effects responsible for the relative low fluorine loss in FTP3 films? The difference between the FTP3 and F10H2 systems can not be explained purely on the basis of thermodynamics since the energy carried by the metal atoms is the same in both cases (KE ~ 0.2 eV). Furthermore, the difference in bond strength (5.33 eV for F10H2²⁷⁸ vs 6.51 eV in the case of FTP3²⁷⁹) is too low to explain the large differences, a factor of 3.5, observed in the F 1s XPS spectra (figure 6.27).

The differences between FTP3 and F10H2 are better revealed when considering the experimental and theoretical losses of fluorine on a per-bond basis (table 6.4). As seen in table 6.4, the relative loss of fluorine is comparatively much lower in the FTP films at higher doses, strongly suggesting that the nature of the matrix rather than the bond strength or the number of C-F bonds per molecule is the major factor influencing fluorine loss. However, the depth-distribution of nickel through the FTP3 monolayer can not be assessed solely on the basis of the XPS data presented so far. If these films are to be useful as dielectric layers in molecular electronic devices, the question of metal penetration into and through FTPn SAMs must be settled.

^dH₂ is always present to some extent in UHV chambers.

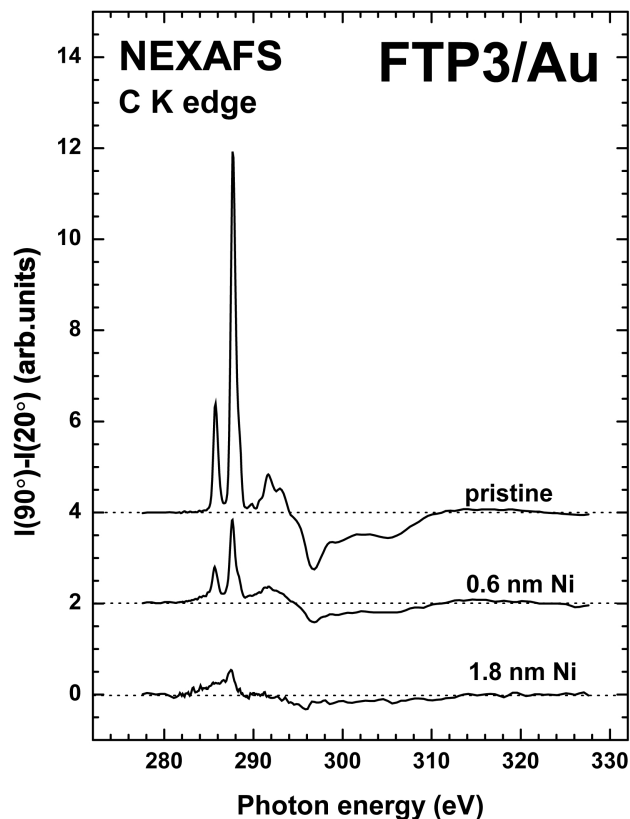


Figure 6.28: C K edge NEXAFS difference spectra ($I_{90}-I_{20}$) of FTP3 at different nickel doses.

6.5.2 Distribution of nickel through FTP3 SAMs

6.5.2.1 Change in average molecular order in FTP3 SAMs upon metal evaporation

The loss of average molecular order in a thin film can be used as a fingerprint of metal penetration since the molecular order of a SAM will be disrupted upon metal penetration.^{27,52} We have probed the change in molecular order as a function of the metal dose by NEXAFS difference curves (figure 6.28). As can be seen in figure 6.28, both the $C1s^{C-C} \rightarrow 1\pi^*$ and $C1s^{C-F} \rightarrow 1\pi^*$ resonances decrease sharply in intensity upon metal evaporation, indicating a loss in molecular order. Note that due to the cleavage of the C-F bonds upon metal deposition, the decrease in the intensity of the $C1s^{C-F} \rightarrow 1\pi^*$ resonance is larger than that of the $C1s^{C-C} \rightarrow 1\pi^*$ resonance and can not be used as a reliable marker for molecular order. However, even at high nickel doses a slight dichroism can be seen and the dichroism at 0.6 nm Ni is still significant. This is in stark contrast with the PPPn systems for which all dichroism is lost, for crosslinked SAMs, upon metal evaporation (section 6.3, page 94). The reduced dichroism indicates that nickel penetrates, at least partly, into the SAM. However, it is known that reactive metals (e.g. Ni, Ti) disrupt the molecular order of self-assembled monolayers.⁵² In addition, the high temperature of the impinging metal (nickel melts at 1728 K at atmospheric pressure) is expected to have some effect as well (see the discussion about the S-Au interface on page 116). Consequently, in the present case, we can not rely on NEXAFS spectroscopy alone to determine if nickel penetrates

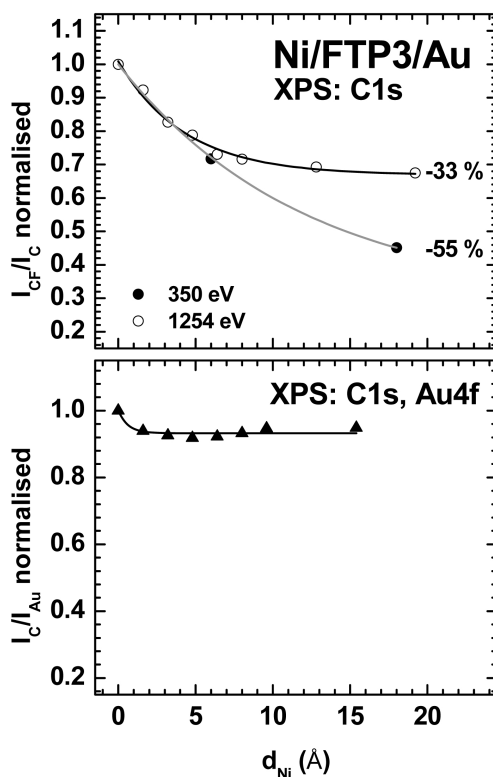


Figure 6.29: Variation of the C 1s XPS intensity as a function of the nickel dose at two different excitation energies. The C-F/C ratio at 350 and 1254 eV (top panel) and the C/Au ratio (bottom panel) are shown.

through the monolayer.

6.5.2.2 Distribution of nickel throughout FTP3 SAMs probed by XPS

The FTP moiety. Although the NEXAFS data shows that metal penetration occurs, it can not precisely quantify and/or locate it. However, by using different excitation energies depth distribution information can be retrieved from XPS data (figure 6.29). The variation of the fluorine signal, extracted from XPS carbon data, is presented in the top panel of figure 6.29. We chose to use the ratio of the CF peak to the total carbon signal as a measure of fluorine loss in the films. This approach allows us to avoid problems related to the variation of λ (due to the changing matrix) and changing overlayer thickness throughout the experiment. No difference in the decay of the C-F signal is observed up to 0.6 nm. However, above 0.6 nm the behaviour at 1254 eV diverges strongly from that at 350 eV, indicating that most of the chemistry occurs at the topmost part of the film. Consequently, we expect nickel to be found mostly at the top of the film. Indeed, unlike its hydrocarbon analogue TP3, a significant portion of the evaporated metal is found at the SAM-ambient interface as evidenced by ion scattering spectroscopy (ISS, figure 6.30). Finally, the bottom panel of figure 6.29 shows that the carbon to gold ratio of FTP3 SAMs does not vary significantly over the course of metal evaporation. This is characteristic of the deposition of metal on top of a monolayer and indicates no, or almost no, metal penetration.^{26,27}

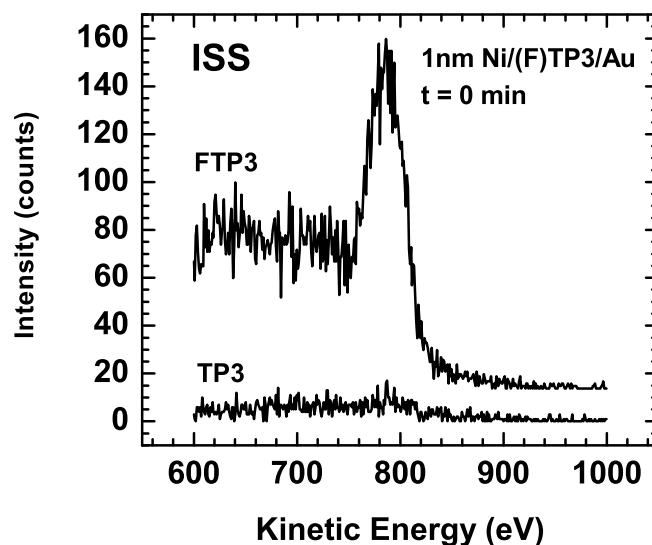


Figure 6.30: ISS spectra of Ni/FTP3 (top trace) and Ni/TP3 (lower trace) at an incident helium ion energy of 1000 eV.

The sulfur-gold interface The S2p HRXPS spectra of various Ni/FTP3 and Ni/F10H2 films are presented in figure 6.31. The intensity of the S2p peak increases with increasing nickel dose in the case of the F10H2/Au system, supporting a model where metal penetrates to the S-Au interface and intercalates itself between the substrate and the head group. In addition, the fwhm of the peaks increases from 0.7 to ~ 1 eV indicating strong disordering of the F10H2 monolayer upon nickel deposition. Significantly, the binding energy of the thiolate peak (**S2**) is shifted to lower binding energies by ~ 0.25 eV indicating a change in the environment of the thiolate. This is consistent with the formation of a nickel overlayer on gold^e. In addition, the **S1** peak at ~ 161 eV vanishes after deposition of just 0.6 nm of nickel. This peak has previously been ascribed to either a "differently bound" thiolate or atomic sulphur (section 4.3). The presence of the **S3** peak at ~ 163.2 eV indicates the formation of dialkylsulfide species as observed for the electron irradiation of thiol-based SAMs on gold (section 5.1). Finally, a new peak, **S4**, is observed at ~ 162.8 eV. This peak can be ascribed to various Ni-S species^{251,281,282} strongly suggesting that the S-Au interface of the F10H2/Au system is extensively modified upon evaporation of nickel and that nickel penetrates to the S-Au interface and reacts with sulphur.

Whereas the S-Au interface of the F10H2/Au system is extensively damaged upon evaporation of nickel, it remains mainly intact in the case of FTP3/Au. Indeed, only a small fraction of the **S3** peak and no **S4** peak are observed. Furthermore, the binding energy of the thiolate peak did not change throughout the deposition of nickel on FTP3/Au. However, the fwhm of the S2p peak also increased from 0.7 to ~ 1 eV indicating strong disordering of the FTP3 monolayer in agreement with NEXAFS data (section 6.5.2.1). Furthermore, whereas the total sulphur intensity increases with increasing nickel dose in the case of F10H2/Au, it decreases for FTP3/Au, indicating the formation of a nickel layer on top of the S-Au interface. Since the proportion of the **S3** peak at

^eThe evaporation of a 0.9 nm thick nickel film on gold leads to a lowering of the work function by ~ 0.15 eV.

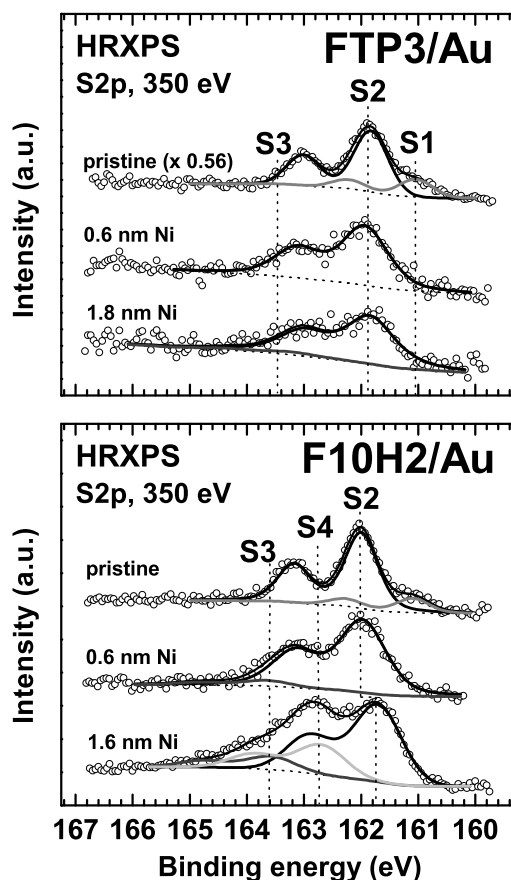


Figure 6.31: S2p HRXPS spectra of Ni/FTP3/Au (top panel) and Ni/F10H2/Au (bottom panel). The various peaks are labelled.

high metal dose and the variation in the fwhm are similar for both FTP3/Au and F10H2/Au, we surmise that the damage to the S-Au interface in FTP3/Au is mainly thermal in nature, i.e. it is mainly caused by the local increase in temperature due to the adsorption of nickel onto the SAMs from the gas phase.²⁸³

6.5.3 The effect of crosslinking on metal penetration in FTP3 SAMs

We have demonstrated above that a pristine FTP3 monolayer on gold was capable of stopping metal penetration through the SAM. Since crosslinking enhances the overall strength of the intermolecular interactions in the SAM by chemically binding the molecules together,^{27,65,66} we expect crosslinked films of FTP3/Au to perform better than their pristine counterparts.

6.5.3.1 Fluorine loss upon metal evaporation as a function of irradiation dose

A major advantage of the FTP3 films with respect to their hydrocarbon counterparts, from a spectroscopic point of view, is the ability to monitor the destiny of fluorine. The more crosslinked the film, the less metal penetrates through the film (figure 6.32). Upon extensive crosslinking

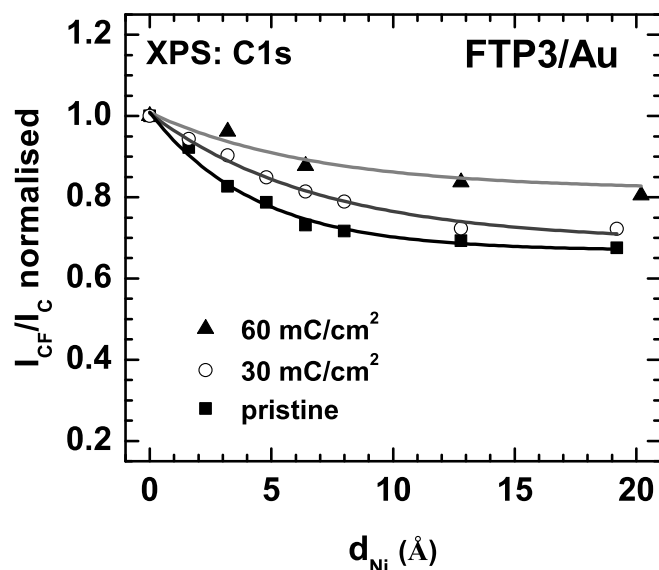


Figure 6.32: Variation of the CF peak intensity with nickel dose for various crosslinked films. Black squares: pristine film; Hollow circles: 30 mC/cm²; Black triangles: 60 mC/cm²

(60 mC/cm²), the loss of fluorine drops from 30 to 20 % at high nickel doses (2 nm or 10 ML) indicating an improved metal stopping efficiency for the crosslinked films. Therefore, crosslinking of the FTP3 films clearly hinders metal penetration.

6.5.3.2 Distribution of nickel in irradiated FTP3 SAMs probed by ARXPS

The angle resolved XPS data for the deposition of nickel on a 30 mC/cm² film (referred to as CL-FTP3 in the rest of this discussion) is shown in figure 6.33. Unlike our reference CL-TPDMT system (section 6.2, page 89), the Ni/C ratio increased with decreasing emission angle at all doses, suggesting deposition of nickel atop the CL-FTP3 SAM, even at sub-monolayer coverage. Furthermore, the change in the nickel to carbon ratio became more rapid as the metal dose increased, indicating the accumulation of nickel on top of the CL-FTP3/Ni assembly. It should be noted that the nickel intensity did not vary significantly with the emission angle as expected for a stable film on top of a SAM.²⁶

6.5.4 Rough estimate of the penetration depth of nickel in FTP3 SAMs

We attempted to provide a rough estimate of the nickel penetration depth of nickel into FTP3 SAMs by evaluating the fluorine loss. Assuming that nickel atoms insert into the first carbon-fluorine bond they encounter with a 100 % yield, and taking into account the loss of fluorine at high metal doses (table 6.5), we were able to give a rough estimate of the penetration depth of nickel into FTP3 SAMs. The values given in table 6.5 are only rough estimations since other factors (e.g. local increase in temperature²⁸³) can be responsible for the loss of fluorine. Therefore, the penetration depth could be smaller than the values indicated above. However, these correlate well with the value derived from energy-resolved XPS data of pristine FTP3 film (0.6 nm, figure 6.29, page 115).

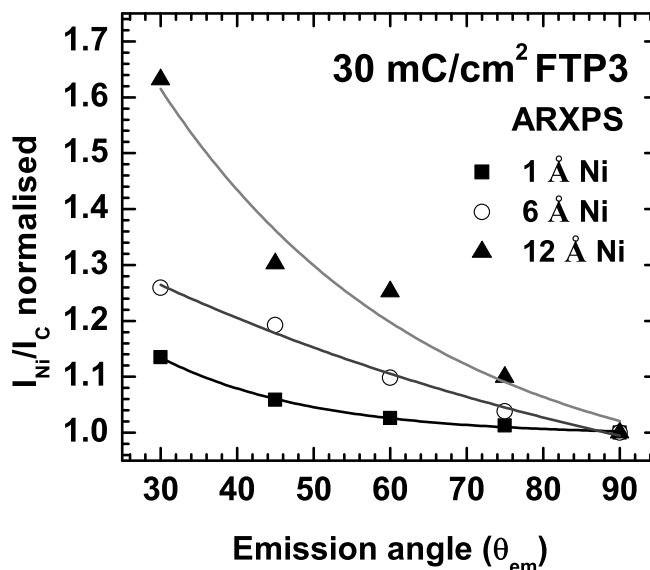


Figure 6.33: ARXPS data (I_{Ni2p}/I_{C1s}) of a 30 mC/cm² film at various nickel doses

e- dose (mC/cm ²)	% F loss	# F lost	Max. penetr. depth (nm)
0	32	4	0.7
30	28	2.5	0.7-0.8
60	19	1.2	0.4-0.7

Table 6.5: Estimation of the maximum penetration depth of nickel through various FTP3 films. Values are only rough estimates.

6.5.5 Summary of nickel deposition on FTP SAMs

We have demonstrated that FTP3 monolayers can advantageously prevent nickel penetration via insertion of the nickel atoms into carbon-fluorine bonds. The attachment of nickel was found to take place primarily at the top of the monolayer (figure 6.34). At low metal doses^f (< 0.6 nm (3 ML)), the FTPn SAMs still showed significant order as seen by NEXAFS spectroscopy. However, at high metal doses, the molecular order was significantly reduced. It should be noted that similar results were obtained for a substrate incubation time (in FTP3 solution) of two hours.^g FTP3's alkyl counterpart, F10H2, did not efficiently prevent metal penetration leading to extensive damage to the SAM-substrate interface. Similarly, TP3, a hydrocarbon analogue to FTP3 did not significantly prevent metal penetration and, unlike FTP3, only traces of metal could be detected at the SAM-ambient interface. Metal-SAM-metal (MSM) assemblies with a

^fNote that due to time constraints we could not investigate fully the 0.6-1.8 nm region. However, this should be investigated in detail since it would yield the maximum metal dose achievable without major loss of orientation. We suspect that the limit will be found around 1 nm.

^gThe standard incubation time was 24 hours.

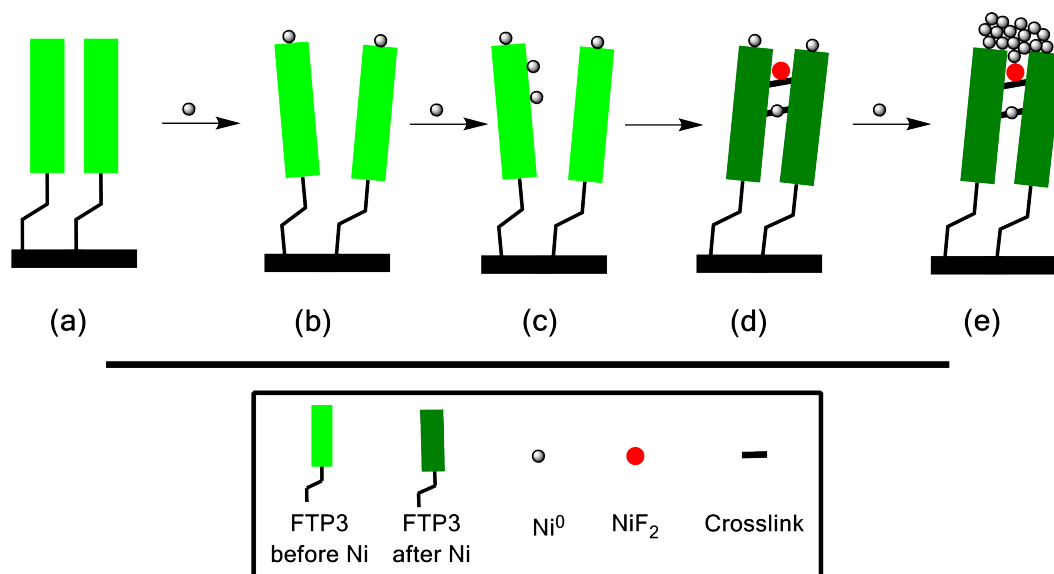


Figure 6.34: Schematic representation of the deposition of nickel on FTP3 thin films.

maximum top metal thickness of 1.8 nm were successfully fabricated, as evidenced by X-ray spectroscopy. Critically, this could be achieved without electron irradiation. Using the FTP3 molecule, an MSM device could be assembled in under half a day at room temperature and using cheap gold on silicon wafers. By comparison, a similar system based on TPDMT would require one to two days of preparation. In addition, FTP3 irradiated with various electron doses (30 and 60 mC/cm^2) were found to prevent metal penetration to a greater extent than pristine SAMs. This, combined with the ability to modify the transport properties of the FTPn films by electron irradiation (section 5.3, page 5.3) makes FTPn films attractive for the fabrication of tailored nanoelectronic devices, e.g. as nanojunctions in spintronic devices. Furthermore, since the metal layer is chemically bound to the FTP3 dielectric layer, we expect the metal film to be stable with time. However, time-dependant investigation are still needed to ascertain the durability of these devices. Preliminary work on the electronic characterisation of these systems will be shown in section 7.1 along with the formation of a SAM atop the metal film in section 7.3.

Chapter 7

Side subjects and perspectives

The work presented in this thesis stands as the ground work to the fabrication and extensive investigation of metal-SAM-metal (MSM) systems based on ferromagnetic metals. Owing to the difficulty in characterisation, these systems have been studied relatively little.¹³¹ Most studies on nanojunctions (Metal-SAM-metal) have been carried out with the top contact being in physical rather than chemical contact with the SAM, i.e. the top electrical contact was not bound to the SAM.^{30,31} In section 7.1, we show preliminary work function measurements of MSM systems. We then turn our attention to the immobilisation of nanoparticles on electron-irradiated SAMs as a way to form the top metal contact (section 7.2). Finally, the formation of a SAM onto the top metal contact will be discussed (section 7.3).

7.1 Work function and band gap of Metal-SAM-Metal systems

7.1.1 Modifying the work function of metal electrodes with SAMs

As seen in section 4.4, the work function (Φ) of a gold surface can be dramatically altered by self-assembled monolayers. While fluorinated SAMs increase the work function of gold (+0.6 eV for FTP3), hydrocarbon monolayers decrease it (-0.8 eV in the case of TP3). This is due to the fact that the sign of the molecular dipoles are inverted for non-fluorinated and fluorinated molecules (figure 7.1).^{50,51,54,130,138,284–289}

The relative changes in work function are mirrored by the relative changes in the energy of the highest occupied molecular orbital (see figure 4.18, page 48). Furthermore, in the case of oligophenyl SAMs, the presence of a linker between the head group and the oligophenyl moiety also modifies the work function by acting as an insulator, thus decoupling the aromatic backbone from the metal surface (section 4.4). It should also be noted that the degree of conjugation between the aromatic rings influences the energy of the highest occupied molecular orbital (HOMO) and, consequently, the work function of the modified gold surface (table 7.1). Calculations on TP3 at the B3LYP/631*-G level show that the energy of the HOMO is increased by as much as 0.25 eV on going from an out-of-plane ($\theta \sim 38^\circ$) to an in-plane ($\theta \sim 0^\circ$) configuration of the terphenyl moiety (figure 7.2).^b By contrast, the fluorine atoms in the FTP moiety forbid such a transition. Calculations show that the HOMO-LUMO gap of FTP3 is identical to that of an out of plane TP3 molecule at 4.8 eV supporting UPS and inverse photo emission data which show a gap of 4.86 ± 0.4 eV for FTP3 and 4.76 ± 0.4 eV for TP3 (section 4.4).

^b θ is the absolute value of the angle between the central and outer rings of the terphenyl units.

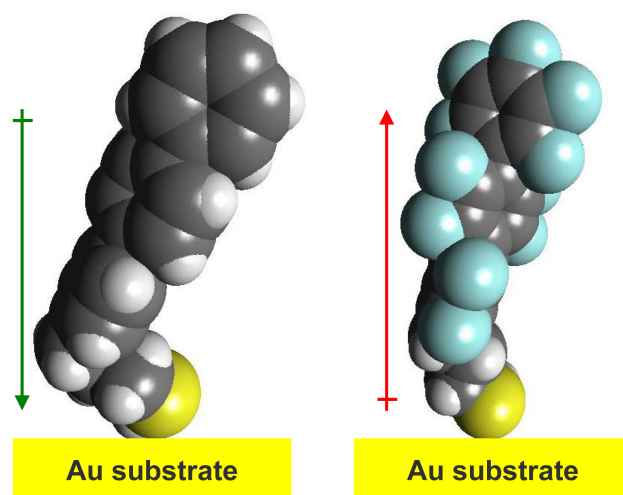


Figure 7.1: Molecular dipole of TP3 (left) and FTP3 (right) on a gold surface. If the dipole points toward the surface (left), the work function decreases. Conversely, if the dipole points toward the molecule (right), the work function increases.

7.1.2 Change in work function upon metal deposition

The deposition of metal on self-assembled monolayers is expected to result in a change in their work function (Φ).²⁹⁰ We expect the amount of change to depend on the work function of the deposited metal. For instance, potassium has a low work function (~ 2 eV) and therefore induces dramatic changes in the work function of alkanethiols on gold.²⁹⁰ By contrast, nickel, the metal used in our studies, has a work function close to that of gold (4.9-5.0 vs 5.1-5.2 eV for gold). This should result in a lower rate of change compared to potassium.

7.1.2.1 Change in the work function of F-SAMs upon nickel deposition

The work function of FTP3/Au and F10H2/Au as a function of the thickness of deposited nickel is shown in figure 7.3. Since both films contain fluorine, their molecular dipoles point away from the surface, therefore, F-SAM modified substrates exhibit a higher work function than the substrate itself (e.g. Au, Ni). We therefore expect that the work function of the total systems (Metal-SAM-Metal) would decrease upon nickel deposition. If nickel fully covers the surface of the SAM, a value of Φ close to that of nickel is expected.

The work function of F10H2 films, shown in the bottom panel of figure 7.3, exhibit a slow, monotonous decay with increasing nickel dose. This behaviour can be attributed to the penetration of nickel through the SAM accompanied by defluorination of the molecules (section 6.5). This is confirmed by sputtering the film with argon (figure 7.4, bottom panel). The work function drops dramatically within the first minute of sputtering to the value typical of a clean nickel film (~ 5 eV) followed by a slow rise up to the value for a clean gold surface (set as 5.1 eV throughout our experiments).

As can be seen in the top panel of figure 7.3, the behaviour of the FTP3 films is radically different. First, the work function drops by 0.5 eV after deposition of ~ 1 Å nickel (compared to a drop of just 0.1 eV for F10H2 films). Then, it stabilises around 5 eV (the value for a clean

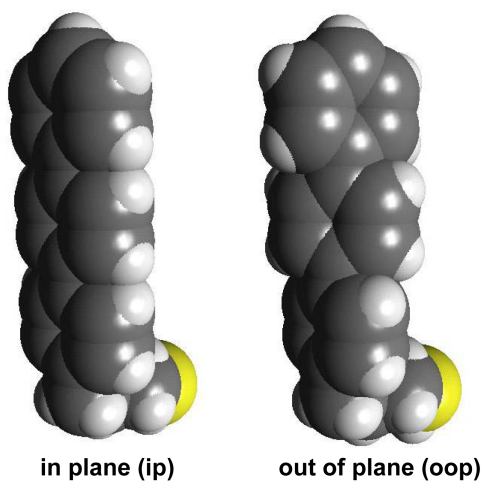


Figure 7.2: In plane and out of plane configurations of TP3

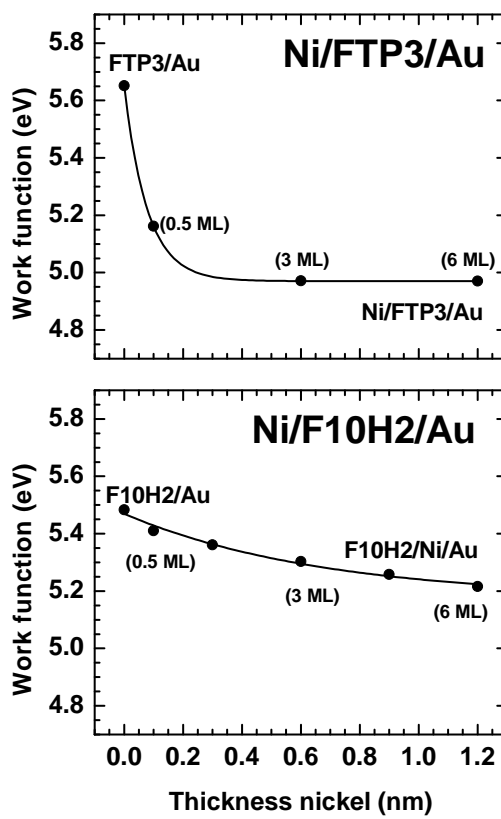


Figure 7.3: Variation of the work function of fluorinated SAMs as a function of nickel thickness. The absolute value of the work function was calculated as explained in section 4.4.4.

	HOMO (theory)	HOMO (expt.)	$\Delta\Phi$
FTP3	-6.97	-3.5	+0.6
ip-TP3	-5.41	-1.9	-0.8
oop-TP3	-5.66	-1.9	-0.8
TPT	-5.28	-1.6	-1.0
AnT3	-5.14	-1.3	-1.0

Table 7.1: Comparison of the change in work function and HOMO for various aryl SAMs. The work function ($\Delta\Phi$) was measured using a Kelvin probe and is given with respect to gold. The theoretical HOMO values were calculated at the B3LYP/631*-G level of theory using the Orca 2.8 software package (F. Neese, TU Bonn). The experimental values were obtained from UPS measurements carried out by the group of Pr. Dowben^a. Note that the difference between calculated (gas phase) and experimental (on Au) values is constant at 3.6 ± 0.1 eV. This is consistent with previous calculations.^{65,66} All values are in eV.

nickel surface) after deposition of $\sim 4 \text{ \AA}$. This result can be interpreted in two ways.

First, as for K/C12/Au, pinning of the energy levels occurs. The initial drop is less important for Ni/FTP3/Au than that for the K/C12/Au system at similar metal doses²⁹⁰ reflecting the differences in work function between nickel (5.0 eV) and potassium (2.0 eV). However, the levelling off behaviour occurs at the same metal dose for both systems ($\sim 2 \times 10^{14} \text{ atoms/cm}^2$). It is our opinion that the agreement between the K/C12/Au and Ni/FTP3/Au data is fortuitous. Indeed, measurements on the F10H2 system, a fluorinated analogue to C12, do not show this good of an agreement. Second, the drop in work function is due to the formation of a top nickel layer. This interpretation is supported by our own spectroscopic data presented in section 6.5 as well as literature data.⁵³ Further evidence is brought by the change in work function as a function of sputtering time (figure 7.4). Whereas sputtering of a Ni/F10H2/Au system yields a clean nickel surface within the first minute of sputtering (figure 7.4, bottom panel), the work function of Ni/FTP3/Au hardly changes over the first minute of sputtering (figure 7.4, top panel), suggesting the formation of a stable metal film several monolayers thick on top of the FTP3 monolayer, consistent with XPS data (section 6.5).

7.1.2.2 Summary

The deposition of nickel on FTP3/Au and F10H2/Au modifies, as expected, the work function of the films. The behaviour of the alkyl F10H2 and the aromatic FTP3 monolayers are radically different. We have shown that while the work function of F10H2/Au changes monotonously with metal dose, in the case of FTP3/Au it drops sharply at low coverages (< 1 monolayers) and levels off at high coverages (from 2 to 6 monolayers). This, together with sputtering and XPS data (section 6.5) suggests the formation of a few monolayer thick metal film on top of the pristine FTP3 SAMs. By contrast, penetration of nickel to the SAM-substrate interface predominates for the alkyl F10H2/Au film. Further investigation of these systems is under way.

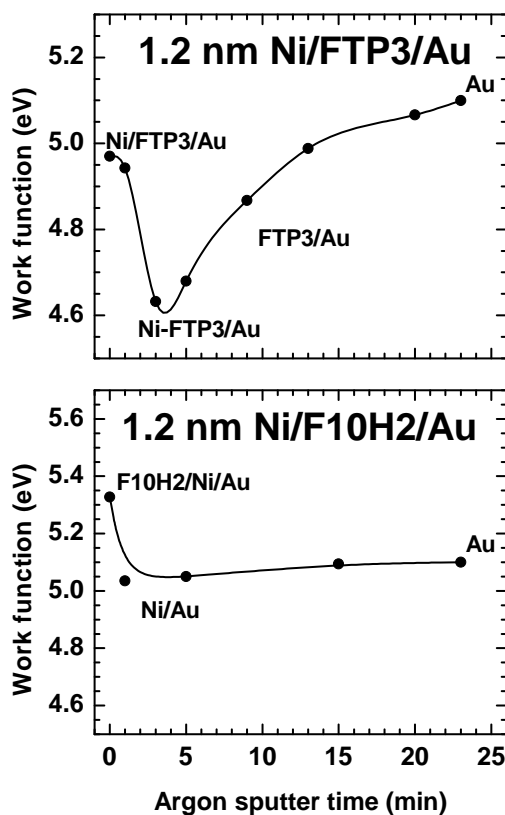


Figure 7.4: Variation of the work function of the Ni/FSAM/Au system as a function of sputtering time. The films were sputtered using 6 keV Ar^+ ions. The absolute value of the work function was calculated as explained in section 3.9.

7.2 Nanoparticles on crosslinked SAMs

7.2.1 Introduction

Pristine and crosslinked self-assembled monolayers can be used to immobilise nanoparticles (NPs)^{291–293} thus forming a NP/SAM/Au assembly which could be used either as-is for nanoelectronics or, our original idea, as seeds for the fabrication of metal films on top of self-assembled monolayers. We hypothesise that, given a close-packed arrangement of the particles, a single monolayer of NPs could efficiently stop metal penetration through the SAM. The drawback of this method would be that the thickness of the metal film would be governed by the diameter of the nanoparticles. SAMs should be stiff enough to prevent penetration of the nanoparticles to the SAM-substrate interface.

Here we propose to use pyridine and thiol terminated self-assembled monolayers for nanoparticle immobilisation. We will focus on the effect of the pre-treatment of the SAMs with electrons on the immobilisation of NPs. Cobalt nanoparticles were used as test system since they have a narrow particle size distribution and their magnetic properties make them potentially useful for

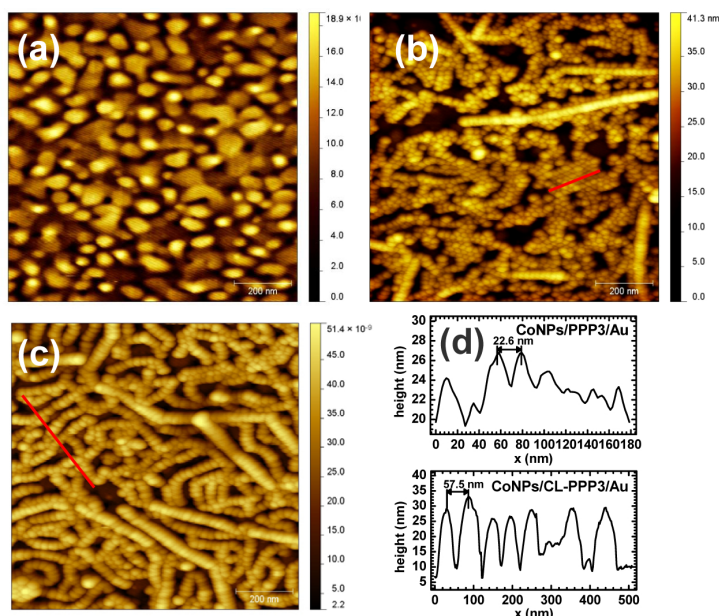


Figure 7.5: AFM images of cobalt nanoparticles on PPP3 and CL-PPP3. (a) PPP3, no nanoparticles, (b) cobalt nanoparticles on pristine PPP3, (c) cobalt nanoparticles on crosslinked PPP3 (30 mC/cm², 10 eV), (d) height profiles for the PPP3 and CL-PPP3 samples. The lines for the height profiles are marked in red in panels (b) and (c) respectively. Incubation time in the nanoparticle solution: 2.25 h at room temperature in all cases.

spintronic applications.^c Furthermore, pyridine and thiols are good ligands for cobalt.

7.2.2 Pyridine terminated monolayers for nanoparticle immobilisation

Figures 7.5 and 7.6 show AFM and SEM images of the immobilisation of cobalt nanoparticles (CoNPs) onto PPP3 and CL-PPP3 (30 mC/cm²). Cobalt nanoparticles adsorb readily on both PPP3 and CL-PPP3 albeit with some differences. As can be seen from panels (c) and (d) in figure 7.6, the packing density of the particles is slightly higher for the crosslinked SAMs. This has been confirmed by UV/Vis measurements of the various CoNP covered PPP3/Au surfaces (data not shown). We surmise that this stems from the marked difference in the packing of the nanoparticles as seen in panels (b) and (c) of figure 7.5 and panels (a) and (b) of figure 7.6. The particles aggregate to form mainly large hexagonally packed domains on the pristine films, owing to the weak Co-N interaction, whereas on the crosslinked SAMs, chain-like superstructures are formed, seemingly following a path. It is not clear at this point what causes this behaviour and further studies would be required to fully understand the mechanism behind this process. However, since the SAM-ambient interface of PPPn monolayers are not significantly modified upon irradiation (section 5.2), i.e. the top nitrogen is retained, we do not expect this effect to be related to a change in the surface chemistry. Furthermore, we would expect any change in surface chemistry to be random and not directed as they appear in our case. As seen in the AFM images

^cCobalt nanoparticles courtesy of Dr. Jianli Zhao.

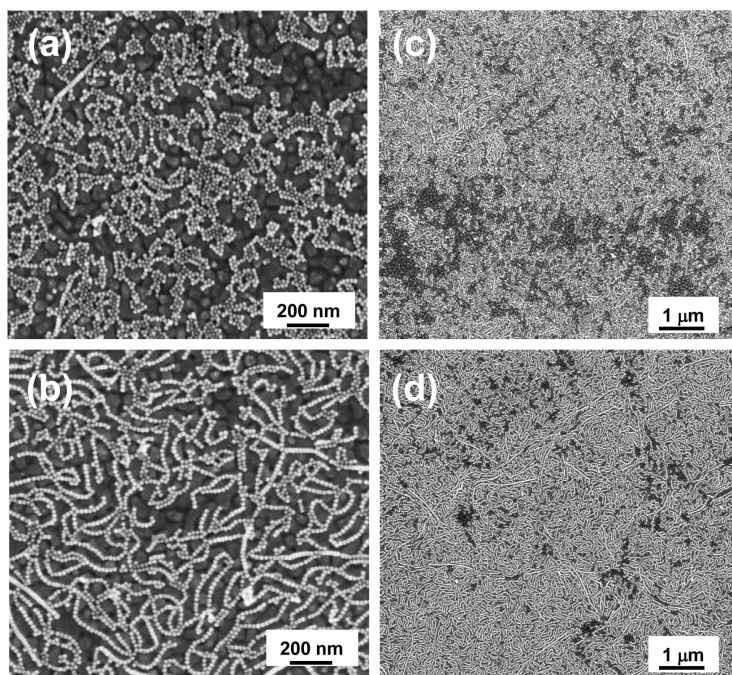


Figure 7.6: SEM images of cobalt nanoparticles on PPP3 and CL-PPP3. (a) and (c) cobalt nanoparticles on pristine PPP3, (b) and (d) cobalt nanoparticles on crosslinked PPP3 (30 mC/cm², 10 eV). Incubation time in the nanoparticle solution: 2.25 h at room temperature in all cases.

(figure 7.5), the particles form mainly monolayers with only a small portion of aggregates. This is significant for technological applications since such aggregates are expected to significantly alter the performance of any potential device. It should be noted that this experiment was repeated with different samples and the same results were obtained.

7.2.3 Thiol terminated monolayers for nanoparticle immobilisation

TPDMT monolayers were used to investigate the immobilisation of cobalt nanoparticles on thiol-terminated SAMs (figure 7.7). The mechanism of attachment to TPDMT is expected to be different from that of PPP3 since, unlike pyridine, covalent bonds are easily formed between cobalt and sulphur. It is therefore reasonable to assume that CoNPs will settle on the TPDMT surface and lose their mobility. The distribution of particles should then be more random and large, well-packed domains, as seen for PPP3 SAMs, are not expected. This is shown in figure 7.7(a) where only small domains can be seen and the particles are mainly randomly arranged. Even though about half of the binding sites are lost upon electron irradiation,²⁶ the density of particles, as for the PPP3 system, seems slightly improved after the irradiation treatment. This can partly be explained by comparing the size of the particles with that of a TPDMT molecule. Although one in two thiol is lost, the particles are big enough (~ 20 nm in diameter whereas the thiol-thiol distance is about 0.5 nm) to fill the void and therefore the loss of thiol is inconsequential for the packing of nanoparticles on SAMs. Note that unlike CL-PPP3 films, no

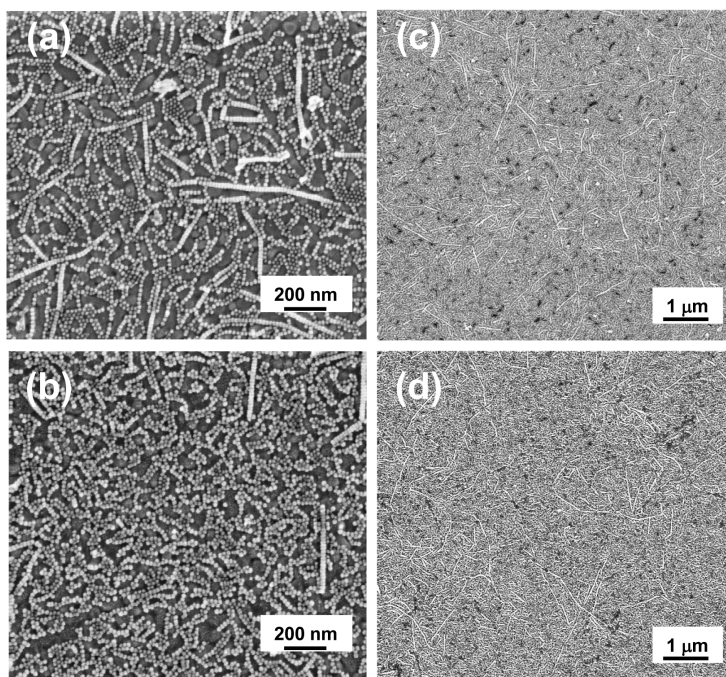


Figure 7.7: SEM images of cobalt nanoparticles on TPDMT and CL-TPDMT. (a) and (c) cobalt nanoparticles on pristine TPDMT, (b) and (d) cobalt nanoparticles on crosslinked TPDMT (30 mC/cm², 10 eV). Incubation time in nanoparticle solution: 2.25 h at room temperature in all cases.

change in the preferred adsorption sites of the particles is observed for CL-TPDMT monolayers, as expected for a random modification of the TPDMT monolayer by electrons.

7.2.4 Nanoparticles as seeds for metal films on top of self-assembled monolayers

Preliminary experiments on the use of nanoparticles to stop metal penetration through SAMs were conducted. Nanoparticles could be used as seeds for metal film deposition. The Ni/NPs/SAM assemblies were characterised by XPS (data not shown). The adsorption of nanoparticles results in a rough surface which influences the XPS results.^{294,295} It is not clear to us at this point what the effect is and how to account for it. Therefore, we are not able to reliably interpret the XPS data at this time. A better method may be to use NEXAFS spectroscopy and monitor the change in molecular orientation.²⁶ However, the cobalt nanoparticles are covered by long aliphatic chains that complicate the interpretation of the data by obscuring the C1s $\rightarrow \pi^*$ transition characteristic of the terphenyl units. More experiments would be required to ascertain the validity of this method.

7.2.5 Summary

Cobalt nanoparticles, which could be important for magnetic applications, can be adsorbed on pyridine and thiol terminated SAMs. For both systems, the pristine and crosslinked films are

suitable. The crosslinked films induced a slight improvement in the particle packing density. Only one monolayer of particles was adsorbed with only small amounts of aggregates in all cases. Improved preparation procedures such as changing the substrate should yield better nanoparticle films making them useful for potential electronic and sensor applications. Unfortunately, the stability of metal films evaporated on CoNPs/SAM/Au assemblies could not be reliably tested.

7.3 SAM-Metal-SAM-Metal assemblies

7.3.1 Introduction

As seen previously, SAMs afford unique opportunities to tune a metal's work function. At the same time, SAMs can be used to protect the metal from oxidation. In addition, the ability to form a well-packed self-assembled monolayer on top of a Metal-SAM-Metal (MSM) assembly is essential for the fabrication of multilayer devices. In this section we will present our first attempt at fabricating a SAM-Metal-SAM-Metal (SMSM) assembly. The system was based on FTPn monolayers.

7.3.2 SMSM systems based on FTP3 and nickel.

The systems were constructed as follows:

- bottom contact: 100 nm gold on silicon wafer
- dielectric: FTP3 monolayer, 30mC/cm² at 10 eV
- top contact: nickel, 1.2 nm deposited by e-beam evaporation
- SAM: FTP2, 24 h in THF (not degassed)

The C1s XPS spectra of the different steps in the preparation of the SMSM assembly are shown in the top panel of figure 7.8 along with the C1s spectra at various sputtering times (bottom panel). The immobilisation of FTP2 on nickel is evidenced by the overall rise in the carbon intensity in general and the sharp rise in the CF peak intensity in particular. Further evidence is provided by collecting XPS spectra during the course of a sputtering treatment (1 keV He⁺). Comparing these spectra to that of Ni/CL-FTP3/Au, one can see that the top monolayer is sputtered away after about 20 minutes under our conditions. This is in line with ion scattering spectroscopy data acquired for alkanethiols on gold.²²⁵ It should be noted that well-ordered terphenyl-based monolayers are sputtered away much less rapidly than their alkanethiol counterparts (a factor of 2-3 times slower is typically observed)^{26,225} indicating that the top SAM in our SMSM assembly is not well-ordered. This was confirmed by extrapolating the XPS spectrum for FTP2/Ni and comparing it with that of a pristine FTP2/Au monolayer (figure 7.9). The lower CF/CC ratio for FTP2/Ni and the difference in the shape of the spectra at the lower binding energy side are clear evidence of a disordered SAM. Note that increasing the incubation time past 24 h did not afford a better monolayer leading us to believe that the nickel film might have oxidised during adsorption of the SAM. This was confirmed by XPS (data not shown). The XPS results were supported by contact angle goniometry data. As can be seen from figure 7.10, the deposition of nickel lead to a dramatic decrease in the water contact angle (WCA) from ~80° down to ~30°. Upon adsorption of FTP2, the water contact angle dramatically increased to ~74°, indicating the formation of a hydrophobic monolayer on top of nickel. However, the WCA of a well-ordered

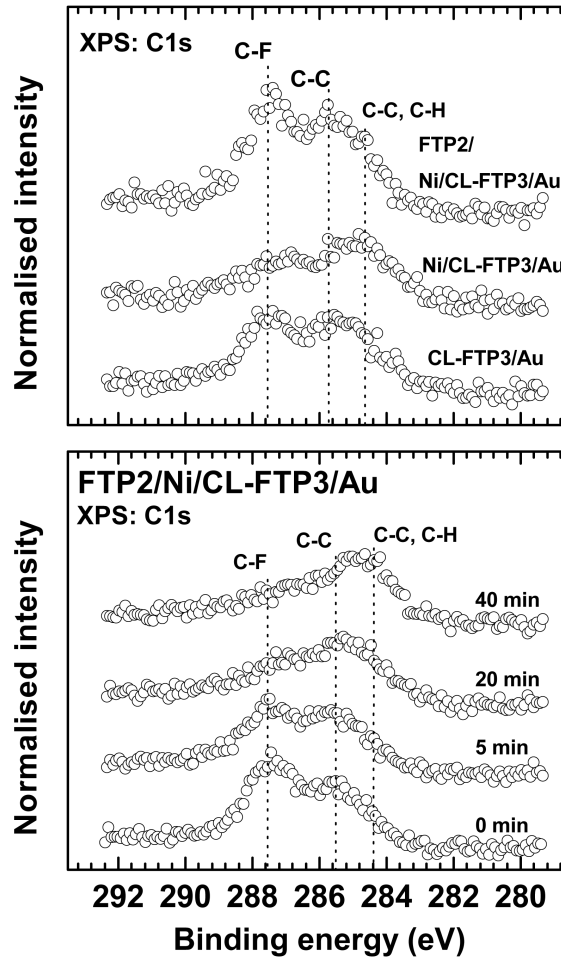


Figure 7.8: XPS C1s spectra of the different stages of the fabrication of an SMSM assembly. Top panel: Assembly of the SAM-Metal-SAM-metal system. Bottom panel: XPS C1s spectra of the SMSM assembly after various sputtering times. The system was sputtered with 1000 eV He^+ ions. The pressure in the measurement chamber was 10^{-8} mbar during sputtering. The extractor current was $3.5 \mu\text{A}$. All spectra were normalised at 285.55 eV.

FTP2 monolayer on gold is about 110° implying, in accordance with our C 1s XPS data, that the SAM on the top nickel contact is disordered. We have no doubt that improving on the preparation conditions (e.g. SAM formation under inert atmosphere) should yield better SAMs.

7.3.3 Summary

We have shown, using CL-FTP3 as bottom SAM, nickel as top metal contact and FTP2 as the top SAM, that the fabrication of SMSM is possible. Provided that care is taken during the preparation, such SAM-metal-SAM-metal assemblies could find use in a variety of applications such as spintronic devices.

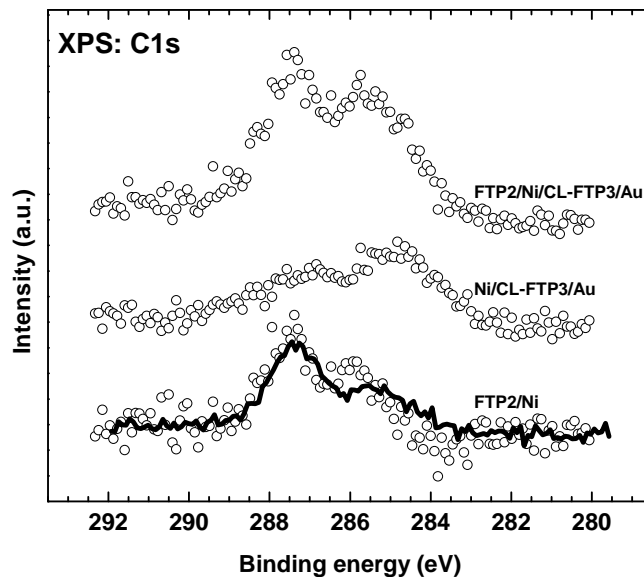


Figure 7.9: Extrapolation of the FTP2/Ni XPS C1s spectrum. The extrapolated spectrum was obtained by subtracting the XPS C1s spectrum of Ni/CL-FTP3/Au (middle spectrum) from that of the SMSM assembly (top spectrum). The spectrum of a pristine FTP2/Au film is shown as a black solid line for comparison.

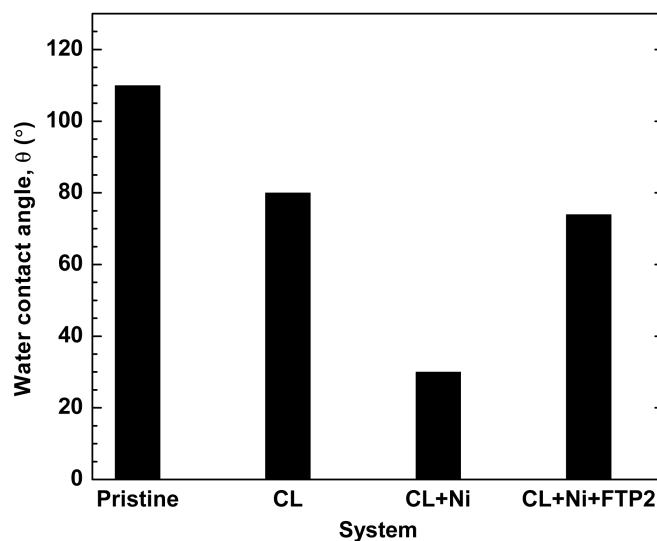


Figure 7.10: Water contact angles at different stages of the fabrication of an SMSM assembly.

Chapter 8

Conclusion

Using a combination of X-ray Photoelectron Spectroscopy (XPS), Near-Edge X-ray Absorption Fine Structure (NEXAFS) spectroscopy, Ultraviolet Photoelectron Spectroscopy (UPS), Inverse Photoelectron Spectroscopy (IPES), InfraRed Reflection Absorption Spectroscopy (IR-RAS) and Kelvin-probe (KP) measurements, we have studied two new series of molecules, namely (4'-(pyridin-4-yl)biphenyl-4-yl)alkanethiol (PPPn, $n = 1,3$) and perfluoroterphenyl-substituted alkanethiols (FTPn, $n = 2,3$), for use as dielectric layers in Metal-Insulator-Metal (MIM) assemblies. [1,1':4',1''-terphenyl]-4,4''-dimethanethiol (TPDMT) SAMs^{26,27,65} were used as reference. All molecules were found to form well packed, highly ordered monolayers, a pre-requisite for use in nano electronic devices. In addition, the electronic structure of a series of well-defined SAMs with *p*-terphenyl and anthracene backbones was studied. The width of the HOMO-LUMO gap was found to depend on the identity of the aromatic backbone, being smallest for the strongly conjugated anthracene moiety and widest for the perfluorinated terphenyl unit. In contrast, the offset of this gap, and especially the position of the HOMO orbital, correlated well with the interfacial dipole which could be monitored by WF measurements. In the case of the perfluorinated terphenyl (FTP3), which is characterised by a comparatively large upward molecular dipole, this resulted in a significant downward shift of the occupied electronic states with respect to the Fermi level (chemical potential), so that the film became more n-type than the corresponding non-fluorinated systems. Comparison of the DFT calculations of the gas-phase molecules with experimental UPS-IPES data suggested that the small aliphatic linker found in all but one of the systems studied acted as an insulator, effectively decoupling the aromatic core's electronic system from the surface.

Monolayers of PPPn and FTPn on gold (PPPn/Au and FTPn/Au respectively) were treated with electrons. We have shown, using SAMs of hexanethiol (C6) and dodecanethiol (C12) as examples, that irradiation of SAMs with electrons results in a variety of complex and interrelated processes. The branching of these processes was found to be dependant upon the chain length of the molecules with desorption of molecular fragments dominating for short chain alkanethiols and bond scission dominating for long chain alkanethiols. Importantly, most bond breaking events were found to occur at the topmost part of the film. These results have potential implication for the use of alkanethiols as resists for electron beam lithography.

Whereas loss of carbon fragments dominates in the case of alkanethiols during electron irradiation, terphenyl-based molecules are crosslinked, forming 2D quasi-polymeric films (denoted with the prefix CL-). In particular, we have studied the electron irradiation of PPPn/Au and FTPn/Au SAMs.

The effects of low energy electron irradiation (50 eV) on PPP1/Au films were studied using

IRRAS, XPS and NEXAFS spectroscopy. The films exhibited a range of behaviours typical of terphenyl thiols such as moderate loss of molecular orientation and damage to the SAM-substrate interface as well as a lack of molecular desorption upon irradiation. In addition, PPP1 was found to undergo irradiation-induced processes that, to the best of our knowledge, have so far not been reported. In particular, close examination of the N1s XPS spectra revealed, in addition to crosslinking, the formation of reduced pyridine species such as 1,4-dihydropyridine upon electron irradiation. The rate of change was rapid with the saturation behaviour being reached at about 25 mC/cm^2 , much lower than the biphenyl and terphenyl systems ($45\text{--}50 \text{ mC/cm}^2$).^{26,202} This was presumably due to the increased electron affinity of pyridine compared to benzene and could lead to reduced device fabrication times. The terminal nitrogen was found to survive the irradiation treatment and as such CL-PPP1/Au films, in contrast to CL-TPDMT films, provide a high density of sites for the nucleation of metal thin films. The extent of crosslinking was also estimated from the N1s XPS data to be 70–80 % (20–30 % of non-crosslinked pyridine).

Similarly to PPPn/Au monolayers, the FTPn films mimic the typical behaviour of aromatic hydrocarbon SAMs under ionising radiation, i.e. these systems exhibit a clear dominance of cross-linking between the individual molecular species over their decomposition making them negative resists for lithographic applications. The cross-linking process follows the cleavage of the primary C-F bonds in the FTP moieties, which, along with the comparably rapid loss of orientational and conformational order of the individual molecules, is the dominant irradiation-induced process in the FTPn SAMs. C-F bond cleavage, followed by the desorption of fluorine in atomic or ionic form, represents an exclusive pathway of fluorine release in the FTPn films, in striking contrast to fluorocarbon aliphatic monolayers (F10H2) where the major channel for such a release is the desorption of fluorocarbon fragments. In addition to desorption, a small fraction of the fluorine atoms released from the cleavage of C-F bonds remain trapped in the matrix as CF_2 species. Both FTPn films studied ($n = 2,3$) react similarly towards ionising radiation, the only differences being a lower stability of the headgroup-substrate interface in the less densely packed FTP2 SAMs and the faster loss of orientational and conformational order in FTP2/Au film as compared to FTP3/Au monolayers.¹¹⁰

Nickel was evaporated onto electron irradiated PPPn, FTPn and TPDMT as well as on pristine FTPn. The organometallic films were investigated using XPS and NEXAFS spectroscopy. Despite our best efforts, nickel penetration into and through the SAMs was found to prevail for the CL-PPPN/Au and CL-TPDMT/Au systems, even at low nickel doses ($\sim 0.1 \text{ nm}$), with only ~ 35 and 45 % of the total deposited nickel immobilised on top of CL-TPDMT/Au and CL-PPPN/Au respectively. Along with metal penetration, the electronic structure of the carbon matrix was modified by the insertion of nickel in the matrix. Furthermore, the HRXPS S2p spectra of Ni/CL-TPDMT/Au and Ni/CL-PPPN/Au revealed a shift of the thiolate peak to lower binding energies compared to thiolates on gold (-0.26 and -0.4 eV respectively). This was used as a marker for nickel penetration for the other mercaptan molecules in this study. The observed nickel penetration through CL-TPDMT/Au was in stark contrast with the data collected previously in our laboratory.^{26,27} It is not clear to us at this time why such a discrepancy should occur and careful re-evaluation of both datasets is under way.

In addition, pyridine and thiol terminated terphenyl SAMs (CL-PPP3 and TPDMT respectively) were used as substrates for the immobilisation of palladium on self-assembled monolayers. Palladium was found, by XPS and NEXAFS spectroscopy, to reside at the top of the monolayer without significantly penetrating through the SAMs. Furthermore, these systems were used as substrates for e-beam metal evaporation. Upon evaporation, a stable metal layer was formed at the SAM-ambient interface with palladium atoms acting as seeds, regardless of the nature of the

bond between palladium and the monolayer (covalent (TPDMT) or coordinated (CL-PPP3)). Thus, palladium chloride was able to fully stop the penetration of ferromagnetic metals (nickel in our case) into and through ultrathin organic films (≤ 3 nm), a critical step toward the fabrication of SAM-based nanoelectronic devices. Most importantly, using TPDMT, pristine monolayers could be used for e-beam evaporation thus eliminating the time-consuming crosslinking step usually required to stop metal penetration through such thin films.^{26,27} This opens the door to the use of the many commercially available dithiol molecules for use as dielectric layers in SAM-based nanojunctions, in particular the aliphatic ones which are readily and cheaply available from commercial sources. Furthermore, this method could be used in conjunction with the electron beam chemical lithography²² and UV-Vis chemical lithography²³ methods developed in our laboratory to rapidly and cheaply pattern nano-circuits onto gold wafers.

Finally, using XPS and NEXAFS spectroscopy, we have demonstrated that FTP3 monolayers can prevent nickel penetration via insertion of the nickel atoms into carbon-fluorine bonds. The attachment of nickel was found to take place primarily at the top of the monolayer (figure 6.34). Similar results were obtained for a substrate incubation time (in FTP3 solution) of two hours. FTP3's alkyl counterpart, F10H2, did not efficiently prevent metal penetration leading to extensive damage to the SAM-substrate interface. Similarly, TP3, a hydrocarbon analogue of FTP3 did not significantly prevent metal penetration and, unlike FTP3, only traces of metal could be detected at the SAM-ambient interface. Metal-SAM-metal (MSM) assemblies with a top metal thickness of up to 1.8 nm were successfully fabricated, as evidenced by X-ray spectroscopy. Critically, this could be achieved without electron irradiation. In addition, FTP3/Au SAMs irradiated with various electron doses (30 and 60 mC/cm²) were found to prevent metal penetration to a higher degree than their pristine counterparts. This, combined with the ability to fine-tune the transport properties of the FTPn films by electron irradiation makes FTPn/Au films attractive for the fabrication of tailored nanoelectronic devices, e.g. as nanojunctions in spintronic devices.

It is my opinion that the two new techniques developed during the course of this doctoral work, namely palladium-ferromagnetic metal alloying and reaction of ferromagnetic metals with aromatic fluorocarbons, could be powerful new tools for the fabrication of SAM-based nanojunctions for spintronic devices, especially if combined with the e-beam and/or UV-Visible lithography techniques (e.g. using alkanethiol resists) developed in our institute.

List of abbreviations

Abbreviation	Definition
---------------------	-------------------

Molecules

C6	hexadecanethiol
C12	dodecanethiol
DDT	dodecanethiol
TP3	<i>p</i> -terphenylpropanethiol
PPP1	(4'-(pyridin-4-yl)biphenyl-4-yl)methanethiol
PPP3	3-(4'-(pyridin-4-yl)biphenyl-4-yl)propane-1-thiol
TPDMT	[1,1':4',1''-terphenyl]-4,4''-dimethanethiol
FTP2	2-(Perfluoroterphenyl-4-yl)ethane-1-thiol
FTP3	3-(Perfluoroterphenyl-4-yl)propane-1-thiol
F10H2	3,3,4,4,5,5,6,6,7,7,8,8,9,9,10,10,11,11,12,12,12-henicosafuorododecane-1-thiol
CL-PPP1	electron irradiated PPP1
CL-PPP3	electron irradiated PPP3
CL-TPDMT	electron irradiated TPDMT
CL-FTP2	electron irradiated FTP2
CL-FTP3	electron irradiated FTP3
THF	Tetrahydrofuran
AcOH	Acetic acid

Techniques

XPS	X-ray Photoelectron Spectroscopy
HRXPS	High Resolution XPS
ARXPS	Angle-Resolved XPS
ERXPS	Energy-Resolved XPS
NEXAFS	Near Edge X-ray Absorption Fine Structure
UPS	Ultraviolet Photoelectron Spectroscopy
IPES	Inverse PhotoElectron Spectroscopy
IRRAS	InfraRed Reflection Absorption Spectroscopy
FT-IR	Fourier Transform InfraRed
STM	Scanning Tunnelling Microscopy
ISS	Ion Scattering Spectroscopy
KP	Kelvin Probe
QCM	Quartz Crystal Microbalance

Abbreviation	Definition
--------------	------------

<u>Miscellaneous</u>	
----------------------	--

SAM	Self-Assembled Monolayer
AT	Alkanethiol
ML	MonoLayer
UHV	Ultra High Vacuum
Φ	Work function
WF	Work function
IP	Ionisation potential
eV	electron volt
BE	Binding Energy
KE	Kinetic Energy
CRR	Constant Retardation Ratio
DFT	Density Functional Theory
HOMO	Highest Occupied Molecular Orbital
LUMO	Lowest Occupied Molecular Orbital
DOS	Density of State
E_F	Fermi level
UV	Ultraviolet
UV/Vis	Ultraviolet/Visible
PVD	Physical Vapour Deposition
TPD	Temperature Programmed Desorption
WCA	Water Contact Angle

Bibliography

- [1] Reed, M. A.; Zhou, C.; Muller, C. J.; Burgin, T. P.; Tour, J. M. *Science* **1997**, *278*, 252–254.
- [2] Collier, C. P.; Wong, E. W.; Belohradsk, M.; Raymo, F. M.; Stoddart, J. F.; Kuekes, P. J.; Williams, R. S.; Heath, J. R. *Science* **1999**, *285*, 391–394.
- [3] Joachim, C.; Gimzewski, J. K.; Aviram, A. *Nature* **2000**, *408*, 541–548.
- [4] Akkerman, H. B.; Blom, P. W. M.; de Leeuw, D. M.; de Boer, B. *Nature* **2006**, *441*, 69–72.
- [5] Simmons, J. G. *J. Appl. Phys.* **1964**, *35*, 2472–2481.
- [6] Simmons, J. G. *J. Appl. Phys.* **1963**, *34*, 238–239.
- [7] Cowell, E. W.; Alimardani, N.; Knutson, C. C.; Conley, J. F.; Keszler, D. A.; Gibbons, B. J.; Wager, J. F. *Adv. Mater.* **2011**, *23*, 74–78.
- [8] Wolf, S. A.; Awschalom, D. D.; Buhrman, R. A.; Daughton, J. M.; von Molnr, S.; Roukes, M. L.; Chtchelkanova, A. Y.; Treger, D. M. *Science* **2001**, *294*, 1488–1495.
- [9] Awschalom, D. D.; Flatte, M. E. *Nat. Phys.* **2007**, *3*, 153–159.
- [10] Grossman, E. N.; Harvey, T. E.; Reintsema, C. D. *J. Appl. Phys.* **2002**, *91*, 10134–10139.
- [11] Drew, A. J. et al. *Nat. Mater.* **2009**, *8*, 109–114.
- [12] Schulz, L. et al. *Nat. Mater.* **2011**, *10*, 39–44.
- [13] Pramanik, C.-G. P. S. B. S. . G. K. H. N., S.; Stefanita; Cahay, M. *Nat. Nano.* **2007**, *2*, 216–219.
- [14] Shaporenko, A.; Brunnbauer, M.; Terfort, A.; Johansson, L. S. O.; Grunze, M.; Zharnikov, M. *Langmuir* **2005**, *21*, 4370–4375.
- [15] Shaporenko, A.; Brunnbauer, M.; Terfort, A.; Grunze, M.; Zharnikov, M. *J. Phys. Chem. B* **2004**, *108*, 14462–14469.
- [16] Frey, S.; Shaporenko, A.; Zharnikov, M.; Harder, P.; Allara, D. *J. Phys. Chem. B* **2003**, *107*, 7716–7725.
- [17] Silien, C.; Buck, M.; Goretzki, G.; Lahaye, D.; Champness, N. R.; Weidner, T.; Zharnikov, M. *Langmuir* **2009**, *25*, 959–967.

- [18] Shaporenko, A.; Elbing, M.; Baszczyk, A.; von Hnisch, C.; Mayor, M.; Zharnikov, M. *J. Phys. Chem. B* **2006**, *110*, 4307–4317.
- [19] Heister, K.; Zharnikov, M.; Grunze, M.; Johansson, L. S. O. *J. Phys. Chem. B* **2001**, *105*, 4058–4061.
- [20] Chesneau, F.; Zhao, J.; Shen, C.; Buck, M.; Zharnikov, M. *J. Phys. Chem. C* **2010**, *114*, 7112–7119.
- [21] Chesneau, F.; Schupbach, B.; Szelagowska-Kunstman, K.; Ballav, N.; Cyganik, P.; Terfort, A.; Zharnikov, M. *Phys. Chem. Chem. Phys.* **2010**, *12*, 12123–12137.
- [22] Ballav, N.; Schilp, S.; Zharnikov, M. *Angew. Chem. Inter. Ed.* **2008**, *47*, 1421–1424.
- [23] Ballav, N.; Weidner, T.; Zharnikov, M. *J. Phys. Chem. C* **2007**, *111*, 12002–12010.
- [24] Goelzhaeuser, A.; Eck, W.; Geyer, W.; Stadler, V.; Weimann, T.; Hinze, P.; Grunze, M. *Advanced Materials* **2001**, *13*, 803–806.
- [25] Aswal, D. K.; Petit, C.; Salace, G.; Gurin, D.; Lenfant, S.; Yakhmi, J. V.; Vuillaume, D. *physica status solidi (a)* **2006**, *203*, 1464–1469.
- [26] Tai, Y.; Shaporenko, A.; Noda, H.; Grunze, M.; Zharnikov, M. *Advanced Materials* **2005**, *17*, 1745–1749.
- [27] Tai, Y.; Shaporenko, A.; Grunze, M.; Zharnikov, M. *J. Phys. Chem. B* **2005**, *109*, 19411–19415.
- [28] Akkerman, H. B.; Kronemeijer, A. J.; van Hal, P. A.; de Leeuw, D. M.; Blom, P. W. M.; de Boer, B. *Small* **2008**, *4*, 100–104.
- [29] Zhitenev, N. B.; Erbe, A.; Meng, H.; Bao, Z. *Nanotechnology* **2003**, *14*, 254–257.
- [30] Nijhuis, C. A.; Reus, W. F.; Whitesides, G. M. *J. Am. Chem. Soc.* **2009**, *131*, 17814–17827.
- [31] Holmlin, R. E.; Haag, R.; Chabiny, M. L.; Ismagilov, R. F.; Cohen, A. E.; Terfort, A.; Rampi, M. A.; Whitesides, G. M. *J. Am. Chem. Soc.* **2001**, *123*, 5075–5085.
- [32] Haick, H.; Niitsoo, O.; Ghabboun, J.; Cahen, D. *J. Phys. Chem. C* **2007**, *111*, 2318–2329.
- [33] Cai, L.; Skulason, H.; Kushmerick, J.; Pollack, S.; Naciri, J.; Shashidhar, R.; Allara, D.; Mallouk, T.; Mayer, T. *J. Phys. Chem. B* **2004**, *108*, 2827–2832.
- [34] Seitz, O.; Dai, M.; Aguirre-Tostado, F. S.; Wallace, R. M.; Chabal, Y. J. *J. Am. Chem. Soc.* **2009**, *131*, 18159–18167.
- [35] Love, J. C.; Estroff, L. A.; Kriebel, J. K.; Nuzzo, R. G.; Whitesides, G. M. *Chem. Rev.* **2005**, *105*, 1103–1169.
- [36] Liu, Y.-J.; Yu, H.-Z. *ChemPhysChem* **2003**, *4*, 335–342.
- [37] Kueller, A.; El-Desawy, M. A.; Stadler, V.; Geyer, W.; Eck, W.; Goelzhaeuser, A. *J. Vac. Sci. Technol. B* **2004**, *22*, 1114–1117.

- [38] Kueller, A.; Eck, W.; Stadler, V.; Geyer, W.; Goelzhaeuser, A. *Appl. Phys. Lett.* **2003**, *82*, 3776–3778.
- [39] Mekhalif, Z.; Laffineur, F.; Couturier, N.; Delhalle, J. *Langmuir* **2003**, *19*, 637–645.
- [40] Mekhalif, Z.; Lazarescu, A.; Hevesi, L.; Pireaux, J. J.; Delhalle, J. *J. Mater. Chem.* **1998**, *8*, 545–551.
- [41] Mekhalif, Z.; Riga, J.; Pireaux, J.-J.; Delhalle, J. *Langmuir* **1997**, *13*, 2285–2290.
- [42] Tortech, L.; Mekhalif, Z.; Delhalle, J.; Guittard, F.; Gribaldi, S. *Thin Solid Films* **2005**, *491*, 253–259.
- [43] Amato, C.; Devillers, S.; Calas, P.; Delhalle, J.; Mekhalif, Z. *Langmuir* **2008**, *24*, 10879–10886.
- [44] Fonder, G.; Cecchet, F.; Peremans, A.; Thiry, P.; Delhalle, J.; Mekhalif, Z. *Surf. Sci.* **2009**, *603*, 2276–2282.
- [45] Fonder, G.; Laffineur, F.; Delhalle, J.; Mekhalif, Z. *J. Colloid Interface Sci.* **2008**, *326*, 333–338.
- [46] Karthaeuser, S. *J. Phys.: Condens. Matter* **2011**, *23*, 013001–.
- [47] Li, F.; Zhou, Y.; Zhang, F.; Liu, X.; Zhan, Y.; Fahlman, M. *Chem. Mater.* **2009**, *21*, 2798–2802.
- [48] Li, H.; Duan, Y.; Paramonov, P.; Coropceanu, V.; Brdas, J.-L. *J. Electron Spectrosc. Relat. Phenom.* **2009**, *174*, 70–77.
- [49] Schalnatz, M. C.; Pemberton, J. E. *Langmuir* **2010**, *26*, 11862–11869.
- [50] Campbell, I. H.; Kress, J. D.; Martin, R. L.; Smith, D. L.; Barashkov, N. N.; Ferraris, J. P. *Appl. Phys. Lett.* **1997**, *71*, 3528–3530.
- [51] Campbell, I. H.; Rubin, S.; Zawodzinski, T. A.; Kress, J. D.; Martin, R. L.; Smith, D. L.; Barashkov, N. N.; Ferraris, J. P. *Phys. Rev. B* **1996**, *54*, R14321.
- [52] deBoer, B.; Frank, M.; Chabal, Y.; Jiang, W.; Garfunkel, E.; Bao, Z. *Langmuir* **2004**, *20*, 1539–1542.
- [53] Ahn, H.; Whitten, J. E. *J. Phys. Chem. B* **2003**, *107*, 6565–6572.
- [54] deBoer, B.; Hadipour, A.; Mandoc, M.; vanWoudenberg, T.; Blom, P. *Adv. Mater.* **2005**, *17*, 621–625.
- [55] Jung, D. R.; Czanderna, A. W. *Crit. Rev. Solid State Mater. Sci.* **1994**, *19*, 1–54.
- [56] Jung, D. R.; Czanderna, A. W.; Herdt, G. C. *J. Vac. Sci. Technol. A* **1996**, *14*, 1779–1787.
- [57] Ohgi, T.; Sheng, H. Y.; Dong, Z. C.; Nejoh, H. *Surf. Sci.* **1999**, *442*, 277–282.
- [58] Tai, Y.; Shaporenko, A.; Eck, W.; Grunze, M.; Zharnikov, M. *Appl. Phys. Lett.* **2004**, *85*, 6257–6259.

- [59] Manolova, M.; Ivanova, V.; Kolb, D.; Boyen, H.-G.; Ziemann, P.; Bttner, M.; Romanjuk, A.; Oelhafen, P. *Surf. Sci.* **2005**, *590*, 146–153.
- [60] Ivanova, V.; Baunach, T.; Kolb, D. M. *Electrochim. Acta* **2005**, *50*, 4283–4288.
- [61] Manolova, M.; Kayser, M.; Kolb, D.; Boyen, H.-G.; Ziemann, P.; Mayer, D.; Wirth, A. *Electrochim. Acta* **2007**, *52*, 2740–2745.
- [62] Baunach, T.; Ivanova, V.; Kolb, D. M.; Boyen, H.-G.; Ziemann, P.; Bttner, M.; Oelhafen, P. *Adv. Mater.* **2004**, *16*, 2024–2028.
- [63] Baunach, T.; Ivanova, V.; Scherson, D.; Kolb, D. *Langmuir* **2004**, *20*, 2797–2802.
- [64] Frey, S.; Rong, H.-T.; Heister, K.; Yang, Y.-J.; Buck, M.; Zharnikov, M. *Langmuir* **2002**, *18*, 3142–3150.
- [65] Feng, D.-Q.; Wisbey, D.; Losovyj, Y. B.; Tai, Y.; Zharnikov, M.; Dowben, P. A. *Phys. Rev. B* **2006**, *74*, 165425–11.
- [66] Feng, D.; Losovyj, Y.; Tai, Y.; Zharnikov, M.; Dowben, P. *J. Mater. Chem.* **2006**, *16*, 4343–4347.
- [67] Vlkel, B.; Kaltenpoth, G.; Handrea, M.; Sahre, M.; Nottbohm, C. T.; Kller, A.; Paul, A.; Kautek, W.; Eck, W.; Glzhuser, A. *Surf. Sci.* **2005**, *597*, 32–41.
- [68] Tai, Y.; Shaporenko, A.; Eck, W.; Grunze, M.; Zharnikov, M. *Langmuir* **2004**, *20*, 7166–7170.
- [69] Nottbohm, C. T.; Beyer, A.; Sologubenko, A. S.; Ennen, I.; Htten, A.; Rsner, H.; Eck, W.; Mayer, J.; Glzhuser, A. *Ultramicroscopy* **2008**, *108*, 885–892.
- [70] Geyer, W.; Stadler, V.; Eck, W.; Zharnikov, M.; Golzhauser, A.; Grunze, M. *Appl. Phys. Lett.* **1999**, *75*, 2401–2403.
- [71] Eck, W.; Stadler, V.; Geyer, W.; Zharnikov, M.; Goelzhaeuser, A.; Grunze, M. *Adv. Mater.* **2000**, *12*, 805–808.
- [72] Eck, W.; Kller, A.; Grunze, M.; Vlkel, B.; Glzhuser, A. *Adv. Mater.* **2005**, *17*, 2583–2587.
- [73] Cyganik, P.; Vandeweert, E.; Postawa, Z.; Bastiaansen, J.; Vervaecke, F.; Lievens, P.; Silverans, R. E.; Winograd, N. *J. Phys. Chem. B* **2005**, *109*, 5085–5094.
- [74] Cabrera-Sanfelix, P.; Arnau, A.; Sanchez-Portal, D. *Phys. Chem. Chem. Phys.* **2010**, *12*, 1578–1584.
- [75] Ratner, D., B.; Castner In *Surface Analysis The principal techniques*; Vickerman, J. C., Ed.; Wiley: Chichester, 1997.
- [76] Brundle, C.; Evans, C. A. J.; Wilson, S. *Encyclopedia of Materials Characterization - Surfaces, Interfaces, Thin Films*; Elsevier, 1992; pp –.
- [77] Scofield, J. H. *J. Electron Spectrosc. Relat. Phenom.* **1976**, *8*, 129–137.
- [78] Cumpson, P. J.; Seah, M. P. *Surf. Interface Anal.* **1997**, *25*, 430–446.

- [79] Jablonski, A. *Surf. Interface Anal.* **1994**, *21*, 758–763.
- [80] Seah, M. P. et al. *Surf. Interface Anal.* **2004**, *36*, 1269–1303.
- [81] Tanuma, S.; Powell, C. J.; Penn, D. R. *Surf. Interface Anal.* **1993**, *20*, 77–89.
- [82] Jablonski, A.; Powell, C. J. *Surf. Sci. Rep.* **2002**, *47*, 33–91.
- [83] Seah, M. P.; Dench, W. A. *Surf. Interface Anal.* **1979**, *1*, 2–11.
- [84] Lamont, C.; Wilkes, J. *Langmuir* **1999**, *15*, 2037–2042.
- [85] Bain, C. D.; Whitesides, G. M. *J. Phys. Chem.* **1989**, *93*, 1670–1673.
- [86] Powell, C.; Jablonski, A. *NIST Electron Effective-Absorption-Length Database, version 1.3, SRD82*; National Institute of Standards and Technology, 2011.
- [87] Tanuma, S.; Powell, C. J.; Penn, D. R. *Surf. Interface Anal.* **1994**, *21*, 165–176.
- [88] Tanuma, S.; Powell, C. J.; Penn, D. R. *Surf. Interface Anal.* **1991**, *17*, 911–926.
- [89] Tanuma, S.; Powell, C. J.; Penn, D. R. *Surf. Interface Anal.* **1988**, *11*, 577–589.
- [90] Tanuma, S.; Shiratori, T.; Kimura, T.; Goto, K.; Ichimura, S.; Powell, C. J. *Surf. Interface Anal.* **2005**, *37*, 833–845.
- [91] Zemek, J.; Jiricek, P.; Houdkova, J.; Olejnik, K.; Jablonski, A. *Surf. Interface Anal.* **2007**, *39*, 916–921.
- [92] Brundle, C.; Conti, G.; Mack, P. *J. Electron Spectrosc. Relat. Phenom.* **2010**, *178–179*, 433–448.
- [93] Cumpson, P. J. *J. Electron Spectrosc. Relat. Phenom.* **1995**, *73*, 25–52.
- [94] Cumpson, P. J. *Appl. Surf. Sci.* **1999**, *144–145*, 16–20.
- [95] Oswald, S.; Zier, M.; Reiche, R.; Wetzig, K. *Surf. Interface Anal.* **2006**, *38*, 590–594.
- [96] Fulghum, J. E. *Surf. Interface Anal.* **1993**, *20*, 161–173.
- [97] Band, I. M.; Kharitonov, Y. I.; Trzhaskovskaya, M. B. *Atomic Data and Nuclear Data Tables* **1979**, *23*, 443–505.
- [98] Schmidt, V. *Rep. Prog. Phys.* **1992**, *55*, 1483.
- [99] Yeh, J. J.; Lindau, I. *Atomic Data and Nuclear Data Tables* **1985**, *32*, 1–155.
- [100] Merzlikin, S. V.; Tolkachev, N. N.; Strunskus, T.; Witte, G.; Glogowski, T.; Wll, C.; Grnert, W. *Surf. Sci.* **2008**, *602*, 755–767.
- [101] Smith, N. V. *Reports on Progress in Physics* **1988**, *51*, 1227.
- [102] Stoehr, J. *NEXAFS Spectroscopy; Springer Series in Surface Science 25*; Springer-Verlag, 1992.
- [103] Hahner, G. *Chem. Soc. Rev.* **2006**, *35*, 1244–1255.

- [104] Watts, B.; Thomsen, L.; Dastoor, P. *J. Electron Spectrosc. Relat. Phenom.* **2006**, *151*, 105–120.
- [105] Niehus, H.; Heiland, W.; Taglauer, E. *Surf. Sci. Rep.* **1993**, *17*, 213–303.
- [106] Brongersma, H.; Draxler, M.; de Ridder, M.; Bauer, P. *Surf. Sci. Rep.* **2007**, *62*, 63–109.
- [107] Niehus, H.; Spitzl, R. *Surf. Interface Anal.* **1991**, *17*, 287–307.
- [108] de Gennes, P. G. *Rev. Mod. Phys.* **1985**, *57*, 827.
- [109] Tadmor, R. *Langmuir* **2004**, *20*, 7659–7664.
- [110] Chesneau, F.; Hamoudi, H.; Schupbach, B.; Terfort, A.; Zharnikov, M. *J. Phys. Chem. C* **2011**, *115*, 4773–4782.
- [111] Palermo, V.; Palma, M.; Samor, P. *Adv. Mater.* **2006**, *18*, 145–164.
- [112] Hayden, B. In *Vibrational Spectroscopy of Molecules on Surface*; Yates, T., J.T.; Madey, Ed.; Plenum: New York, 1987.
- [113] Chesneau, F. Toward reagentless electrochemically addressable microarrays: synthesis of suitable monomers and anchor molecules. M.Sc. thesis, Simon Fraser University, 2008.
- [114] Tanuma, S.; Powell, C. J.; Penn, D. R. *Surf. Interface Anal.* **2005**, *37*, 1–14.
- [115] Tanuma, S.; Powell, C. J.; Penn, D. R. *Surf. Interface Anal.* **2003**, *35*, 268–275.
- [116] Heister, K.; Zharnikov, M.; Grunze, M.; Johansson, L. S. O.; Ulman, A. *Langmuir* **2001**, *17*, 8–11.
- [117] Heister, K.; Rong, H.-T.; Buck, M.; Zharnikov, M.; Grunze, M.; Johansson, L. S. O. *J. Phys. Chem. B* **2001**, *105*, 6888–6894.
- [118] Moulder, W. E. S. P. E. B. K. D., J. F.; Stickle In *Handbook of X-ray Photoelectron Spectroscopy*; Chastian, J., Ed.; Perkin-Elmer Corp.: Eden Prairie, MN, 1992.
- [119] Batson, P. E. *Phys. Rev. B* **1993**, *48*, 2608–.
- [120] Zubavichus, Y.; Shaporenko, A.; Grunze, M.; Zharnikov, M. *J. Phys. Chem. A* **2005**, *109*, 6998–7000.
- [121] Neese, F. e. a. Orca 2.8. <http://www.thch.uni-bonn.de/tc/orca/>.
- [122] Almenningen, A.; Bastiansen, O.; Fernholt, L.; Cyvin, B. N.; Cyvin, S. J.; Samdal, S. *J. Mol. Struct.* **1985**, *128*, 59–76.
- [123] Almenningen, A.; Bastiansen, O.; Gundersen, S.; Samdal, S.; Skancke, A. *J. Mol. Struct.* **1985**, *128*, 95–114.
- [124] Bordat, P.; Brown, R. *Chem. Phys.* **1999**, *246*, 323–334.
- [125] Goossens, D. J.; Gutmann, M. J. *Phys. Rev. Lett.* **2009**, *102*, 015505.
- [126] Sushko, M. L.; Shluger, A. L. *Adv. Mater.* **2009**, *21*, 1111–1114.

- [127] Love, J. C.; Wolfe, D. B.; Haasch, R.; Chabynyc, M. L.; Paul, K. E.; Whitesides, G. M.; Nuzzo, R. G. *J. Am. Chem. Soc.* **2003**, *125*, 2597–2609.
- [128] Carro, P.; Corthey, G.; Rubert, A. A.; Benitez, G. A.; Fonticelli, M. H.; Salvarezza, R. C. *Langmuir* **2010**, *26*, 14655–14662.
- [129] Alloway, D. M.; Hofmann, M.; Smith, D. L.; Gruhn, N. E.; Graham, A. L.; Colorado, R.; Wysocki, V. H.; Lee, T. R.; Lee, P. A.; Armstrong, N. R. *J. Phys. Chem. B* **2003**, *107*, 11690–11699.
- [130] Heimel, G.; Romaner, L.; Bredas, J.-L.; Zojer, E. *Langmuir* **2008**, *24*, 474–482.
- [131] Noda, H.; Tai, Y.; Shaporenko, A.; Grunze, M.; Zharnikov, M. *J. Phys. Chem. B* **2005**, *109*, 22371–22376.
- [132] Dediu, V.; Murgia, M.; Maticcotta, F. C.; Taliani, C.; Barbanera, S. *Solid State Commun.* **2002**, *122*, 181–184.
- [133] Naber, W. e. a. *J. Phys. D: Appl. Phys.* **2007**, *40*, R205–.
- [134] Petta, J. R.; Slater, S. K.; Ralph, D. C. *Phys. Rev. Lett.* **2004**, *93*, 136601–.
- [135] Dowben, P.; Rosa, L. G.; Ilie, C. C.; Xiao, J. *J. Electron Spectrosc. Relat. Phenom.* **2009**, *174*, 10–21.
- [136] Grave, C.; Risko, C.; Shaporenko, A.; Wang, Y.; Nuckolls, C.; Ratner, M.; Rampi, M.; Zharnikov, M. *Adv. Funct. Mater.* **2007**, *17*, 3816–3828.
- [137] Liu, J.; Schupbach, B.; Bashir, A.; Shekhah, O.; Nefedov, A.; Kind, M.; Terfort, A.; Woll, C. *Phys. Chem. Chem. Phys.* **2010**, *12*, 4459–4472.
- [138] Hong, J.-P.; Park, A.-Y.; Lee, S.; Kang, J.; Shin, N.; Yoon, D. Y. *Appl. Phys. Lett.* **2008**, *92*, 143311–3.
- [139] Saudari, S. R.; Frail, P. R.; Kagan, C. R. *Appl. Phys. Lett.* **2009**, *95*, 023301–3.
- [140] Hamadani, B. H.; Corley, D. A.; Ciszek, J. W.; Tour, J. M.; Natelson, D. *Nano Lett.* **2006**, *6*, 1303–1306.
- [141] Azzam, W.; Bashir, A.; Terfort, A.; Strunskus, T.; Wll, C. *Langmuir* **2006**, *22*, 3647–3655.
- [142] Chen, F.; Li, X.; Hihath, J.; Huang, Z.; Tao, N. *J. Am. Chem. Soc.* **2006**,
- [143] Chen, F.; Tao, N. *J. Acc. Chem. Res.* **2009**, *42*, 429–438.
- [144] Brunner, H.; Lukas, R. *Chem. Ber.* **1979**, *112*, 2528–2538.
- [145] Garner, S. E.; Orpen, A. G. *J. Chem. Soc., Dalton Trans.* **1993**, 533–541.
- [146] Trotter, J. *Acta Cryst.* **1961**, *14*, 1135–1140.
- [147] Hargreaves, A.; Rizvi, S. H. *Acta Cryst.* **1962**, *15*, 365–373.
- [148] Lii, J. H.; Allinger, N. L. *J. Am. Chem. Soc.* **1989**, *111*, 8576–8582.

- [149] Himmel, H.-J.; Terfort, A.; Woll, C. *J. Am. Chem. Soc.* **1998**, *120*, 12069–12074.
- [150] Hamor, M. J.; Hamor, T. A. *Acta Cryst. B* **1978**, *34*, 863–866.
- [151] Rietveld, H. M.; Maslen, E. N.; Clews, C. J. B. *Acta Cryst. B* **1970**, *26*, 693–706.
- [152] Schuepbach, B.; Bolte, M.; Zharnikov, M.; Terfort, A. *Eur. J. Org. Chem.* **2010**, *2010*, 3041–3048.
- [153] Hitchcock, A. P.; Fischer, P.; Gedanken, A.; Robin, M. B. *J. Phys. Chem.* **1987**, *91*, 531–540.
- [154] Plashkevych, O.; Yang, L.; Vahtras, O.; gren, H.; Petterson, L. G. M. *Chem. Phys.* **1997**, *222*, 125–137.
- [155] Zharnikov, M.; Grunze, M. *J. Phys.: Condens. Matter* **2001**, *13*, 11333–.
- [156] Laibinis, P. E.; Whitesides, G. M.; Allara, D. L.; Tao, Y. T.; Parikh, A. N.; Nuzzo, R. G. *J. Am. Chem. Soc.* **1991**, *113*, 7152–7167.
- [157] Himmelhaus, M.; Gauss, I.; Buck, M.; Eisert, F.; Wll, C.; Grunze, M. *J. Electron Spectrosc. Relat. Phenom.* **1998**, *92*, 139–149.
- [158] Yang, Y. W.; Fan, L. J. *Langmuir* **2002**, *18*, 1157–1164.
- [159] Ishida, T.; Choi, N.; Mizutani, W.; Tokumoto, H.; Kojima, I.; Azehara, H.; Hokari, H.; Akiba, U.; Fujihira, M. *Langmuir* **1999**, *15*, 6799–6806.
- [160] Weidner, T.; Kramer, A.; Bruhn, C.; Zharnikov, M.; Shaporenko, A.; Siemeling, U.; Trager, F. *Dalton Trans.* **2006**, 2767–2777.
- [161] Schreiber, F. *Prog. Surf. Sci.* **2000**, *65*, 151–257.
- [162] Edinger, K.; Goelzhaeuser, A.; Demota, K.; Woell, C.; Grunze, M. *Langmuir* **1993**, *9*, 4–8.
- [163] Poirier, G. E. *Langmuir* **1997**, *13*, 2019–2026.
- [164] Yang, G.; Liu, G.-y. *J. Phys. Chem. B* **2003**, *107*, 8746–8759.
- [165] Cyganik, P.; Buck, M.; Strunskus, T.; Shaporenko, A.; Witte, G.; Zharnikov, M.; Wll, C. *J. Phys. Chem. C* **2007**, *111*, 16909–16919.
- [166] Kaefer, D.; Witte, G.; Cyganik, P.; Terfort, A.; Woell, C. *J. Am. Chem. Soc.* **2006**, *128*, 1723–1732.
- [167] Kang, J. F.; Ulman, A.; Liao, S.; Jordan, R.; Yang, G.; Liu, G.-y. *Langmuir* **2001**, *17*, 95–106.
- [168] Dauselt, J.; Zhao, J.; Kind, M.; Binder, R.; Bashir, A.; Terfort, A.; Zharnikov, M. *J. Phys. Chem. C* **2011**, *115*, 2841–2854.
- [169] Zharnikov, M.; Frey, S.; Heister, K.; Grunze, M. *Langmuir* **2000**, *16*, 2697–2705.
- [170] Azzam, W.; Wehner, B. I.; Fischer, R. A.; Terfort, A.; Woll, C. *Langmuir* **2002**, *18*, 7766–7769.

- [171] Hamoudi, S. K. P. S. B. F. P. T. A. A. D., H.; Neppl; Zharnikov, M. *Phys. Rev. Lett.* **2011**, *submitted*.
- [172] Venkataraman, N. V.; Zurcher, S.; Rossi, A.; Lee, S.; Naujoks, N.; Spencer, N. D. *J. Phys. Chem. C* **2009**, *113*, 5620–5628.
- [173] Brundle, C. R.; Robin, M. B.; Kuebler, N. A. *J. Am. Chem. Soc.* **1972**, *94*, 1466–1475.
- [174] Mizuguchi, J.; Wooden, G. *Berichte der Bunsengesellschaft fuer physikalische Chemie* **1991**, *95*, 1264–1274.
- [175] Senju, T.; Mizuguchi, J. *J. Phys. Chem. B* **2005**, *109*, 7649–7653.
- [176] Chen, C.-H.; Huang, M.-L.; Wang, S.-C.; Klauser, R.; Shaporenko, A.; Zharnikov, M. *J. Phys. Chem. B* **2006**, *110*, 17878–17883.
- [177] Hamoudi, H.; Chesneau, F.; Patze, C.; Zharnikov, M. *J. Phys. Chem. C* **2011**, *115*, 534–541.
- [178] Kind, M.; Woell, C. *Prog. Surf. Sci.* **2009**, *84*, 230–278.
- [179] Zharnikov, M.; Geyer, W.; Golzhauser, A.; Frey, S.; Grunze, M. *Phys. Chem. Chem. Phys.* **1999**, *1*, 3163–3171.
- [180] Mueller, H. U.; Zharnikov, M.; Volkel, B.; Schertel, A.; Harder, P.; Grunze, M. *J. Phys. Chem. B* **1998**, *102*, 7949–7959.
- [181] Olsen, C.; Rowntree, P. A. *J. Chem. Phys.* **1998**, *108*, 3750–3764.
- [182] Giske, K. Effect of packing density on the resistance of self-assembled monolayers to electron and ion irradiation. M.Sc. thesis, University of Heidelberg, 2006.
- [183] Diaz, J.; Paolicelli, G.; Ferrer, S.; Comin, F. *Phys. Rev. B* **1996**, *54*, 8064–.
- [184] Merel, P.; Tabbal, M.; Chaker, M.; Moisa, S.; Margot, J. *Appl. Surf. Sci.* **1998**, *136*, 105–110.
- [185] Yannoulis, P.; Dudde, R.; Frank, K.; Koch, E. *Surf. Sci.* **1987**, *189-190*, 519–528.
- [186] Dhez, O.; Ade, H.; Urquhart, S. G. *J. Electron Spectrosc. Relat. Phenom.* **2003**, *128*, 85–96.
- [187] Ferragina, C.; Massucci, M. A.; Mattogno, G. *J. Inclusion Phenom. Macrocyclic Chem.* **1989**, *7*, 529–536.
- [188] Kessel, R.; Schultze, J. W. *Surf. Interface Anal.* **1990**, *16*, 401–406.
- [189] Hendrickson, D. N.; Hollander, J. M.; Jolly, W. L. *Inorg. Chem.* **1969**, *8*, 2642–2647.
- [190] Zhou, X.; Goh, S. H.; Lee, S. Y.; Tan, K. L. *Appl. Surf. Sci.* **1998**, *126*, 141–147.
- [191] Lahaye, J.; Nanse, G.; Fioux, P.; Bagreev, A.; Broshnik, A.; Strelko, V. *Appl. Surf. Sci.* **1999**, *147*, 153–174.
- [192] Evangelisti, C.; Panziera, N.; Pertici, P.; Vitulli, G.; Salvadori, P.; Battocchio, C.; Polzonetti, G. *J. Catal.* **2009**, *262*, 287–293.

- [193] Stout, D. M.; Meyers, A. I. *Chem. Rev.* **1982**, *82*, 223–243.
- [194] Tanner, D. D.; Yang, C. M. *J. Org. Chem.* **1993**, *58*, 1840–1846.
- [195] Lunn, G.; Sansone, E. B. *J. Org. Chem.* **1986**, *51*, 513–517.
- [196] Mayo, F. R. *J. Org. Chem.* **1936**, *01*, 496–503.
- [197] Burrows, G. H.; King, L. A. *J. Am. Chem. Soc.* **1935**, *57*, 1789–1791.
- [198] Brown, O.; Butterfield, R.; Millington, J. *Electrochim. Acta* **1982**, *27*, 1655–1662.
- [199] Failes, R. L.; Joyce, J. T.; Watton, E. C. *J. Chem. Soc., Faraday Trans. 1* **1973**, *69*, 1487–1490.
- [200] Burrow, P. D.; Ashe, A. J.; Bellville, D. J.; Jordan, K. D. *J. Am. Chem. Soc.* **1982**, *104*, 425–429.
- [201] Wentworth, W. E.; Kao, L. W.; Becker, R. S. *J. Phys. Chem.* **1975**, *79*, 1161–1169.
- [202] Turchanin, A.; Kaefer, D.; El-Desawy, M.; Wooell, C.; Witte, G.; Goelzhaeuser, A. *Langmuir* **2009**, *25*, 7342–7352.
- [203] Perry, C. C.; Wagner, A. J.; Howard Fairbrother, D. *Chem. Phys.* **2002**, *280*, 111–118.
- [204] Clark, D. T.; Brennan, W. J. *J. Fluorine Chem.* **1988**, *40*, 419–434.
- [205] Mackie, N. M.; Castner, D. G.; Fisher, E. R. *Langmuir* **1998**, *14*, 1227–1235.
- [206] Munro, H. S.; Till, C. *J. Polym. Sci. A Polym. Chem.* **1988**, *26*, 2873–2880.
- [207] Zharnikov, M.; Frey, S.; Heister, K.; Grunze, M. *J. Electron Spectrosc. Relat. Phenom.* **2002**, *124*, 15–24.
- [208] Zharnikov, M., M.; Grunze *J. Vac. Sci. Technol. B* **2002**, *20*, 1793.
- [209] Wagner, K. V. A. L. F. D. H., A. J.; Han *J. Phys. Chem. B* **2000**, *104*, 3291.
- [210] Hagenstrm, H.; Schneeweiss, M. A.; Kolb, D. M. *Electrochim. Acta* **1999**, *45*, 1141–1145.
- [211] Hagenstrom, H.; Schneeweiss, M.; Kolb, D. *Langmuir* **1999**, *15*, 7802–7809.
- [212] Herrero, E.; Buller, L.; Abruna, H. *Chem. Rev.* **2001**, *101*, 1897–1930.
- [213] Kokkinidis, G. *J. Electroanal. Chem.* **1986**, *201*, 217–236.
- [214] Kolb, D.; Przasnyski, M.; Gerischer, H. *J. Electroanal. Chem.* **1974**, *54*, 25–38.
- [215] Robertson, J.; Tiani, D.; Pemberton, J. *Langmuir* **2007**, *23*, 4651–4661.
- [216] Vaskevich, A.; Sinapi, F.; Mekhalif, Z.; Delhalle, J.; Rubinstein, I. *J. Electrochem. Soc.* **2005**, *152*, C744–C750.
- [217] Zhang, J.; Sung, Y.-E.; Rikvold, P. A.; Wieckowski, A. *J. Chem. Phys.* **1996**, *104*, 5699–5712.

- [218] Aldakov, D.; Bonnassieux, Y.; Geffroy, B.; Palacin, S. *ACS Applied Materials & Interfaces* **2009**, *1*, 584–589.
- [219] Gao, J.; Tang, F.; Ren, J. *Surf. Coat. Technol.* **2005**, *200*, 2249–2252.
- [220] Yagi, S.; Murase, K.; Tsukimoto, S.; Hirato, T.; Awakura, Y. *J. Electrochem. Soc.* **2005**, *152*, C588–C592.
- [221] Claro, P. C. d. S.; Schilardi, P. L.; Blum, B.; Castez, M. F.; Salvarezza, R. C. *Phys. Rev. B* **2007**, *76*, 205436–5.
- [222] Ballav, N.; Koelsch, P.; Zharnikov, M. *J. Phys. Chem. C* **2009**, *113*, 18312–18320.
- [223] Barriet, D.; Lee, T. R. *Curr. Opin. Coll. Interf. Sci.* **2003**, *8*, 236–242.
- [224] Chen, W.; Huang, C.; Gao, X. Y.; Wang, L.; Zhen, C. G.; Qi, D.; Chen, S.; Zhang, H. L.; Loh, K. P.; Chen, Z. K.; Wee, A. T. S. *J. Phys. Chem. B* **2006**, *110*, 26075–26080.
- [225] Herdt, G. C.; Jung, D. R.; Czanderna, A. W. *The Journal of Adhesion* **1997**, *60*, 197–222.
- [226] Silien, C.; Buck, M. *J. Phys. Chem. C* **2008**, *112*, 3881–3890.
- [227] Colavita, P.; Miney, P.; Taylor, L.; Priore, R.; Pearson, D.; Ratliff, J.; Ma, S.; Ozturk, O.; Chen, D.; Myrick, M. *Langmuir* **2005**, *21*, 12268–12277.
- [228] Thome, J.; Himmelhaus, M.; Zharnikov, M.; Grunze, M. *Langmuir* **1998**, *14*, 7435–7449.
- [229] Manolova, M.; Boyen, H.-G.; Kucera, J.; Gro, A.; Romanyuk, A.; Oelhafen, P.; Ivanova, V.; Kolb, D. M. *Adv. Mater.* **2009**, *21*, 320–324.
- [230] Amii, H.; Uneyama, K. *Chem. Rev.* **2009**, *109*, 2119–2183.
- [231] Reinhold, M.; McGrady, J. E.; Perutz, R. N. *J. Am. Chem. Soc.* **2004**, *126*, 5268–5276.
- [232] Sun, A. D.; Love, J. A. *Dalton Trans.* **2010**, *39*, 10362–10374.
- [233] Zheng, T.; Sun, H.; Ding, J.; Zhang, Y.; Li, X. *J. Organomet. Chem.* **2010**, *695*, 1873–1877.
- [234] Atesin, T. A.; Li, T.; Lachaize, S.; Brennessel, W. W.; Garcia, J. J.; Jones, W. D. *J. Am. Chem. Soc.* **2007**, *129*, 7562–7569.
- [235] van der Boom, M. E.; Liou, S.-Y.; Shimon, L. J.; Ben-David, Y.; Milstein, D. *Inorg. Chim. Acta* **2004**, *357*, 4015–4023.
- [236] Chiusoli, G. P.; Catellani, M.; Costa, M.; Motti, E.; Della Ca', N.; Maestri, G. *Coord. Chem. Rev.* **2010**, *254*, 456–469.
- [237] Evans, M. E.; Burke, C. L.; Yaibuathes, S.; Clot, E.; Eisenstein, O.; Jones, W. D. *J. Am. Chem. Soc.* **2009**, *131*, 13464–13473.
- [238] Frieman, B. A.; Taft, B. R.; Lee, C. T.; Butler, T.; Lipshutz, B. H. *Synthesis-stuttgart* **2005**, 2989–2993.
- [239] Liang, L.-C.; Chien, P.-S.; Huang, Y.-L. *J. Am. Chem. Soc.* **2006**, *128*, 15562–15563.

- [240] Mukai, T.; Hirano, K.; Satoh, T.; Miura, M. *J. Org. Chem.* **2009**, *74*, 6410–6413.
- [241] Nakao, Y.; Kanyiva, K. S.; Hiyama, T. *J. Am. Chem. Soc.* **2008**, *130*, 2448–2449.
- [242] Torrens, H. *Coord. Chem. Rev.* **2005**, *249*, 1957–1985.
- [243] Rumin, R.; Guennou, K.; Pichon, R.; Ptilon, F. Y.; Muir, K. W.; Yufit, D. S. *J. Organomet. Chem.* **1997**, *533*, 177–185.
- [244] Li, X.; Sun, H.; Yu, F.; Flaerke, U.; Klein, H.-F. *Organometallics* **2006**, *25*, 4695–4697.
- [245] Bellina, F.; Rossi, R. *Tetrahedron* **2009**, *65*, 10269–10310.
- [246] Hofmann, P.; Unfried, G. *Chem. Ber.* **1992**, *125*, 659–661.
- [247] Nova, A.; Reinhold, M.; Perutz, R. N.; Macgregor, S. A.; McGrady, J. E. *Organometallics* **2010**, *29*, 1824–1831.
- [248] Johnson, S. A.; Huff, C. W.; Mustafa, F.; Saliba, M. *J. Am. Chem. Soc.* **2008**, *130*, 17278–17280.
- [249] Akhter, S.; White, J. *Surf. Sci.* **1987**, *180*, 19–46.
- [250] Dickinson, T.; Povey, A. F.; Sherwood, P. M. A. *J. Chem. Soc., Faraday Trans. 1* **1977**, *73*, 327–343.
- [251] Best, S. A.; Brant, P.; Feltham, R. D.; Rauchfuss, T. B.; Roundhill, D. M.; Walton, R. A. *Inorg. Chem.* **1977**, *16*, 1976–1979.
- [252] Sinharoy, S.; Smith, M.; Levenson, L. L. *J. Vac. Sci. Technol.* **1977**, *14*, 475–478.
- [253] Khaire, T. S.; Pratt, W. P.; Birge, N. O. *Phys. Rev. B* **2009**, *79*, 094523.
- [254] Bauer, A.; Bentner, J.; Aprili, M.; Della Rocca, M. L.; Reinwald, M.; Wegscheider, W.; Strunk, C. *Phys. Rev. Lett.* **2004**, *92*, 217001.
- [255] Silien, C.; Lahaye, D.; Caffio, M.; Schaub, R.; Champness, N. R.; Buck, M. *Langmuir* **2011**, *27*, 2567–2574.
- [256] Moreau, X.; Campagne, J. M.; Meyer, G.; Jutand, A. *Eur. J. Org. Chem.* **2005**, *2005*, 3749–3760.
- [257] Bater, C.; Sanders, M.; Craig Jr., J. *Surf. Sci.* **2000**, *451*, 226–231.
- [258] Valerio, G.; Toulhoat, H. *J. Phys. Chem. A* **1997**, *101*, 1969–1974.
- [259] Schaefer, H.; Wiese, U.; Rinke, K.; Brendel, K. *Angew. Chem. Int. Ed. Engl.* **1967**, *6*, 253–254.
- [260] Dell’Amico, D. B.; Calderazzo, F.; Marchetti, F.; Ramello, S. *Angew. Chem. Int. Ed. Engl.* **1996**, *35*, 1331–1333.
- [261] Soulen, J. R.; Chappell, W. H. *J. Phys. Chem.* **1965**, *69*, 3669–3671.
- [262] Olmstead, M. M.; Ginwalla, A. S.; Noll, B. C.; Tinti, D. S.; Balch, A. L. *J. Am. Chem. Soc.* **1996**, *118*, 7737–7745.

- [263] Fuggle, J. C.; Hillebrecht, F. U.; Zeller, R.; Zolstroknieriek, Z.; Bennett, P. A.; Freiburg, C. *Phys. Rev. B* **1983**, *27*, 2145.
- [264] Hillebrecht, F. U.; Fuggle, J. C.; Bennett, P. A.; Zolstroknieriek, Z.; Freiburg, C. *Phys. Rev. B* **1983**, *27*, 2179.
- [265] Matienzo, J.; Yin, L. I.; Grim, S. O.; Swartz, W. E. *Inorg. Chem.* **1973**, *12*, 2762–2769.
- [266] Toulhoat, H. P.; Gravil, P. A.; Valerio, G. *Abstr. Papers Amer. Chem. Soc.* **1999**, *218*, 28.
- [267] Oudar, J. In *Corrosion Mechanisms in Theory and Practice*, 2nd edition, 2nd ed.; Marcus, P., Ed.; CRC Press, 2002; p 27.
- [268] Donath, M. *Surf. Sci. Rep.* **1994**, *20*, 251–316.
- [269] Sinharoy, S.; Levenson, L. *Thin Solid Films* **1978**, *53*, 31–36.
- [270] Clark, D. T.; Feast, W. J.; Kilcast, D.; Musgrave, W. K. R. *J. Polym. Sci. Polym. Chem. Ed.* **1973**, *11*, 389–411.
- [271] Pacile, D.; Papagno, M.; Rodriguez, A. F.; Grioni, M.; Papagno, L.; Girit, C. O.; Meyer, J. C.; Begtrup, G. E.; Zettl, A. *Phys. Rev. Lett.* **2008**, *101*, 066806–.
- [272] Lalitha, S.; Manoharan, P. T. *J. Electron Spectrosc. Relat. Phenom.* **1989**, *49*, 61–75.
- [273] Kovcs, G.; Bertti, I.; Radnczi, G. *Thin Solid Films* **2008**, *516*, 7942–7946.
- [274] Zaera, F. *Surf. Sci.* **1989**, *219*, 453–466.
- [275] Goretzki, H.; Rosenstiel, P. v.; Mandziej, S. *Fres. J. of Anal. Chem.* **1989**, *333*, 451–452.
- [276] Adelhelm, M. K. F. H. A. L. S., C.; Balden *Journal of Physics: Conference Series* **2008**, *100*, 062033.
- [277] Carlo, S.; Wagner, A.; Fairbrother, D. *J. Phys. Chem. B* **2000**, *104*, 6633–6641.
- [278] Lide, D., Ed. *Handbook of Chemistry and Physics*; CRC Press, 1995.
- [279] Price, S. J. W.; Sapiano, H. J. *Canadian Journal Of Chemistry-Revue Canadienne De Chimie* **1974**, *52*, 4109–4111.
- [280] Rsch, N.; Ackermann, L.; Pacchioni, G. *Chem. Phys. Lett.* **1992**, *199*, 275–280.
- [281] van der Heide, H.; Hemmel, R.; van Bruggen, C. F.; Haas, C. *J. Solid State Chem.* **1980**, *33*, 17–25.
- [282] Wagner, C. D.; Taylor, J. A. *J. Electron Spectrosc. Relat. Phenom.* **1980**, *20*, 83–93.
- [283] Mueller, K.-H. *Phys. Rev. B* **1987**, *35*, 7906–.
- [284] Chen, C.-Y.; Wu, K.-Y.; Chao, Y.-C.; Zan, H.-W.; Meng, H.-F.; Tao, Y.-T. *Organic Electronics* **2011**, *12*, 148–153.
- [285] Cheng, X.; Noh, Y.-Y.; Wang, J.; Tello, M.; Frisch, J.; Blum, R.-P.; Vollmer, A.; Rabe, J. P.; Koch, N.; Sirringhaus, H. *Adv. Funct. Mater.* **2009**, *19*, 2407–2415.

- [286] De Renzi, V. *Surf. Sci.* **2009**, *603*, 1518–1525.
- [287] Heimel, G.; Romaner, L.; Brdas, J.-L.; Zojer, E. *Surf. Sci.* **2006**, *600*, 4548–4562.
- [288] Heimel, G.; Romaner, L.; Zojer, E.; Bredas, J.-L. *Acc. Chem. Res.* **2008**, *41*, 721–729.
- [289] Hugosson, H. W.; Eriksson, O.; Jansson, U.; Ruban, A. V.; Souvatzis, P.; Abrikosov, I. A. *Surf. Sci.* **2004**, *557*, 243–254.
- [290] Ge, Y.; Weidner, T.; Ahn, H.; Whitten, J. E.; Zharnikov, M. *J. Phys. Chem. C* **2009**, *113*, 4575–4583.
- [291] Wall, J. S.; Hu, B.; Siddiqui, J. A.; Ottenbrite, R. M. *Langmuir* **2001**, *17*, 6027–6029.
- [292] Bae, S. S.; Lim, D. K.; Park, J. I.; Cheon, J.; Jeon, I. C.; Kim, S. *Applied Physics A-materials Science & Processing* **2005**, *80*, 1305–1310.
- [293] Hata, K.; Fujita, M.; Yoshida, S.; Yasuda, S.; Makimura, T.; Murakami, K.; Shigekawa, H.; Mizutani, W.; Tokumoto, H. *Appl. Phys. Lett.* **2001**, *79*, 692–694.
- [294] Oswald, S. *Surf. Sci.* **2008**, *602*, 291–299.
- [295] Oswald, S.; Oswald, F. *Surf. Interface Anal.* **2008**, *40*, 700–705.

Appendix A

List of scientific contributions

A.1 Published scientific papers

1. Chesneau, F. Hamoudi H., Schuepbach, B., Terfort, A. and Zharnikov, M. *Modification of self-assembled monolayers of perfluorophenyl-substituted alkanethiols by low-energy electrons*, *J. Phys. Chem. C* 2011, *in press*
2. Hamoudi H., Chesneau, F., Patze, C. and Zharnikov, M. *Chain-length-dependent branching of irradiation-induced processes in alkanethiolate self-assembled monolayers*, *J. Phys. Chem. C* **2011**, *115* (2), 534-541
3. Chesneau, F. *et al.* *Self-assembled monolayers of perfluoroterphenyl-substituted alkanethiols: specific characteristics and odd-even effects*, *Phys. Chem. Chem. Phys.* **2010**, *12*, 12123-12137
4. Chesneau, F., Zhao, J. and Zharnikov, M. *Adsorption of long-chain alkanethiols on Au(111) - a look from the substrate by high resolution X-ray photoelectron spectroscopy*, *J. Phys. Chem. C* **2010**, *114* (15), 7112-7119

A.2 Scientific papers in preparation

Note that the titles given only mean to reflect the work describe in the planned publications and are by no means final.

1. Chesneau, F. and Zharnikov, M. *Palladium chloride prevents metal penetration during e-beam evaporation.*
2. Chesneau, F. and Zharnikov, M. *Metallisation of self-assembled monolayers of perfluorophenyl-substituted alkanethiols*

3. Kong, L., Chesneau, F., Zhengzheng, Z., Staier, F., Terfort, A., Dowben, P.A. and Zharnikov, M. *The electronic structure of aromatic monomolecular films the effect of molecular spacer and interfacial dipole*
4. Chesneau, F., Bjoern Schuepbach, Terfort, A. and Zharnikov, M. *Effect of low energy electron irradiation on pyridine-terminated self-assembled terphenyl monolayers*
5. Wagner, S., Rakotomalala M., Chesneau F., Zevaco, T. and Doering M. *NMR characterization of DOPO derivatives*

A.3 Conference contribution

1. Chesneau, F., Hamoudi, H., Patze, C. and Zharnikov, M. *The effect of chain-length on the branching of irradiation-induced processes in alkanethiolate molecular films*, DPG meeting, March 2011, Dresden, Germany
2. Chesneau, F., Schuepbach, B., Szelagowska-Kunstman, K., Ballav, N., Cyganik, P., Terfort, A. and Zharnikov, M. *Molecular Organization and Odd-Even Effects in Perfluoroterphenyl-Based Monomolecular Films*, AVS 57th International Symposium and Exhibition, October 2010, Albuquerque, USA
3. Chesneau, F., Schuepbach, B., Szelagowska-Kunstman, K., Ballav, N., Cyganik, P., Terfort, A. and Zharnikov, M. *Self-assembled monolayers of perfluoroterphenyl-substituted alkanethiols*, DPG meeting, March 2010, Regensburg, Germany

List of Tables

2.1	Selection of attenuation lengths	7
3.1	Preparation conditions for the samples used in the present work	25
4.1	Torsion angles of the outer rings of the perfluoroterphenyl moiety of FTP3	33
4.2	Torsion angles of the outer rings of reference fluorinated compounds	34
4.3	Assignment of C-K edge NEXAFS resonances of FTP3 films	36
4.4	Assignment of F-K edge NEXAFS resonances of FTP3 films	36
5.1	Fitting parameters for the variation of the intensity of the N1s HRXPS features in PPP1 films upon electron irradiation	70
6.1	Values of the polar angle for the resonance at 285 eV for TPDMT and CL-PPP3 films with and without palladium	103
6.2	Assignment of the C 1s HRXPS peaks of Ni/FTP3/Au	108
6.3	Assignment of the C K-edge NEXAFS π^* transitions of Ni/FTP3/Au	111
6.4	Theoretical and experimental fluorine loss	113
6.5	Estimation of the maximum penetration depth of nickel through various FTP3 films	119
7.1	Comparison of the change in work function and HOMO for various aryl SAMs .	124

List of Figures

1.1	Schematic representation of an organic-based spintronic device	2
1.2	The molecules studied in this work	3
2.1	The XPS process	5
2.2	C1s HRXPS spectrum of F10H2/Au	5
2.3	The effect of inelastic collisions of electrons in the substrate on the XPS signal .	6
2.4	The universal curve for elements	7
2.5	Schematic representation of an ARXPS experiment	9
2.6	Schematic representation of an ERXPS experiment	9
2.7	Schematic representation of an UPS experiment	10
2.8	Schematic representation of an IPES experiment	11
2.9	Schematic representation of the transitions probed by NEXAFS spectroscopy . .	12
2.10	Schematic representation of the processes occurring during a NEXAFS experiment	13
2.11	Schematic representation of the different NEXAFS measurement methods	13
2.12	Schematic representation of the interaction of X-rays with π^* and σ^* orbitals of a diatomic molecule	13
2.13	Plot of the ratio of NEXAFS intensities measured at 90° and 20° as a function of the molecular orbital angle	14
2.14	Schematic representation of an ISS experiment	15
2.15	Schematic representation of a drop on a surface	16
2.16	Schematic representation of the advancing and receding contact angles of a drop on a surface	16
2.17	Schematic representation of a KP experiment	17
2.18	Selection rules for the reflection of the electrical component of an infrared light off of a metal surface	18
3.1	Schematic representation of the LHS12 UHV system	20

3.2	Metal evaporator calibration performed with a QCM	24
4.1	Schematic view of a SAM constituent	28
4.2	Chemical structure of the precursor molecules of the SAMs studied in this chapter	29
4.3	C1s, N1s and S2p spectra of PPP3/Au	30
4.4	O1s spectra of PPP3/Au and C12/Au	31
4.5	NEXAFS C K-edge difference spectrum of PPP3/Au	32
4.6	Calculated molecular structures of FTP and TP moieties	34
4.7	NEXAFS spectrum of FTP3 on gold at 55°	35
4.8	NEXAFS difference spectra of FTP3 on gold	37
4.9	A schematic drawing of the FTP3 molecule	38
4.10	Angular dependence of the π^* orbitals in FTP3 films	38
4.11	S2p and C1s HRXPS spectra of FTP3/Au	40
4.12	C1s HRXPS spectrum of FTP3/Au at different excitation energies	41
4.13	F1s HRXPS spectrum of FTP3/Au	41
4.14	STM of FTP3 films	42
4.15	A schematic drawing of the SAM precursor molecules used in section 4.4 along with their acronyms	44
4.16	Combined UPS and IPES spectra of the TPT, TP3, FTP3, and Ant3 SAMs . . .	46
4.17	Positions of the HOMO and LUMO orbitals and the HOMO-LUMO gap for the TPT, TP3, FTP3, and Ant3 films	47
4.18	Calculated (DFT) HOMO and LUMO orbitals of the TPT, TP3, FTP3, and Ant3 molecules	48
4.19	Positions of the HOMO and LUMO orbitals and the HOMO-LUMO gap for the TPT, TP3, FTP3, and Ant3 films	49
4.20	UV-vis spectra of the TPT, TP3, FTP3, Ant3, and perfluoroterphenyl molecules in solution	50
4.21	UV-vis spectra of the Ant3 molecule in solution and on the surface	51
5.1	Schematic drawings of positive and negative resists	52
5.2	S 2p HRXPS spectra of pristine and irradiated C6 and C12 SAMs	54
5.3	Dose dependencies of the intensities related to the headgroup-derived species in C6 and C12 on gold	55
5.4	C 1s XPS spectra of pristine and irradiated C6 and C12 SAMs	56
5.5	Relative thicknesses of C6 and C12 SAMs as functions of the irradiation dose . .	57

5.6	IRRAS spectra of pristine and irradiated C6 and C12 SAMs	58
5.7	Schematic drawing of the excited state quenching in alkanethiol SAMs	59
5.8	IRRAS of PPP1/Au and calculated IR spectra of the PPP moiety before and after electron irradiation	63
5.9	HRXPS C1s spectra of PPP1/Au monolayers at various electron irradiation doses	64
5.10	NEXAFS C K-edge spectra (55°) of PPP1/Au monolayers at various electron irradiation doses	65
5.11	NEXAFS C K-edge difference spectra ($I_{90}-I_{20}$) of PPP1/Au monolayers at various irradiation doses	66
5.12	Variation of the average molecular tilt angle with irradiation dose	66
5.13	S2p HRXPS of PPP1/Au at various irradiation doses	67
5.14	N1s HRXPS of PPP1/Au before and after irradiation	68
5.15	Various possible nitrogen-containing motifs	69
5.16	Variation of the N1s HRXPS intensity of PPP1 films with irradiation dose	70
5.17	Electron irradiation-induced processes in PPP1 films	72
5.18	C 1s and F 1s XPS spectra of FTP3/Au over the course of irradiation	74
5.19	Normalised intensities of the C1s(C-F) and F1s emission for FTP3/Au as functions of the irradiation dose	75
5.20	Normalised intensities of the π_2^* resonance in the carbon K-edge NEXAFS spectra of FTP3/Au	75
5.21	Normalised C1s intensity and thickness for FTP3, TP3 and F10H2	76
5.22	S 2p XPS spectra of pristine and irradiated FTP2/Au and FTP3/Au	77
5.23	Average tilt angle of the π^* orbitals in FTP2/Au (top panel) and FTP3/Au (bot- tom panel)	78
5.24	Average tilt angle of the π^* orbitals in FTP2/Au (top panel) and FTP3/Au (bot- tom panel)	79
5.25	Water contact angles (WCA) θ_{adv} and θ_{rec} and WCA hysteresis for FTP3/Au . .	80
5.26	SEM images of etched FTP3/Au template preliminary patterned by electrons . .	81
5.27	Variation of the work function of FTP films as a function of irradiation dose . . .	82
5.28	Schematic representation of electron-induced modification of FTPn/Au	82
6.1	Schematic view of a Metal-SAM-Metal system	85
6.2	Channel creation upon metal evaporation on SAMs	86
6.3	Difference in metal penetration upon crosslinking	87
6.4	Using the spacer unit to stop metal penetration	87

6.5	Structures of the F10H2 and FTP3 molecules	88
6.6	C1s HRXPS and C K-edge 55° NEXAFS spectra of CL-TPDMT SAMs before and after deposition of 1.2 nm nickel	90
6.7	C K-edge NEXAFS difference spectra and HRXPS carbon to gold ratio of CL-TPDMT SAMs before and after deposition of 1.2 nm nickel	91
6.8	ARXPS of a CL-TPDMT film after deposition of 0.1 nm nickel	92
6.9	HRXPS S2p spectra of CL-TPDMT SAMs before and after deposition of 1.2 nm nickel	92
6.10	C1s HRXPS and C K-edge 55° NEXAFS spectra of CL-PPP1 SAMs before and after deposition of 1.2 nm nickel	95
6.11	C K-edge NEXAFS difference spectra and XPS carbon to gold ratio of CL-PPP1 and CL-PPP3 SAMs before and after deposition of nickel	96
6.12	Ni2p XPS spectra of TPDMT and PPP3 SAMs after adsorption of nickel chloride	97
6.13	N1s and S2p HRXPS spectra of CL-PPP1 SAMs before and after deposition of 1.2 nm nickel	98
6.14	HRXPS N1s and S2p spectra of CL-PPP3 and TPDMT monolayers before and after palladium adsorption	100
6.15	NEXAFS difference spectra of CL-PPP3 and TPDMT monolayers before and after palladium adsorption	101
6.16	HRXPS Pd3d spectra of Pd/CL-PPP3 and Pd/TPDMT monolayers before and after nickel evaporation	102
6.17	HRXPS N1s and S2p spectra of Pd/CL-PPP3 and Pd/TPDMT monolayers before and after nickel evaporation	103
6.18	NEXAFS difference spectra of Pd/CL-PPP3 and Pd/TPDMT monolayers before and after nickel evaporation	104
6.19	XPS Cl2p and Ni2p spectra of Pd/TPDMT monolayers before and after nickel evaporation	105
6.20	Variation of the Pd _{3d} and Cl2p XPS intensity of Ni/Pd/TPDMT monolayers with nickel doses	106
6.21	XPS Ni2p normalised intensities of the NiCl and Ni ⁰ peaks of Ni/Pd/TPDMT at various nickel doses	107
6.22	Model for the deposition of nickel on Pd/TPDMT SAMs	107
6.23	C 1s HRXPS spectra of FTP3 SAMs at various metal doses	109
6.24	C K edge NEXAFS spectra of Ni/FTP3 at the magic angle	110
6.25	Deconvolution of the C K edge NEXAFS π^* region of Ni/FTP3 at the magic angle	110

6.26	Ni2p XPS spectra of Ni/FTP3 at low nickel coverage (< 3 ML)	112
6.27	F1s XPS spectra of Ni/FTP3 and Ni/F10H2 at various nickel doses.	112
6.28	C K edge NEXAFS difference spectra of FTP3 at different nickel doses	114
6.29	Variation of the C 1s XPS intensity as a function of the nickel dose at two different excitation energies	115
6.30	ISS spectra of Ni/FTP3 and Ni/TP3	116
6.31	S2p HRXPS spectra of Ni/FTP3/Au and Ni/F10H2/Au	117
6.32	Variation of the CF peak intensity with nickel dose for various crosslinked films .	118
6.33	ARXPS data (I_{Ni2p}/I_{C1s}) of a 30 mC/cm ² film at various nickel doses	119
6.34	Schematic representation of the deposition of nickel on FTP3 thin films	120
7.1	Molecular dipole of TP3 and FTP3 on a gold surface	122
7.2	In plane and out of plane configurations of TP3	123
7.3	Variation of the work function of fluorinated SAMs as a function of nickel thickness	123
7.4	Variation of the work function of the Ni/FSAM/Au system as a function of sput- tering time	125
7.5	AFM images of cobalt nanoparticles on PPP3 and CL-PPP3	126
7.6	SEM images of cobalt nanoparticles on PPP3 and CL-PPP3	127
7.7	SEM images of cobalt nanoparticles on TPDMT and CL-TPDMT	128
7.8	XPS C1s spectra of the different stages of the fabrication of an SMSM assembly	130
7.9	Extrapolation of the FTP2/Ni XPS C1s spectrum	131
7.10	Water contact angles at different stages of the fabrication of an SMSM assembly	131

Eidsstattliche Erklärung

Ich erkläre hiermit, dass ich die vorgelegte Dissertation selbst verfasst und mich keiner anderen als der von mir ausdrücklich bezeichneten Quellen und Hilfen bedient habe.

Heidelberg, den 30. Mai 2011

